Physical characterisation of near-Earth asteroids in search of the YORP effect

A thesis submitted for the degree of
Doctor of Philosophy

by

Lord Robin Dover

School of Physical Sciences

University of Kent
Canterbury
United Kingdom

March 2025

"A million people can call the mountains a fiction, yet it need not trouble you as you stand atop them"

- xkcd 154

DECLARATION

This thesis has not been submitted as an exercise for a degree at any other university. Except where stated, the work described therein was carried out by me alone.
I give permission for the Library to lend or copy this thesis upon request.

SIGNED:

ACKNOWLEDGEMENTS

First and foremost, I would like to thank my supervisor, Stephen Lowry, for his guidance, support, understanding, and encouragement over the course of the past ~~three~~ ~~four~~ ~~five~~ six years. Similarly, I would like to thank Agata Rożek for going above and beyond in supporting me throughout everything, including my never-ending pleas for help with `convexinv` and `SHAPE`. I must also thank Tarik Zegmott for all of the above, particularly in regard to the La Palma trips where he turned me into a competent observer.

I would like to thank the Science and Technology Facilities Council and the University of Kent for providing a scholarship to fund this work, along with all of the staff that supported me. I am grateful to Penny Wozniakiewicz and James Burt for helping me navigate the more turbulent moments of the past few years; to Hannah Tonry for all the outreach fun; and to Tim Kinnear for his computational wizardry and delightfully long-winded discussions about aeroplanes.

My gratitude extends to my (somewhat virtual) officemates: to Sam Jackson for his constant supply of tailored YORP memes and 24/7 asteroid chats; to Niall Miller for his enlightened approach to all things (especially flat-fielding); to David Campbell for letting me write these words at work; and to Sam Rolfe for making sure that I do.

None of this would have been possible without the support of my family and friends. I will forever be indebted to them for their generosity and kindness - so I shall preemptively forgive them for not making it past the abstract. Sincerely, it means a lot to be supported by someone when they don't even understand what you're doing or why it's taking so long.

I'd especially like to thank my parents, for always encouraging me to be curious and do what I love.

Finally: thank you, Alisha. You are the most patient partner in the universe, and I never would have made it without you. I would have to write another thesis to list all things I should thank you for - but I think you'd prefer it if I didn't 🙂

ABSTRACT

The Yarkovsky–O'Keefe–Radzievskii–Paddack (YORP) effect is a thermal recoil force that is experienced by small bodies when they re-emit energy absorbed from sunlight. Due to the complex shapes and surfaces of asteroids, this re-emission is anisotropic, causing a torque that can modify an asteroid's rotation rate and spin-axis orientation. This effect, which is loosely analogous to a windmill, has a profound influence on the evolution of the Solar System.

In order to better understand the YORP effect, it must be measured for a large number of asteroids. Almost 25 years since it was first predicted, the YORP effect has been observationally detected with twelve asteroids. Measuring the YORP effect requires that an asteroid is monitored over a significant period of time, and the asteroid must be well-characterised before it can be assessed for YORP. This means that the shapes, spin rates, and spin-axis orientations of asteroids must be measured, often requiring the use of both optical and radar observations.

This thesis presents the results of a project to characterise four asteroids and search for evidence of the YORP effect acting upon them. This work forms part of a larger research collaboration, originating with a European Southern Observatory (ESO) Large Programme (LP) to monitor 40 near-Earth asteroids. The asteroids considered in this work are (23187) 2000 PN9, (29075) 1950 DA, (85275) 1994 LY, and (159402) 1999 AP10. The results presented here include an independently-developed shape model for

each of these asteroids, and a comprehensive search for signs of YORP-driven rotational acceleration.

For (23187) 2000 PN9, a high-resolution shape model was developed using a combination of optical lightcurves and planetary radar observations. A spin-state analysis shows that the asteroid is in a state of constant-period rotation, with any undetected YORP acceleration being significantly constrained. The asteroid is found to be YORP-evolved, and bears a striking resemblance to other asteroids with 'YORPoid' morphologies.

Following a previously reported indication of YORP acting upon (29075) 1950 DA, this work includes an extensive campaign to follow up and confirm a detection of rapid rotational deceleration. The previously reported measurement is verified and constrained by this work, using both previously published and newly developed shape models with a mix of old and new datasets. Two possible explanations are offered for the peculiar result: either there is a previously overlooked flaw in the tools and methods used to characterise asteroids, or this is the first detection of a hitherto unknown physical phenomenon.

Finally, analyses of (85275) 1994 LY and (159402) 1999 AP10 fail to detect YORP, but the asteroids are characterised and constraints are placed on any potential YORP acceleration. 1994 LY provides a good example of YORP false positives, and the results of this work will be beneficial to future studies of the asteroid system. The model of 1999 AP10 developed for this work has already contributed to significant results, and proves the viability of developing physical models using small optical telescopes over relatively short timescales.

Like many theses, this work ultimately raises more questions than it answers. The results for 2000 PN9 are conclusive, while an exhaustive analysis of 1950 DA has only deepened the mystery surrounding its rapid spin-down. 1994 LY and 1999 AP10 have been analysed as far as is sensible with existing data, but are shown to be worthy of further study when they are next observable.

CONTENTS

Declaration **i**

Acknowledgements **ii**

Abstract **iii**

List of Tables **x**

List of Figures **xv**

Publications **xvi**

1 Small bodies in the inner Solar System **1**

1.1 Formation of the Solar System 2

1.2 Asteroids in the inner Solar System 6

1.2.1 Surveying the physical properties of asteroids 9

1.2.2 The spin barrier 13

1.3 The thermal response of asteroids 16

1.3.1 The Yarkovsky effect 16

1.3.1.1 Implications of the Yarkovsky effect 20

1.3.1.2 Measuring drift rates . . . 22
1.3.2 The YORP effect . . . 24
1.3.2.1 Implications of the YORP effect . . . 26
1.3.2.2 Advances in YORP research . . . 31
1.3.2.3 Direct detection . . . 34

2 Observing near-Earth asteroids in search of YORP 39

2.1 Overview . . . 40
2.2 Photometric lightcurve observations . . . 41
2.2.1 The YORP campaign . . . 41
2.2.1.1 Telescopes used in the YORP campaign . . . 42
2.2.1.2 Other sources for lightcurves . . . 48
2.2.2 Conducting observations of NEAs . . . 48
2.2.3 Data reduction . . . 55
2.2.3.1 Asteroid lightcurve extraction using relative photometry 60
2.3 Planetary radar . . . 69
2.3.1 Facilities . . . 70
2.3.2 Radar observations . . . 73
2.3.2.1 Continuous wave spectra . . . 74
2.3.2.2 Delay-Doppler imaging . . . 77

3 Physical modelling and YORP analysis of near-Earth asteroids 80

3.1 Convex inversion of optical lightcurves . . . 81
3.1.1 Measuring shape with `convexinv` . . . 83
3.1.2 Period determination . . . 86
3.1.3 Pole and shape optimisation . . . 89
3.1.4 Fitting for YORP . . . 90
3.2 Modelling with radar data . . . 94

3.2.1 Input files for SHAPE . . . 95
3.2.1.1 Parameter (par) file . . . 96
3.2.1.2 Model (mod) file . . . 97
3.2.1.3 Observation (obs) file . . . 101
3.2.2 Developing a shape model . . . 101
3.3 Searching for YORP . . . 106
3.3.1 Simulating asteroid lightcurves . . . 107
3.3.1.1 Ray tracing for non-convex shapes . . . 110
3.3.2 Measuring rotational acceleration via phase offset anaylsis . . . 114

4 Optical and radar observations of (23187) 2000 PN9 117

4.1 Introduction . . . 118
4.2 Observations of 2000 PN9 . . . 120
4.2.1 Optical lightcurves . . . 121
4.2.2 Radar data . . . 128
4.3 Physical modelling . . . 129
4.3.1 Modelling with lightcurves . . . 129
4.3.2 Modelling with radar . . . 133
4.3.2.1 Differences and limitations of the models . . . 139
4.4 Disk-integrated properties . . . 141
4.5 Geophysical properties . . . 143
4.6 YORP analysis . . . 145
4.7 Discussion . . . 147
4.7.1 YORPoids . . . 148
4.7.1.1 Future work . . . 151

5 Rotational deceleration of (29075) 1950 DA 153

5.1 Introduction . . . 154

5.1.1 Prior investigation 156
5.2 Follow-up campaign 160
5.2.1 Phase offset analysis 166
5.2.2 Convex inversion analysis 168
5.2.2.1 Phase offsets with the convex model 172
5.3 Discussion 173
5.3.1 Future work 175

6 YORP analyses of 1999 AP10 and 1994 LY 178
6.1 Introduction 179
6.2 1999 AP10 179
6.2.1 Observations of 1999 AP10 181
6.2.2 Physical modelling 187
6.2.2.1 Phase offsets & discussion 189
6.3 1994 LY 193
6.3.1 Observations of 1994 LY 194
6.3.2 Physical modelling 200
6.3.2.1 Phase offsets & discussion 202

7 Conclusions & future work 206
7.1 Summary of findings 207
7.2 The future of asteroid characterisation & YORP research 211
7.2.1 Missions to small bodies 212
7.2.2 Future observatories 214
7.2.3 Modelling and theory 218

Bibliography 223

Acronyms 265

A Supplementary figures and tables **270**

B File formats for modelling procedures **299**

LIST OF TABLES

1.1 List of published YORP detections 38

4.1 Optical lightcurves of 2000 PN9 125

4.2 Radar observations of 2000 PN9 127

4.3 Geometric properties of 2000 PN9 138

4.4 Comparison of top-shaped NEAs 149

5.1 Optical lightcurves of 1950 DA 164

5.2 Summary of YORP measurements for 1950 DA 175

6.1 Optical lightcurves of 1999 AP10 184

6.2 Optical lightcurves of 1994 LY 197

A.1 Targets for the YORP observing campaign 272

LIST OF FIGURES

1.1 ALMA image of HL Tauri 4

1.2 Orbital distribution of asteroids in the inner Solar System 5

1.3 Map of asteroids in the Solar System 6

1.4 NEA discovery statistics 8

1.5 SPHERE imaging of four asteroids 10

1.6 Comparison between models of 2001 KZ66 13

1.7 Spin rate vs. diameter for asteroids in the Solar System 14

1.8 The diurnal Yarkovsky effect 19

1.9 The seasonal Yarkovsky effect 19

1.10 The V-shaped spread of an asteroid family 21

1.11 Yarkovsky drift of (6489) Golevka 23

1.12 YORP acting on a simple winged sphere 25

1.13 Simulated obliquity dependence of YORP 27

1.14 YORP dependence on thermal conductivity 28

1.15 A collection of top-shaped asteroids 30

1.16 Changes in the directly measured period of 2000 PH5 due to YORP . . 36

1.17 Phase offset due to YORP for 2000 PH5 36

2.1 The Galileo National Telescope 44
2.2 The Very Large Telescope 45
2.3 The Isaac Newton Telescope 46
2.4 The Isaac Newton Group of Telescopes 47
2.5 Observability information for 1950 DA 50
2.6 An example airmass plot 52
2.7 Example finder charts 53
2.8 A demonstration of CCD image reduction 58
2.9 Starlink satellite trails 61
2.10 Raw vs. relative lightcurve 62
2.11 Background star selection 64
2.12 Point Spread Functions 65
2.13 Radar detections of asteroids since 1980 71
2.14 The William E. Gordon telescope 73
2.15 Goldstone Solar System Radar 74
2.16 Example cw spectrum 76
2.17 Delay-Doppler image mapping 78
2.18 Delay-Doppler images of 2003 SD220 79

3.1 Example of a periodogram 88
3.2 Results from a convex inversion pole scan 90
3.3 Example of a convex hull model 91
3.4 Example of a YORPogram 93
3.5 Visualisation of YORP scan planes 94
3.6 Diagram of a shape model facet 107
3.7 Diagram of facet blocking parameters 111

3.8 Ray tracing schematic 112
3.9 Example synthetic lightcurves 113
3.10 Example of a phase offset diagram 115

4.1 Orbit of 2000 PN9 119
4.2 Observing geometries for 2000 PN9 120
4.3 INT lightcurve of 2000 PN9 124
4.4 Period scan for 2000 PN9 130
4.5 Convex inversion pole scan of 2000 PN9 131
4.6 Convex hull model of 2000 PN9 133
4.7 Radar period scan of 2000 PN9 135
4.8 Lightcurve and radar pole scan of 2000 PN9 136
4.9 Comparison of prograde and retrograde model synthetic lightcurves for 2000 PN9 137
4.10 Synthetic lightcurves of 2000 PN9 138
4.11 Combined radar and lightcurve shape model of 2000 PN9 139
4.12 Combined radar and lightcurve shape model of 2000 PN9 140
4.13 Geophysical analysis of 2000 PN9 144
4.14 Phase offset analysis for 2000 PN9 146

5.1 Orbit of 1950 DA 155
5.2 Combined radar and lightcurve shape model of 1950 DA 158
5.3 1950 DA phase offsets from Zegmott (2021) 159
5.4 Projected phase offsets for 1950 DA 161
5.5 Observing geometries for 1950 DA 162
5.6 Example lightcurve fit for the convex model of 1950 DA 167
5.7 Phase offsets for 1950 DA (2019-2021, radar model) 167
5.8 Period scan for 1950 DA 169

5.9 Convex inversion pole scan of 1950 DA 169
5.10 YORP scan of 1950 DA 170
5.11 Convex hull model of 1950 DA 171
5.12 Example lightcurve fit for the convex model of 1950 DA 172
5.13 Phase offsets for 1950 DA (2019-2021, convex model) 173

6.1 Orbit of 1999 AP10 180
6.2 Delay-Doppler image of 1999 AP10 181
6.3 Observing geometries for 1999 AP10 182
6.4 Period scan for 1999 AP10 188
6.5 1999 AP10 YORPogram 189
6.6 Convex inversion pole scan of 1999 AP10 190
6.7 Convex hull model of 1999 AP10 191
6.8 Phase offsets for 1999 AP10 192
6.9 Example lightcurve fit for the model of 1999 AP10 192
6.10 Orbit of 1994 LY 193
6.11 Observing geometries for 1994 LY 195
6.12 Period scan for 1994 LY 200
6.13 Convex inversion pole scan of 1994 LY 201
6.14 1994 LY YORPogram 202
6.15 Convex hull model of 1994 LY 203
6.16 Convex hull model of 1994 LY 204
6.17 Example lightcurve fit for the model of 1994 lying 204
6.18 Phase offsets for 1994 LY 205

7.1 2000 PN9 compared to other YORPoids 208
7.2 Comparison of 1950 DA phase offset YORP fits 209
7.3 A montage of asteroid models 211

7.4 Green Bank radar image of the Moon 217

A.1 Map of asteroids in the Solar System 271

A.2 Synthetic lightcurves for the lightcurve-only model of 2000 PN9 273

A.3 Delay-Doppler fits for Goldstone observations of 2000 PN9 in 2001 . . . 276

A.4 Delay-Doppler fits for Arecibo observations of 2000 PN9 in 2001 277

A.5 Delay-Doppler fits for Goldstone observations of 2000 PN9 in 2006 . . . 278

A.6 Delay-Doppler fits for Arecibo observations of 2000 PN9 in 2001 279

A.7 cw spectra fits for Arecibo observations of 2000 PN9 in 2001 280

A.8 cw spectra fits for Arecibo observations of 2000 PN9 in 2001 281

A.9 Synthetic lightcurves for the `SHAPE` model of 2000 PN9 282

A.10 Synthetic lightcurves for Zegmott's model of 1950 DA 285

A.11 Synthetic lightcurves for the convex model of 1950 DA 287

A.12 Synthetic lightcurves for the convex model of 1999 AP10 290

A.13 Synthetic lightcurves for the convex model of 1994 LY 295

B.1 Standard lightcurve file format 300

B.2 Lightcurve input file for `convexinv` 302

B.3 Example of a `SHAPE` parameter file 303

B.4 Example of a `SHAPE` model file 304

B.5 Example of a `SHAPE` obs file 305

PUBLICATIONS

During the course of this work.

Refereed publications

M. Brozović et al. including **L. Dover**. Radar and Optical Observations and Physical Modeling of Binary Near-Earth Asteroid 2018 EB.
The Planetary Science Journal, May 2024, Volume 5, Issue 5, pp. 123-146

C. Herbert et al. including **L. Dover**. A survey for variable young stars with small telescopes: IX - Evolution of Spot Properties on YSOs in IC 5070.
Monthly Notices of the Royal Astronomical Society, April 2024, Volume 529, Issue 4, pp. 4856-4878

D. Froebrich et al. including **L. Dover**. A survey for variable young stars with small telescopes: VIII – Properties of 1687 Gaia selected members in 21 nearby clusters.
Monthly Notices of the Royal Astronomical Society, April 2024, Volume 529, Issue 2, pp. 1283-1298

L. Dover, S. C. Lowry, A. Rożek et al. Physical modelling of near-Earth asteroid (23187) 2000 PN9 with ground-based optical and radar observations.
Monthly Notices of the Royal Astronomical Society, November 2023, Volume 525, Issue 3, pp. 4581-4595
(Based on Chapter 4 of this thesis)

D. Froebrich et al. including **L. Dover**. A survey for variable young stars with small telescopes - VI. Analysis of the outbursting Be stars NSW284, Gaia19eyy, and VES263.
Monthly Notices of the Royal Astronomical Society, April 2023, Volume 520, Issue 4, pp. 5413-5432

A. Rożek, S. C. Lowry, B. Rozitis, **L. R. Dover** et al. Physical properties of near-Earth asteroid (2102) Tantalus from multi-wavelength observations.
Monthly Notices of the Royal Astronomical Society, July 2022, Volume 515, Issue 3, pp. 4551-4564

S. L. Jackson, B. Rozitis, **L. R. Dover** et al. The effect of aspect changes on Near-Earth Asteroid phase curves.
Monthly Notices of the Royal Astronomical Society, April 2022, Volume 513, Issue 2, pp. 3076-3089
(Based on Chapter 6 of this thesis)

D. Froebrich et al. including **L. R. Dover**. A survey for variable young stars with small telescopes - IV. Rotation periods of YSOs in IC 5070.
Monthly Notices of the Royal Astronomical Society, October 2021, Volume 506, Issue 4, pp. 5989-6000

J. J. Evitts et al. including **L. Dover**. A survey for variable young stars with small telescopes: II - mapping a protoplanetary disc with stable structures at 0.15 au.
Monthly Notices of the Royal Astronomical Society, March 2020, Volume 493, Issue 1, pp. 184-198

J. J. Evitts et al. including **L. Dover**. A survey for variable young stars with small telescopes: II - mapping a protoplanetary disc with stable structures at 0.15 au.
Monthly Notices of the Royal Astronomical Society, March 2020, Volume 493, Issue 1, pp. 184-198

Conference abstracts & posters

S. L. Jackson, B. Rozitis, **L. Dover** et al. The Dependence of Near-Earth Asteroid Phase Curves on Aspect Geometry.
Asteroids, Comets and Meteors Conference 2023

S. L. Jackson, B. Rozitis, **L. Dover** et al. Using Hapke Modelling to Probe Near-Earth Asteroid Phase Curves.
54th Annual DPS Meeting

A. McGilvray et al. including **L. Dover**. Shape Model of 2015 DP155 Using Radar and Lightcurve Observations.
54th Annual DPS Meeting

S. L. Jackson et al. including **L. Dover**. Phase Curve Variability of near-Earth Asteroids.
European Planetary Science Congress 2021

S. L. Jackson et al. including **L. Dover**. Phase Curve Variability of near-Earth Asteroids.
European Planetary Science Congress 2021

L. Dover, S. C. Lowry, A. Rożek et al. Physical modelling of YORP-evolved NEA (23187) 2000 PN9 from optical and radar observations.

Royal Astronomical Society Early Career Poster Exhibition 2020
(Based on Chapter 4 of this thesis)

L. Dover, S. C. Lowry, A. Rożek et al. Physical modelling of YORP-evolved NEA (23187) 2000 PN9 from optical and radar observations.
European Planetary Science Congress 2020
(Based on Chapter 4 of this thesis)

D. W. Repp et al. including **L. Dover**. Shape Modeling of Potentially Hazardous Asteroid 2015 DP155 from Radar and Lightcurve Observations.
51st Annual Lunar and Planetary Science Conference

R. Kokotanekova et al. including **L. Dover**. Testing the surface evolution hypothesis of JFCs with ground photometric observations.
EPSC-DPS Joint Meeting 2019

S. C. Lowry et al. including **L. Dover**. Physical Model of Near-Earth Asteroid (1917) Cuyo and Detection of a Mass-Lofting Event.
EPSC-DPS Joint Meeting 2019

A. Rożek et al. including **L. Dover**. Physical characterisation of near-Earth asteroid (2102) Tantalus from optical and radar observations.
EPSC-DPS Joint Meeting 2019

Observing proposals

L. Dover, S. C. Lowry, T. Zegmott. Detection of Rotational Deceleration due to the Asteroidal YORP Effect.
Isaac Newton Telescope (I/2021B/08) - 6 nights awarded

L. Dover, S. C. Lowry, T. Zegmott. Rotational deceleration of near-Earth asteroid 1950 DA due to the YORP effect.
William Herschel Telescope (SW2021a22) - 15 hours awarded

S. C. Lowry, **L. Dover**, T. Zegmott et al. Detection of Rotational Deceleration due to the Asteroidal YORP Effect.
Very Large Telescope (108.22L3) - 4 nights awarded

S. C. Lowry, **L. Dover**, A. Rożek et al. YORP-Induced Physical Evolution of Near-Earth Asteroids (23187) 2000 PN9 & (85275) 1994 LY.
New Technology Telescope (106.21C1) - 6 nights awarded

L. Dover, S. C. Lowry, A. Rożek et al. YORP-Induced Physical Evolution of Near-Earth Asteroids (23187) 2000 PN9 & (85275) 1994 LY.
Isaac Newton Telescope (I/2020B/05) - 4 nights awarded

S. C. Lowry et al. including **L. Dover**. Detection of a Mass Lofting Event on Asteroid Cuyo from YORP Rotational Spin-up.
New Technology Telescope (105.20E1) - 6 nights awarded, executed in P107

A. Rożek et al. including **L. Dover**. Direct Detections of the Asteroidal YORP Effect - Continued Photometric Monitoring.
Liverpool Telescope (PL/19B/17) - 21 hours awarded

T. Zegmott et al. including **L. Dover**. Physical Characterisation of the Near-Earth Asteroid (29075) 1950 DA.
Isaac Newton Telescope (I/2019B/12) - 3 nights awarded

T. Zegmott et al. including **L. Dover**. Physical Characterisation of the Near-Earth Asteroid (29075) 1950 DA and Detection of the YORP Effect.
Nordic Optical Telescope (19B/044) - 2 nights awarded

F. Marocco et al. including **L. Dover**. Understanding ultracool atmospheres with Gaia.
Very Large Telescope (0101.C-0717) - 29 hours awarded

CHAPTER 1

SMALL BODIES IN THE INNER SOLAR SYSTEM

1.1 Formation of the Solar System

The Solar System formed 4.6 billion years ago, when a molecular cloud underwent gravitational collapse. More than 99% of the cloud's mass went into the formation of the Sun, with remaining material collapsing into a circumstellar disk due to its initial angular momentum. This protoplanetary disk is the origin of most bodies in the Solar System*, beginning with the coagulation of dust particles to form planetesimals. This was followed by the formation of rocky planets, some of which went on to become the cores of the gas giants after accreting gas from the protoplanetary disk.

The growth of dust particles to kilometre-sized asteroids, and eventually planets, begins with collisional sticking of micron-sized dust particles in the protoplanetary disk. Low-energy impacts between silicate particles form fractal aggregates (Dominik and Tielens, 1997; Blum and Wurm, 2000), which drives the growth of particles to macroscopic scales. Particle growth beyond the millimetre or centimetre scale is severely limited by fragmentation and bouncing collisions (Güttler et al., 2010). It is possible that vertical mixing or radial drift allows centimetre-sized particles to sweep up reservoirs of smaller particles and grow directly into $\sim$ 100 m planetesimals (Windmark et al., 2012), but this is not sufficient to account for all planetesimals formed in the protoplanetary disk.

The particle growth barrier is overcome when particles are concentrated in high-density regions of the protoplanetary disk and undergo gravitational collapse. Turbulence driven by magnetorotational instability in the protoplanetary disk can create high-pressure regions, where planetesimals can grow to thousands of kilometres in size (Johansen et al., 2011). Instability in the protoplanetary disk can lead to the formation of large-scale vortices which trap dust particles and rapidly produce planetesimals in as little as five orbits (Lyra et al., 2009). Streaming instability also contributes to the rapid formation of planetary bodies, where high-density dust filaments decelerate

*It should be noted that a high fraction of Oort cloud objects may originate from other stellar systems (Levison et al., 2010).

surrounding gas, leading to runaway dust accumulation within the increasingly isolated filament (Youdin and Goodman, 2005; Johansen and Youdin, 2007).

As different volatiles condense to solid particles at different temperatures, the composition of a planetesimal can indicate where it formed in the Solar System. The snow line for each volatile constrains how close to the Sun a planetesimal could have been when it formed. In the inner Solar System, only silicate or metallic volatiles could condense due to their high melting points. The planetary embryos that formed from these materials were hence smaller than those that formed further from the Sun, where more solid material was available.

Under the core accretion model, the larger planetary embryos had sufficient gravitational strength to accrete significant volumes of gas from the protoplanetary disk. As the giant planets are primarily formed of hydrogen and helium, which were the most abundant gases in the protoplanetary disk, they must have formed before the disk dissipated. The ice giants, which have a higher core-to-envelope ratio than the gas giants, formed in regions of the disk where solid accretion was slower. This delayed the gas accretion, giving the planets less time to grow before the dissipation of the protoplanetary disk. Closer to the Sun, rocky planetary embryos continued to grow after the dissipation of the disk through solid accretion and collisions to form the terrestrial planets.

This paradigm of planet formation is unable to replicate the planetary configurations seen in both our Solar System and extrasolar systems. For example, simulations are unable to produce a Mars-sized planet, instead producing much larger planets in similar orbits (Raymond et al., 2009). The Grand Tack hypothesis (Walsh et al., 2011) resolves this by introducing the inward migration of the giant planets. After Jupiter cleared its own orbit in the disk (similar to the rings seen in Figure 1.1), it gravitationally interacted with surrounding gas resulting in a slow Sun-ward migration. This type of planetary migration may account for the abundance of 'hot Jupiter' exoplanets that have been observed. Jupiter's migration was, however, disrupted by the much faster

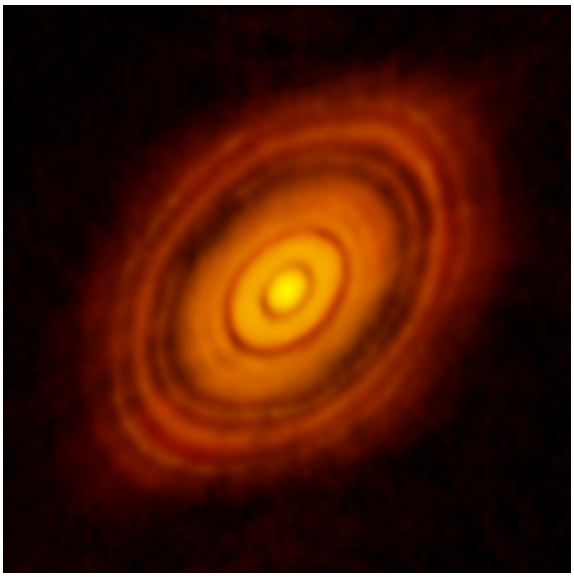

Figure 1.1: Atacama Large Millimeter Array (ALMA) image of HL Tauri and its protoplanetary disk. Bright regions show the presence of pebble-sized dust grains around the star. The ring-like gaps in the disk correspond to the orbits of large planetesimals or newly formed planets. The inner and outer diameters of the innermost ring are approximately equal to the orbits of Uranus and Neptune, respectively. This image is reprinted from the National Radio Astronomy Observatory[a].

[a] https://science.nrao.edu/facilities/alma/science_sustainability/hl-tau/view

inward migration of Saturn. It is thought that extrasolar systems with hot Jupiters are the result of undisrupted Sun-ward migration of gas giants. Jupiter and Saturn eventually migrated outwards, which the earlier Nice model (Gomes et al., 2005; Tsiganis et al., 2005; Morbidelli et al., 2005) describes through gravitational interactions with inner disk planetesimals. This migration halted when the disk dissipated, leaving Jupiter and Saturn in resonance close to their current orbits. The migration of Jupiter and Saturn caused significant disruption within the Solar System, scattering planetesimals such that a much smaller reservoir of solid material was available to an embryonic Mars.

The disruption caused by the migration of Jupiter and Saturn resulted in many planetesimals being ejected, while others survived in stable orbits to form the Main Belt (Petit et al., 2001; O'Brien et al., 2007; Raymond and Morbidelli, 2014). Crucially, a significant population of asteroids were also delivered to Earth-crossing orbits (Gomes et al., 2005). The present distribution of asteroids in the Solar System, shown in Figure 1.2, demonstrates Jupiter's continuing influence over small bodies. The Kirkwood gaps, which are seen between 1.8 AU and 4.3 AU, are regions of instability where asteroids are strongly perturbed by an orbital resonance with Jupiter. Phenomena such as asteroid

collisions and the Yarkovsky effect continue to deliver asteroids into the Kirkwood gaps, where they are quickly cleared. Some of these asteroids are ejected from the Solar System, while others can be injected to Earth-crossing orbits. Jupiter is thus a significant contributor to the ongoing replenishment of the potentially hazardous asteroid (PHA) population. A further example of Jupiter's influence on small bodies is the existence of the Trojan and Hilda asteroids, which can be clearly seen in Figure 1.3. The Trojan asteroids librate around Jupiter's L_4 and L_5 points, while the Hilda group is in a 3:2 orbital resonance with Jupiter.

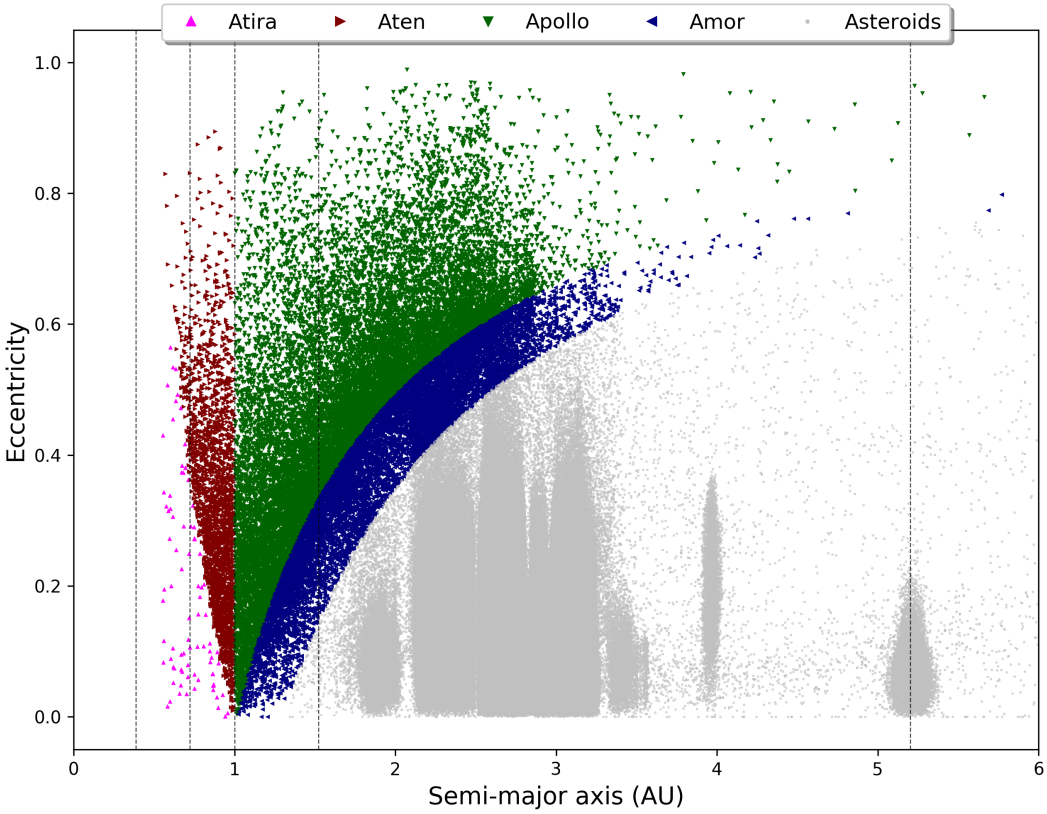

Figure 1.2: The distribution of asteroids in the inner Solar System. Near-Earth objects are marked in colours corresponding to their orbital groups. Atira asteroids are marked in magenta, Atens in maroon, Apollos in green and Amor asteroids are in blue. Ungrouped asteroids are marked in grey. The semi-major axes of the planets are marked with dashed black lines. The Kirkwood gaps can be seen between 1.8 AU and 4.3 AU. This plot was generated using Jet Propulsion Lab (JPL) small body element tables[a].

[a] `https://ssd.jpl.nasa.gov/sb/elem_tables.html`

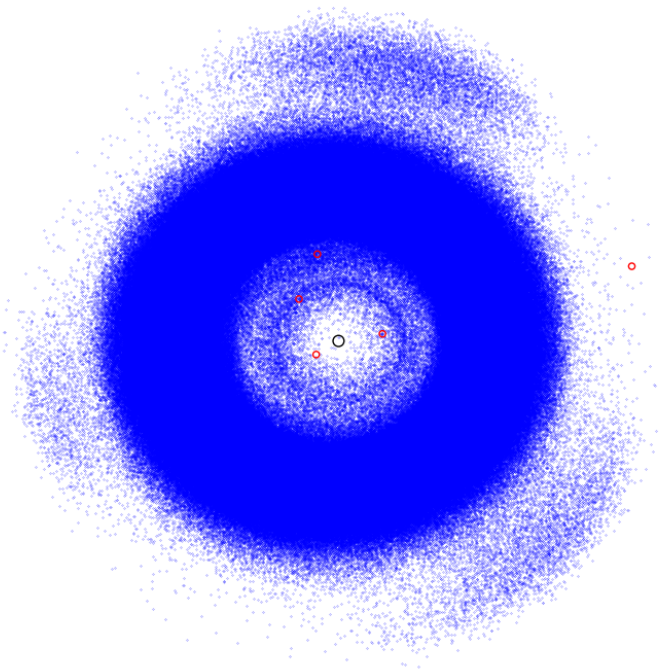

Figure 1.3: The location of every known minor planet in the inner Solar System (up to 5.5 AU). The Sun in marked in the centre with a black circle, planets are marked with red circles, and asteroids with blue points. In this view, the planets and most minor planets are orbiting in the anti-clockwise direction. The Jupiter Trojans can be seen 60° ahead and behind Jupiter, and the Hilda family can be seen opposite Jupiter. These images are reprinted from the Minor Planet Center[a]. See Figure A.1 for an expanded version of this figure showing the innermost and outer Solar System.

[a] https://www.minorplanetcenter.net/iau/lists/MPLists.html

1.2 Asteroids in the inner Solar System

Of the 1,269,215 small bodies reported by the Minor Planet Center, only 4,497 are comets. Despite the cumulative mass of the Kuiper Belt being two orders of magnitude greater than that of the Main Belt (Morbidelli et al., 2015; Di Ruscio et al., 2020), observational and research biases have resulted in the vast majority of catalogued Solar System small bodies (SSSBs) being asteroids belonging to three main groups: near-Earth asteroids (NEAs), main-belt asteroids (MBAs), and Trojans. Bodies belonging to other groups - such as Kuiper belt objects (KBOs) and Trans-Neptunian objects (TNOs) - remain severely under-represented in the known SSSB population. As this project is centred on NEAs, further discussion will henceforth focus on asteroids in the inner Solar System.

There are four orbital subgroups of NEAs, defined by their semi-major axes (a) and perihelion or aphelion distances (q or Q). Two of these groups, the Apollo and Aten asteroids, are on Earth-crossing orbits. Apollo asteroids have a larger semi-major axis

than Earth's orbit, but with a perihelion distance that is lower than Earth's aphelion distance (a > 1.0 AU, q < 1.017 AU). Aten asteroids have a semi-major axis that is smaller than Earth's orbit, with an aphelion distance that is greater than Earth's perihelion distance (a < 1.0 AU, Q > 0.983 AU). Amor asteroids have orbits that are entirely exterior to the Earth's orbit, but within the orbit of Mars (1.017 AU < q < 1.3 AU, a > 1.0 AU). Atira asteroids have orbits that are entirely contained within Earth's orbit (a < 1.0 AU, Q < 0.983 AU).

There are various motivations for studying NEAs, with the most paramount incentive being the mitigation of asteroid impacts. As evidenced by the Tunguska and Chelyabinsk events, asteroids pose a threat to life and property on Earth. Asteroid research contributes to planetary defence through the discovery, tracking and characterisation of PHAs. Early discovery and tracking is essential when assessing and responding to impact hazards (Harris et al., 2015), which has lead to various large NEA discovery surveys such as Lincoln Near Earth Asteroid Research (LINEAR), the Catalina Sky Survey, and Panoramic Survey Telescope and Rapid Response System (Pan-STARRS), which are collectively responsible for 84% of NEA discoveries seen in Figure 1.4. Physical modelling contributes to planetary defence through the provision of shape, size and spin-state measurements that are essential to the successful execution of asteroid deflection missions, as has been demonstrated with the Double Asteroid Redirection Test (Cheng et al., 2018; Naidu et al., 2020).

The determination of an asteroid's chemical composition, and its formation mechanism, can reveal the conditions under which it formed. This information is valuable when developing models for Solar System evolution and planet formation (Morbidelli et al., 2015; Johansen et al., 2015). Following the formation of the planets, asteroids continued to influence the development of life on Earth. It has been proposed that the prerequisite materials for abiogenesis, including water and various 'building block' molecules, were delivered to Earth via asteroid impacts (Sarafian et al., 2014; Oba et al., 2022). Later impacts are thought to have affected the development of life, as has

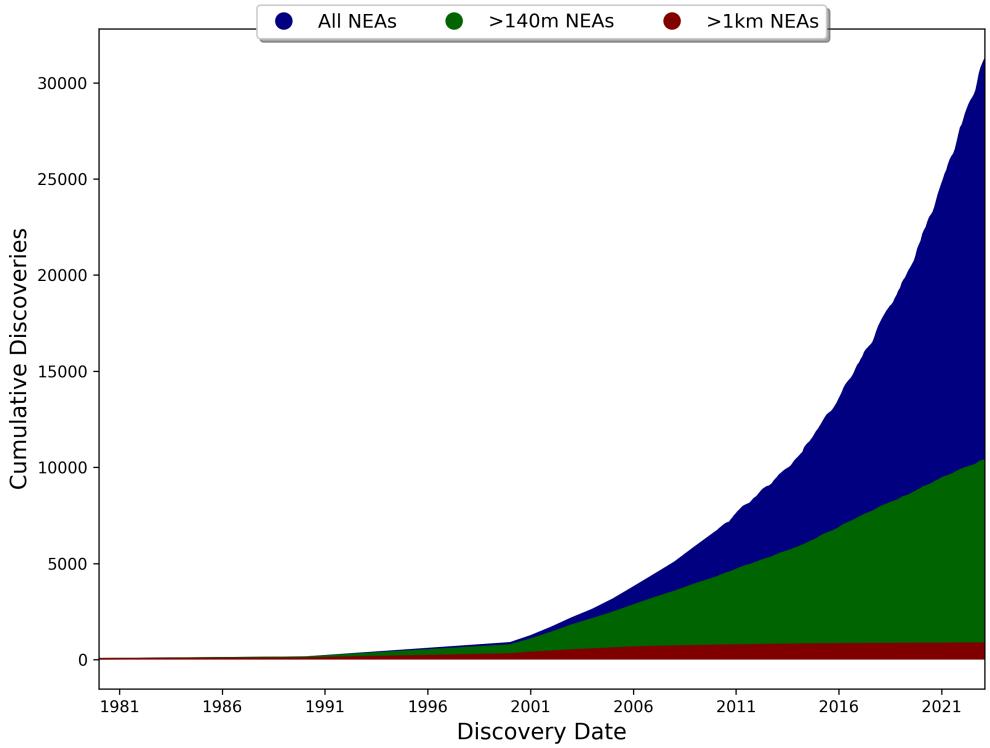

Figure 1.4: The cumulative number of discovered NEAs against time. The maroon and green regions represent the cumulative total discoveries with diameters greater than 1 km and 140 m, respectively. The blue region represents all discovered NEAs. This figure was created using data provided by the Center for Near Earth Asteroid Studies[a].

[a] `https://cneos.jpl.nasa.gov/stats/`

been demonstrated with the link between the Chicxulub impact and the K-T extinction event (Schulte et al., 2010).

Practical considerations make NEAs particularly attractive targets for research. Firstly, their proximity to Earth leads to a higher apparent brightness and a wider range of possible viewing geometries. This makes them excellent targets for ground-based observations, where even the smallest ($\sim$ 0.5 m) research telescopes are able to routinely make useful measurements. Secondly, NEAs are among the easiest bodies in the Solar System to reach with spacecraft, with shorter journey times and more forgiving mass budgets than missions to the outer Solar System. Advances in mission planning mean that a single mission can visit multiple asteroids to perform a flyby or

rendezvous (Barucci et al., 2011; Englander et al., 2017; Olkin et al., 2021). Because small bodies have very low escape velocities, sample return missions can be performed using only a fraction of the fuel that would be required to return from a major planetary body. The relative novelty of missions to small bodies, combined with the number and variety of objects, means that relatively simple instrument packages are able to yield impactful results. All of these factors combine to present a high ratio of science return to mission expenditure for NEA missions.

1.2.1 Surveying the physical properties of asteroids

Upon discovery, asteroids are tracked by a variety of facilities in order to determine their orbital and physical characteristics. Perhaps the most important measurements are diameter and spectral type, in both the contexts of planetary defence and asteroid research.

A wide range of surface compositions are seen among asteroids, which are categorised into taxonomic types based on their reflectance spectra, broadband photometric colours, and albedo. The most widely used taxonomic systems are the Tholen (Tholen, 1984) and Bus-DeMeo (DeMeo et al., 2009) classifications. Asteroids are divided into groups, and sub-groups, based on spectral characteristics that are taken to be proxies for mineralogy. The NEA population is dominated by two spectral classes: the S-type and C-type. S-type, or 'stony' asteroids have a siliceous mineralogy that produces a moderately steep reddish spectral slope and a relatively high albedo. C-type, or 'carbonaceous' asteroids have a composition rich in carbon and other volatiles, producing a relatively flat, featureless spectrum with a darker surface. Subgroups of these classes exist to intermediate between other, spectral types, with objects in these sub-groups being transitional members that have undergone varying degrees of space weathering or thermal processing. For example, the Sq-type describes objects that exhibit both S- and Q-type spectral features.

Very few observational facilities are able to optically resolve asteroids. While high

performance adaptive optics systems such as the Very Large Telescope's (VLT's) Spectro-Polarimetric High-contrast Exoplanet Research instrument (SPHERE) are capable of directly measuring asteroid size and shape (Vernazza et al., 2021), this is limited to relatively few objects and is generally limited to bodies that are tens of kilometres across. Stellar occultations provide further opportunity for direct measurements of size and shape (Millis et al., 1987; Ďurech et al., 2011), however these events are relatively uncommon and again limited to larger bodies.

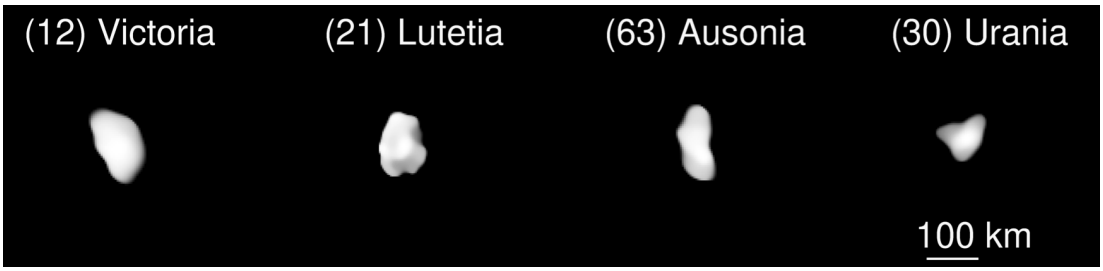

Figure 1.5: Deconvolved imaging of four asteroids from VLT/SPHERE. This figure was reprinted from Vernazza et al. (2021).

Radar observations (see Section 2.3) are more productive when it comes to the direct measurement of asteroid sizes and shapes. Planetary radar facilities have detected over 1,000 asteroids, providing well-constrained diameters for many of them. A portion of these asteroids have been directly imaged with spatial resolutions ranging between 5 and 100 metres, allowing for detailed physical modelling. Power limitations restrict these observations of asteroids to those that are within tens of lunar distances of Earth, meaning that radar observations are also only able to sample a small portion of the total asteroid population.

With so few ground-based facilities that are capable of resolving asteroids, the vast majority of asteroid size and shape estimates are derived from photometric measurements using optical and infrared telescopes. For a spherical asteroid, the diameter D is a function of visual geometric albedo ρ_v and absolute magnitude H:

$$D = \frac{1329}{\sqrt{\rho_v}} \, 10^{-0.2H} \tag{1.1}$$

The visual geometric albedo ρ_v describes the fraction of visible-wavelength light (measured in the Johnson V filter) that is reflected by the asteroid's surface, assuming Lambertian scattering from a flat disk with an equivalent cross-section. An asteroid's albedo can be measured using radiometric and polarimetric measurements (Chapman et al., 1975), but this is impractical for large samples. Instead, albedos are typically set to representative values for the asteroid's taxonomic class, which will be determined using spectra or broadband photometric colours (Tholen, 1984; Bus and Binzel, 2002).

The absolute magnitude H is the V-band magnitude that would be observed from Earth when the heliocentric distance $R_\odot$ and geocentric distance $R_\oplus$ are both 1 AU, and the phase angle $\alpha = 0$. The absolute magnitude H is thus an intrinsic value describing the asteroid. A measurement of the apparent magnitude V can hence be used to determine H using:

$$V(R_\odot, R_\oplus, \alpha) = H + 5\ log_{10}(\frac{R_\odot R_\oplus}{R_0^2}) - 2.5\ log_{10}\ q(\alpha) \tag{1.2}$$

Where $q(\alpha)$ is the phase integral and R_0^2 is a 1 AU conversion factor. The phase integral is related to the geometric albedo by $\rho_v = A_B/q(\alpha)$, where the Bond albedo A_B is the fraction of incident Solar radiation reflected by the surface across all wavelengths. Using this, photometric observations can be used to estimate diameters for most known SSSBs.

The next physical characteristic that is usually determined for an NEA is its rotation period. Repeated photometric measurements, typically taken over the course of several hours or nights, can be used to construct a lightcurve. This is easier for fast rotators[†], where several full rotations can be observed over the course of one night. Once several lightcurves have been taken, an asteroid's synodic period can quickly be determined using the Fourier analysis of lightcurves (FALC) technique (Harris et al., 1989), as described in Section 3.1. In cases where a large baseline can be achieved, a more

[†]In this work, 'fast rotator' generally refers to asteroids with rotation periods below ∼2.5 h

accurate result can be obtained using convex inversion (see Section 3.1) to determine the sidereal period. Period uncertainties for these bulk measurements vary, ranging from seconds to tens of minutes, which is generally sufficient for population statistics.

Lightcurve observations can also provide information about shape and spin orientation. A simple analysis of lightcurve amplitude can constrain an asteroid's axis ratios, while convex inversion techniques (see Section 3.1) can be used to measure the asteroid's rotational pole and construct a convex hull model of its shape. The DAMIT database (Durech et al., 2010) contains over 16,000 lightcurve-derived shape models for asteroids that do not otherwise have nonconvex shape models, which would have to be developed using radar, spacecraft, occultation or adaptive optics (AO) observations.

Large optical surveys for time-domain astronomy are increasingly contributing to the total sample of asteroids with modelled shape and spin-states. Observations from Gaia DR3 have been used to construct shape models for an additional ∼7,300 asteroids (Ďurech and Hanuš, 2023), while the upcoming Legacy Survey of Space and Time (LSST) is also expected to significantly expand the population of surveyed SSSBs.

While bulk measurements of the size, shape and spin of asteroids are useful, there are significant biases and limitations that one must consider before drawing conclusions. While there has not yet been a comprehensive debiasing of the characterised asteroid population, it is clear that observational limitations are a significant factor:

- Observations favour asteroids that make very close approaches to Earth. These objects have potentially been influenced by tidal forces during previous encounters.
- An asteroid's apparent brightness depends on its albedo and diameter, making larger or more reflective asteroids easier to observe.
- It is preferable to observe an asteroid over multiple viewing geometries when measuring phase curves, spin-states and shapes. This introduces a bias on obliquity, inclination, eccentricity and orbital period.

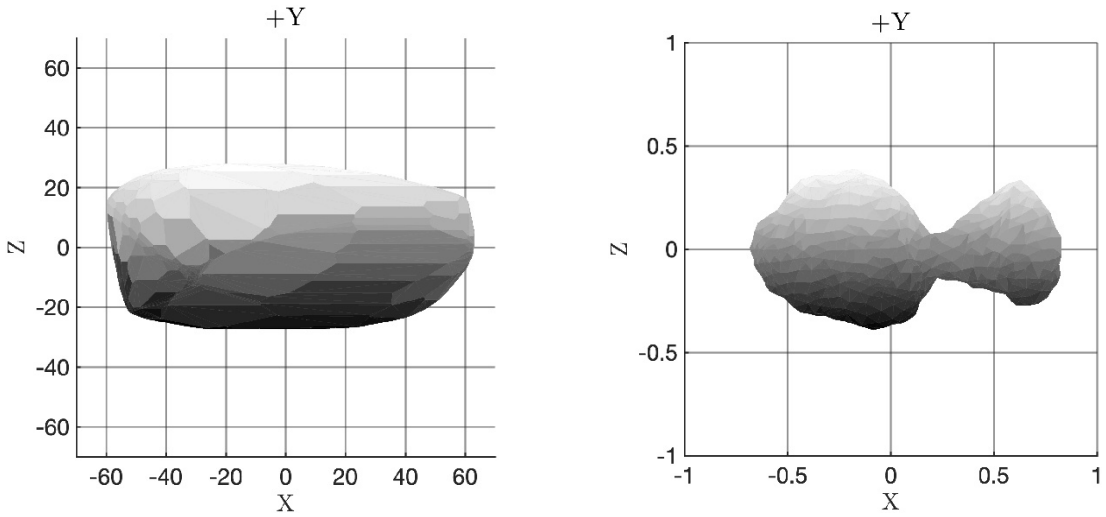

Figure 1.6: Convex hull (left) and radar (right) models of NEA 2001 KZ66. This figure was reproduced from Zegmott et al. (2021).

- Elongated shapes produce higher amplitude lightcurves, making them easier to observe and model than asteroids with more spherical shapes.
- Fast rotators are easier to observe, as one or more rotations can be captured in a single night.

In addition to these sampling biases, convex hull models do not provide detailed information about an asteroid's shape. As demonstrated in Figure 1.6, a lightcurve-derived model of 2001 KZ66 hides the fact that it is a bilobate body. The development of non-convex models is essential to understanding the true shape distribution - and hence formation and evolution - of NEAs. At the time of writing, only approximately 100 asteroids have non-convex models[‡].

1.2.2 The spin barrier

With a large population of asteroids that have known diameters and rotation rates, a relationship between the two quantities can be identified. Figure 1.7, which shows the spin rate and diameter for 18,669 asteroids, reveals a distinct lack of asteroids with a

[‡]`https://astro.troja.mff.cuni.cz/projects/damit/asteroid_models/index/sort:nonconvex/direction:desc`

period shorter than 2.2 h. First reported by Harris (1996), this spin barrier indicates that asteroids with a diameter above ∼200 m are predominantly rubble piles that would break up with faster rotation, while smaller fast-rotating objects must be monolithic to survive rapid rotation.

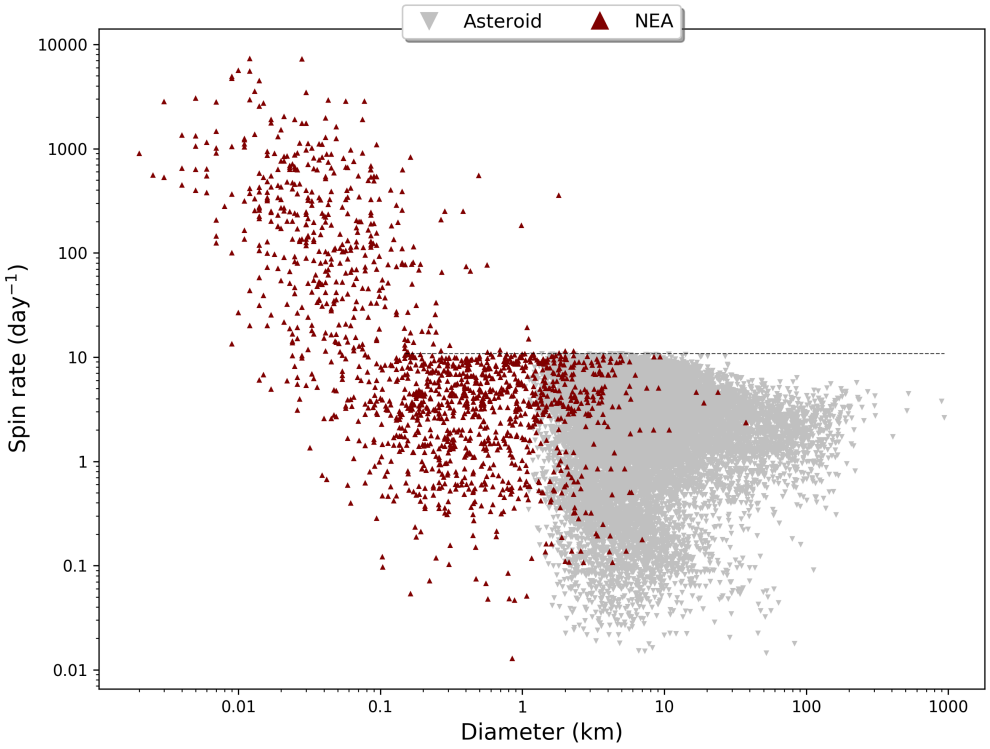

Figure 1.7: The distribution of spin rate and diameter for asteroids in the Solar System. Near-Earth asteroids are marked in maroon, while others (e.g. main-belt asteroids) are marked in grey. The spin-breakup barrier is highlighted with a dashed line. This plot was generated using data from the Small Body Database[a] and the Lightcurve Database (Warner et al., 2009).

[a] `https://ssd.jpl.nasa.gov/tools/sbdb_query.html`

Rubble pile asteroids can in fact survive beyond the 2.2 h spin limit, although this has rarely been seen. Holsapple (2007) finds that the spin limits of small (< 3 km) and large (> 10 km) asteroids are determined by different regimes. In small asteroids a strength regime applies, with even a small amount of internal strength being sufficient to support a body beyond the 2.2 h barrier. Perhaps the most well-known example of this is (29075) 1950 DA, whose rotational breakup is being prevented by the presence

of internal cohesive forces (Rozitis et al., 2014). In larger asteroids, where a gravity regime applies, internal forces become insignificant and the spin limit is determined by gravity.

The spin limit can be given by:

$$\omega_{strength} = C\sqrt{\frac{\kappa}{\rho}}(\bar{r})^{-5/4} \tag{1.3}$$

where C is a shape and friction coefficient, κ is the strength coefficient, ρ is the bulk density, and $\bar{r}$ is the mean radius. C is given by:

$$C = (\alpha\beta)^{1/3}\sqrt{\frac{5(3s(1+\beta^2) - \sqrt{3(1-\beta^2+\beta^4)})}{3s^2(1+\beta^2)^2 - 1 + \beta^2 - \beta^4}} \tag{1.4}$$

Where s is a coefficient of friction, and with the body aspect ratios $\alpha = c/b$ and $\beta = b/a$ (Holsapple, 2007).

The consequence of this is that rubble pile asteroids close to or beyond the 2.2 h barrier are small, near-spherical bodies supported by cohesive forces. The narrow transition region between stable spin configurations and breakup, where internal strength is almost entirely responsible for a body's survival, is especially important to the understanding of asteroid evolution. Studies of these near-breakup bodies provide insights into the internal structures of asteroids, while also furthering understanding of reshaping or mass lofting that might occur as a result of rapid rotation. Furthermore, it informs models of Solar System evolution that predict asteroid binary formation via the spin-breakup of small bodies. In Section 1.3.2.1, the behaviour of asteroids within this transition region, and the consequences of spin-breakup, are discussed more fully.

1.3 The thermal response of asteroids

The inner Solar System is not a peaceful place. Celestial bodies are subject to constant interference from external forces, whether that be through collisions, gravitational interactions, or insolation. Small asteroids, which are less massive, are the most affected by this.

Evolution of the orbit, shape and spin configuration of small bodies is dictated through these interactions. The aforementioned binary formation process (Section 1.2.2) relies upon an asteroid being driven through the spin barrier by external forces, as do the spin-down processes that produce extremely slow rotators. While collisions and gravitational interactions impart the greatest torques, they are impulsive and highly infrequent. Thermal radiation from the Sun, however, is constantly acting on every asteroid in the Solar System. The thermal response of an asteroid will result in changes to its orbit and spin-state via the Yarkovsky and YORP effects, which impart small but constant external forces to accelerate asteroids throughout their dynamical lives. Integrating these thermal forces over millions of years, they become the primary drivers of an asteroid's evolution.

1.3.1 The Yarkovsky effect

The Yarkovsky effect is named after Ivan Osipovich Yarkovsky (1844-1902), an accomplished Polish-Russian civil engineer who first described the effect. According to since abandoned theories of the luminiferous æther, celestial bodies should experience drag as they pass through a medium on their orbits around the Sun. Yarkovsky postulated that the seemingly eternal orbits of the planets are caused by another force that compensates for friction in the æther (Beekman, 2005).

The arrival of the Great September Comet (Penrose, 1882) highlighted the issue of planetary drag. As described by Beekman (2005), the comet was not decelerated during

its close approach to the Sun, where drag from the æther was thought to be significantly higher. While some saw this as a sign that the æther doesn't exist, Yarkovsky believed that the driving force had increased to counter the increased drag.

Yarkovsky identified that this driving force must be radiation pressure from the Sun, as it would be inversely proportional to the square of distance. This explains how the supposed driving and braking forces could remain balanced for Sun-grazing comets. In order to explain how this force acted against the direction of motion, instead of away from the Sun, Yarkovsky explained that the rotation of bodies allows them to absorb and store radiation then re-remit it behind them to produce an acceleration. While this theory is grounded in obsolete theories of physics, it correctly predicts a real natural phenomenon. A pamphlet describing this effect was distributed by Yarkovsky in 1901, however it was largely overlooked. Recalling the pamphlet from memory, Öpik (1951) reformulated the theory using modern physics to describe how rotating bodies absorb and re-emit thermal infrared photons, producing a small recoil force. Öpik named this process the Yarkovsky effect.

When thermal photons are absorbed by an asteroid, they are not immediately re-emitted. The delay between absorption and re-emission depends on the thermal inertia Γ of the asteroid, measured in J m^{-2} K^{-1} s$^{-1/2}$, which is given by:

$$\Gamma = \sqrt{K\rho C} \tag{1.5}$$

where K is the thermal conductivity of the surface (W m^{-1} K^{-1}), ρ is the asteroid's density (kg m^{-3}) and C is the specific heat capacity of the material on the surface (J kg^{-1} K^{-1}). The higher Γ is, the longer it takes for radiation to be re-emitted. Solar insolation is dependent on the semi-major axis (and eccentricity) of the asteroid's orbit, meaning that the effect is stronger in the inner Solar System. The acceleration experienced by an asteroid also depends on obliquity, period and spin-axis, as together with thermal inertia they determine the direction of the recoil force. As per the square-

cube law, the surface area to volume ratio of small asteroids means they experience the greatest acceleration from the Yarkovsky effect.

There are two components to the Yarkovsky effect, the first of which is a diurnal effect. Without thermal inertia, the hottest part of an asteroid's surface would always be the sub-Solar point. This would result in acceleration away from the Sun, due to the sunward direction of re-emitted radiation. Because asteroids do have significant thermal inertia, the surface is hottest during afternoon or evening. As shown in Figure 1.8, this causes a component of the recoil force to be tangential to the asteroid's orbital motion. With prograde rotation, this creates a driving force that raises the orbit of the asteroid. Conversely, retrograde rotation leads to a braking force that lowers the asteroid's orbit.

The second component is a seasonal effect, where axial tilt causes a temperature gradient across the asteroid's northern and southern hemispheres. Due to thermal inertia, a hemisphere is not at its hottest until after its pole is pointing towards the Sun. Because of this delay, the force arising from the re-emission of thermal radiation has a component that is tangential to the asteroid's orbit. This force will always reduce the asteroid's orbital velocity, regardless of the direction and rate of spin. This is illustrated in Figure 1.9, where the seasonal component is maximised due the body's spin-axis lying in the orbital plane.

When these components are combined, the net force will determine the acceleration - or Yarkovsky drift - of the asteroid. While it only produces small accelerations, the Yarkovsky effect plays a crucial role in the orbital evolution of the Solar System.

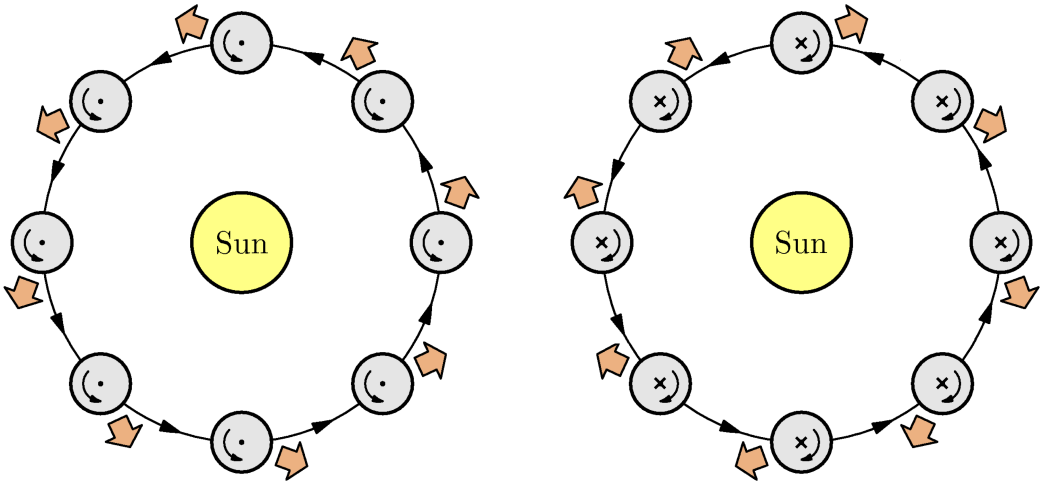

(a) Prograde rotation (b) Retrograde rotation

Figure 1.8: The diurnal component of the Yarkovsky effect, for a spherical object with 0° (prograde) and 180° (retrograde) obliquity in a circular orbit. The orange arrows show the direction in which the asteroid would be accelerated, which is opposite to the direction of the emitted radiation. In the case of (a), the asteroid's orbital velocity is increasing, so it will migrate outwards. In (b), the asteroid's semi-major axis is decreasing, so it will drift sunward. For both of these examples, there would be no seasonal component to the Yarkovsky effect as the axis of rotation is perpendicular to the orbital plane. This figure was reproduced with modification from Vokrouhlický et al. (2011).

Figure 1.9: The seasonal component of the Yarkovsky effect, for a spherical object in a circular orbit with its rotation axis in the orbital plane (90° obliquity). At points A and C, the southern and northern hemispheres are not heated respectively. This means that all reflected and re-emitted radiation at those points causes a recoil force away from the Sun, however this force averages to zero across one orbit. Due to thermal inertia, the poles are hottest at points B and D, which leads a temperature differential when the sub-Solar point is close to the equator. This results in a thermal recoil against the direction of travel, creating a braking force that lowers the asteroid's orbit. Unlike the diurnal component, the asteroid will migrate inwards regardless of whether its rotation is prograde or retrograde. In this idealised example, the diurnal component would not affect the asteroid's semi-major axis. This figure was reproduced from Vokrouhlický et al. (2011).

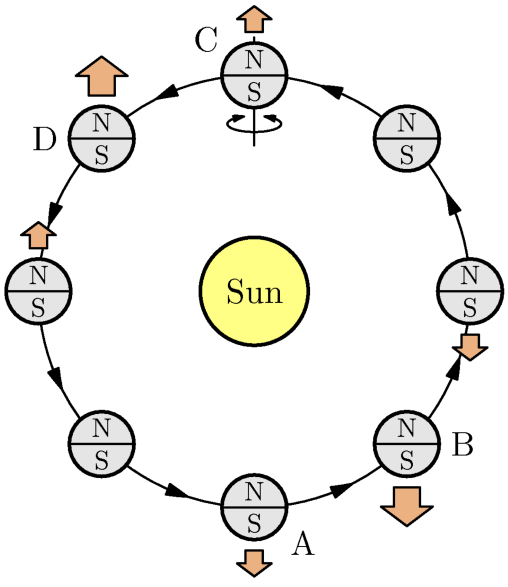

1.3.1.1 Implications of the Yarkovsky effect

The Yarkovsky effect can be used to explain various phenomena in the Solar System, whilst measurements of Yarkovsky drift can provide insight into an asteroid's physical properties.

The rate of lunar cratering has remained relatively consistent over the past 3 Gyr (Grieve and Shoemaker, 1994; McEwen et al., 1997), which implies that the population of near-Earth objects (NEOs) is being replenished at a steady state. With the main belt being the largest reservoir of small bodies in the inner Solar System, classical theories relied upon major collisions or gravitational perturbations to deliver NEAs to Earth-crossing orbits. These processes should rapidly inject bodies into near-Earth orbits, where they have relatively short lifetimes.

As explained in Bottke et al. (2006), this is contradicted by the cosmic ray exposure (CRE) ages of meteorites on Earth. Relatively few meteorites are found to have short (<10 Myr) CRE lifetimes, while iron meteorites are typically an order of magnitude older than stony meteorites. This suggests that the injection mechanism is slow, and strongly dependent on material composition. This is consistent with what would be expected for asteroids that are migrating via Yarkovsky drift; however, non-gravitational acceleration results in migration timescales that are too long for the observed meteorite flux.

Instead of direct inward migration via Yarkovsky drift, MBAs are delivered into resonance zones that transport them towards Mars and eventually Earth (Farinella and Vokrouhlicky, 1999). Contemporary studies of asteroid dynamics (e.g. Nesvorný et al. (2023)) now depend on non-gravitational forces to explain the current NEO population.

Upon delivery to an Earth-crossing orbit, the Yarkovsky effect remains crucial in the context of planetary defence. Including Yarkovsky drift in a PHA's orbit solution will improve its accuracy, which in some cases can have a significant influence on the impact probability (e.g. Vokrouhlický et al. (2015b)).

Aside from replenishment of the NEA population, the Yarkovsky effect plays a critical role in asteroid evolution through its influence on asteroid families. Formed by the collisional disruption of larger bodies, fragments of various sizes are initially dispersed through their post-impact velocity. As these families age, the Yarkovsky effect alters the semi-major axes of their constituent asteroids (Vokrouhlický et al., 2006a). Due to the dependence on diameter, the smaller asteroids become more widely spread. This results in a V-shape distribution of absolute magnitude (or inverse diameter) against semi-major axis, as shown in Figure 1.10.

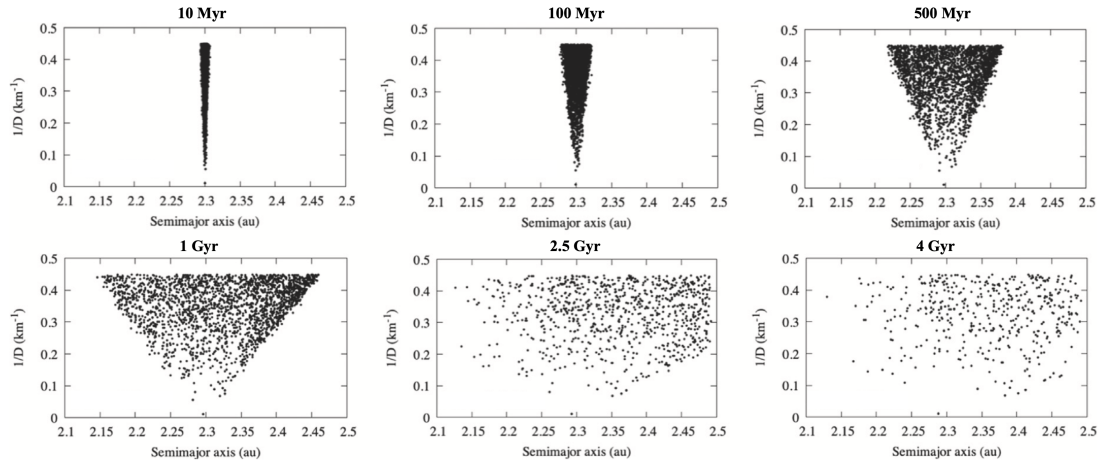

Figure 1.10: The inverse diameter (which is analogous to absolute magnitude) against semi-major axis for a simulated asteroid family as it ages. Smaller fragments experience the most Yarkovsky drift, resulting in a V-shaped spread that widens over time. This figure was reproduced with modification from Deienno et al. (2021).

The distribution of these V-plots can be used to determine the age of an asteroid family (Vokrouhlický et al., 2006b; Spoto et al., 2015; Ferrone et al., 2023). It is also possible to identify new asteroid families by searching for these V-shaped distributions (Carruba et al., 2019; Ferrone et al., 2023), which can be difficult to find amongst a busy MBA background.

In addition to implications on the dynamical history of small bodies, measurements of Yarkovsky drift can be used to constrain the physical properties of individual asteroids. Due to the obliquity dependence of the diurnal component of the Yarkovsky

effect, one can use absolute magnitude and the rate of change of semi-major axis ($\frac{da}{dt}$) to infer whether rotation is prograde or retrograde (Vokrouhlický et al., 2015b). If the diameter and spin-state are known, an asteroid's drift rate can be used to constrain its bulk density and thermal inertia (e.g. Chesley et al. (2003)).

1.3.1.2 Measuring drift rates

Chesley et al. (2003) made the first detection of the Yarkovsky effect, for the asteroid (6489) Golevka. Due to the superior accuracy of radar astrometry, its orbital solution was precise enough to model the asteroid's future position both with and without the influence of non-gravitational forces. Figure 1.11 shows the error ellipses in delay-Doppler space for the projected position of Golevka; the first (SUM1) includes astrometric uncertainty (OBS) and perturbations caused by gravitational interactions with small bodies (SBM) and planetary masses (PLM). SUM2 includes the aforementioned uncertainties plus Yarkovsky drift (and associated uncertainty YRK), which was modelled using the asteroid's shape and spin-state. New Arecibo astrometry in 2003, which was not included in the orbit solution, revealed that the Golevka lies within the error ellipse of SUM2 and has hence been subjected to non-gravitational acceleration due to the Yarkovsky effect. This confirmation of Golevka's orbital drift was used to constrain its bulk density and thermal inertia.

This method, which relies upon extensive radar observations and detailed physical modelling of the asteroid, is resource-intensive and cannot be applied to large samples of asteroids. Fortunately, it is not the only way to measure Yarkovsky drift. The Yarkovsky effect's influence on the orbital distribution of asteroid families, described in Section 1.3.1.1, can be used to measure the drift rate of family members. As they share a parent body, it is possible to calculate the drift rate that is required to change an object's semi-major axis from that of its parent body to the present-day value. This method was first used by Nesvorný and Bottke (2004), resulting in drift rates for ~ 70 MBAs.

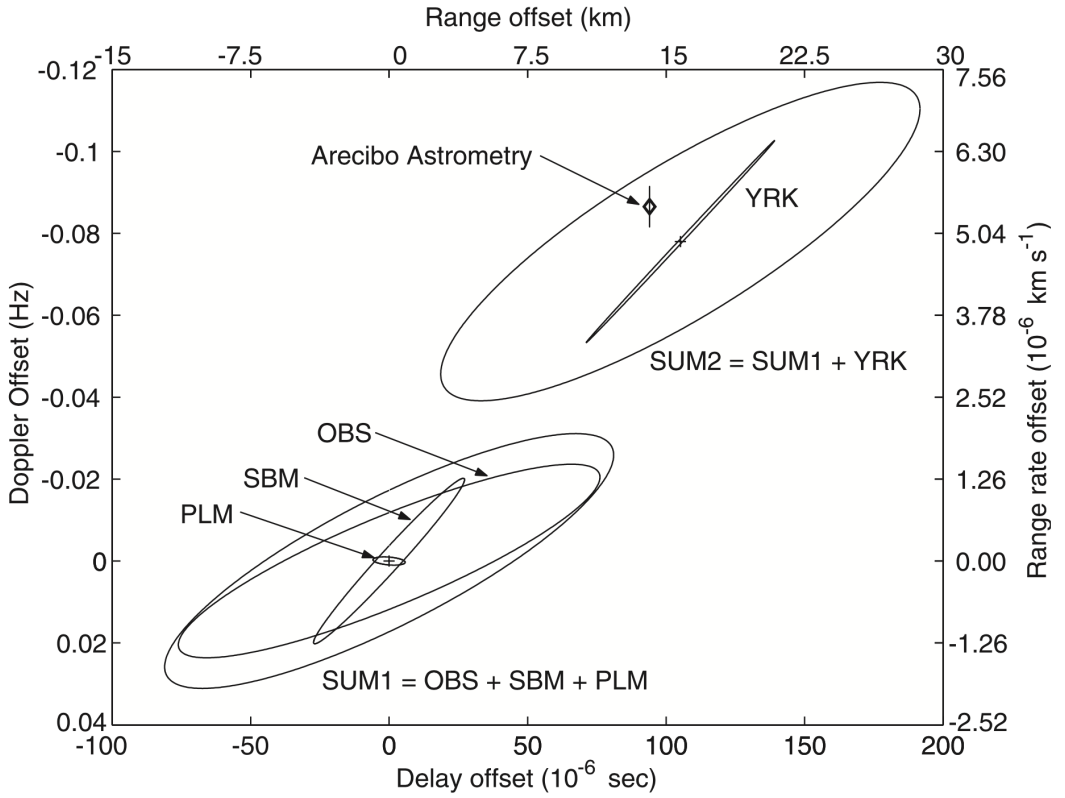

Figure 1.11: The first direct detection of the Yarkovsky effect, acting on (6489) Golevka, achieved through astrometry with radar imaging. The expected position of Golevka in radar delay-Doppler space is shown with purely gravitational (SUM1) and gravitational plus Yarkovsky (SUM2) forces acting upon it, with 90% confidence ellipses. The X axis denotes delay offset, which is also converted to range offset. The Y axis shows the Doppler offset, which is also converted to a range rate (radial velocity) offset. Gravitational interactions include both small body mass (SBM) and planetary mass (PLM) perturbations, with SUM2 also including uncertainty in the predicted Yarkovsky drift (YRK). The Arecibo measurement is marked with a diamond, showing that the observer-asteroid distance and relative velocity are consistent with a Yarkovsky-induced offset to the classical (i.e. purely gravitational) orbit model. This figure was reproduced from Chesley et al. (2003).

It is possible to more directly measure Yarkovsky drift through the analysis of astrometric data, avoiding the need for extensive modelling. This method allows for relatively large samples of asteroids to be analysed. An arbitrary transverse acceleration value is defined that is dependent on the orbital parameter A_2, which is the transverse non-gravitational acceleration parameter. This means that A_2 is proportional to the semi-major axis drift rate (Farnocchia et al., 2013). The ratio of A_2 and its uncertainty σ_{A_2} gives a signal-to-noise ratio for the Yarkovsky detection, for which

a minimum threshold can be defined. While this method does not produce Yarkovsky detections that are as robust as those that rely upon thermophysical modelling, it has resulted in hundreds of new detections (Greenberg et al., 2020).

1.3.2 The YORP effect

The Yarkovsky-O'Keefe-Radzievskii-Paddack (YORP) effect is closely related to the Yarkovsky effect. The result of one effect will change the magnitude of the other, with significant consequences for asteroid evolution.

Named after scientists that played key roles in its theoretical formulation, the YORP effect is similar to the Yarkovsky effect in that it arises from the reflection and re-emission of thermal radiation (Rubincam, 2000). Unlike the Yarkovsky effect, which depends on thermal inertia causing a delay between absorption and re-emission, the YORP effect is caused by the asymmetric shapes of small bodies. Because thermal radiation is not absorbed and re-emitted uniformly across the body, the recoil force exerts a small torque. This torque, which is somewhat analogous to a windmill effect, affects both the spin rate and spin-axis orientation of small bodies. A perfectly symmetrical body would have zero net torque, while near-spherical bodies generally experience negligible torques. Figure 1.12 illustrates the YORP effect with a simplified diagram of a black body asteroid with a rotationally-averaged asymmetry.

The YORP torque $\vec{\tau}$ is generally divided into two components. The first, $\vec{\tau_\omega}$, is the torque about the maximum moment of inertia, which is generally aligned with the rotation axis. This component acts to change the spin rate of the body. The second component $\vec{\tau_\epsilon}$ affects the asteroid's obliquity[§]. The rates of change for rotation and obliquity are thus given by:

$$\frac{d\omega}{dt} = \frac{\tau_\omega}{C} \qquad\qquad \frac{d\epsilon}{dt} = \frac{\tau_\epsilon}{C_\omega} \tag{1.6}$$

[§]Note that obliquity is defined as the angle between the unit spin vector $\hat{\omega}$ and the normal to the orbital plane $\hat{N}$.

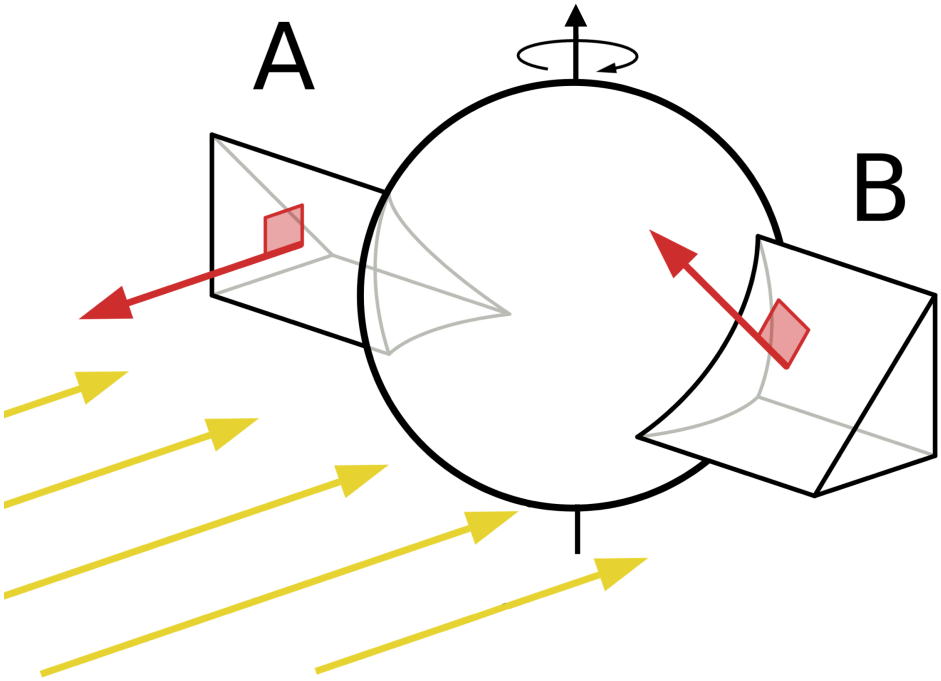

Figure 1.12: This 'Rubincam's propeller' diagram, popularised by Rubincam (2000), shows the YORP effect acting upon a simplified model of an asymmetric asteroid, in this case a sphere with two wings labelled A and B. The asteroid's rotation axis, and direction of roatation, are indicated. Incident sunlight is shown with five yellow arrows. While the Sun-facing areas of the wedges A and B are equal, re-emitted photons are at a normal to the surface (as shown by red arrows). This means that the recoil is felt in different directions at A and B, creating a torque. While both wings are pushed away from the Sun, the vertical component of the recoil on B means that the horizontal (sunward) recoil force is smaller on B than it is on A. This means that the asteroid will be turned, with A moving away from the sun and B towards it. In this spin-up configuration, the asteroid's rotation rate will increase. The vertical component of B will cause the asteroid to tilt, changing the orientation of its rotation axis. The simple model assumes zero thermal conductivity and zero obliquity. This image reproduced via Wikimedia Commons[a], with modification.

[a] https://commons.wikimedia.org/wiki/File:YORP_effect_-_wedged_sphere.svg

Where:

$$\tau_\omega = \vec{\tau} \cdot \hat{\omega} \qquad \tau_\epsilon = \frac{\vec{\tau} \cdot (\hat{\omega} cos\epsilon)}{sin\epsilon} \tag{1.7}$$

and C is the principal axis of inertia (Rubincam, 2000; Vokrouhlický and Čapek, 2002).

Observational detections of YORP (see Section 1.3.2.3) focus on $\vec{\tau_\omega}$, as rotational acceleration can sometimes be measured over relatively short ($\gtrsim$3 yr) baselines. YORP accelerations are typically on the order of $\sim 10^{-8}$ rad/day^2, which corresponds to a $\sim$10 M yr spin-rate doubling time for an initial rotation period of 5 hours.

1.3.2.1 Implications of the YORP effect

The YORP effect was originally believed to only have a significant impact on spin rates, with minimal contribution to the obliquity of small bodies. Furthermore, the importance of the YORP effect was generally considered to be limited to small (< 5 km) asteroids.

Both of these assumptions proved to be incorrect. Observations of Koronis family asteroids show that their obliquities are grouped into two 'spin clusters' (Slivan, 1995; Slivan, 2002; Slivan et al., 2003). These obliquity of these clusters are 'opposite' to each other, meaning that the two groups are prograde and retrograde rotators with a common spin-axis. This alignment of spin axes in the Koronis family, which affects asteroids up to 50 km in size, cannot be explained by collisions and gravitation. Vokrouhlický et al. (2003) presented the case for YORP being the driving mechanism behind spin-axis orientation in the Koronis family. This indirect detection was the first observational evidence for YORP, and highlighted the under-estimated impact of YORP on the spin-states of small bodies. More recent studies have reinforced this conclusion (Slivan et al., 2023), while evidence for YORP-induced spin evolution has also been identified in other asteroid families (Kryszczyńska, 2013).

Several studies have been conducted to simulate the effects of YORP on both real and synthetic shape models, which is useful for testing YORP theory and making predictions about the NEA population. Vokrouhlický and Čapek (2002) simulated the YORP components $\vec{\tau_\omega}$ and $\vec{\tau_\epsilon}$ over a range of obliquities for a variety of objects. The results of this are shown in Figure 1.13. In this simulation, asteroids approach shape-dependent stable obliquities then continue to experience rotational acceleration,

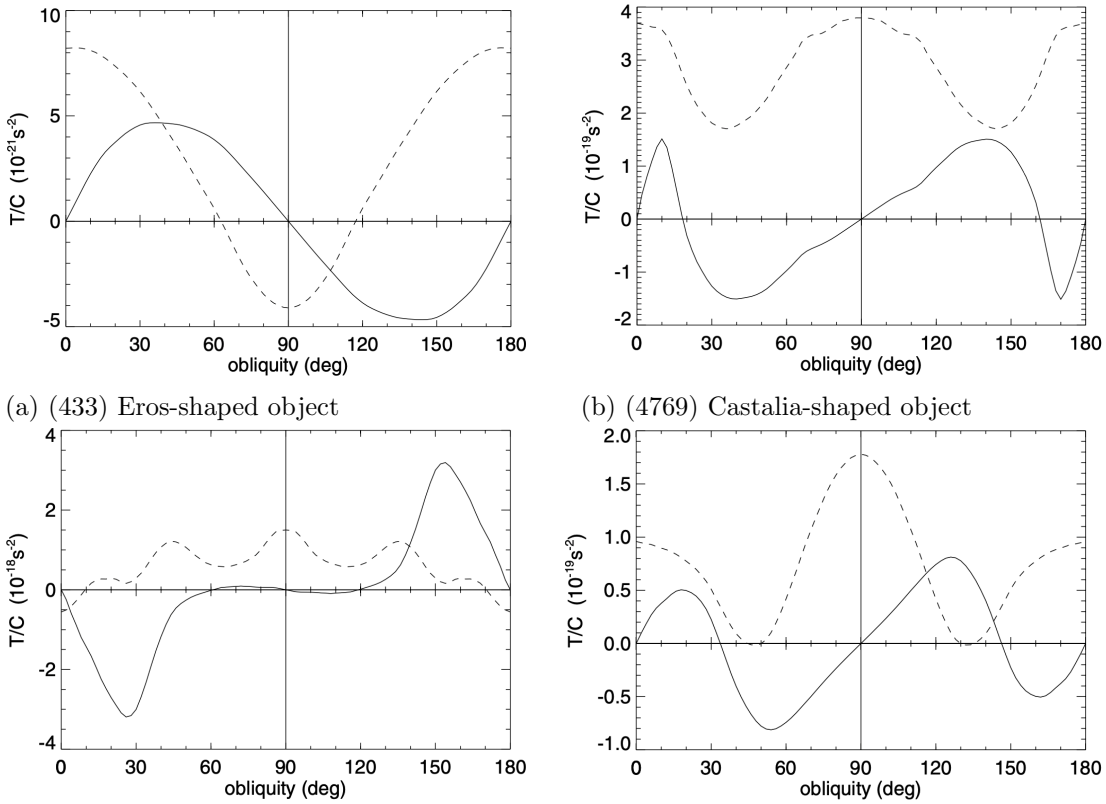

(a) (433) Eros-shaped object

(b) (4769) Castalia-shaped object

(c) (6489) Golevka-shaped object

(d) (1620) Geographos-shaped object

Figure 1.13: Simulated YORP torques as a function of obliquity. The dashed line denotes the spin rate torque $\vec{\tau_\omega}$ and the solid line denotes the obliquity torque $\vec{\tau_\epsilon}$. YORP torques (labelled T) are scaled by the principal moment of inertia C. The bodies are on circular orbits at 2.5 AU, with YORP torques averaged over rotational and orbital motion. Note that $\vec{\tau_\epsilon}$ is always zero at 90° obliquity, and $\vec{\tau_\omega}$ always peaks at 0°, 90° or 180°. These figures were reproduced from Vokrouhlický and Čapek (2002).

leading to spin-breakup or tumbling for spin-up and spin-down respectively. Another study conducted by Čapek and Vokrouhlický (2004) introduced thermal conductivity, which prior studies assumed was zero. This study showed that YORP-induced changes in obliquity are strongly dependent on thermal conductivity, and further demonstrates that YORP preferentially modifies obliquities until they are at a normal to the orbital plane.

When YORP causes an asteroid's obliquity to change, there is a feedback effect that modifies the strength of both YORP components. As can be seen in Figures 1.13 and 1.14, the magnitude of both the spin and obliquity YORP torques is dependent on the

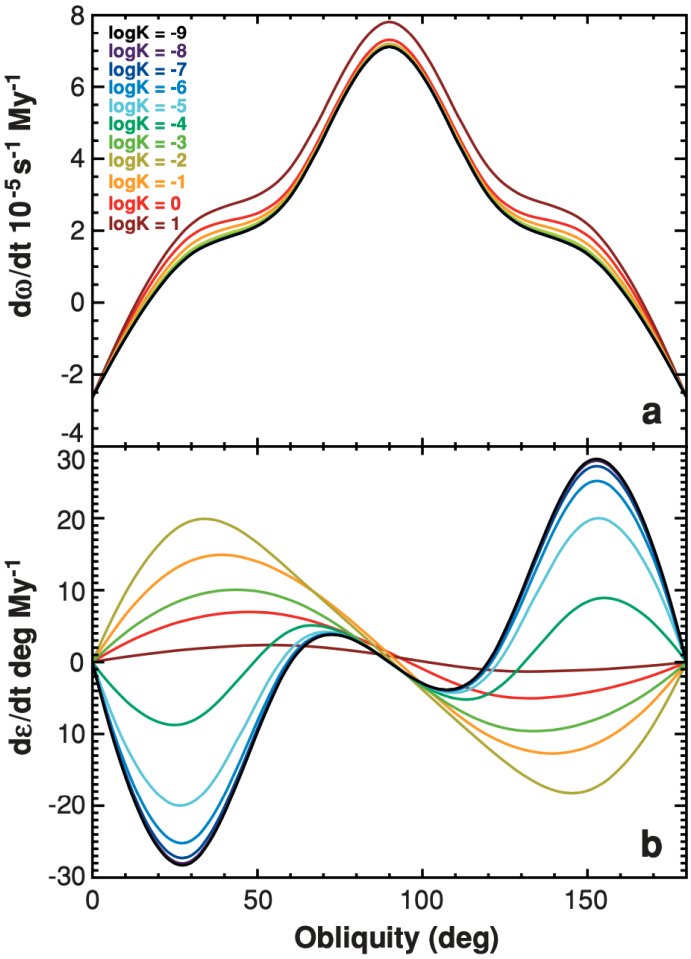

Figure 1.14: The YORP dependence on thermal conductivity, for a (6489) Golevka-shaped object over a range of obliquities. Spin acceleration $d\omega/dt$ is shown in (a), and the rate of change of obliquity $d\epsilon/dt$ is shown in (b). Each coloured line corresponds to a different thermal conductivity value, as indicated in (a). A circular orbit at 2.5 AU is assumed, and YORP acceleration is averaged over both rotational and orbital motion. This figure was reproduced from Bottke et al. (2006), which is itself modified and reproduced from Čapek and Vokrouhlický (2004).

current obliquity value. This can lead to a continuously changing YORP torque, which in some cases may even result in the direction of acceleration being reversed. Upon reaching a preferred asymptotic obliquity, asteroids can experience spin down until the asteroid reaches a tumbling state, which leads to a reorientation of the spin-axis (Rubincam, 2000). Dissipation of internal energy then restores principal axis rotation and restarts the process of YORP-driven spin evolution (Vokrouhlický and Čapek, 2002). Simulations of these 'YORP cycles' find that cycle times are widely distributed, with most examples ranging from 0.01 to 1 M yr (Rossi et al., 2009). For an object at the 0.1 M yr peak of this distribution, an object would experience ∼150 YORP cycles in the mean NEO lifetime.

There are several mechanisms that can interrupt the YORP cycle. When driven to

rapid rotation, centrifugal forces can trigger landslides, mass shedding or even catastrophic breakup (Holsapple, 2010). This YORP-driven reconfiguration of the surface, or even overall shape, will feed back via an adjusted thermal torque. One outcome of this is that the magnitude of the YORP torque can be significantly reduced when asteroids undergo spin deformation to become near-spherical and smooth out larger surface features. If this YORP self-limitation (Cotto-Figueroa et al., 2015) occurs before asteroids cross their individual rotational fission thresholds, they can effectively become trapped in a steady state of rapid rotation. This apparent evolutionary dead end does not exist for rigid bodies, meaning that YORP self-limitation could be producing an excess of rapidly rotating rubble piles. Rapid rotators with this YORP-driven 'spinning top' shape are hence known as YORPoids. It should be noted, however, that the characteristic spinning top shape of a rapidly rotating rubble pile does not explicitly confirm past reshaping via YORP, as it has been shown that collisional disruption can also produce top-shaped bodies (Statler, 2015; Michel et al., 2020).

Despite being unfavourable targets for observation and shape modelling, YORPoids are relatively common amongst the population of modelled or directly imaged asteroids, which also includes MBAs such as (2867) Steins and (152830) Dinkinesh (Keller et al., 2010; Levison et al., 2024a), the former of which is relatively large. While this sample remains small, and biased, it could be an early indicator for the proliferation of YORP-evolved rubble piles. One distinctive feature common to these asteroids is the presence of an equatorial bulge, or ridge, which can be seen in Figure 1.15. This rotation-induced feature is a result of interior material flowing outwards due to the increased centrifugal force, and surface material flowing towards the equator. In cases where there is an inhomogeneity of interior density, which will offset the centre of mass from the centre of the body, YORP-driven spin acceleration can cause asteroids to become stretched and bifurcated, as is seen with (25143) Itokawa (Scheeres and Gaskell, 2008; Lowry et al., 2014).

If the YORP spin up of a rubble pile does not self-limit, the asteroid will continue to

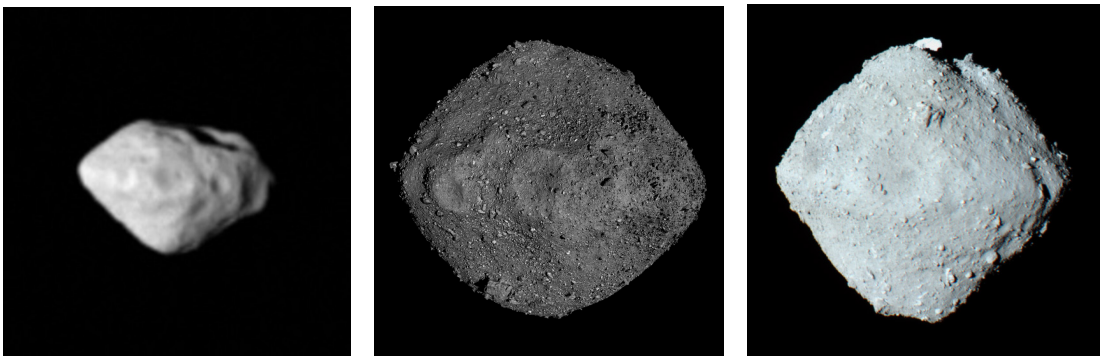

(a) (2867) Steins (b) (101955) Bennu (c) (162173) Ryugu

Figure 1.15: A selection of YORPoids with equatorial ridges, as imaged by spacecraft. Images: ESA/NASA/Goddard/University of Arizona/JAXA

rotationally accelerate until centrifugal forces overcome cohesion and gravity to incite mass lofting or fission. In the case of the former, the shedding of material can cause outbursts, which were previously thought to be caused by collisions (Jewitt et al., 2015). For the latter, the debris from a spin breakup event can fall back onto the main body of the asteroid to form a more prominent ridge, or reform as a secondary body (Walsh et al., 2008; Jacobson and Scheeres, 2011a; Hyodo and Sugiura, 2022). Newly formed secondaries do not necessarily remain bound to the primary, with some companions spiralling outwards and separating into individual systems. With binary asteroids comprising ∼15% of the NEA population (Pravec and Harris, 2007), and many of them thought to have formed with YORP spin-up as a driving factor (Walsh and Jacobson, 2015), the formation of multiple systems has become one of the most significant consequences of the YORP effect seen in the Solar System.

Collisional disruption is thought to be another driver of binary formation, although this is also influenced by YORP. The Yarkovsky effect, which induces orbital drift and can hence cause collisions, is dependent on spin rate and obliquity. As these parameters are affected by YORP, the two effects are coupled (Vokrouhlický et al., 2015a). The consequences of the Yarkovksy effect discussed in Section 1.3.1.1 are thus indirect consequences of YORP, while Yarkovksy-driven orbital drift will adjust the strength of YORP via the modification of mean semi-major axis.

There may be indirect evidence of the YORP effect in extrasolar systems. As stars evolve through the giant branch, small bodies in their systems will be subjected to increased flux and hence stronger YORP torques. This will rapidly accelerate the process of YORP-induced spin breakup to such an extent that the vast majority of small bodies in the inner system will be destroyed. Veras et al. (2014) finds that objects with diameters between 0.1 - 10 km cannot survive within 7 AU of a star during its giant phase, leading to the creation of a vast debris field that can expand to 100 AU (Veras and Scheeres, 2020). This offers a viable explanation to planetary debris disks and metal pollution observed in white dwarfs, without requiring the presence of a major planet during the giant phase (Veras et al., 2022).

1.3.2.2 Advances in YORP research

There are two primary branches of YORP research: observations and theory. The former, which is discussed in Section 1.3.2.3, focuses on the physical characterisation of asteroids to make new YORP detections and build a better picture of the shape and spin-state distribution of the asteroid population. This means that development is required not only for observational techniques, but for the tools that are used to interpret data and use them to construct physical models.

The greatest revelation from YORP observations has been the lack of YORP detections in a spin-down configuration, which implies a strong preference for YORP to act in the spin-up sense. Advances in YORP theory attempt to explain this spin-up excess, while other advances improve understanding of asteroid evolution and explain or predict characteristics regarding the shape, spin-state, composition, multiplicity and orbital configuration of asteroids in the Solar System.

Unlike the example shown in Figure 1.12, the overall shape and mass of an asteroid are not the only factors affecting how YORP will act upon a small body. The physical and material properties of the asteroid, as well as its surface structure, are crucial components in the manifestation of YORP.

Early models for YORP treat asteroids as black bodies. More advanced thermal models (e.g. Rozitis and Green (2012)) introduce a reflection component and simulate more realistic emission. The introduction of non-Lambertian thermal beaming, whereby the path of emitted photons is in the direction of the Sun instead of at a normal to the surface, leads to a strong dependence on small-scale surface roughness. It can also contribute to self-heating in craters or other large concavities, which is sometimes referred to as crater-induced YORP (Rozitis and Green, 2013; Zhou et al., 2022).

It is also common for models to assume uniform density throughout an asteroid. In the case of (25143) Itokawa, a suspected contact binary, Lowry et al. (2014) made an observational detection of YORP that could only be reconciled with models when they did not assume the same density for the two lobes of the asteroid. This makes density homogeneity an important factor for YORP, especially for bilobate asteroids.

Rubincam (2000) utilises spherical harmonic models to describe the shapes of asteroids. These models are generally limited to large-scale features that affect the overall shape of the asteroid, meaning that simulations of YORP did not account for topographical variation on very small scales. Statler (2009) shows that craters and boulders can have a dramatic impact on the magnitude and sign of YORP torques, revealing a strong sensitivity to surface features, also noting that spin-up or spin-down induced changes to the surface could produce significant feedback through the modification of shape or obliquity. Asteroid models derived from radar observations typically have spatial resolutions ranging from tens to hundreds of metres, meaning that this small-scale dependence could cause a disparity between empirical and simulated measurements of YORP for a body with a known shape.

Further investigation of this small-scale dependence (Golubov and Krugly, 2012; Golubov et al., 2014; Ševeček et al., 2016) lead to the formulation of a tangential component to the YORP effect. Tangential YORP (TYORP) arises from the thermal conductivity of centimetre- to decimetre- sized features, which can lead to an east-west temperature gradient. Thermal photons depart on a path that is tangential to the

asteroid's surface, always producing recoil in the positive (spin-up) direction. The net YORP torque felt by an asteroid is hence the resultant of 'normal' YORP (NYORP) and TYORP components, which are comparable in magnitude.

Early TYORP models simulate walls or boulders, akin to the NYORP wedges from Rubincam (2000). Golubov and Lipatova (2022) builds upon these models by introducing a component of TYORP that is produced by regolith roughness, finding that regolith TYORP can be comparable to (metre-scale) boulder TYORP and NYORP. A relatively symmetrical asteroid could hence undergo spin modification that is dominated by TYORP, with a dependence on surface roughness at both small and large scales.

If only NYORP is considered, one would expect a near-equal number of asteroids in spin-up and spin-down configurations. As previously noted, all observational detections to date have been in a spin-up configuration. Even accounting for the small size of the sample and its biases, this result is highly improbable. This extraordinary lack of spin-down detections is partially explained by TYORP; due to the always-positive sign of the tangential component, the presence of TYORP would result in an excess of asteroids in a spin-up configuration. This may increase the number of rapid rotators, thus increasing rates of YORP-induced spin breakup which would in turn produce more binaries. It is important to note that TYORP does not rule out spin-down; it only makes it less common. The issue is further complicated by an observed excess of slowly-rotating tumblers, which are likely the product of YORP spin-down. This means that even with TYORP producing a spin-up excess, the lack of spin-down detections remains unexpected.

It is possible for NYORP and TYORP components to balance in such a way that asteroids become trapped in a state of rotational equilibrium (Golubov et al., 2018; Golubov and Scheeres, 2019). Up to 20% of asteroids may be able to reach this state, effectively halting spin modification and trapping them in evolutionary 'sinks'. As asteroids with irregular shapes are more likely to reach this state, in-situ study of a

'sink' asteroid could further theories of TYORP by inferring its strength from simulated NYORP torques using a sub-metre resolution shape model. Similarly, the detection of YORP spin-up on an asteroid with small or negative simulated NYORP torques would provide strong evidence for the presence of TYORP.

Another branch of YORP research is the binary YORP (BYORP) effect. In a binary system, a synchronous secondary will behave as if it is an asymmetric protuberance on the primary (Ćuk and Burns, 2005). BYORP will thus modify the secondary's orbital velocity, causing inward or outward migration, which results in increased and decreased eccentricity respectively for the mutual orbit. In the case of inward migration, the secondary will eventually collide with the primary and form a contact binary. Outward migration may lead to disassociation, leading to the creation of an asteroid pair, although it is more likely that the system will enter a chaotic state until synchronous rotation can be re-established in the opposite direction, ultimately resulting in inward BYORP migration (Ćuk and Nesvorný, 2010). It is also possible for opposing torques from BYORP and mutual body tides to cancel out, resulting in an equilibrium state (Jacobson and Scheeres, 2011b). Observations of (66391) 1999 KW4 are consistent with this equilibrium state (Scheirich et al., 2015), although BYORP drift rates are much lower than expected (McMahon and Scheeres, 2010). This suggests that present theory may overestimate BYORP and its interplay with mutual tides, although it could also be due to the limited spatial resolution of the radar shape models that are used to simulate BYORP. There have been further indications of both inward and outward BYORP drift (Scheirich et al., 2021) in binary systems, meaning that there is direct evidence for all three configurations of BYORP-driven orbital evolution.

1.3.2.3 Direct detection

Empirical advancement of YORP theory largely depends upon two areas of investigation. The first is the detailed physical and thermal modelling of individual asteroids through telescopic, radar or spacecraft observations. This makes it possible to more

precisely calculate the expected YORP torque acting on a given asteroid, using present theory. Secondly, the number of asteroids with directly detected rotational acceleration must be increased. A larger sample improves population statistics, whilst also providing more opportunities to test YORP theory through the comparison of simulated and measured YORP torques for individual asteroids. Fortunately the modelling and direct detection processes are interlinked, as the latter can rarely be achieved without first determining the asteroid's shape.

The first direct detection of YORP was jointly reported by Lowry et al. (2007) and Taylor et al. (2007), which used different methods to measure the rotational acceleration of (54509) 2000 PH5[¶]. As the asteroid was a known rapid rotator (P $\sim$ 0.2 h), it was possible to use a small subset of lightcurves from 2002 and 2003 to determine a sidereal rotation period of 0.20290020 h with a 1σ uncertainty of 10^{-8} h. This initial period P_0 was then used as a baseline against which later measurements could be compared, to detect changes in the rotation rate. Lightcurves between 2001 and 2005 were then grouped into sets spanning one year, and each set was used to determine a yearly averaged sidereal rotation period. This allowed for four separate period measurements, including P_0. As shown in Figure 1.16, there is a linear trend in the change in period against time. This implies a constant rate of rotational acceleration consistent with a YORP spin-up of $(3.49\pm0.35)\times10^{-6}$ rad/day^2. This remains the strongest YORP detection to date, which is to be expected when considering that 2000 PH5 is also the smallest asteroid to have a YORP detection.

Instead of measuring period directly, Taylor et al. (2007) measures the YORP spin-up of 2000 PH5 through the analysis of its rotational phase. Radar observations were used to construct a three-dimensional model describing the shape of the asteroid, which was then used to construct a corresponding synthetic lightcurve for each observed lightcurve. A shape model is necessary for this as the shape of the lightcurve is affected by the relative positions of the observer, Sun and asteroid. For each pair of synthetic and

[¶]2000 PH5 has since been renamed as (54509) YORP.

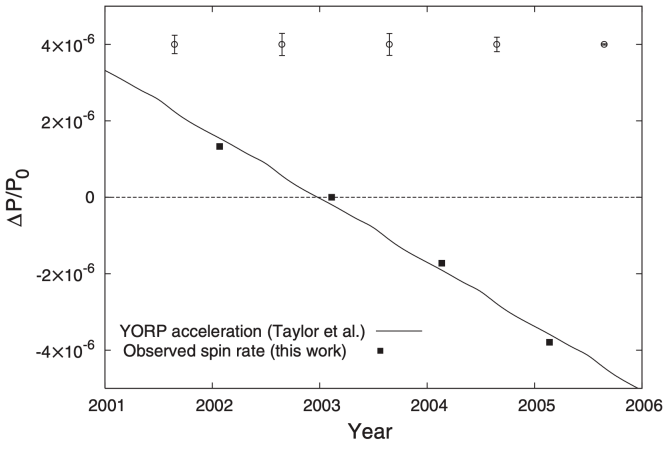

Figure 1.16: The fractional change in yearly averaged sidereal rotation period $\Delta P/P_0$ for 2000 PH5 over four years. The solid black line marks the predicted change in period due to YORP, and the dashed black line denotes constant-period rotation. Changes in period caused by close encounters with Earth are shown as open circles, which are offset to the top of the figure for better visibility. This figure was reproduced from Lowry et al. (2007).

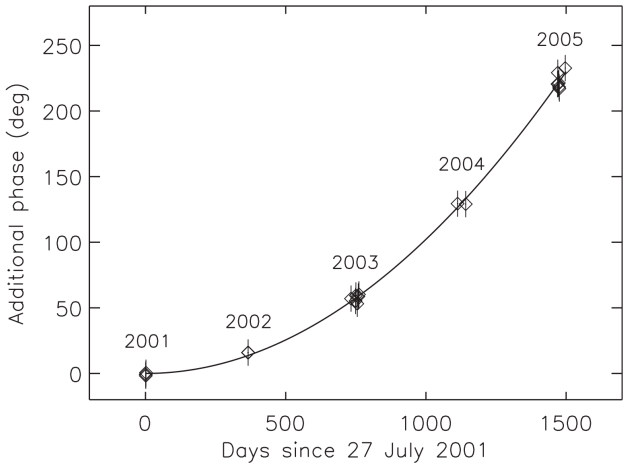

Figure 1.17: The offset in rotation phase between observed and synthetic lightcurves for (54509) 2000 PH5. The solid black line is a quadratic fit that was used to determine the YORP torque acting on the asteorid. This figure was reproduced from Taylor et al. (2007).

observed lightcurves after T_0, a phase offset was necessary to properly align the model lightcurve with the data. As shown in Figure 1.17, the required phase offset increases quadratically with time. This implies that the period is changing at a constant rate, with YORP being the only known physical mechanism for this. The coefficients of the quadratic fit were used to determine a YORP acceleration of $(3.49\pm0.35)\times10^{-6}$ rad/day^2, precisely matching the rate measured by Lowry et al. (2007).

Since the initial YORP detection on 2000 PH5, considerable effort has gone into making further detections of YORP. At the time of writing there are twelve asteroids

with robust YORP detections, which are listed in Table 1.1. Where YORP analyses have been conducted but not yielded detections, it has been possible to put upper limits on potential YORP torques. Examples of this include (85990) 1999 JV6 (Rożek et al., 2019a) and (23187) 2000 PN9 (Dover et al., 2023; Sect. 4). There is also the case of (3200) Phaethon, where there is evidence for a constant rate of spin up under torques that are too strong to be YORP alone (Marshall, priv. communication).

The twelve asteroids with YORP detections, listed in Table 1.1, all have retrograde rotation and obliquities between 141° and 177° (with the exception of 2000 WN10), diameters below 3.5 km, and relatively short rotation periods. This is largely a result of previously discussed observational and modelling biases, and the fact that small fast-rotating NEAs will be most obviously affected by YORP. All detections are also in a spin-up configuration, which is unexpected. Approximately half of YORP detections are expected to be in a spin-down configuration, yet if this was the case there is only a 0.02% probability of making twelve consecutive spin-up detections (ignoring observational biases). It is thus far more likely that there is a spin-up excess, as predicted by theories of TYORP. A preliminary detection for the first observed case of YORP spin-down was first reported in Zegmott (2021), and is expanded upon in this work (see Section 5).

The purpose of this thesis is to make new observational detections of YORP through the development of asteroid shape models. Each additional YORP detection contributes to the field by growing the sample, allowing for more extensive testing of YORP theories, and improving both the observational and analytical methods used to search for YORP. In order to develop these models and detect YORP, this work continues a first-of-its-kind observing campaign that utilises long-term monitoring of NEAs with optical facilities to gather data for modelling and YORP analysis.

Asteroid	P [h]	ν [10^{-8} rad/day^2]	D [km]	λ, β [°]	ϵ [°]	Ref.
(1620) Geographos	5.223	1.15 ± 4%	2.56	(58, -49)	149.9	1
	5.223	1.14 ± 2%	2.56	(56.7, -51.2)	149.0	2
(1625) Toro	10.198	0.33 ± 10%	3.5	(75, -69)	160.1	2
	10.198	0.32 ± 9%	3.5	(60, -72)	166.7	3
(1862) Apollo	3.065	5.3 ± 25%	1.4	(50, -71)	159.6	4
	3.065	5.5 ± 22%	1.45	(48, -72)	162.3	5
(2100) Ra-Shalom	19.820	0.29 ± 69%	2.3	(257, -52)	158	6
	19.820	0.22 ± 72%		(278, -60)	165	7
(3103) Eger	5.701	1.4 ± 14%	1.5	(226, -70)	155.6	8
	5.701	1.1 ± 15%	1.5	(226, -70)	155.6	9
	5.701	0.85 ± 6%		(214, -71)	177	7
(10115) 1992 SK	7.320	8.3 ± 7%	1	(94, -56)	141	2
(25143) Itokawa	12.132	3.54 ± 11%	0.33	(128.5, -89.7)	178.4	10
(54509) YORP†	0.203	349 ± 10%	0.113	(180, -85)	174.3	11,12
(68346) 2001 KZ66	4.986	8.43 ± 8%	0.797	(170, -85)	158.5	13
(101955) Bennu	4.296	4.61 ± 40%	0.492	(87, -65)	159.6	14
	4.296	6.34 ± 14%	0.492	(87, -65)	159.6	15
(138852) 2000 WN10	4.464	5.5 ± 13%	0.3	(318, 60)	10	6
(161989) Cacus	3.755	1.9 ± 16%	1	(254, -62)	143.3	9
	3.755	1.91 ± 3%		(251, -62)	177	7

† Previously named 2000 PH5.

References. (1) Ďurech et al. (2008a); (2) Ďurech et al. (2022a); (3) Tian et al. (2022); (4) Kaasalainen et al. (2007); (5) Ďurech et al. (2008b); (6) Ďurech et al. (2023); (7) Rodríguez et al. (2024); (8) Ďurech et al. (2012); (9) Ďurech et al. (2018a); (10) Lowry et al. (2014); (11) Lowry et al. (2007); (12) Taylor et al. (2007); (13) Zegmott et al. (2021); (14) Nolan et al. (2019), (15) Hergenrother et al. (2019)

Table 1.1: All published YORP detections to date. For each asteroid, the table lists period P, YORP strength ν, diameter D, the rotational pole in the ecliptic coordinate system, and obliquity ϵ. Where not previously published, obliquities were calculated using the published rotational pole and the latest orbital elements from JPL[a]. Note that diameters are unavailable for YORP solutions obtained using convex hull models.

[a] `https://ssd.jpl.nasa.gov/sb/orbits.html`

CHAPTER 2

OBSERVING NEAR-EARTH ASTEROIDS IN SEARCH OF YORP

2.1 Overview

A wide range of techniques are used to study asteroids ranging from laboratory analyses of meteorites to flagship spacecraft missions. The empirical understanding of NEA formation and evolution relies upon using all of these experimental methods to analyse a diverse range of asteroids. The overwhelming majority of NEAs have their physical characteristics determined through remote sensing with ground and space-based observatories. These facilities mainly use optical–, NIR–, and/or radio–wavelength techniques including: photometry, polarimetry, spectroscopy, direct imaging, and observations of stellar occultations.

While relatively rare, spacecraft missions provide 'ground truth' for remote observations with high-resolution imaging, while these space-borne laboratories can also provide invaluable in-situ measurements of asteroids and their immediate environment. At the time of writing, three missions have successfully returned samples from asteroids to Earth. The first was the Hayabusa mission to (25143) Itokawa (Fujiwara et al., 2006), followed by the Hayabusa2 mission to (162173) Ryugu (Watanabe et al., 2017), and the OSIRIS-REx mission to (101955) Bennu (Lauretta et al., 2017). These results from these recent missions, along with ongoing missions such as Hera and Lucy (Cheng et al., 2016; Karatekin et al., 2018; Levison et al., 2021), have significant bearing on the context of the results presented in this thesis.

This thesis primarily utilises two forms of observational data: rotational lightcurves taken with a variety ground-based optical telescopes, and radar observations from the Arecibo and Goldstone facilities. As new optical data were obtained during this project, the full planning and execution process for observing runs will be explained, followed by a description of the methods used to process images and extract lightcurve data. The radar data incorporated into this research will also be covered, detailing the Arecibo and Goldstone facilities and the data that were obtained from them.

2.2 Photometric lightcurve observations

Optical imaging is the most common method used to observe asteroids, for a variety of reasons. Firstly, the proliferation of ground-based telescopes means that these instruments have relatively high availability, whilst remaining relatively inexpensive to construct and operate. Secondly, the discovery of asteroids and subsequent orbit determination relies upon the wide-field imaging capabilities of small– to medium–sized telescopes. Thirdly, optical imaging is the most forgiving technique in terms of the minimum signal required for useful observations. The lower apparent brightness limit allows for observations of NEAs that are smaller and/or more distant when compared to the limits of spectrographs, polarimeters, adaptive optics systems or radar transmitters.

The most basic form of analysis on optical imaging is photometry. As previously discussed in Section 1.2.1, a single image can be used to constrain an NEA's effective diameter if its distance and albedo are known. A sequence of images is more useful, as it can be used to construct a lightcurve that shows changes in brightness caused by the body's rotation. This thesis makes extensive use of rotational lightcurves to determine the spin and shape properties of NEAs, the vast majority of which were obtained as part of a long-term campaign to observe NEAs in search of YORP.

2.2.1 The YORP campaign

Since 2010, a collaboration lead by Prof. Stephen Lowry has monitored a sample of 40 NEAs in search of new YORP detections. The aim of the campaign is to conduct regular observations to build a substantial lightcurve dataset for each target that spans several years. It is important to collect lightcurves over multiple apparitions, as the shape of an asteroid's lightcurve will change with the relative positions of the observer, asteroid, and Sun. This relationship between viewing geometry and lightcurve shape is crucial when developing a model that describes an asteroid's geometric shape and spin orientation. This also allows for more robust testing of synthetic lightcurves created

using each model, as they should accurately recreate the observational data for a full range of viewing geometries. Furthermore, YORP detections require a minimum of three measurements that show a significant change in period or relative phase. As YORP torques are very small, it can take several years to manifest changes to spin rate that are above detection thresholds.

The targets of this campaign are strong candidates for YORP detection due to their small size, proximity to the Sun, and short spin periods. This not only makes them likely to experience stronger YORP torques, but ensures they can be routinely observed with medium to large telescopes. Their short rotation periods are especially beneficial, as it allows for a full rotation phase to be captured during a single night. A full list of YORP candidates for this campaign is given in Table A.1.

The vast majority of data obtained for the YORP campaign was obtained via an ESO Large Programme, also lead by PI Prof. Stephen Lowry. This ESO LP marks the beginning of the overall YORP campaign, running from April 2010 to April 2014. In addition to this, an auxiliary campaign has run from 2010 to present that utilises ESO telescopes post-2014 as well as a variety of other telescopes, mostly based in the USA and Spain's Canary Islands. The auxiliary campaign is designed to extend the dataset obtained via the LP and follow up on preliminary results. This campaign comprises a mix of formal short-term observing programmes as well as target-of-opportunity observations conducted under wider small bodies programmes.

2.2.1.1 Telescopes used in the YORP campaign

New Technology Telescope (809) – The NTT at La Silla Observatory conducted the most observations for the YORP campaign, forming the backbone of the ESO LP and contributing significantly to the auxiliary campaign.

The NTT is a 3.58 m Ritchey-Chrétin optical telescope with an alt-az mount. Built to showcase new technologies, it was the first operational telescope to use an active

optics system, whereby actuators actively change the shape of its flexible monolithic primary mirror to prevent any deformation due to environmental conditions or mechanical stress (Tarenghi and Wilson, 1989). Without this technology, it would not have been possible to build 8 m class telescopes such as VLT or segmented primary mirrors. The 'dome' was also a revolutionary design at the time, utilising a compact design that minimises both internal air volume and the external surface area that is subjected to wind, whilst also providing superior ventilation.

Observations at the NTT for the YORP campaign utilised the ESO Faint Object Spectrograph and Camera - version 2 (EFOSC2) camera, which is one of two instruments installed in the Nasmyth foci (Snodgrass et al., 2008). EFOSC2 has a 2048×2048 charge-coupled device (CCD)vc with a 4.1'×4.1' field of view, yielding a pixel scale of 0.12" per pixel. The camera is typically used in imaging mode with the V and R filters, although some spectroscopy was conducted as part of the LP. Observing runs with the NTT typically last two or three nights for the auxiliary and LP programmes respectively.

The author was involved in four NTT runs for the YORP auxiliary campaign, two of which were as PI and primary observer. Due to travel restrictions imposed by the Covid-19 pandemic, these runs were all changed from visitor mode to designated visitor mode, where the telescope is controlled remotely through a web interface. Remote observations like these are may become the norm in the near future, due to changes in financial and environmental policy.

Very Large Telescope (309) – The VLT comprises four 8.2 m optical/NIR Ritchey-Chrétin telescopes at Paranal Observatory, each of which is referred to as a Unit Telescope (UT). These units are capable of working together as an optical interferometer, but are more often used independently, with each UT having its own set of unique instruments. UT3, also known as Melipal, was used in both the LP and the auxiliary programme.

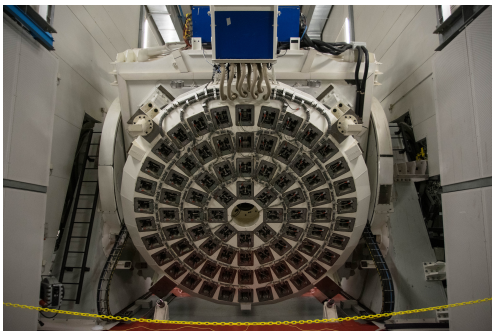

Figure 2.1: The Galileo National Telescope, which is effectively a twin of the NTT with a near-identical design. The photograph on the left shows the design of the enclosure, and the image on the right shows the rear of the mirror, with the active optics actuators visible. Photographs taken by L. Dover in May 2019.

Each unit telescope has a monolithic mirror with an active optics system, and up to three instruments at the two Nasmyth foci and single Cassegrain focus (Gray, 2000). The YORP campaign utilised the red (MIT) chip of the Focal Reducer and low dispersion Spectrograph 2 (FORS2) instrument on UT1, which is an imager and low-resolution spectrograph (Appenzeller et al., 1998). It has a field of view of 6.8'×6.8', which with FORS2's 2048×2048 CCD yields a pixel scale of 0.2"/pix.

The LP also made use of the now decommissioned Visible Multiobject Spectrograph (VIMOS) instrument, which was fitted to Nasmyth B on UT3, and the VLT Imager and Spectrometer for mid-Infrared (VISIR) instrument mounted on UT3. These data were not included in this work.

The author was participated in two VLT runs contributing to this thesis, leading a two-night run as part of a follow-up campaign on the YORP target (29075) 1950 DA (see Sec. 5). Both of these runs were in designated visitor mode.

Table Mountain Observatory (673) – The auxiliary programme has made extensive use of JPL's 0.6 m telescope at TMO in California, USA. This Ritchey-Chrétin optical telescope is fitted with a 1024×1024 CCD giving a field of view (FOV) of 8.9'×8.9'.

Figure 2.2: An aerial view of Paranal Observatory. The four UTs of the VLT are visible along with the VLT Survey Telescope (visible behind the fourth UT) and four 1.8 m auxiliary telescopes. Image provided by ESO.

Hale Telescope (675) – The 5.1 m Hale telescope at Palomar Observatory (California, USA), also known as the 200-inch telescope, was used in the auxiliary campaign to provide imaging with its Large Format Camera. This instrument has six 2048×4096 chips, each of which has an FOV of 6.1'×12.3'.

Danish Telescope (809) – ESO's 1.54 m Danish telescope (ESOD) at La Silla Observatory was used in the auxiliary campaign, mostly through the Microlensing Network for the Detection of Small Terrestrial ExoPlanets (MiNDSTEp) and Near Earth Object Rapid Observation, Characterisation and Key Simulations (NEOROCKS) consortia. Observations were taken with the Danish Faint Object Spectrograph and Camera (DFOSC) instrument, which is fitted with a 2148×2102 CCD with a 13.3'×13.3' FOV. The author participated in planning for several observing runs with ESOD, obtaining data on four YORP targets.

Figure 2.3: The Isaac Newton Telescope. The WFC, which is mounted on the prime focus, can be seen on the left. Photograph taken by L. Dover in October 2019.

Isaac Newton Telescope (950) – The 2.54 m INT at Observatorio del Roque de los Muchachos has been used extensively in the auxiliary campaign. The Cassegrain telescope, which is set on an equatorial mount, was originally based at Herstmonceux Castle in the UK before it was moved to La Palma in 1979.

Observations with the INT used the Wide Field Camera (WFC), an imager with four 2154×4200 CCDs to give a large 34'×34' FOV with a pixel scale of 0.33"/pix (Ives et al., 1996). YORP campaign observations often used an 1820×1820 window to reduce CCD readout time, reducing the FOV to 10'×10'.

The author participated in nine observing runs with the INT, including two visitor-mode trips, four runs as the lead observer, and four as PI. One run was cancelled due to the Cumbre Vieja volcanic eruption in 2021.

Other YORP campaign telescopes – These telescopes used in the YORP campaign, but the author did not directly observe with them or extract lightcurves from data they produced:

- 4.2 m William Herschel Telescope (950) at Observatorio del Roque de los Muchachos

Figure 2.4: The Isaac Newton Group of Telescopes, as viewed from Roque de Los Muchachos. The positions of the William Herschel Telescope (WHT), Liverpool Telescope (LT) and INT are indicated. Photograph taken by L. Dover in October 2019.

- 2.6 m Nordic Optical Telescope (950) at Observatorio del Roque de los Muchachos
- 2.2 m ESO Telescope (809) at La Silla Observatory
- 2.0 m Faulkes Telescope South (413) at Siding Spring Observatory
- 2.0 m Liverpool Telescope (950) at Observatorio del Roque de los Muchachos
- 0.4 m Physics Innovations Robotic Telescope Explorer (PIRATE) (954) at Teide Observatory*
- 0.4 m telescope at Beacon Observatory

*PIRATE has since been upgraded to a 0.6 m Planewave CDK24 telescope.

2.2.1.2 Other sources for lightcurves

YORP campaign observations are often used in conjunction with lightcurve data from other sources. These data are typically taken from public archives, although data are occasionally shared from ongoing NEA campaigns conducted by collaborators.

The majority of data were obtained from the Lightcurve Database (LCDB) (Warner et al., 2009), which is usually accessed via Asteroid Lightcurve Data Exchange Format (ALCDEF) service (Stephens and Warner, 2018). These data are typically from small (<1 m) telescopes used by both professional and amateur observers. The majority of these data are provided by Palmer Divide Observatory (716) and Palmer Divide Station (U82), which consist of a variety of <0.5 m telescopes.

This work also includes data provided by former members of the International Scientific Optical Network (ISON) (Molotov et al., 2009). The analysis of (23187) 2000 PN9 (Sec. 4) utilises ISON observations from the following facilities:

- 2.6 m Shain Telescope at Crimean Astrophysical Observatory (095)
- 1.0 m telescope at Tien-Shan Astronomical Observatory (N42)
- 0.7 m telescope at Abastumani Astropysical Observatory (119)
- 0.7 m telescope at Chuhuiv Observatory (121)

2.2.2 Conducting observations of NEAs

While the saying "No plan survives first contact with the enemy" is often true for observational astronomy, meticulous preparation is nevertheless essential when observing NEAs. Unlike deep sky objects, asteroids do not have fixed co-ordinates on the celestial sphere and their distance to the observer varies greatly over short timescales. Long term observability must be considered as some asteroids are easy to observe often, while others may only be observable once every few years, making them a higher priority.

Covering a full range of viewing geometries is also important, for the previously discussed benefits when shape modelling. Conversely, it is also beneficial to repeat viewing geometries to make it easier to measure shifts in rotational phase between apparitions. For an example of the long term variability of viewing geometry and how observations can be spread across a range of observer-Sun-asteroid configurations, see Figure 4.2 in Section 4.2.

The apparent magnitude of an asteroid depends on both its diameter and the total path distance for light from the Sun being reflected back towards Earth. The limiting magnitude - that is the faintest object that an instrument can make useful measurements on - mainly depends on telescope size, sky brightness, and atmospheric conditions. In ideal conditions, a telescope such as the INT can make useful V-band observations of asteroids just beyond the 20th magnitude. Lightcurve amplitude is also important, as larger photometric uncertainties can be tolerated. If the shape and spin-state of the asteroid are already known, these can be simulated to determine the expected amplitude and thus the minimum signal-to-noise ratio (SNR) for useful observations.

Aside from brightness, it is preferential to observe objects at a low airmass to minimise the atmosphere's degrading effects on image quality. The asteroid's position in the sky - and hence its airmass - partly depends on solar elongation. Solar elongation is the angle between the Sun, Earth and asteroid. If this angle is below $\sim 75^{\circ}$, the asteroid will appear close to the horizon during dawn or twilight and be very difficult to observe.

Observer latitude will also affect the asteroid's apparent position in the sky, as well as the length of the night. Targets must be observable for long enough to observe a significant portion of their rotation, as they may only be at an acceptable airmass when it is close to twilight. It is impractical to calculate observability for every telescope that could potentially be used, so initial planning is limited to one location in each hemisphere. These locations are La Palma and La Silla, since those are the locations

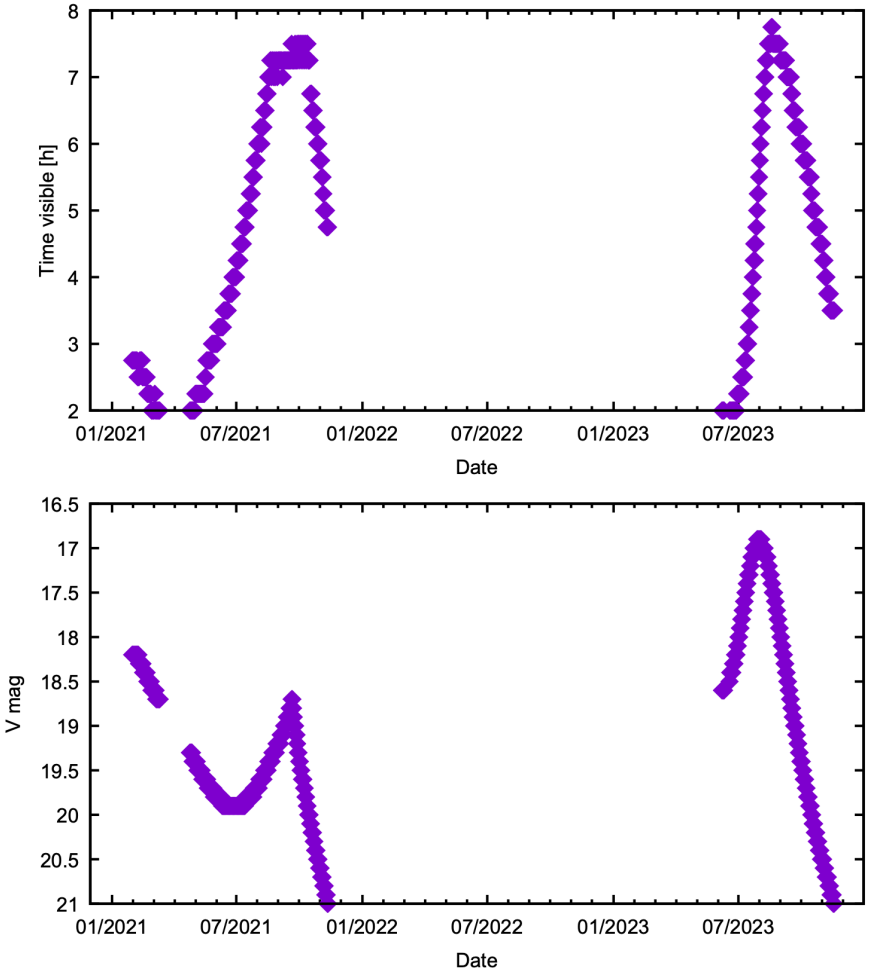

Figure 2.5: A chart used to aid planning observations of (29075) 1950 DA from La Silla between January 2021 and December 2023, with a magnitude limit of V = 21. The top panel shows how many hours the asteroid is above the horizon during darkness, and the lower panel shows the apparent magnitude of the asteroid predicted by JPL Horizons[a]. In this case 1950 DA would ideally be observed during the summer of 2021, and in summer/autumn 2023, using medium to large telescopes. Note that while this plot does not indicate airmass or how many hours of visibility are during twilight, the peak ∼8 hours of visibility can only be achieved with low airmasses outside of twilight.

[a] `https://ssd.jpl.nasa.gov/horizons.cgi`

of the telescopes used the most in the YORP campaign. Asteroid observability from these locations is indicative of what may be achieved from other observatories, which can be considered after refining target lists.

Observations below an altitude of 30° are generally avoided, although not forbidden. This is due to both airmass and telescope pointing restrictions. Low altitude observa-

tions with telescopes such as the INT also require raising a lower dome shutter, which can take up valuable observing time. The phase of the Moon, and its angular separation from the target, must also be considered. A full moon will significantly reduce SNR across most of the sky. Observations beyond 30° from the moon are generally acceptable, although exact separation limits depend on target brightness, moon phase and atmospheric conditions.

Observing runs are typically awarded with full nights, although it is rare for a single object to be observable for an entire night. Because of this, multiple targets must be selected to ensure that the telescope can make useful science observations without pause. This usually means making a compromise with regard to observability and the number of hours spent on each object. This is further complicated by uncertainty as to which dates will be awarded, as proposals usually offer windows in which the requested number of nights could be allocated. Airmass plots, such as the one shown in Figure 2.6, are very useful for this. In this example from an observing run on the NTT which was prioritising (29075) 1950 DA, the first 2.5 hours were spent on (31221) 1998 BP26, followed by 4.5 hours on (29075) 1950 DA then 2.75 hours on (30825) 1990 TG1. This ensured a minimum of one full rotation for each asteroid was covered, while observing targets at their highest airmasses.

The motion of asteroids relative to the stars means that they pass across various fields, which can potentially introduce problems. If the asteroid is crossing the galactic plane, it may spend a significant amount of time crossing close to or in front of background stars. This is a problem when performing photometry, as the flux from those stars is difficult to isolate from the asteroid's flux. In extreme cases, it is not worth observing asteroids as they pass through these fields. On the other hand, too few stars is also a problem. Relative photometry usually requires 3-7 bright background stars, which may not always be possible. For telescopes with small fields of view, an asteroid can move into an entirely new field in a matter of hours. This means that telescope pointing should result in overlapping fields with a few common background stars that

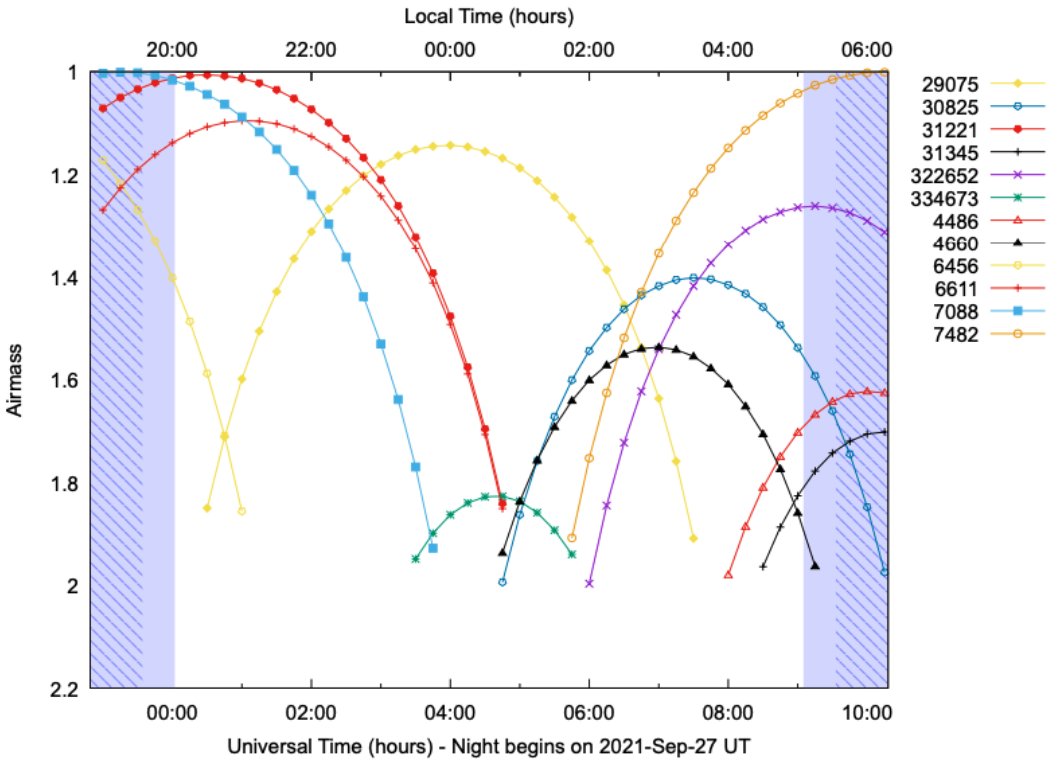

Figure 2.6: An airmass plot for late September 2021 at La Silla, showing all visible YORP targets brighter than V=21. The arc-shaped lines show the airmass for each asteroid throughout the night. The plot runs from sunset to sunrise, with the hatched blue region denoting civil and nautical twilight (where the Sun is up to 12° below the horizon), while the solid blue regions mark astronomical twilight (where the Sun is between 12° and 18° below the horizon). Note the position of (29075) 1950 DA, which corresponds to the plot shown in Figure 2.5.

can be used to photometrically link consecutive fields. Finally, bright stars in the field can saturate CCDs. Sometimes these can be avoided with careful pointing, however when this is not possible the asteroid may not be observable for several hours.

Finder charts are used to inspect the fields, while also providing an invaluable reference when first acquiring the asteroid during observations. An example of this is shown in Figure 2.7. Some instruments, such as EFOSC2 and WFC, have significant CCD artefacts on the centre of the chip that require pointing offsets to avoid. Observations are usually conducted with a quincunx (⚄) dithering pattern, where the telescope is moved ∼5” between images to further minimise the impact of CCD defects.

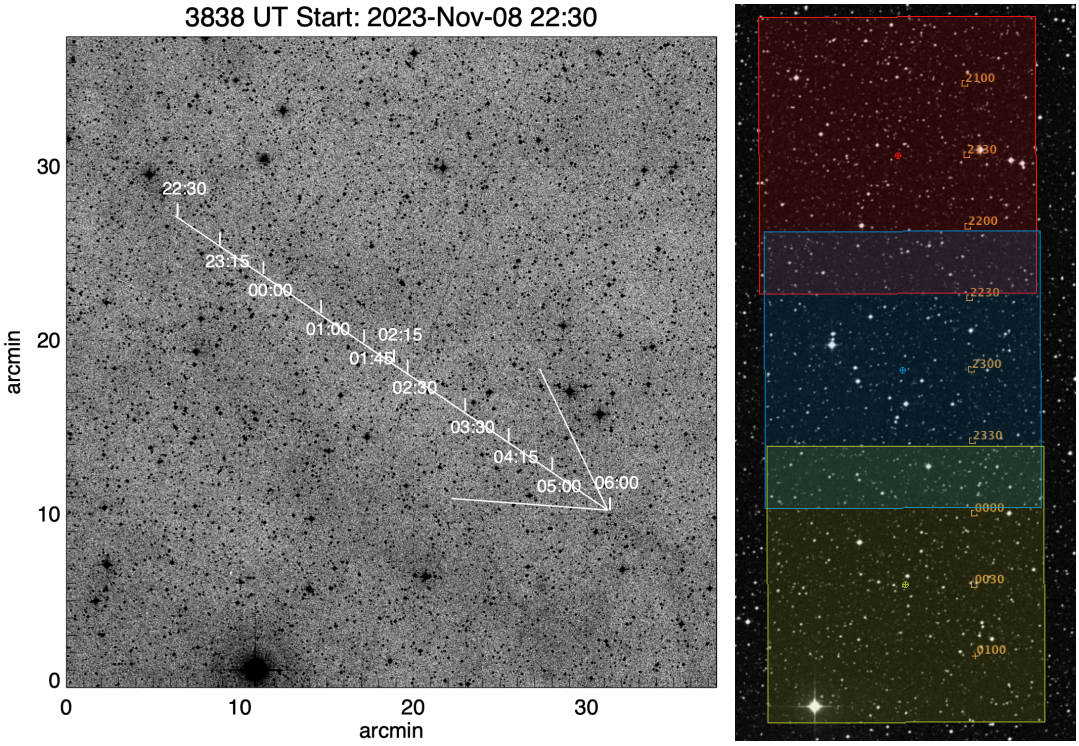

Figure 2.7: Two finder charts used to help plan and conduct observations. The image on the left is a finder chart for INT observations of (3838) Epona, with the white arrow showing Epona's path during the night. An archive image is used to show the field behind Epona, whose position is marked at regular time intervals to aid in planning and acquisition. As the telescope used differential tracking, the field would continuously change between images. The panel on the right shows a finder chart for INT observations of (85275) 1994 LY. For this run, the telescope imaged three fixed fields while the asteroid passed through them, making sure to overlap the fields. The red, blue and yellow boxes show the telescope's FOV for each field. The asteroid's position at various times is marked. Note that there is a pointing offset applied to avoid placing the target over the centre of the WFC's CCD, which has a large artefact.

Finally, exposure times and a tracking mode must be chosen. YORP observations aim for a minimum SNR of 50, which can usually be achieved with relatively short integration times. Telescope exposure time calculators (e.g. SIGNAL[†]) are used to determine the SNR that can be achieved for a given exposure time.

There is a trade-off between exposure time and temporal resolution, the latter of which is essential to resolve lightcurve features. Short integrations improve resolution but increase photometric uncertainty, and CCD readout times mean that there are

[†]`http://catserver.ing.iac.es/signal/`

diminishing returns for decreasing exposure time. Extremely short exposures (<10 s) can also introduce a shutter bias on some cameras. Longer exposure times improve the photometry, but reduce temporal resolution. If exposures are greater than ∼5% of an asteroid's rotation period, the temporal resolution may be too low to resolve important lightcurve features.

An asteroid's apparent rate of motion will determine how it must be tracked. For the desired exposure time, an asteroid's motion during the integration may exceed what is contained within the seeing disk. This results in the asteroid becoming trailed or streaked in the image. Trailing complicates photometry, and is thus undesirable. If the asteroid's motion, the preferred exposure time, and anticipated atmospheric seeing would lead to this, a decision must be made. The first option is to reduce the exposure time; the second is to use differential tracking and have the telescope move continuously to match the asteroid's motion. The latter is preferred, as the only consequences are that background stars may become slightly trailed and the observer must periodically update tracking rates. A differentially tracking telescope can optionally return to its original position after each exposure, keeping the stars in the same positions between images, while the asteroid moves across the field as it would with sidereal tracking. It is, however, more common to simply point the telescope once and then continuously track the asteroid. This results in the asteroid that appears to be stationary between images while the stars move through the field. If using sidereal tracking, or differential tracking with a pointing reset after every image, then the telescope must be moved periodically to keep the asteroid within the field. Consecutive fields must overlap so that stars common to them can be used to photometrically link sets of background stars, as shown in Figure 2.7. The majority of YORP campaign observations are conducted using differential tracking, as high rates of apparent motion are a natural consequence of observing NEAs when they are closest to Earth.

2.2.3 Data reduction

All imaging for this project was conducted using CCDs, which are the standard sensors for cameras used in astronomical imaging. While complementary metal-oxide-semiconductor (CMOS) sensors are increasingly popular for small telescopes, they are not yet widespread amongst professional facilities.

CCDs are arrays of photo-sensitive pixels, each of which comprises a thin silicon wafer over a capacitor. When a photon strikes the silicon sheet, an electron is released and stored by the capacitor. Over the course of an exposure, each pixel will store a charge that is proportional to the number of photons that struck it. At the end of the exposure, a voltage is applied to transfer charges across the first row of pixels to a voltage converter that translates the accumulated charge for each pixel into a digital unit, known as an analogue-to-digital unit (ADU) or count. The next column is then shifted across and the row is again read out pixel-by-pixel, repeating the process until the entire array has been measured. An array of ADU values is then recorded, forming a raw image that is usually stored in the Flexible Image Transport System (FITS) format.

Raw images from a CCD must be processed before lightcurves can be extracted. A range of calibration frames are taken at the start and end of the night, which are used to correct for imperfections in the telescope and CCD. The steps taken to reduce science imaging in this project are all standard processes that have been described in detail in various publications (e.g. Berry and Burnell (2005)). These steps, which are summarised below, were used by the author (unless otherwise stated) to reduce all imaging data for this thesis.

Bias Subtraction – Bias refers to the baseline electrical noise across a CCD, which is caused by the potential difference across the chip. Thermal gradients and manufacturing imperfections cause this noise to be non-uniform, or biased. To measure the

bias of a CCD, a series of zero-second exposures are taken. These are averaged to form a master bias, which can then be subtracted from any images where the camera was exposed to light.

Dark Frames – Thermal excitation of electrons will contribute to the counts measured by each pixel, with the effect getting stronger for longer exposures. Dark frames are taken to measure this effect, where exposures are taken in total darkness to measure the build-up of counts from thermal currents across the pixel array. Exposure times for dark frames should ideally match the exposure times used in science imaging, although dark frames can be scaled to different exposure times. Similar to bias frames, this is an additive effect so a master bias can simply be subtracted from light-exposed images. The proprietary CCDs used on medium and large telescopes usually utilise cryogenic cooling to negate this effect, so dark frames are not necessary. Peltier-cooled commercial CCDs, which are rarely cooled beyond -20° C, do require dark frame subtraction. Dark frame subtraction was not necessary for observations processed by the author, but some lightcurves provided by collaborators did have dark frames subtracted during data reduction (e.g. PIRATE observations of 1994 LY).

Bad Pixel Correction – As CCDs age, pixels can fail and under– or over–report charge, resulting in images with 'hot' pixels or dead pixels. These pixels can be removed using pixel maps associated with the instrument, or manually corrected by interpolating over bad pixels using values from the immediate area. Bad pixels are only an issue if they cover the asteroid or reference stars, so it is preferable to avoid them with pointing adjustments. This is one of the many reasons that dithering is considered good practice, as it drastically reduces the likelihood of hot pixels affecting measurements on every image. Newer instruments may not have any bad pixels to remove.

Flat Fielding – A variety of issues are resolved with flat field corrections. The design of a telescope often results in optical paths that deliver fewer photons to the

edges of the chip, vignetting the image. Dust and other contaminants on the mirrors will also reduce the number of photons delivered to certain regions on the chip, and variation in the sensitivity of pixels will result in a non-uniform response. The combined effect of these issues causes uniformly illuminated fields to appear with non-uniform brightness, with both large-scale gradients and local artefacts appearing in images. The severity of these deviations is dependent on the wavelength of light being measured, so each filter is affected differently. To isolate these deficiencies, 'flat field' images are taken. A set of observations of a uniformly illuminated field, ideally of clear twilight sky, are taken for each filter during the evening. As sky brightness rapidly decreases during this time, exposure times are adjusted between images to keep the mean pixel count between 10,000 and 40,000. Depending on weather, and how many filters are going to be used for science imaging, it is not always possible to obtain enough flat field images prior to observations. Ideally, there should be five fields per filter, with a pointing offset after each image. These can later be median combined to remove any stars or non-uniformity in field illumination, which can be an issue for very large FOVs. Should time pressure or weather prevent the acquisition of required flat fields, they can also be taken in the morning twilight. Alternatively, 'dome flats' can be taken. These are images taken with the telescope pointing to an illuminated flat white surface inside the telescope dome. Most telescope enclosures have lightboxes or screens mounted high inside the dome for this purpose. Flat field images from other nights can also be used, although they should ideally be taken within a few days of science images they will be used to reduce. As the mean pixel count will vary between flat field images, they are normalised by dividing each image by its median value to produce a map of the CCD's response. The median is used to avoid extreme values, as stars can appear in some images. Along with pointing offsets, flats can be taken with sidereal tracking disabled to further minimise the impact of stars appearing in individual flat fields. Each filter's set of normalised flat fields are then averaged to create master flats. Science images are then corrected by dividing images by the corresponding master flat field.

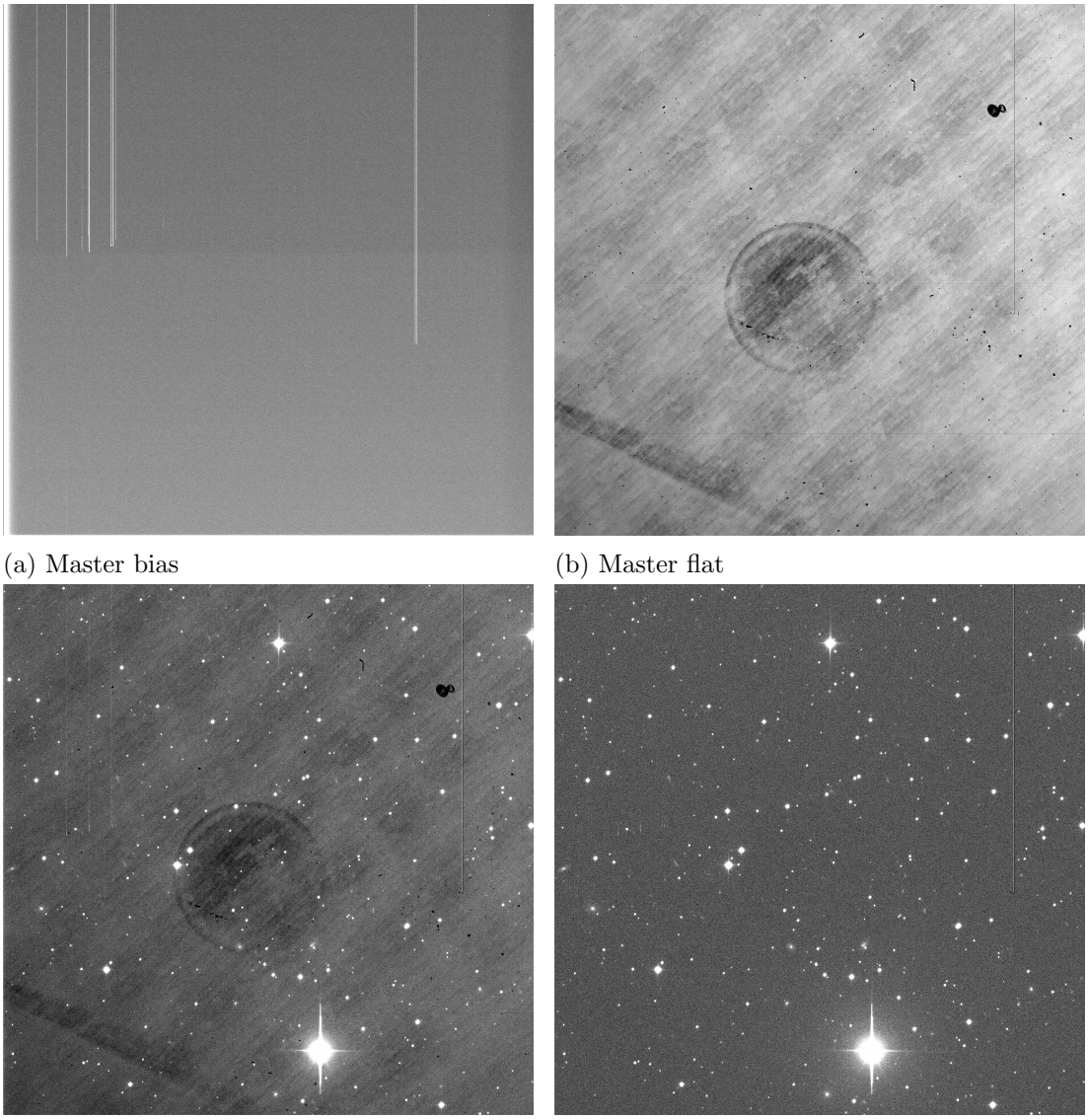

(a) Master bias

(b) Master flat

(c) Raw science image

(d) Reduced science image

Figure 2.8: These images, taken in August 2020 with the WFC, show the calibration frames and the difference between the raw and processed science frame. The science image and flat field were taken using the Harris V filter. Note that a column of hot pixels remains in the reduced image; since it did not interfere with photometric measurements it was not deemed necessary to remove it.

Fringe Removal – Light can be reflected between the layers of a CCD, resulting in both constructive and destructive interference. This results in patterns in the image where there are small differences in brightness, which should be removed prior to conducting photometry. Longer wavelengths are more susceptible to this, with the effect worsening for narrowband filters. Some broadband filters used in the YORP campaign, such as EFOSC2's R filter, are also affected by fringing. The shape of fringe patterns seen with a specific filter and CCD combination does not change, but the intensity varies with exposure time and atmospheric conditions. Fringing is caused by emission lines in the sky, and is most noticeable in deep exposures, so flat fielding is not sufficient for fringe mapping. Instead, long exposures are taken of sparsely populated fields to create fringe maps. These maps can be scaled to the range of intensities measured in a science image, and then subtracted from it to remove the fringe patterns. For this thesis, NTT R filter observations of 1994 LY required de-fringing. This reduction step was carried out by Dr. Tarik Zegmott, using NTT fringe maps made available by ESO and an automatic fringe correction tool described by Snodgrass and Carry (2013).

Cosmic Ray Removal – Cosmic rays are the least predictable source of error in images, as they are high-energy particles that strike the CCD and excite electrons over several pixels. They can randomly appear anywhere in an image, so each frame must be inspected to check that cosmic rays do not fall within apertures used for photometry. This can be done manually, or automatically. Cosmic rays are removed through interpolation, similarly to hot pixels, however their random distribution across images means that they must be removed on an image-by-image basis, instead of interpolating over the same pixels for every image. Cosmic ray removal was not necessary for any of the images reduced by the author, but it may have been performed for some lightcurves provided by collaborators.

Miscellaneous Issues – Various other issues can affect images, some of which can be difficult to identify. For example, during observing runs with the INT for this thesis,

there were several issues with the WFC's shutter that resulted in regions of the chip being under– or over–exposed. This is not always obvious when looking at photometric data, hence visual inspection of the images and careful consideration of observer logs helps to identify these problems. If these issues are isolated to a very small number of frames, they are usually excluded from any subsequent analysis.

During the course of this project, a new major nuisance for astronomers has emerged. Satellite 'megaconstellations', which comprise thousands of satellites in low-Earth orbit, have dramatically increased instances of satellite trails appearing in images. There is no technique that can remove these satellite trails while preserving photometric data, meaning that substantial numbers of images cannot be used. This effect is at its most severe just before and after twilight, when satellite solar panels reflect the most sunlight towards Earth. This issue will continue to worsen as more satellites are launched (McDowell, 2020), with no clear solution in sight.

2.2.3.1 Asteroid lightcurve extraction using relative photometry

After the science images have been reduced, the lightcurve extraction process can begin. A lightcurve is a plot of an asteroid's apparent brightness against time, so the brightness of the asteroid must be measured in each image. In some cases, groups of images are stacked to improve SNR, in which case the brightness is measured for each stack. As YORP analysis requires timing information with $\sim$1 s precision, care is taken to ensure each time measurement corresponds to the middle of the integration.

An asteroid lightcurve should isolate brightness changes caused by the object's rotation, and not include variation caused by weather, airmass or sky brightness. All objects in the field will be equally affected by these factors, hence the brightness of the asteroid is measured relative to background stars. This is done for each image, allowing for brightness correction on an image-by-image basis. This results in smaller photometric uncertainties than other methods, such as using a standard star or calibrating to field stars, because it does not add additional uncertainty from the catalogue mag-

Figure 2.9: In this image, which was taken by the author using the Beacon telescope in April 2020, each diagonal white line is a trail caused by a *Starlink* satellite passing through the field. Shortly after being launched, these satellites appear in groups or 'trains' that gradually spread out over several weeks. Launches like this will eventually happen every few days just to replenish failed or retired satellites, wreaking havoc on ground-based observatories.

nitudes of the reference stars. The only limitation of relative photometry is that this calibration is self-contained: brightness variation is recorded, but the actual brightness is not calibrated to a standard photometric system. While this does rule out some measurements, such as colour and diameter, the YORP campaign's sole focus is minimising uncertainty in lightcurve shape, especially at turnover points that help to constrain phase offset measurements. For this reason, relative photometry is the preferred method for this work as it produces the best possible lightcurves by minimising photometric uncertainty.

As such, the following steps must be taken to measure the relative brightness of the asteroid in each image. Lightcurve extraction was mostly performed using IRAF[‡]

[‡]`https://iraf-community.github.io`

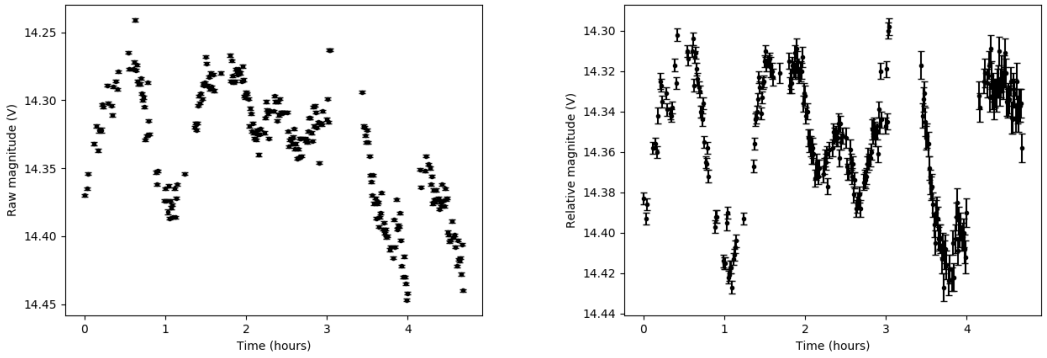

(a) Raw asteroid lightcurve (b) Relative asteroid lightcurve

Figure 2.10: A raw (a) and relative (b) lightcurve for 1994 LY, taken with the INT on 2020-08-10. The raw lightcurve is a direct measurement of the asteroid's brightness, while the relative lightcurve shows the difference in brightness between the asteroid and a set of stable background stars. As this lightcurve covers two rotations, the asteroid would be expected to return to the same brightness at its peaks and troughs. While conditions were stable for the first 2 hours of the night, these observations continued into the morning twilight. This caused raw measurements to show a decrease in brightness, where in reality the asteroid was brightening. While uncertainties are larger during this twilight period, it is clear in the relative lightcurve that the peaks at 0.5 and 1.5 hours are repeated at 3.5 and 4.5 hours respectively.

(Tody, 1986) and SAOImage ds9 (Joye and Mandel, 2003), along with various Python and Bash scripts.

Asteroid Co-ordinates – The first step is to manually mark the position of the asteroid in each image, using pixel co-ordinates. While this could be done automatically with plate solved images and an ephemeris service, it is a relatively fast process and provides an opportunity to visually inspect each image. As the asteroid can sometimes be very faint, and there can be multiple asteroids in the field, a finder chart is used to confirm the position of the asteroid. Blinking the images is also useful, as it is easier to spot an object that is moving relative to static background stars (or vice versa, depending on the pointing and tracking strategy). It is at this stage that images may first be flagged for potential issues, such as satellite/aircraft trails or periods of poor weather. The observing logs can also be useful, as they often include notes describing known issues. Once the asteroid's position has been marked in each image, the human-

marked co-ordinates are submitted to a centroiding algorithm to determine the precise position of the asteroid in each frame.

Background Stars – Relative lightcurves typically utilise up to ten background stars. With potentially hundreds of images per night, it is not practical to manually mark the positions of background stars in every image. Fortunately, stars do not (significantly) move relative to each other over the course of one night. This means that the position of only one background star needs to be measured for every image, with the remaining background stars only requiring a positional measurement in the first image. The co-ordinate offset between each background star and the first 'anchor' star is calculated, and those offsets can be applied to every image to determine the position of each background star in all images. These calculated co-ordinates are then submitted to a centroiding procedure to measure their exact positions.

For observations of fast moving asteroids, or very long lightcurves, the background stars may not remain in the telescope's field across all images. If a substantial number of them do remain present across all images, background stars are simply dropped as they move out of view. This results in slightly larger photometric uncertainties, but is generally the best option. Where this is not possible, and most or all stars are lost, the lightcurve must be broken into sets of background stars. There must be at least one star that is present in consecutive sets, which is used to link the fields. When this happens, stars from the old field can be mapped onto stars in the new field using the change in the 'link' star brightness(es) during the field change. If the field is continuously changing, there is flexibility in when to end one set of background stars and switch to the next. Each field change complicates the analysis, and introduces more uncertainty, however opting for more frequent field changes provides greater flexibility to select better sets of background stars. In most cases, only two to three field changes are required, although up to seven have been used for lightcurves extracted for this thesis.

Background stars must be selected carefully. Stars that are too faint will have large

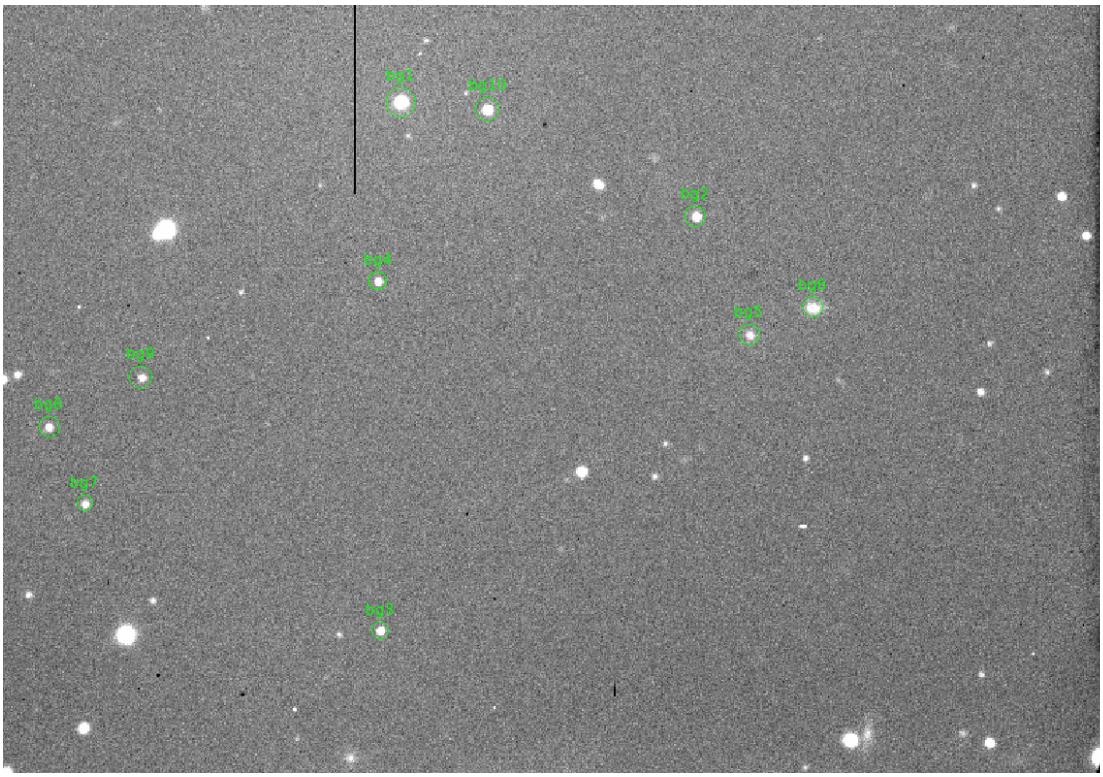

Figure 2.11: The background stars used for a lightcurve of 2000 PN9 taken with the NTT on 2020-11-03. Each background star, enclosed in a green circle, is labelled for personal reference. The asteroid is visible as a bright source halfway between 'bg3' and 'bg5'. Note that the circle diameters are irrelevant, and do not correspond to a centroid radius or photometric aperture size.

photometric uncertainties, so including them in a set of reference stars can worsen the final results. Similarly, stars that are too bright will saturate the CCD and result in non-linear response. Saturation is sometimes obvious through visual inspection, however the point spread function (PSF) must be inspected to confirm that a star is not saturated. An example of this is shown in Figure 2.12. It is good practice to include as many suitable background stars as possible, as they will later be checked for variability. If a star's brightness varies in a way that is not consistent with other stellar sources in the field, it is removed. It is also wise to select stars from across the field, and not in one small cluster, to reduce the impact of any biases that may have survived the reduction process. After photometry has been performed, stars should also be checked to see if there are any unexpected jumps in brightness caused by cosmic rays or artefacts, so they can be temporarily removed for affected frames. It is rare

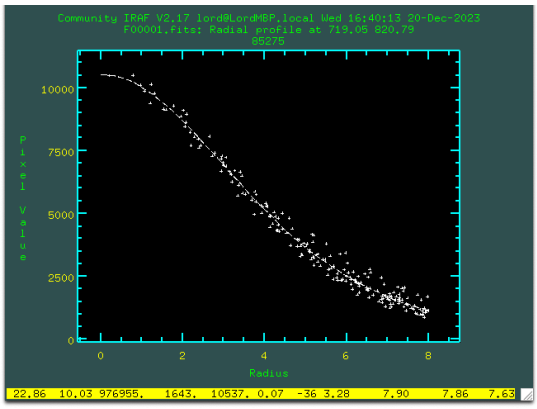

(a) Radial profile (normal)

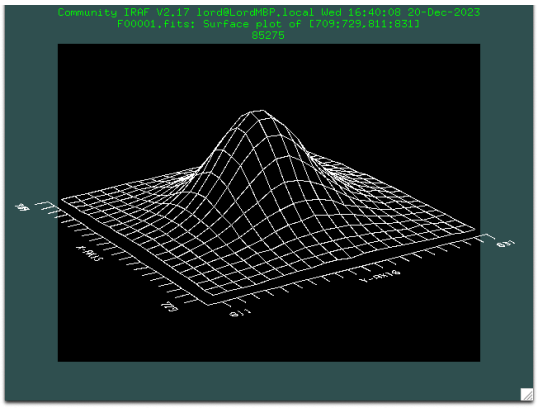

(b) Surface profile (normal)

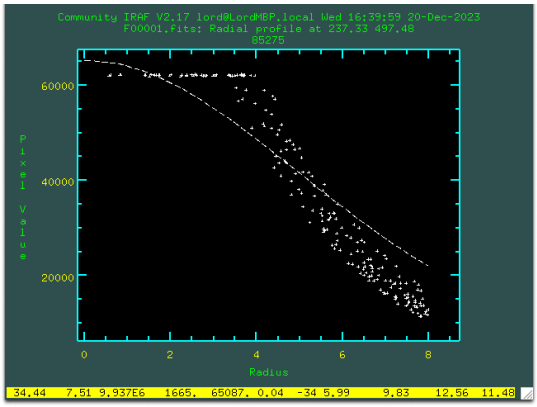

(c) Radial profile (oversaturated)

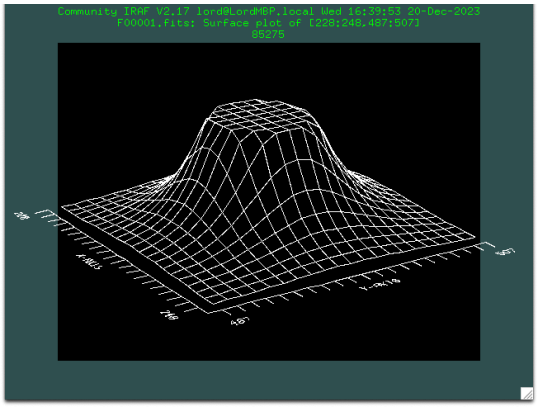

(d) Surface profile (oversaturated)

Figure 2.12: The PSF of two stars, shown with radial (a, c) and surface (b, d) plots. Radial plots show pixel counts against distance from the centroid in any direction, with a dashed line showing a Gaussian fit to each measurement. Surface profiles show the same information, but use a three-dimensional representation to show how counts vary in both the X and Y directions with counts in the Z axis. A correctly exposed source will have Gaussian shape, as shown in (a) and (b). An over-exposed source that has saturated the CCD will plateau, as seen in (c) and (d).

for there to be ten suitable background stars for the full duration of a lightcurve, with three to seven stars being the most common.

Relative Photometry – Aperture photometry is performed to measure the instrumental magnitude of both the asteroid and background stars. An aperture is drawn over the source, and the sum of counts within this aperture is recorded. This aperture will contain counts coming from both the source and the sky background, which must be removed to isolate the source intensity. To do this, an annulus is drawn outside the

aperture to contain a region of empty sky. The median counts per pixel within this region is taken to be the sky background, which is then multiplied by the number of pixels within the photometric aperture and subtracted from the aforementioned aperture sum. The resulting value is an isolated measurement of the source intensity I. The instrumental magnitude m_i is thus given by:

$$m_i = -2.5log_{10}\frac{I}{t_{exp}} \tag{2.1}$$

where t_{exp} is the exposure time of the image, measured in seconds.

The diameter of the aperture will affect the value of I, and the radius should be the same for both the asteroid and background stars within each image. Photometry is typically performed using a range of diameters that are a function of the full width at half maximum (FWHM), which characterises the PSF that describes how light from a point source is spread out over the CCD.

The minimum FWHM a telescope can achieve depends on its diameter, which determines how light from a point source will be diffracted and spread across the image. The minimum resolving power - which is *approximately* 2×FWHM - is given by the Rayleigh Criterion:

$$\theta = 1.22\frac{\lambda}{D} \tag{2.2}$$

where θ is the minimum angular size that can be resolved, λ is the wavelength of the incoming light, and D is the telescope's diameter.

The light from any point source will thus be spread into a disk with diameter no less than θ following a Gaussian profile, as shown in Figure 2.12b. In practice, most ground-based telescopes will never approach a resolving power close to θ due to the affects of the atmosphere. The atmospheric seeing, which is a measure of light being spread as it passes through the atmosphere, will limit the telescope and determine the

FWHM of the PSF. For high altitude observatories with good conditions, seeing ranges from ∼0.4" to ∼1.2", with seeing once again being approximately equal to 2×FWHM, as the PSF will result in very few source photons being spread more than 1×FWHM away from the centroid in any direction.

When performing photometry, a range of aperture sizes are used. These are typically 1×FWHM, 1.5×FWHM, 2×FWHM, and 3×FWHM. The value that produces the lowest photometric uncertainty is chosen, which is usually 2×FWHM as the aperture will contain ∼99% of the counts coming from the source.

Each measurement of m_i has an associated uncertainty Δm_i, which is calculated by IRAF's `phot` procedure using:

$$\Delta m_i = \frac{1.0857}{I}\sqrt{\frac{I}{g} + A\sigma^2 + \frac{A^2\sigma^2}{n_{sky}}} \tag{2.3}$$

where g is the CCD gain (in electrons per ADU), A is the aperture area in square pixels, σ is the standard deviation of sky pixel value, and n_{sky} is the number of pixels contained within the sky annulus.

To perform relative photometry and correct for changes in atmospheric conditions, a reference image must be selected. This is typically the first image in a lightcurve sequence. As background stars are assumed to have constant magnitudes, any change in a star's instrumental magnitude from its brightness in the reference image must be caused by changes in atmospheric conditions. For each star n, this magnitude offset is given by m_n with uncertainty δ_n. Measuring the average magnitude shift across all background stars in each image s provides a correction factor $\bar{m_s}$ which can be subtracted from the asteroid's instrumental magnitude in the image to remove non-rotational brightness variation. This average magnitude shift can be calculated as follows:

$$\bar{m_s} = \frac{\sum_n w_n m_n}{\sum_n w_n} \tag{2.4}$$

where $w_n = \delta_n^{-2}$, which weights the average toward stars with smaller uncertainties.

The asteroid's relative magnitude in each image is hence given by:

$$m_{rel} = m_{i_{ast}} - \bar{m_s} \tag{2.5}$$

with an uncertainty $\Delta m_{rel} = \sqrt{\Delta m_{i_{ast}}^2 + \Delta \bar{m}_s^2}$.

Plotting relative magnitude against time (using the exposure mid-point) results in a relative lightcurve. Before this lightcurve can be used, additional checks must be made to ensure there are no frames with flux contribution from aforementioned cosmic rays or other artefacts. Plots of m_i against time for both the asteroid and background stars should be inspected for outliers, and variation should be consistent across background stars. Individual frames or background stars should be removed accordingly.

If an asteroid passes close to or over a star, that star's flux can contribute to the measurement. While it is sometimes possible to subtract stellar flux, this was not done for any lightcurves included in this research. Instead, frames were removed if there was a non-negligible flux contribution from stars within the asteroid's photometric aperture. These frames were identified through flux profile inspections of images where the asteroid passed within two aperture radii of a star.

If there is very low SNR on the asteroid, images can be co-added or 'stacked' to produce a cleaner lightcurve. In this process, batches of images are combined such that the flux from several images can be summed to increase signal on the source against the random background noise. When images are combined, the desired source must be in the same location in each image. Because asteroids move between images, it is necessary to create two separate series of stacks, with one that aligns images on the asteroid and one that aligns them on the background stars. Once properly aligned,

each batch of images can be combined to create a stacked image with summed counts and integration time. Photometry is then repeated on the two series of stacked images to produce a new lightcurve.

This stacking process was used for a significant number of lightcurves presented in this thesis, typically using batches of three images. Most stacks were created using 'rolling' groups of images, e.g. 1-2-3, 2-3-4, 3-4-5, instead of simple groups of 1-2-3, 4-5-6, 7-8-9 etc. This mitigates the loss in temporal resolution caused by the latter method, resulting in a smoothed lightcurve. This makes it especially important to ensure that images comprising each stack were taken close together, and not separated by pauses or removed frames, otherwise it would be averaging over a significant portion of the asteroid's rotation. As previously mentioned, is also critical that the associated time measurement is the exact mid-point between the start of the first exposure and the end of the last exposure.

Unless otherwise stated, all lightcurves presented in this thesis were extracted by the author.

2.3 Planetary radar

The overwhelming majority of observational astronomy relies upon passive methods, detecting energy that was produced by distant objects and delivered to Earth. Radar astronomy is unique in being the only technique that uses active observations, where signals are transmitted from Earth to illuminate remote bodies. Planetary radar has been used to study objects across the Solar System, ranging from cm-scale NEOs to the outer planets and their moons, and has proven to be especially valuable for the study of NEAs.

Radar observations give the observer the privilege of configuring the signals that will illuminate an asteroid, with control over key parameters such as frequency or polarisation. When a radar transmission reaches an asteroid, the surface properties of its

surface will determine what portion of the signal is reflected. Photons reaching the farthest parts of the asteroid will take slightly longer to be reflected back towards Earth, while the rotation of the asteroid will cause the reflection's frequency to be Doppler shifted in opposite directions on two hemispheres of the asteroid. The difference between the transmission and echo signals hence reveals information such as the asteroid's distance, surface composition, shape and spin-state.

Radar observations are the biggest source of non-convex shape models for asteroids, which are critical to increasing the number of YORP detections (e.g. Zegmott et al. (2021)). As shown in Figure 2.13, over 1000 asteroids have been detected with radar. However, the relative obscurity of radar astronomy means that there is limited capacity for shape modelling, with only a few dozen radar shape models published to date. The reliability of these shape models has been proven through comparison with in-situ observations, such as with Itokawa (Ostro et al., 2005; Fujiwara et al., 2006), Toutatis (Hudson et al., 2003; Zou et al., 2014) or Bennu (Nolan et al., 2013; Dellagiustina et al., 2019).

This work utilised radar observations to develop a radar-based physical model of 2000 PN9 (Section 4), while other work for this thesis was sometimes informed by radar observations, or contributed to radar models developed by collaborators. All radar data was provided pre-processed by members of the #TeamRadar collaboration in preparation for shape modelling.

2.3.1 Facilities

Data were provided from two radar telescopes, which until recently were the only facilities with a dedicated radar observing programme. The primary motivation for radar observations is planetary defence, as radar astrometry (known as ranging) can significantly improve orbit solutions for PHAs. Observations suitable for physical modelling are harder to obtain, due to the increased requirements for SNR and spatial resolution.

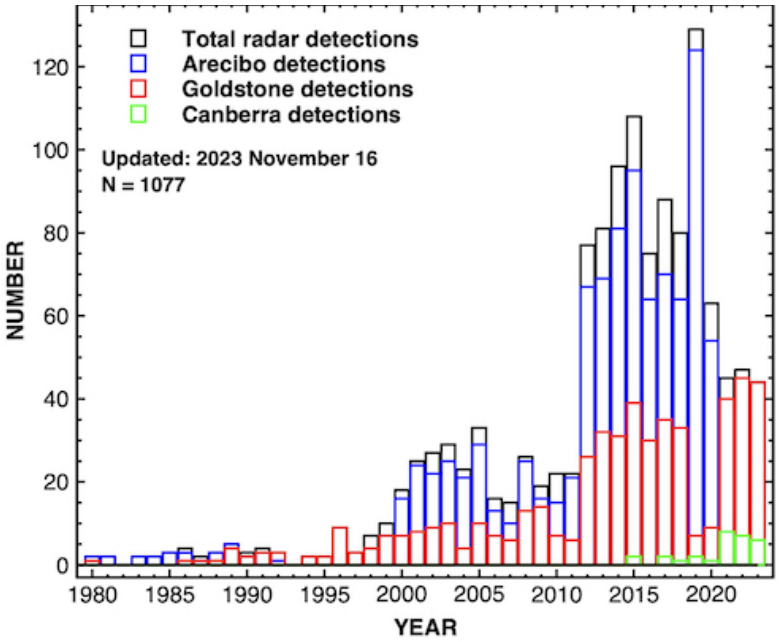

Figure 2.13: A histogram showing the number of asteroids newly detected by planetary radar facilities every year from 1980 to 2023. This figure was reprinted from JPL[a].

[a] https://echo.jpl.nasa.gov/lanceradar_detected_neas_summary/asteroid.radar.history.figures.html

Fundamentally, a planetary radar is a large radio telescope that has been fitted with a powerful transmitter. The observer will transmit a signal towards a Solar System object, which could take seconds to minutes to arrive. When the signal reaches the object, a portion of it will be reflected back towards Earth. The surface properties of the target will affect the strength of the reflection, with the rest being absorbed or scattered. The reflected signal - or echo - will be modified by the physical and rotational properties of the body. As the echo reaches the observer, the telescope ceases transmission and switches to a receiving mode. The echo's intensity, delay and Doppler shift can then be recorded. Cycling between transmit and receive mode requires the telescope to make physical movements, which can take tens of seconds. During very close approaches, the return travel time of the transmitted signal may be too short to allow for a useful transmission time - or integration - before the telescope must switch to its receiving mode. To avoid this issue, a second telescope can be used to observe in a bi-static mode. In this configuration, one telescope continuously transmits while

another continuously receives (Brozović et al., 2018).

Radar observability is primarily affected by target range, size and albedo. For kilometre-sized NEAs, this typically corresponds to a limit of ∼15 lunar distances. Being limited to close approaches, and mostly relying upon two northern-hemisphere facilities, severely limits asteroid observability when compared to optical observations. Despite this, planetary radar has made a considerable contribution to the field.

Arecibo Observatory – The William E. Gordon telescope was a 305 m fixed-dish radio telescope at Arecibo Observatory (Puerto Rico, USA). Equipped with a 2380 MHz (12.6 cm) S-band transmitter (Virkki et al., 2022), it was the world's most powerful civilian radar system. The telescope, which was built into a natural geographical depression, comprised a spherical dish with a cable-mounted steerable transmitter/receiver unit - known as the Gregorian Dome - which could be moved over the dish to directionally transmit or receive up to 19° from the zenith. Since its construction in 1963, it remained the world's largest single-aperture telescope until 2016, when it was supplanted by the Five-hundred-metre Aperture Spherical Telescope (FAST). Although, FAST's design means that it cannot be fitted with a radar transmitter. In 2020, storm damage caused a cascade of structural failures resulting in the total destruction of the Arecibo telescope. Since the conception of planetary radar, Arecibo has been the primary source of observational data. Its destruction has had a severe impact on the fields of asteroid research and planetary defence, with there being no plans for a direct replacement in the immediate future.

Goldstone Solar System Radar – The GSSR facility consists of the fully steerable 70 m Deep Space Station 14 (DSS-14) 'Mars' antenna equipped with an 8560 MHz (3.5 cm) X-band transmitter (Rodriguez-Alvarez et al., 2022). DSS-14 is located in the Mojave Desert (California, USA) and is a part of the NASA's Deep Space Network, which is used to communicate with spacecraft. When not being used to support deep space missions, GSSR is used for science observations. Following the destruction of Arecibo,

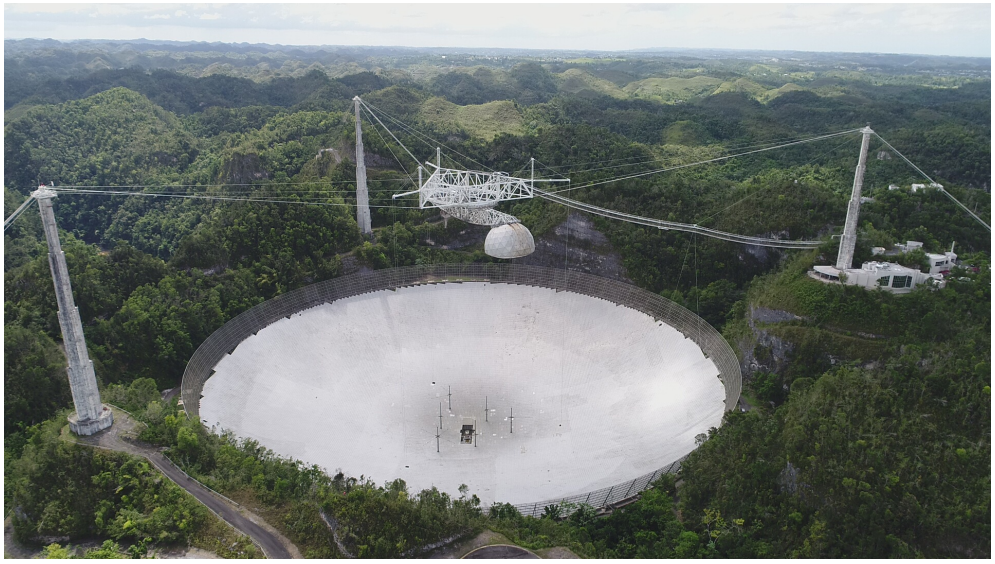

Figure 2.14: The William E. Gordon telescope at Arecibo Observatory, Puerto Rico (USA). The Gregorian dome, which housed the transmitter and receiver, can be seen suspended above the dish by cables. The failure of these cables lead to the telescope's demise, with the instrument gantry and support structures falling onto the dish. Image provided by UCF[a].

[a] https://www.ucf.edu/news/a-second-cable-fails-at-nsfs-arecibo-observatory-in-puerto-rico/

Goldstone is now the primary source of planetary radar observations, with efforts from the similar DSS-43 in Canberra (Australia) also making a notable contribution in recent years.

2.3.2 Radar observations

Two methods are used to observe NEAs with radar: continuous wave (cw) spectra (also known as Doppler-only) and delay-Doppler imaging. As previously explained, differences between the transmission and echo can reveal information about an asteroid's shape, size, rotation and surface composition. Both cw spectra and delay-Doppler imaging provide information about an asteroid's properties, and can be used as input data for shape modelling procedures.

Figure 2.15: The 70 m DSS-14 'Mars' antenna, or GSSR, which is the largest of five dishes at the Goldstone Deep Space Communications Complex in California (USA). The dish is used to communicate with spacecraft beyond the Solar System, such as the Voyager probes, and so was designed to be fully steerable in order to maximise communication windows. This means that NEAs can also be observed over a wider range of altitudes than a fixed-dish design would allow. Image provided by NASA[a].

[a] https://www.nasa.gov/image-detail/goldstone-dss14-08/

2.3.2.1 Continuous wave spectra

The simpler of the two observing techniques, useful cw spectra can be obtained with a lower SNR and are primarily used for correcting orbit solutions, in addition to making measurements of scattering, radar cross-section and physical radius (Pettengill and Jurgens, 1979).

A monochromatic and circularly polarised signal is transmitted and subsequently received, with the return travel time being approximately equal to the signal integration as previously explained. The reflected signal will not be monochromatic, having its frequency both shifted and broadened into a spectrum as a result of the asteroid's motion causing a Doppler shift in the reflection.

Ephemeris values for the asteroid's centre of mass are used to subtract the expected Doppler shift caused by its radial velocity. The measured deviation between the transmission frequency and the echo's corrected centre-of-mass frequency f_0 thus describes the offset between the predicted and actual radial velocity. This is used to refine the

asteroid's orbital solution. Radar observations are critical to planetary defence as there is no other way to determine orbits so precisely with remote observations.

Broadening of the frequency is caused by the asteroid's rotation; one side of the asteroid will be receding while the other will be approaching, causing a Doppler shift. The extent to which a cw spectrum is broadened depends on asteroid size, shape, rotation rate, viewing angle and signal wavelength. These parameters can be constrained with sufficient rotational coverage, meaning that cw spectra can be used to measure the radius, period, and sometimes shape of an asteroid (Ostro et al., 1988; Ostro et al., 1990b).

The telescope's receiver detects the echo when a voltage is induced, creating an analogue voltage time series. This is converted into a digital signal by sampling at a frequency f_s. The number of samples taken, n_s, is hence given by $n_s = \tau \cdot f_s$ where τ is the integration time. An n-point fast Fourier transform (FFT) is used to reduce the digital signal, where n is a divisor of n_s. The frequency resolution is thus given by f_s/n. Using $n = n_s$ provides the highest possible resolution of $1/\tau$. The number of 'looks', N_{looks}, which is analogous to the number of optical images used to form a stack, is given by n_s/n. The SNR of the spectrum scales with $\sqrt{N_{looks}}$, but frequency resolution increases with n, leading to a trade-off. Lowering the frequency resolution has the added benefit of smoothing the spectrum to reduce the prominence of spiky features, which would otherwise cause issues in shape modelling software. It is customary to plot cw spectra with echo power measured in standard deviations above the noise, against Doppler frequency. An example of this is shown in Figure 2.16.

Continuous wave observations can also be used for radar polarimetry. Echo power is recorded in both the same circular (SC) and opposite circular (OC) polarisations, with the original transmission having the SC polarisation. For mirror-like backscattering, the echo's SC component would be zero, while reflections off a surface that is very rough (on scales comparable to wavelength) will have a significant SC component (Ostro et al., 2002). It should be noted that for radar observations, the reflecting 'surface'

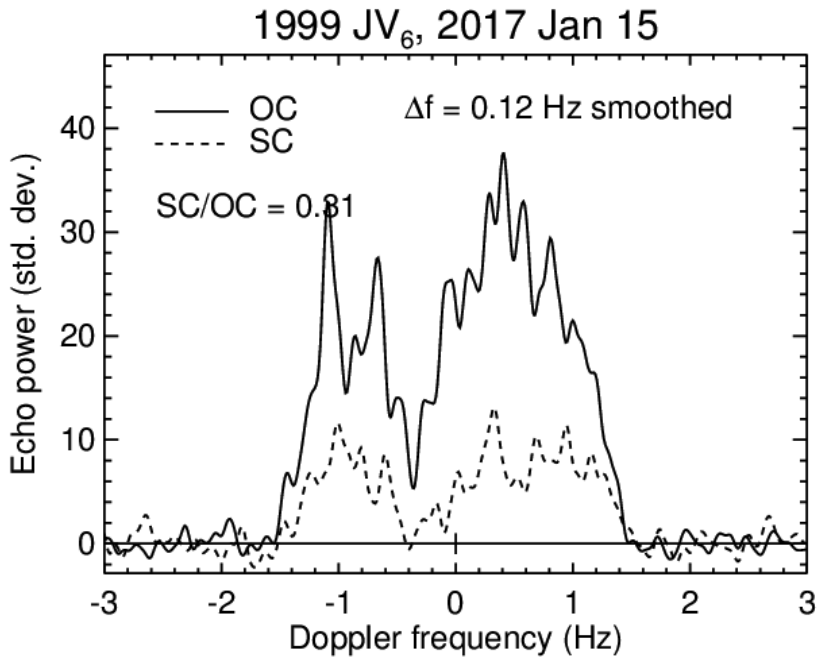

Figure 2.16: A continuous wave spectrum of (85990) 1999 JV6 taken with Arecibo in January 2017. Echo power, in standard deviations, is plotted for the opposite circular (OC) and same circular (SC) polarisations against Doppler frequency, using solid and dashed lines respectively. The spectrum was smoothed to a frequency resolution of 0.12 Hz. The asteroid's bilobate shape (Rożek et al., 2019a) can be inferred from the double peak. This figure was obtained from the Lunar and Planetary Institute (LPI)[a].

[a] https://www.lpi.usra.edu/resources/asteroids/asteroid/?asteroid_id=1999JV6

includes the penetration depth of the radio signal, which is typically several centimetres. Nevertheless, the SC/OC ratio is generally used to infer the roughness or complexity of an asteroid's surface. Results from the OSIRIS-REx mission, however, have cast doubt upon this interpretation of SC/OC ratios. Circular polarisation ratios suggest that Bennu is relatively smooth above the cm-scale (Nolan et al., 2013). However, the spacecraft data show that Bennu's surface is much rougher than this with larger scale boulders than expected (Dellagiustina et al., 2019). Eros and Itokawa, which are both S-complex asteroids that have been visited by spacecraft, have SC/OC ratios of 0.22 ± 0.06 and 0.26 ± 0.04 respectively (Magri et al., 2001; Ostro et al., 2004). Due to dissimilar formation processes, these asteroids exhibit differences in actual surface roughness (Susorney et al., 2019), despite the similar SC/OC ratios. While radar

polarimetry can be used to reliably infer the surface roughness of small bodies (Hickson et al., 2021), it should not be assumed that SC/OC is a direct analogue.

2.3.2.2 Delay-Doppler imaging

As previously discussed, an asteroid's shape will lead to variation in travel time, known as delay, for signals reflected off different parts of the asteroid. This means that a coherent transmission will have an incoherent echo, with the reflection being spread in time (or delayed) over several μs. With continuous transmission, this means that earlier transmissions that were reflected from a distant part of the asteroid will return to the receiver at the same time as later transmissions reflecting off closer parts of the asteroid. Delay-Doppler imaging encodes the transmitted signal so the echo, once decoded, can be associated with its original transmission time to calculate the delay and spatially resolve echo signals.

Signals are encoded using phase modulation. A pseudo-random binary phase code (Ostro, 1993; Magri et al., 2007) inverts the phase for a duration known as the baud length b, measured in seconds. This code repeats after a number of binary elements L, thus the code's total duration p is given by $p = L \cdot b$. The input for L must not cause self-correlation, as elements of the binary code should not be able to be shifted by less than an integer multiple of L to create the same binary pattern. For example, $L = 6$ might produce 100100 which can be shifted by 3 to repeat the pattern and cause self-coherence. If the pattern was instead 1000000 ($L = 7$), it would not repeat. The value of L is always set to a prime number to minimise the probability of repetition. The code is then repeated during the transmission time τ, such that the total number of code repetitions n_r is given by $n_r = \frac{\tau}{p}$.

When receiving, the maximum number of delay samples that can be decoded during the code repetition time p is given by L_s. If the number of samples per baud length, χ, is greater than one, then a portion of each baud cannot be sampled. The number of delay samples that will actually be decoded is thus given by L_χ. The signal is decoded

by correlating the binary code with the signal, resulting in a one-dimensional array with an analogue voltage time series for L_χ delay steps. As with cw spectra, the voltage time series for each delay step is subjected to an n-point FFT where $n = n_r$ gives the highest frequency resolution. Again, the number of 'looks' can be increased to improve SNR. The result is an array, or image, of delay against Doppler shift, with each pixel's value representing echo power. The array is normalised such that the mean noise outside the echo is 0, with an rms value of 1. The resultant images can then be further summed to increase 'looks', and delay can be binned, to improve SNR. The final delay resolution translates to the spatial resolution of the images, which typically ranges from several metres to hundreds of metres depending on the SNR.

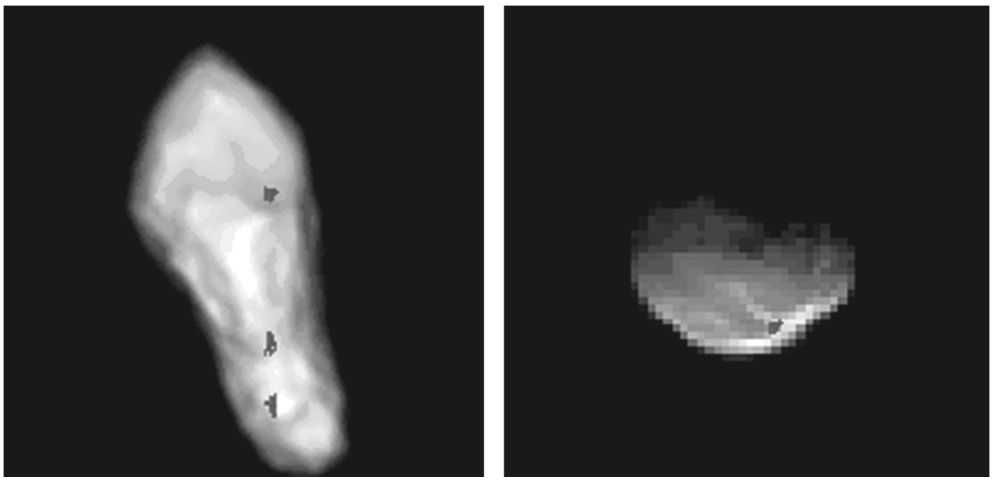

Figure 2.17: A synthetic plane-of-sky image of (4179) Toutatis (left) and a corresponding synthetic delay-Doppler image of the asteroid. The delay-Doppler image is oriented such that it is radar-illuminated from bottom, with range increasing vertically, and Doppler increasing horizontally. The three grey regions on the image on the left share delay and Doppler values, and are thus overlapping as a single grey region on the delay-Doppler image on the right. This figure was reprinted from Ostro et al. (2002).

There are several important considerations that must be made when interpreting delay-Doppler images. Unlike direct optical imaging, they are not plane-of-sky images. Multiple points on an asteroid's surface can produce the same delay and Doppler shift, meaning that spatially separated elements on an asteroid's surface can share a pixel. Most notably, it is not possible to determine between radiation reflected from positive and negative latitudes, resulting in the two hemispheres becoming 'folded' in an image.

Any two points of an asteroid that are an equal distance from the observer, with the same radial velocity, will appear at the same location in an image. An example of this is shown in Figure 2.17.

Despite the complications of interpreting delay-Doppler images, they are an invaluable resource for modelling NEAs. With spatial measurements on the scale of metres, and Doppler-measured spin rates, these radar observations enable science that would otherwise be impossible without in-situ measurements.

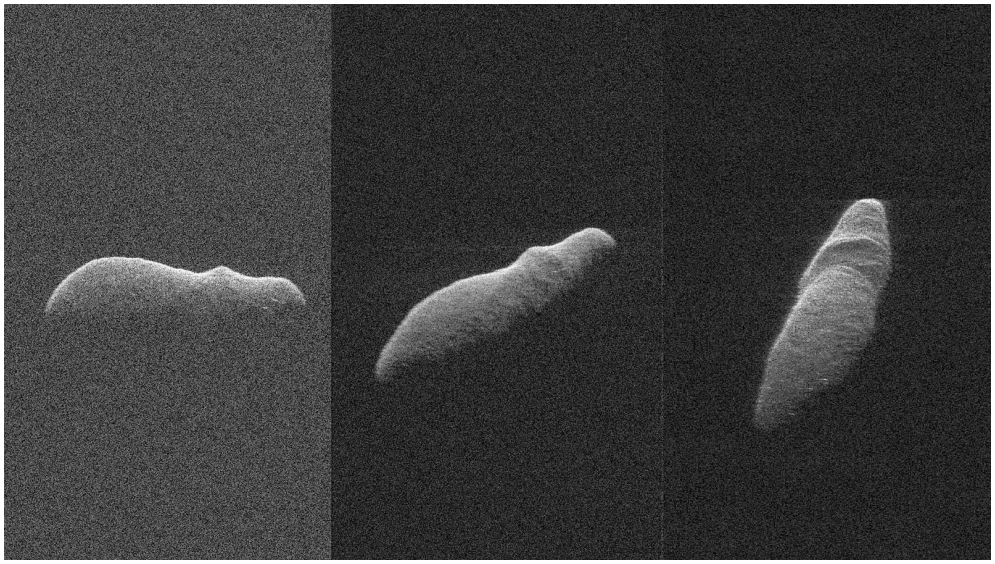

Figure 2.18: Delay-Doppler images of (163899) 2003 SD220, each taken a day apart in December 2018. These images are oriented such that they are radar-illuminated from the top, with delay increasing towards the bottom and Doppler frequency increasing towards the right. Image provided by JPL[a].

[a] https://www.jpl.nasa.gov/news/holiday-asteroid-imaged-with-nasa-radar

CHAPTER 3

PHYSICAL MODELLING AND YORP ANALYSIS OF NEAR-EARTH ASTEROIDS

3.1 Convex inversion of optical lightcurves

It is relatively easy to collect optical lightcurves for large samples of the asteroid population. Since these observations started becoming routine, methods to extract information from lightcurves have been highly sought after.

Russell (1906) was the first to explore the "inverse problem" of decoding brightness variability in asteroids. Critically, Russell's solution only considered observations taken at opposition, where the Solar phase angle is zero. This limitation was applied due to the limitations of contemporary telescopes and their analogue cameras. Knowing that asteroids were rotating objects, there were two explanations for the brightness variability that was measured in lightcurves. The first was that asteroids had significant albedo variegation, with dark spots akin to those observed on the Sun. The second possibility was that, unlike stars, asteroids have non-spherical shapes, causing the reflecting surface area to vary throughout an asteroid's rotation.

Russell determined that the spin-axis orientation of asteroids should, in theory, always be measurable with rotational lightcurves, albeit with no distinction between prograde and retrograde spin. He also, however, ruled out the possibility of measuring albedo variegation or shape. The reason for this is that are an infinite number of albedo and convex shape combinations could produce the same lightcurve. This apparent degeneracy became consensus, with astronomers believing that analyses of rotational lightcurves were mostly limited to revealing spin rate and pole orientation.

Decades later, after significant improvements to optical facilities, observations of asteroids away from opposition became routine. With a variety of viewing geometries available within asteroid lightcurve datasets, there was renewed interest in developing techniques for lightcurve analysis. Harris et al. (1989) demonstrated that synodic rotation periods could be measured relatively quickly via Fourier analysis of lightcurves (FALC). This technique was a significant improvement over previous methods. FALC remains a standard method for measuring rotation periods using individual or clus-

tered lightcurves, and until recently (Ďurech et al., 2022b), it was responsible for the majority of asteroid period measurements.

Efforts to measure convex shapes and pole orientations relied upon simplified asteroid shape models, such as triaxial ellipsoids (Magnusson et al., 1989). For irregular asteroids, more accurate shapes could be achieved by combining eight octants of ellipsoids with different semi-axes, with a constraint where two semi-axes of adjacent ellipsoids must be equal (Cellino et al., 1989).

A photomorphographic analysis technique for convex inversion (Kaasalainen and Torppa, 2001; Kaasalainen et al., 2001) quickly proved itself to be the most accurate technique for determining an asteroid's convex shape (Barucci et al., 1992). This method ostensibly solves the inverse problem by using a range of viewing geometries and making several assumptions, such as principal axis rotation. Another key assumption is that there is no albedo variegation. Previous work severely over-estimated the significance of albedo variegation, inhibiting the development of shape models. While there is some colour variation on asteroid surfaces, it is rarely enough to contribute to the shape of an asteroid's lightcurve (Magnusson, 1991; Sears, 2015). If albedo variegation can be measured, using extensive optical and thermal imaging, then this can be factored into the shape modelling process.

Kaasalainen's convex inversion technique has become the primary tool for asteroid shape and pole determination, with this work making extensive use of its implementation in the `convexinv` code. Originally written in Fortran, `convexinv` was later converted to C by Ďurech et al. (2010), with subsequent modification by Dr. Agata Rożek (Rożek, 2017), Prof. Stephen Lowry, and Dr. Sam Duddy for the YORP campaign.

3.1.1 Measuring shape with `convexinv`

This work utilised `convexinv` to measure the sidereal rotation period, pole, convex shape, and YORP acceleration for a number of asteroids. A convex shape model, also known as a convex hull, is a representation of an asteroid's shape with its concavities filled, analogous to a 'gift-wrapped' version of the asteroid. These models indicate the overall shape of an asteroid, but are not a direct representation of the asteroid's appearance, as previously demonstrated in Figure 1.6. Nevertheless, they can accurately reproduce lightcurves and are able to reliably produce general shape and spin parameters.

Attempting to model non-convex models of asteroids with lightcurves alone is impractical, as varying the depth of craters or valleys will lead to a number of degenerate solutions. Convex hulls are thus the preference for modelling asteroids using lightcurves. It should however be noted that convex hull models are dimensionless, as uniformly scaling the axes of an asteroid will not change the shape of its lightcurve. Due to this, shape parameters are typically reported without an associated uncertainty.

Kaasalainen presents the inverse problem of asteroid lightcurves as:

$$\vec{L} = A\vec{g} \tag{3.1}$$

where the vector $\vec{L}$ is the observed asteroid brightness, $\vec{g}$ is a vector containing the parameters being fitted, and A is a matrix describing the relation between $\vec{L}$ and $\vec{g}$. The parameters described by $\vec{g}$ can include any combination of shape and albedo variegation, although as previously discussed, albedo is usually assumed to be constant thus $\vec{g}$ only describes shape.

For a model $\vec{g}$, and a lightcurve dataset $\vec{L}$, a solution to the inverse problem can be found by minimising χ^2, which is given by:

$$\chi^2 = \sum_i \left|\left| \frac{\vec{L}^{(i)} - A^{(i)}\vec{g}}{\overline{L}^{(i)}} \right|\right|^2 \tag{3.2}$$

where i is the index number of each lightcurve, $\overline{L}^{(i)}$ is the mean brightness of lightcurve i, expressed as intensity.

The code uses the conjugate gradient method (Press et al., 1992) to optimise χ^2, creating models $\vec{g}$ whose model lightcurve $A\vec{g}$ is compared to the observed lightcurve $\vec{L}$. The general solution is thus given by $\chi^2 = ||\vec{L} - A\vec{g}||^2$. As the parameters contained within $\vec{g}$ are adjusted, the code assesses χ^2 to follow the 'downhill' direction until a minimum value is found.

This method for lightcurve inversion does not require a calibrated magnitude or consider photometric uncertainties.

The former can be an advantage, as relative photometry can produce smaller photometric uncertainties than calibrated photometry, producing cleaner lightcurves. The lack of consideration for photometric uncertainties is, however, is a notable weakness. Newer versions of `convexinv` have introduced a weighting system, but the modified version used in this work (Section 3.1.4) ignores photometric uncertainties. This means that very poor lightcurves can decrease the quality of a model, thus care must be taken when selecting which data to include in the development of a model.

Initially, the shape model is constructed using a spherical harmonic series, which has relatively few variables to optimise. Once an initial optimisation has been performed, the continuous surface of the polyhedron is converted to discrete facets that can be individually modified by subsequent iterations of χ^2 optimisation.

The matrix A contains information describing the viewing geometry for each lightcurve i, albedos for each facet j, and the chosen scattering laws. This matrix is given by:

$$A_{ij} = S_j\left(\mu_{\oplus}^{(ij)}, \mu_{\odot}^{(ij)}\right)\overline{\omega}_j \tag{3.3}$$

where S_j and $\overline{\omega}_j$ define the scattering law and albedo, respectively. The illumination of each facet is given by $\mu_{\oplus}^{(ij)} = \vec{E}_{\oplus,i} \cdot \vec{n}_j$, and its visibility to Earth by $\mu_{\odot}^{(ij)} = \vec{E}_{\odot,i} \cdot \vec{n}_j$, with $\vec{E}_{\oplus}$ and $\vec{E}_{\odot}$ being unit vectors in the asteroid's frame of reference that point towards Earth and the Sun respectively. Each facet's normal is given by $\vec{n}_j$. If either $\mu_{\oplus}^{(ij)}$ or $\mu_{\odot}^{(ij)}$ are equal to zero, the facet does not have a direct line of sight to both the Earth and Sun and thus cannot contribute to lightcurve intensity.

Each facet is defined within a set of facet normals $\vec{n}_j$ and areas g_j. A convex polyhedron must have a closed surface with positive values for each facet area g_j, thus $\sum_j \vec{n}_j \, g_j = 0$ must be preserved. To limit g_j to positive values, it is expressed as $g_j = e^{a_j}$, with a_j as the free parameter that `convexinv` may adjust to optimise χ^2. This also ensures that there is a unique solution for optimising χ^2, as the exponential function is monotonic.

In some cases, $\vec{g}$ is optimised in Equation 3.2 such that $\sum_j \vec{n}_j \, g_j \neq 0$, meaning that there is a small residual. This can be caused by minor albedo variegation or non-convex features on the asteroid, thus a regularisation parameter is introduced in the form of a very small 'dark' facet that accounts for these features.

Finally, the shape model is converted from `convexinv` 's representation to a triangular mesh that can be interpreted by other procedures, such as those used to display the 3D model or perform phase offset analysis.

The convex inversion method described above assumes that the spin-state has been provided. A sidereal rotation period is used to propagate the asteroid's rotation forward in time and determine the phase of each lightcurve, with YORP acceleration providing an additional complication. The viewing geometry of each lightcurve, and hence each lightcurve's shape, depends on the asteroid's pole. This means that the shape model produced by `convexinv` is fully dependent on the spin configuration.

While it is possible to optimise for pole and period alongside shape, the number of unconstrained free variables makes it computationally demanding and often leads to

multiple degenerate solutions. Instead, an asteroid's sidereal period should be measured prior to measuring shape or pole orientation, so that it can be used as the input period. By providing a well-constrained input period, only minor period adjustments are necessary while simultaneously solving for shape. This drastically reduces the computational workload, cutting the number of modelling runs from millions to thousands. This method is described in Section 3.1.2. Similarly, this work did not directly optimise pole orientation within `convexinv`, instead using a pole search method that is described in Section 3.1.3.

The subsequent sections hence describe the step-by-step process for efficiently solving the inverse problem to measure the shape, spin-state and rotational acceleration of NEAs using lightcurves.

Example input files for `convexinv` are provided in Appendix B.

3.1.2 Period determination

As previously discussed, `convexinv` must be used to generate shape models for the full range of period, pole and YORP torque combinations being considered. Sensible ranges for these variables would result in an enormous number of combinations. Fortunately, an asteroid's sidereal rotation period can be measured very accurately without needing to constrain other parameters. This means that the period can be measured first and used as an input parameter for `convexinv`, vastly reducing the number of model iterations needed for the subsequent measurement of shape and pole.

Previously reported periods are available for all YORP candidates, most often being synodic measurements made with FALC. These measurements typically have unacceptably large uncertainties, and synodic period measurements can deviate from the sidereal value by several minutes. Nevertheless, these values can be used to significantly constrain the bounds of a new period search. In some cases, more reliable measurements are available from previous lightcurve inversion or radar observations. In many cases,

it is difficult to distinguish between integer multiples of a minimum possible period, so a report of a 2.5 h period may acknowledge alternative solutions of 5 h or 7.5 h.

The `period_scan` package contained within `convexinv` can be used to measure an asteroid's rotation period using convex inversion. Using the methods described in Section 3.1.1, shape models are developed for six random and unique poles for each iteration over a user-specified period range. This range has the minimum and maximum periods of P_1 and P_2 respectively. The number of iterations within this range, N, is given by:

$$N = (P_2 - P_1)\frac{2\Delta T}{p \cdot P_1^2} \tag{3.4}$$

where ΔT is the time between the oldest and newest lightcurves and p is a scaling parameter, which affects the density of trial periods. The scaling parameter is typically set to 0.8, as higher values result in severe oversampling that increases computational time without yielding additional valid minima. The step size is given by $p \cdot \Delta P$, where ΔP is the minimum separation between minima, given by:

$$\Delta P = \frac{P^2}{2\Delta T} \tag{3.5}$$

with P being the trial period.

As the `convexinv` code is not parallelised, period scans are typically broken into sub-scans with smaller $P_2 - P_1$ ranges for pseudo-parallelisation, which in this case is actually faster than using parallelised code. An added benefit of this is that p can be adjusted between sub-scans to offer variable resolution. Wide ($\sim$10 h) scans were sometimes used in this work to investigate multiple reported periods, with 'fine' scans over expected minima and 'coarse' scans between them. While coarse scans are faster, they are only useful if there are more sub-scans than available CPU cores. In cases where coarse scans were useful, a sub-scan launching script was used to optimise total

run time by balancing the cumulative number of sub-scan steps in each core's queue.

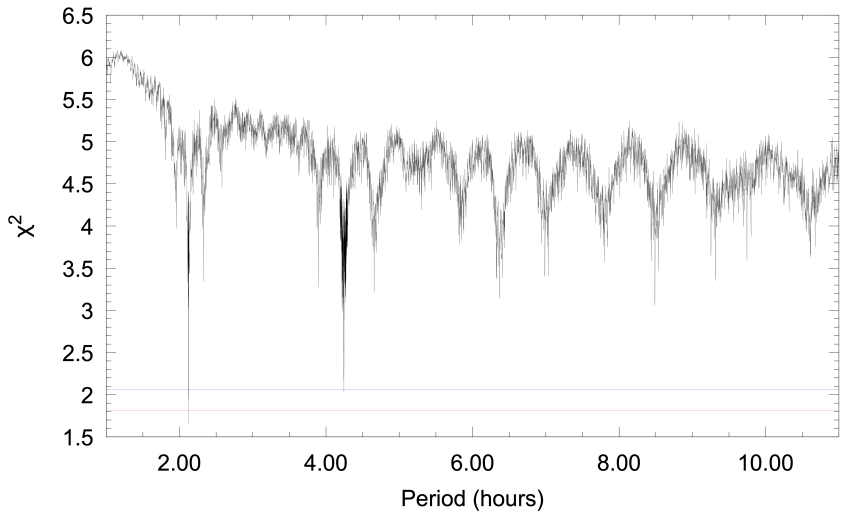

Figure 3.1: Results from a wide period scan of (29075) 1950 DA conducted as part of this work, ranging from 1 h to 11 h. Smaller χ^2 values correspond to a better goodness-of-fit. The red and blue lines show 10% and 25% increases over the global minimum χ^2 value, which lies at 2.12 h. In this case, the 2.12 h solution is clearly differentiated from the next best solution, which is approximately at 4.2 h (i.e. 2× 2.12 h).

The output of a period scan, which is concatenated from sub-scan outputs, is a table containing period, χ^2 fit, rms deviation, the number of iterations and the proportional dark facet area. The poles and shape models are not recorded. Plotting χ^2 against period to produce a periodogram, such as the one shown in Figure 3.1, provides a graphical representation of the search results. The global minimum is taken as the asteroid's period, although other minima within 1σ of the global minimum should also be investigated in subsequent stages of modelling. The uncertainty of the period measurement is taken as the maximum deviation from the global minimum that is within 1σ of the minimum χ^2 value.

In the case of rotational acceleration, the period measured here is refined during YORP fitting to determine an initial period, P_0, for each YORP value that is tested. This is discussed in Section 3.1.4.

3.1.3 Pole and shape optimisation

The orientation of an asteroid's spin-axis is described by its pole, which is defined using its ecliptic longitude λ and ecliptic latitude β. The 'preferred' rotation of the Solar System is such that prograde rotation is defined as anti-clockwise rotation when viewing Earth's north pole. Prograde rotators and retrograde rotators thus have poles with positive and negative ecliptic latitudes respectively.

The pole is always measured at the positive end of the Z-axis in a body-centric coordinate system. For principal axis rotators - which most NEAs are - the Z-axis of a shape model should always be aligned with the principal axis of inertia, thus the Z-axis will be the rotation axis. The other principal axes are not normally aligned with the X- and Y- axes.

While pole coordinates can be set to a free parameter in `convexinv`, this introduces additional local minima and slows down the modelling process. Instead, `convexinv` is set to iterate over a grid of fixed poles. With the already provided input period, the code only has to significantly optimise the shape parameters for each pole in the grid. This grid will normally have an initial resolution of $5^\circ \times 5^\circ$, meaning that 2,485 optimised shape models will be generated during an initial 'pole scan'. At later stages, localised scans can be conducted at a higher grid resolution to refine initial pole solutions. The scan may also be repeated with lightcurves added or removed, or with a different input period.

The model that produces the lowest overall χ^2 fit is taken as the candidate solution describing the asteroid's shape and spin-state. The scan should converge towards the best-fit pole solution, so the pole scan results are plotted in the χ^2 plane for inspection, as shown in Figure 3.2. The candidate model will then be converted into a polyhedron comprising a triangular mesh, for interpretation by other procedures. The 3D model can then be displayed graphically for a visual inspection, checking for non-physical or otherwise unexpected features. Synthetic lightcurves can be produced using this model

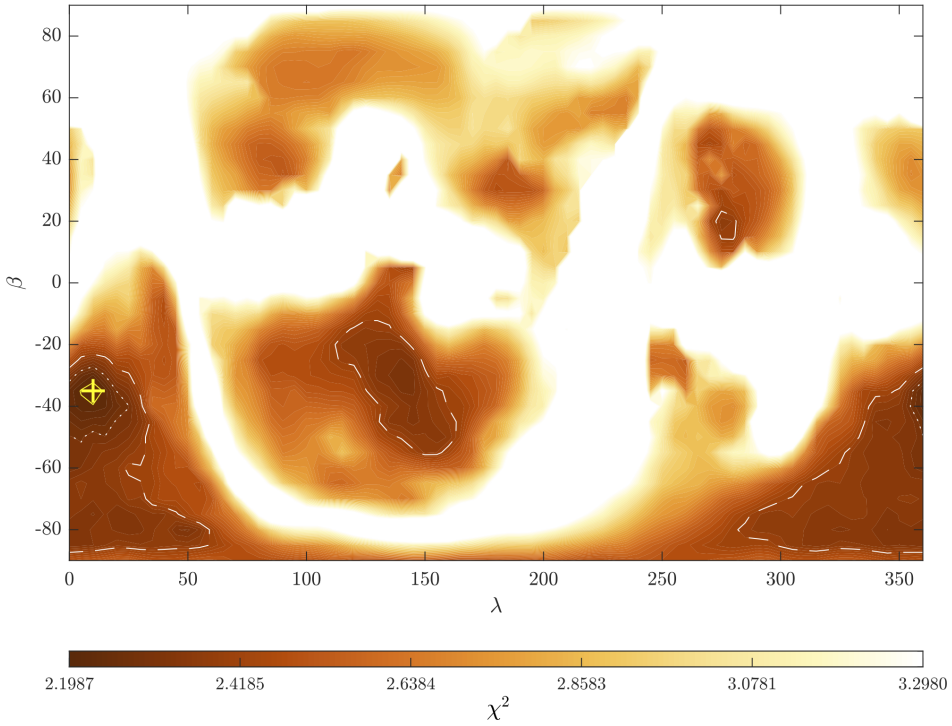

Figure 3.2: The results of a 5° × 5° `convexinv` pole scan of (159402) 1999 AP10, conducted as part of this work. For each pole in ecliptic coordinates λ and β, the χ^2 fit of the solution is plotted with darker colours for lower values, representing a better fit. The location of the global minimum is marked with a yellow cross, and solutions within 1%, 5%, and 10% of this best solution are enclosed by solid yellow, white dotted and white dashed lines respectively. Values more than 50% larger than the minimum value are shown in white. This pole scan shows clear convergence towards a southern solution, which is somewhat constrained in longitude. The convex shape model produced for this scan's best-fit pole is shown in Figure 3.3.

to check its ability to reproduce lightcurves; this is discussed in Section 3.3.1. Similar to lightcurve uncertainties, the maximum pole deviation within 1σ of the minimum χ^2 value is taken as the uncertainty of the pole measurement.

3.1.4 Fitting for YORP

The standard version of `convexinv` does not accommodate for changing rotation periods, meaning that YORP cannot be factored into the models it produces. As previously discussed, members of the YORP collaboration modified `convexinv` to factor in the spin acceleration component of YORP, $\vec{\tau_\omega}$. This means that shape and spin-state can

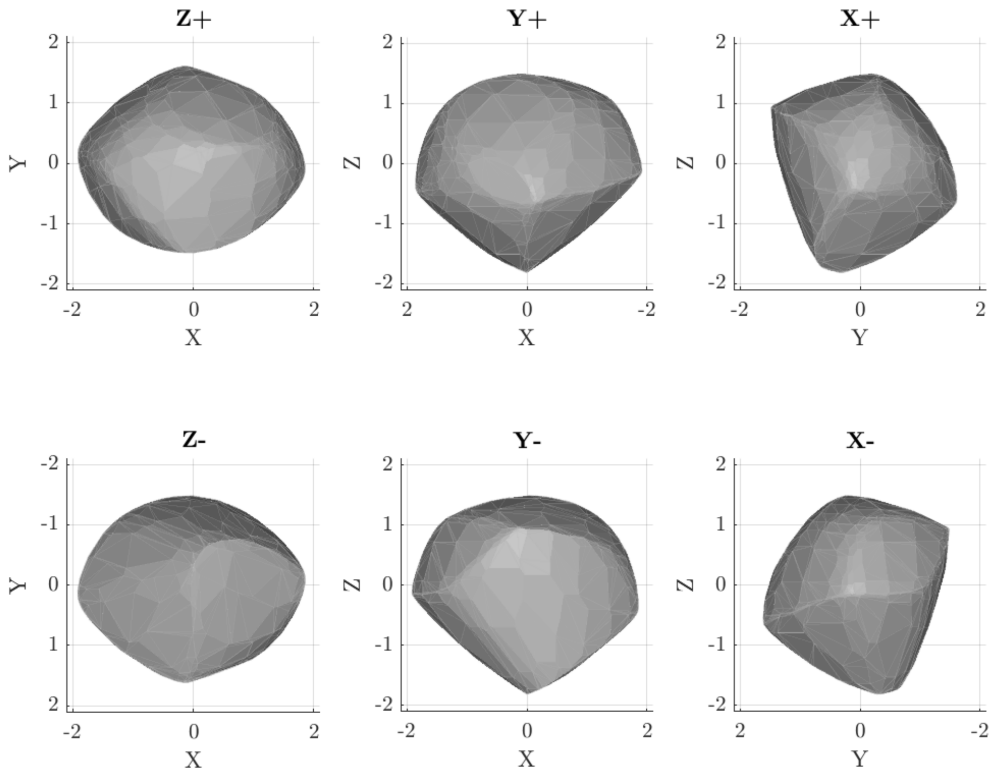

Figure 3.3: The convex shape of (159402) 1999 AP10, which was developed as part of this work (Sect. 6.2) and published in Jackson et al. (2022). This shape model was developed as part of the pole scan shown in Figure 3.2, finding the pole solution of $(\lambda, \beta) = (8°, -36°)$. The top row shows the model from the positive end of the Z, Y and X axes in the body-centric coordinate system, and the bottom row shows the same axes from the negative end. Principal axis rotation is assumed, with the Z-axis being aligned with the pole axis. The X axis is set such that it is in the plane-of-sky during the first lightcurve, and all units are dimensionless. This convex hull is consistent with a top-shaped or 'YORPoid' asteroid, which is in agreement with a visual inspection of radar imaging observations.

be modelled with the incorporation of specific YORP values. If the overall best-fitting model has a non-zero YORP acceleration applied, then that model's YORP value can be taken as a preliminary YORP detection for the asteroid.

The linear acceleration caused by YORP translates to a quadratic change in the asteroid's phase (as compared to a constant period model), $\varphi(t)$, measured in radians. This is described by:

$$\varphi(t) = \varphi(T_0) + \omega\,(t - T_0) + \frac{1}{2}\nu(t - T_0)^2 \tag{3.6}$$

where:

- t is the Julian date of the lightcurve being considered.
- $\varphi(T_0)$ is the initial rotation phase.
- T_0 is the Julian date when the X-axis is in the plane of sky, and the time from which the model's rotation is propagated. This is usually close to the first lightcurve input to `convexinv`.
- ω is the asteroid's rotation rate in radians per day.
- ν is rotational acceleration, measured in radians per day squared. As rotational acceleration is nominally caused by YORP, it can be said that $\nu \equiv \vec{\tau_\omega} \equiv \dot{\omega}$.

The YORP-modified version of `convexinv` is not able to optimise for YORP directly. Instead, it iterates over a fixed range of YORP values similar to the fixed grid of poles in Section 3.1.3. Each YORP plane constitutes a full pole scan, meaning that wide high-resolution scans with >100 YORP steps are computationally expensive and rarely justified.

The results of a YORP scan are presented in a 'YORPogram', an example of which is shown in Figure 3.4. If there is a 'YORP bowl', meaning a convergence towards a global minimum, high-resolution follow-up scans will be used to search for minima within this bowl. Each point on a YORPogram represents a unique model; these should be checked to ensure that the shapes and poles converge across YORP planes towards the best-fit solution. If there is significant shape or pole deviation between the overall best-fit YORP model and the best-fit constant-period model, then the YORP solution may be a false positive caused by `convexinv` forcing extreme changes to accommodate the lightcurve phase offsets.

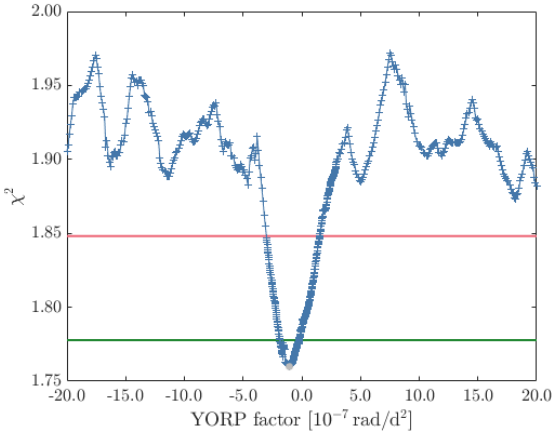

.

Figure 3.4: A YORPogram indicating the spin-down of (85275) 1994 LY, showing a global minimum at -11×10^{-8} rad/day^2, indicated by a grey dot. The green and red lines correspond to solutions within 1% and 5% of the best solution, respectively. This solution is not considered to be a robust indication of YORP spin-down, for reasons discussed in Section 6.3

YORP scans optimise for the period P and thus also the initial period P_0, which is the initial value at T_0 which is propagated according to YORP strength. For the initial YORP scan, the input period used by `convexinv` remains the same for all YORP planes, sometimes resulting in P becoming stuck in local minima. There should be a linear relationship between model YORP strengths and their optimised output periods P, which means that solutions with poorly optimised periods can be easily identified. The results of an initial YORP scan are used to measure this linear relationship, and then use this relationship to calculate a new P_0 for each iteration of YORP in subsequent scans. This brings each model's input period closer to what its optimised period is expected to be, correcting poorly optimised solutions.

Any YORP acceleration detected through a convex inversion YORP scan should generally be followed up with a phase-offset analysis, ideally using a non-convex model. Uncertainties are not always reported for these YORP results, but if required, they can be calculated with the same method used for period and pole uncertainties. This process is described in Section 3.3.2. Where only lightcurve data are available, `convexinv` YORP scans are especially useful in that they can provide a more accurate model with which to measure phase offsets. Where radar data are available, convex inversion remains worthwhile as it is a relatively fast process compared to the development of a radar model. If there is no sign of YORP acceleration from a `convexinv` YORP scan, it may not be worth investing resources into developing a radar model to search

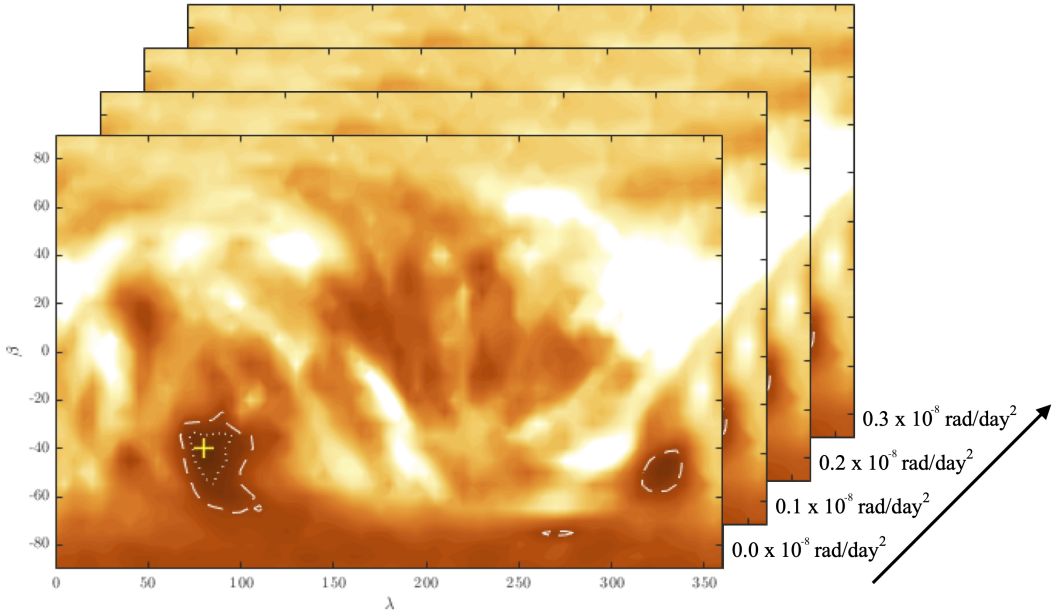

Figure 3.5: This visualisation of a YORP scan shows that each 'layer', or YORP plane, is a full pole scan akin to the one shown in Figure 3.2. The four planes shown here are part of a larger scan of (85275) 1994 LY that included hundreds of YORP planes. The best-fitting model from each YORP plane in this scan is represented in the YORPogram in Figure 3.4.

for YORP, as was the case for 1999 AP10 (Sec. 6.2). Additionally, radar models can benefit from constrained input parameters taken from prior convex hull models.

3.2 Modelling with radar data

Prior to the development of delay-Doppler imaging, radar observations were mostly focused on using cw spectra for ranging and the determination of radar cross-section, radius, scattering properties and SC/OC ratios (Pettengill and Jurgens, 1979; Ostro, 1988). The first use of radar for shape modelling used cw spectra to measure the polar silhouettes of an asteroid's convex hull (Ostro et al., 1988), requiring rotational coverage from multiple viewing geometries.

The development of delay-Doppler imaging techniques (Snyder, 1987a; Snyder, 1987b;

Ostro et al., 1990a; Hudson, 1994), which are discussed in Section 2.3.2.2, revealed information on the non-convex shapes of NEAs which could be used to develop three-dimensional shape models.

Similar to lightcurve data, modelling with radar data is an inverse problem. This can be resolved with sufficient observational coverage, although it is best to constrain as many parameters as possible prior to the development of a shape model, similar to the lightcurve inversion processes described in Section 3.1. The software used to develop radar models, `SHAPE` (Magri et al., 2007), is more complex than convex inversion and requires more input parameters, more CPU time and significant human supervision.

Fundamentally, `SHAPE` works on the same principle as `convexinv` by attempting to minimise the χ^2 fit of the model to observations. `SHAPE` is able to invert both radar and lightcurve data, using both types simultaneously to produce the best possible model. Using both types of data is computationally demanding, so lightcurves are usually added gradually after several rounds of fitting to radar data. Lightcurves are especially useful in breaking the degeneracy between diameter and spin-state seen in Doppler space, so it is beneficial to include some in the earliest stages of modelling.

A `convexinv` model consists of a file describing a body's shape, pole, and period, with scattering laws specified within the fitting procedures. `SHAPE` model files are more complicated, describing properties such as shape, pole, period, rotational acceleration, and scattering laws for both the optical and radar regimes. `SHAPE` also requires two additional input files describing fitting parameters and the observational data; these files, and the overall process of developing shape models with `SHAPE`, are described in the sections below.

3.2.1 Input files for SHAPE

The aforementioned input files for `SHAPE` are the parameter (par) file, the model (mod) file and the observations (obs) file. As with `convexinv` in Section 3.1, examples of

SHAPE input files are provided in Appendix B.

3.2.1.1 Parameter (par) file

The parameter file contains a set of instructions describing which action is to be performed by SHAPE , and the parameters used for said actions. The most important action is 'fit', which executes the modelling process with the stated parameters. The 'write' action is used to write the results from running 'fit', producing various figures such as plane-of-sky projections of the output model and synthetic delay-Doppler images. There are many other actions, such as one to perform delay corrections, all of which are detailed in the SHAPE documentation.

The par file also includes a series of penalty functions. These are used to suppress certain features on the model during fitting, with each penalty having an associated weight that is used to increase the χ^2 value for shapes that exhibit the penalised feature. The strength of these weights is arbitrary, and a given value will not have the same effect on different datasets or asteroid morphologies. These penalties are adjusted throughout the modelling process to prevent non-physical features being fitted, but care is taken to avoid penalising real features and deviations in the asteroid's shape. There are a number of penalties available, with the most important ones used in this work listed below:

- *nonsmooth* – Subdues topographical variation on the facet-scale, reducing excessive spikiness or 'hedgehogging', which can be a caused by overfitting of noisy data.
- *concavity* – Comparable to *nonsmooth*, this reduces the appearance of concavities that may appear in the form of deep wells.
- *nonpa_uni* – Suppresses non-principal axis rotation, which is detected when the third principal axis is larger than the first and second axes.

- *inertiadev_uni* – Reduces misalignment between the rotation axis and the body's Z-axis.

- *comdev* – Discourages any disparity between the body's centre of mass and the origin of the three axes of the body-centric coordinate system.

There are many parameters used by the various actions in the par file, some of which apply to several actions, and others only applying to one. Most of these are left to their default or recommended values, but some are data-dependent or are critical factors for their respective actions. Examples of this would be the resolution of the plane-of-sky view, or the step sizes that `SHAPE`'s fitting action uses when optimising spin, shape and size parameters.

3.2.1.2 Model (mod) file

`SHAPE` always requires an input model, meaning that a mod file must be provided before fitting can begin. The shape, spin and reflective properties of the asteroid are described by parameters in the file that can be set to fixed or free during the fitting process. `SHAPE`'s fitting procedure optimises free parameters and writes a new mod file as its output, which can be used in subsequent fitting runs with adjusted par and obs files.

The initial model is constructed manually, using previously measured values where possible. This work conducted full pole scans with `SHAPE` , meaning that an independent model was created for each pole solution in a $10^\circ \times 10^\circ$ grid. While the pole is often already constrained from previous lightcurve inversion, it is useful to independently measure the pole with radar data. The convex shape produced by `convexinv` can be used to inform the input model, although it is not always directly imported as it can hinder the fitting of non-convex features. Visual inspection of delay-Doppler images is also useful, as they are indicative of shape and can reveal information hidden by the convex shape, such as the lobes of contact binary. Radar data are also useful for

initial diameter estimates, which are more constrained than photometrically derived measurements.

Asteroid shape components can be expressed in four different formats, with various `SHAPE` actions available to convert mod files between them. These are:

- *Ellipsoid* – A tri-axial ellipsoid, with a smooth featureless surface and symmetry about each axis.
- *Ovoid* – Similar to an ellipsoid, but with a distortion to make the ends of each axis wider or narrower.
- *Harmonic* – A spherical harmonic expansion, which can produce highly irregular shapes.
- *Vertex* – A component comprising a pre-determined number of triangular facets.

A model can be expressed as multiple separated components, which is necessary for complex shapes such as contact binaries (e.g. Zegmott et al. (2021)). This work used single-component shape models for all modelling, defined in the ellipsoid and vertex formats. Ellipsoid models are the simplest to define, and hence the fastest to optimise. The parameters are the longest axis (2a), measured in kilometres, the elongation (a/b) and flattening (b/c). Internally, `SHAPE` realises ellipsoid shapes as vertex models that imitate a geometric tri-axial ellipsoid.

The vertex format gives the highest degree of adjustability, with each vertex being individually adjustable for high-resolution fitting of surface features. This also means that vertex models are the most computationally intensive to fit, as there are hundreds - sometimes thousands - of vertices to optimise. The number of vertices is set in the mod file, usually starting with a low number that is increased between modelling runs as the shape becomes more constrained. It is important to monitor the mean facet edge length, as there is no benefit to exceeding the spatial resolution of delay-Doppler imaging. A vertex shape is described in the mod file by the number of vertices, followed

by a set of scaling factors that multiply the base axial dimensions. After these lines, each vertex is defined with two lines per vertex, working from the north pole to the south pole. The second line of each vertex description gives its base displacement in the three axes of the body-centric coordinate system. The first line describes the vertex deviation (in km) from the base vertex displacement, which is a coefficient that modifies the following parameters that describe the direction cosines of the deviation. After each vertex is defined, the number of facets is given, followed by each facet being defined by vertex numbers of each of the facet's three vertices. The vertex deviation is the only vertex parameter that is adjusted during fitting, with the direction cosines and base displacement remaining fixed. The scaling factors preceding the vertex descriptions are also adjusted during fitting.

The photometric and radar scattering properties are also defined in the mod file. For radar scattering, there are a variety of laws available. The simplest is the Cosine law, described by `SHAPE`'s documentation, Mitchell et al. (1996), and Ostro (2007), which is given by:

$$\frac{d\sigma}{dA} = R(C+1)cos^{2C}\theta \tag{3.7}$$

where σ is the radar cross-section, A is the target's surface area, R is the Fresnel reflectivity (at normal incidence), and θ is the scattering angle. C is a parameter derived from the rms slope, with larger angles corresponding to increased specular scattering.

The Hagfors quasi-specular scattering law, also described by `SHAPE` documentation and Ostro (2007), introduces a cut-off angle, above which there is zero radar scattering. For incidence angle φ, the Hogfors law takes the form:

$$\frac{d\sigma}{dA} = \frac{CR}{2}(cos^4\varphi + Csin^2\varphi)^{-3/2} \tag{3.8}$$

`SHAPE` can use different scattering laws for different datasets, which is especially

useful when including both delay-Doppler and cw data. In addition to the quasi-specular Hagfors law, there are also Gaussian and quasi-specular Cosine laws available, and various other options that combine pairs of scattering laws.

When including lightcurve data, optical scattering laws must also be included in the mod file. There are five options: Geometric, Lambertian, Lommel-Seeliger, Hapke and Kaassalainen. As with radar scattering laws, each input dataset can utilise a different law, which can be useful when mixing photometric filters. If a facet is illuminated - as determined by the viewing geometry given by the obs file - then the chosen scattering law will determine the flux contribution from each facet on the model (recalling that `SHAPE` uses facet models for its internal representations of non-facet-defined models). The first three laws simply require an albedo parameter, while the others incorporate other parameters such as incidence angle and opposition surge amplitude.

This work primarily makes use of the Kaasalainen scattering law, for which `SHAPE` uses a modified version of the version published in Kaasalainen et al. (2001), which is itself a combination of the Lambertian and Lommel-Seeliger scattering laws.

The Lambertian scattering law calculates each facet's flux contribution using:

$$F = sf(R) \cdot I_0 cos(\varphi) \tag{3.9}$$

Where $sf(R)$ is a scaling factor that incorporates the albedo R, and I_0 is an intensity scaling factor that is dependent on viewing geometry. The Lommel-Seeliger scattering law is given by:

$$F = sf(R) \cdot I_0 \frac{cos(\varphi)}{cos(\varphi) + cos(\theta)} \tag{3.10}$$

Because this work utilises relative lightcurves, the albedo parameter R is set to a fixed value that is not optimised during fitting.

Finally, the mod file gives the spin parameters, including T_0, the asteroid's orientation at T_0, and spin rates for each axis, with the first two axes having a fixed spin rate of zero for principal axis rotation. YORP acceleration can be included in the mod file, however it is generally not feasible to perform YORP scans (similar to Sec. 3.1.4) with `SHAPE` due to its computational expense, so YORP is typically set to zero.

3.2.1.3 Observation (obs) file

The obs file contains a list of every input dataset, which can be optical lightcurves, cw spectra or delay-Doppler imaging. When data are added, such as lightcurves during the later stages of modelling, new entries are made in the obs file describing the data.

Each entry contains ephemeris data, lists of data files, and weights to be applied when fitting to the data. Normally all weights are set to 1, but poor quality data could be given lower values. Additional information is provided in each entry that is specific to its data type, such as transmitter frequency and delay resolution for delay-Doppler observations.

3.2.2 Developing a shape model

At the time of writing, only a few dozen asteroids have been fully modelled with `SHAPE`. While there is a general process (Magri et al., 2007; Magri et al., 2011) the various steps will vary depending on how much is already known about the asteroid, the asteroid's physical properties, and the available data.

Firstly, the obs file must be prepared to describe the observational data. When used with the 'fit' action, every dataset described within the obs file will be used to fit the model. This means that the obs file will change as more data are gradually introduced between rounds of fitting. To test models, the 'write' action is used to generate synthetic observational data and plane-of-sky images that correspond to real observations. Ideally, a model should be tested against all available data, not just the

data that were used to fit the model. For this reason, it is good practice to have two obs files: one for fitting, and one for evaluation. The former changes between fitting runs, while the latter always includes all available data.

As previously discussed, an initial model should be provided. This could be a previously published convex or non-convex shape model, or a manually constructed ellipsoid shape, with the latter usually still taking spin-state information from a `convexinv` analysis. The 'write' action should be used with this model to produce synthetic delay-Doppler images, as they should be a reasonable approximation of the real observations. The model may need to be modified several times before it is satisfactory, and only then can fitting begin. When fitting, `SHAPE` cycles through each free parameter in the mod file, using a constained-least-squares method to optimise them one-by-one until a global minimum is found. The overall fit of a model is described as the objective function, which is the sum of χ^2 and penalty functions. The objective function is given by:

$$\chi^2(\mathcal{M}) = \sum_j \sum_i w_{j,i}(y_{j,i}(\mathcal{M}) - x_{j,i})^2 + \sum_i \Big| p_i(\mathcal{M}) \Big| \tag{3.11}$$

where:

- $\mathcal{M}$ is the asteroid model described by shape, size, spin, and reflection parameters.
- j is an index that iterates through different types of observation (delay-Doppler, cw spectra or lightcurves).
- i is an index that iterates through observations of type j.
- $w_{j,i}$ is a weighting factor for each observation.
- $y_{j,i}$ are synthetic observations created using the model.
- $x_{j,i}$ are real observations.
- p_i are penalty functions.

`SHAPE` records χ^2 for the initial parameter value, then adjusts it by a user-defined step size and recalculates χ^2. `SHAPE` then determines the direction of the minimum and continues in that direction using increasing step sizes until χ^2 begins to increase. Having bracketed a minimum, `SHAPE` will then pinpoint the minimum until it is within a user-specified tolerance of the minimum possible objective function. The tolerance is defined as a fractional plus absolute tolerance value. `SHAPE` will then shift by another step size in search of nearby minima, although there is a danger it can miss multiple minima within one bracket, hence step sizes are very important. `SHAPE` will continue to optimise a parameter until the number of iterations reaches a fixed limit, or the difference between two iterations is smaller than a user-defined prevision. It will then move on to the next free parameter and repeat the process until all parameters have been optimised.

For the initial round of fitting, each additional dataset included in the obs file will have a significant impact on computation time, so data selection is important. A mix of all three types (radar imaging, cw spectra and lightcurves) is generally best, with the aim to cover a full range of viewing geometries and rotational phase using as few datasets as possible. As fitting is relatively coarse at this stage, it is sensible to use low-resolution delay-Doppler imaging.

To reduce processing time, masks can be applied to the radar data. For cw spectra, frequency bins containing only background can be ignored. For delay-Doppler imaging, a mask can be constructed in both delay and Doppler space to ignore background noise. Care must be taken when doing this, as delay corrections during fitting could move the asteroid into a masked region. Mask sizes can be refined later during the modelling process, so it is wise to begin with a less 'tight' mask.

It is best to use an ellipsoid shape model for the early stages of modelling, as there are only three shape parameters to optimise. More complex shapes, such as a hull from `convexinv`, will have hundreds, if not thousands of shape parameters. Similar to the steps used for `convexinv`, it is best to optimise the spin-state before focusing on shape

parameters. A search is conducted over a grid of fixed poles (see Sec. 3.1.3), typically using a lower initial search resolution of $10^\circ \times 10^\circ$ due to the increased computational requirements.

The first `SHAPE` fitting run optimises the sidereal rotation period and initial rotation phase for each pole. Unlike `convexinv`, `SHAPE` does not require rotation phase to be zero at T_0. Instead, the zero rotation phase is defined as where the body's X-axis crosses the plane-of-sky. A parameter in the mod file describes additional rotation phase at the user-defined T_0, and this is set to a free parameter. If an ellipsoid shape is used, then the shape parameters can also be adjusted during the initial fitting run. Otherwise, the shape is fixed while the spin parameters are optimised.

Once the spin parameters have been sufficiently constrained, the focus shifts to optimising the asteroid's shape. At this stage, the pole search is normally constrained to a smaller region with a higher grid resolution, which will eventually be constrained to a single pole solution during later stages of modelling. To optimise shape, the output models from the pole scan are converted to a low-resolution vertex or spherical harmonic format. More data may be included at this stage. Another fitting run is then conducted, with both shape and spin parameters being optimised for the fixed pole(s). After this run, the user will assess the results with the 'write' and 'moments' actions.

The next steps are determined by the results of each fitting run. If non-physical features are emerging, then penalty strengths may need to be increased. Conversely, if natural features are suppressed, the penalties may need to be reduced. The *nonsmooth* penalty, for example, will produce completely smooth spherical shapes if it is set too high. Otherwise, a variety of fitting parameters can be adjusted, more data can be included, and the spatial resolution of the model can be slightly increased. One should avoid adjusting too many things between fitting runs, however, as it will be difficult to identify which changes are responsible for improvements or failures in the next run. If the shape model(s) from a run are an improvement over the input model(s), then its output model(s) will become the input model(s) for the next fitting run. Otherwise,

the previous run's input model(s) will be re-used.

There are several cycles of this fitting process, gradually refining the shape and spin-state of the asteroid. Eventually, modelling will reach a point of diminishing returns. The final stages of modelling will use the full observational dataset, and the number of vertices will be increased to create a high-resolution shape where the mean facet edge length is comparable to the spatial resolution of delay-Doppler imaging. It is at this stage that small-scale features such as craters or boulders can be fine-tuned until no further improvement is possible, after which the model is 'locked in'. Uncertainties on the model's period and pole can then be measured, using the previously described method used for convex hull models. There is no established procedure for measuring uncertainties for `SHAPE` model dimensions; some authors have used a nominal 10-20% uncertainty on each axis length, while others use a range of statistical or systematic methods to provide an estimate. For consistency, this work compares the final model to the latest `SHAPE` pole scan results to apply the 1σ deviation method that is used for all other measurements. This is the same method used in Rożek et al. (2019a), Zegmott et al. (2021), and Rożek et al. (2022).

It is possible to then perform a YORP scan using this single pole solution (Zegmott, 2021), using the best-fitting constant-period model as an input which is re-fit to a range of YORP values. It should be noted that because each radar imaging set provides a 'snapshot' of the asteroid's shape, there is less scope for adjusting a model's shape in response YORP. Instead, `SHAPE` will primarily adjust the spin parameters of a model to optimise for each fixed YORP value. In most cases, it is easier to fit spin parameters during a later phase offset analysis instead of having to re-model the asteroid in `SHAPE`. As such, YORP scans with `SHAPE` are only considered if the user is not satisfied with the results of a phase offset analysis using a detailed non-convex shape model.

3.3 Searching for YORP

As previously discussed, there are three established techniques for detecting YORP. Firstly, the change in rotation period can be measured directly (Fig. 1.16). This technique is the simplest, however it is both the least sensitive and the most observationally demanding method. It is thus generally limited to small, fast-rotating asteroids with frequent close approaches to Earth.

The second method, described in Secs. 3.1.4 & 3.2.2, incorporates spin acceleration into the modelling process to identify which YORP strength produces the best fit. This is mostly done using lightcurve observations, as they are the most abundant and the least computationally demanding. The limitations of this technique mean that spin acceleration is difficult to constrain, often resulting in YORP detections that are not considered robust.

The third option, which is detailed in this section, is the phase offset analysis technique first described in Section 1.3.2.3. This method, which uses a shape model to generate synthetic lightcurves to compare against real observations, is the primary focus of the YORP campaign. There are several thousand convex hull models published in the Database of Asteroid Models from Inversion Techniques (DAMIT) (Ďurech et al., 2010), as well as several dozen published radar shape models and a handful of spacecraft-derived models. Phase offset analysis generally produces the most constrained YORP detections, and does not explicitly require the development of a new model, hence it is the favoured technique.

To perform a phase offset analysis, synthetic lightcurves must be produced using the provided model. This process is described in the following section.

3.3.1 *Simulating asteroid lightcurves*

This work utilised a series of `MATLAB` procedures used to to construct synthetic lightcurves of asteroids, to both assess the model fits and perform phase offset analyses. These procedures were developed by group members at Kent, with Dr. Agata Rożek having recently performed a significant expansion and overhaul of the code and documentation.

These procedures require that the asteroid's shape is described using triangular facets. The provided models are usually described by one of two forms. The first is a mod file from `SHAPE` in the vertex format (Sec. 3.2.1.2). The second is an `obj` file from `convexinv`. The `obj` format is a popular standard for 3D model files, although it only contains shape information so spin and surface properties must be provided separately.

An `obj` file contains an array with four columns. The `MATLAB` procedures are able to interpret these model files, then convert and store the shape internally across two arrays. The first column in an `obj` file contains either 'v' or 'f' to denote whether the row describes a vertex or a facet respectively. For vertices, the next three columns contain the Cartesian coordinates of each vertex V_i. For rows of facets, the three columns list the indices of the facet's three constituent vertices.

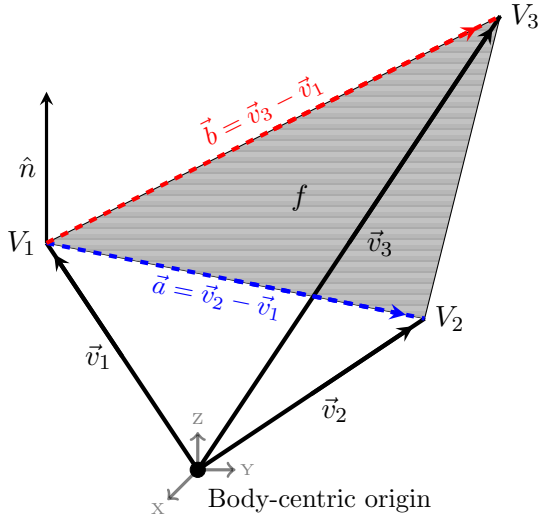

Figure 3.6: In this example, the facet f (shaded) is defined using four rows of four columns within the model file. The vertices V_1, V_2 and V_3 are each described in rows that begin with 'v' followed by the Cartesian coordinates of the vertex. The facet is constructed using a row beginning with 'f' followed by the index numbers of the rows describing V_1, V_2 and V_3. Also shown are the vectors between the centre of the body and each vertex $\vec{v}_i$, the facet normal vector $\hat{n}$, and the vectors $\vec{a}$ and $\vec{b}$ from V_1 to V_2 and V_3 respectively. This figure is based on a representation shown in Rożek (2017).

A visualisation of an individual facet described by the file is shown in Figure 3.6. Using this example, the area of the facet is given by:

$$A_f = \frac{1}{2}|\vec{a} \times \vec{b}| \tag{3.12}$$

and the facet normal, whose origin is V_1, is calculated using:

$$\hat{n} = \frac{\vec{a} \times \vec{b}}{2A_f} \tag{3.13}$$

where the vectors $\vec{a}$ and $\vec{b}$ are the vectors from V_1 to V_2, and V_1 to V_3 respectively, hence $\vec{a} = \vec{v}_2 - \vec{v}_1$ and $\vec{b} = \vec{v}_3 - \vec{v}_1$. The vertices of each facet are ordered such that the normal always faces the outside of the model.

When simulating a lightcurve, a facet can only contribute to the asteroid's brightness if it is illuminated. This depends on the asteroid's rotational phase and the relative positions of the observer, Sun, and the asteroid, which can be obtained from ephemerides. These are included with a file describing the observational data. The vectors from the asteroid to Earth and the Sun are averaged and normalised for each lightcurve, resulting in the unit vectors $\hat{E}_\odot$ and $\hat{E}_\oplus$. It should be noted that this means the observing geometry is assumed to be constant throughout the duration of a lightcurve. While usually negligible, lightcurves taken during very close approaches may have significant variation in viewing geometry that necessitates special handling.

As the unit vectors $\hat{E}_\odot$ and $\hat{E}_\oplus$ are in the ecliptic reference frame, they must be transformed into the body-centric reference frame using rotation matrices:

$$\hat{E}'_\oslash = \begin{pmatrix} cos\phi_0 & sin\phi_0 & 0 \\ -sin\phi_0 & cos\phi_0 & 0 \\ 0 & 0 & 1 \end{pmatrix} \begin{pmatrix} cos\tilde{\beta} & 0 & -sin\tilde{\beta} \\ 0 & 1 & 0 \\ sin\tilde{\beta} & 0 & cos\tilde{\beta} \end{pmatrix} \begin{pmatrix} cos\lambda & sin\lambda & 0 \\ -sin\lambda & cos\lambda & 0 \\ 0 & 0 & 1 \end{pmatrix} \hat{E}_\oslash \tag{3.14}$$

where:

- $\hat{E}'_{\oslash}$ can represent $\hat{E}'_{\odot}$ or $\hat{E}'_{\oplus}$.
- $\hat{E}_{\oslash}$ can represent $\hat{E}_{\odot}$ or $\hat{E}_{\oplus}$.
- ϕ_0 is the rotation phase at the model's t_0, in degrees.
- $\tilde{\beta}$ is $90° - \beta$, where β is the ecliptic latitude of the model's pole.
- λ is the ecliptic latitude of the model's pole.

The rotation phase of the asteroid ϕ is calculated using Equation 1.3, and then the Sun and Earth unit vectors are rotated accordingly using:

$$\hat{E}''_{\oslash} = \begin{pmatrix} cos\phi & sin\phi & 0 \\ -sin\phi & cos\phi & 0 \\ 0 & 0 & 1 \end{pmatrix} \hat{E}'_{\oslash} \tag{3.15}$$

For a facet to contribute to lightcurve brightness, it must be illuminated by the Sun and be visible from Earth. If this is the case, then both $\mu_{\odot}$ and $\mu_{\oplus}$ must be greater than zero, where $\mu_{\oslash} = \hat{E}_{\oslash} \cdot \hat{n}$. For a facet with an area dA, its brightness contribution dL is thus:

$$dL = S(\mu_{\odot}, \mu_{\oplus}) \cdot \bar{\omega} \cdot dA \tag{3.16}$$

where the scattering law S and albedo $\bar{\omega}$ are as first described in Equation 3.3. Lightcurve construction procedures can use the Lambertian, Lommel-Seeliger or Kaasalainen scattering laws which were previously discussed in Section 3.2.1.2.

The lightcurve can then be generated, calculating the sum of facet brightness contributions for each step of the asteroid's rotation between the specified start and stop times. The brightness is converted to the magnitude scale and shifted to force a mean

value of zero, ready for comparison with real relative lightcurves. For non-convex shapes, however, additional steps are required.

3.3.1.1 Ray tracing for non-convex shapes

Convex shapes are, by nature, unable to cast shadows across their own surfaces. Non-convex shape models, such as those produced by `SHAPE`, are more reliable representations of asteroids because they can be used to simulate the effects of self-shadowing. If an element on an asteroid's surface has its path to the Sun or Earth obstructed by another surface element - such as a boulder or crater rim - then it cannot reflect sunlight towards the observer and contribute to the asteroid's overall brightness. The fractional plane-of-sky surface area that is in shadow will increase for observations at high phase angles and equatorial sub-observer latitudes, significantly affecting the shape and amplitude of rotational lightcurves. It is thus necessary to account for self-shadowing when producing synthetic lightcurves of non-convex shapes.

In this case, self-shadowing is calculated in `MATLAB` using a ray tracing algorithm (Rożek, 2017). Shape models can have thousands of facets, and each facet must be tested against every other facet to determine if shadowing can occur. For a facet i and its potential blocker j, the facet centre coordinates $V_{C,i}$ and $V_{C,j}$ are determined using the vectors pointing to the facet vertices, such that the vector pointing toward a facet's centre is given by $\vec{v}_C = \frac{1}{3}(\vec{v}_1 + \vec{v}_3 + \vec{v}_3)$. For the centre of facet j to block the centre of facet i, two conditions should be satisfied: $V_{C,j}$ must be above the local horizon of $V_{C,i}$, and $V_{C,i}$ must be below the local horizon of $V_{C,j}$. If these conditions are satisfied, the facet j is listed as a potential blocker for i.

To check these conditions, the relative position of facet i and facet j is calculated as a vector:

$$\vec{p}_{i,j} = \vec{v}_{C,i} - \vec{v}_{1,j} \tag{3.17}$$

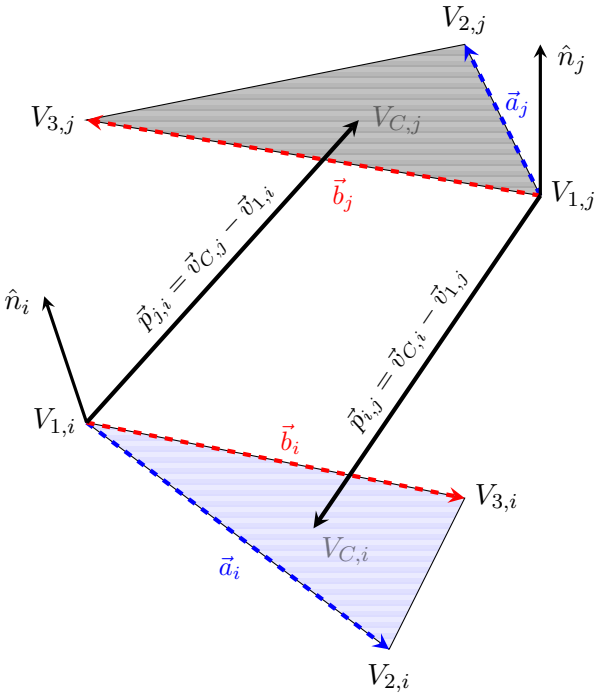

Figure 3.7: A diagram showing relevant quantities for the determination of self-shadowing. A facet i (shaded in blue) and its potential blocker j (shaded in grey) are shown. Each facet has the vertices V_1, V_2 and V_3, with a facet centre at the coordinates V_C. From the first vertex of both facets, a surface normal $\hat{n}$ is shown as well as the vector $\vec{p}$ to the centre of the opposing facet. For each facet, the vector $\vec{v_C}$, not shown, points to V_C from the centre of the body. The vectors $\vec{a}$ and $\vec{b}$ describe the edges from the first vertex to the second and third respectively. This figure is based on a representation shown in Rożek (2017).

where $\vec{v}_{C,i}$ points from the body's origin to the centre of the facet i ($V_{C,i}$), hence $\vec{v}_{C,i} = \vec{v}_{1,i} + \vec{v}_{2,i} + \vec{v}_{3,i}$ where $\vec{v}_{n,i}$ points towards the nth vertex of facet i from the origin. To determine if j is above the local horizon of i, $\vec{p}_{i,j}$ is projected onto the surface normal ($\hat{n}_i$) of the facet i. Taking the dot product of these results in a scalar, $D_{i,j}$, which describes the distance between $V_{C,j}$ and the plane containing i along $\hat{n}_i$. If $D_{i,j} = \hat{n}_i \cdot \vec{p}_{i,j} > 0$, then $V_{C,j}$ is above the local horizon of $V_{C,i}$. Similarly, if $D_{j,i} = \hat{n}_j \cdot \vec{p}_{j,i} < 0$, then $V_{C,i}$ is below the local horizon of $V_{C,j}$. With both these conditions being met, facet j is considered a potential shadow caster for facet i.

For a given viewing geometry and rotation phase, self-shadowing is only relevant for facets that would otherwise be illuminated. For a facet i, potential shadow casters are only considered if both $\mu_{\odot,i}$ and $\mu_{\oplus,i}$ are positive. If this is the case, each shadow caster j must also be illuminated in order to potentially cast a shadow, hence $\mu_{\odot,j}$ and $\mu_{\oplus,j}$ must also be positive. If these conditions are met for i and any number of potential shadow casters j, then rays are traced from the centre of each facet j ($V_{C,j}$) in the direction of $\hat{E}''_{\oslash}$ to determine if there is a direct line of sight between them.

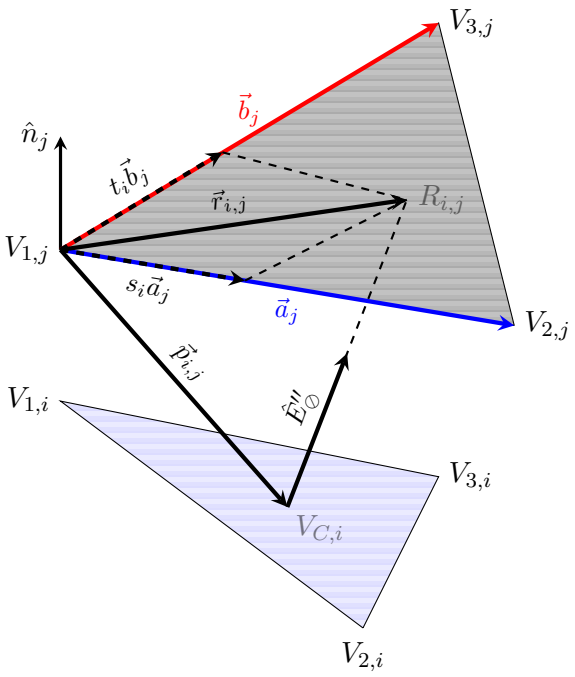

Figure 3.8: This illustration shows how the ray tracing algorithm determines whether facet j casts a shadow on the facet i. A ray is traced from the centre of i ($V_{C,i}$) towards j along the path of $\hat{E}''_{\oslash}$, which will intercept the plane of j. If the intercept point $R_{i,j}$ falls within the facet j, then j is a potential shadow caster for i. The relevant vectors described in Equations 3.18, 3.19 and 3.20 are shown. This figure is based on a representation shown in Rożek (2017).

The ray will intercept the plane of i at a point $R_{i,j}$, whose position is described with a vector $\vec{r}_{i,j}$ from the first facet of i ($V_{1,i}$) towards $R_{i,j}$. The position of this interception point is given by:

$$\vec{r}_{i,j} = \vec{p}_{i,j} - \frac{\hat{n}_j \cdot \vec{p}_{i,j}}{\hat{n}_j \cdot \hat{E}''_{\oslash}} \hat{E}''_{\oslash} \tag{3.18}$$

Recalling that $D_{j,i} = \hat{n}_j \cdot \vec{p}_{j,i}$ and $\mu_{\oslash} = \hat{E}_{\oslash} \cdot \hat{n}$ have already been computed, they can be substituted in to simplify the calculation.

The vector $\vec{r}_{i,j}$ is given by $\vec{r}_{i,j} = s_{i,j}\vec{a}_j + t_{i,j}\vec{b}_j$, where $s_{i,j}$ and $t_{i,j}$ are non-orthogonal projections of the vector $\vec{r}_{i,j}$ onto $\vec{a}_j$ and $\vec{b}_j$ respectively. As shown in Figures 3.7 and 3.8, $\vec{a}_j$ and $\vec{b}_j$ define the edges of j from the first vertex to the second and third vertices respectively.

If both $s_{i,j} > 0$ and $t_{i,j} > 0$, and $s_{i,j} + t_{i,j} < 1$, then the intersection point $R_{i,j}$ lies on facet j, obstructing the view from i to Earth or the Sun and thus casting a shadow. To determine the values of $s_{i,j}$ and $t_{i,j}$, the dot products with $\vec{r}_{i,j}$ must be calculated:

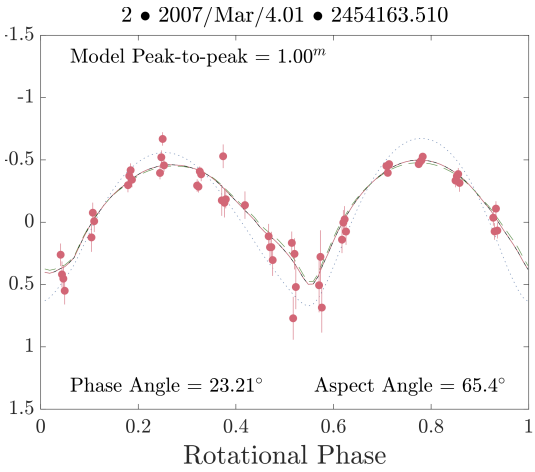

(a) Convex model (no shadowing possible)

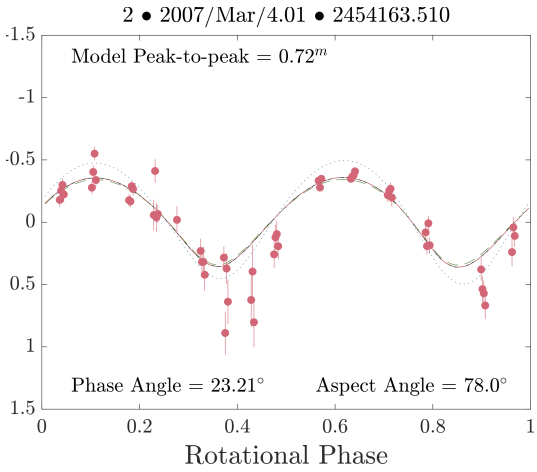

(b) Non-convex model (without shadowing)

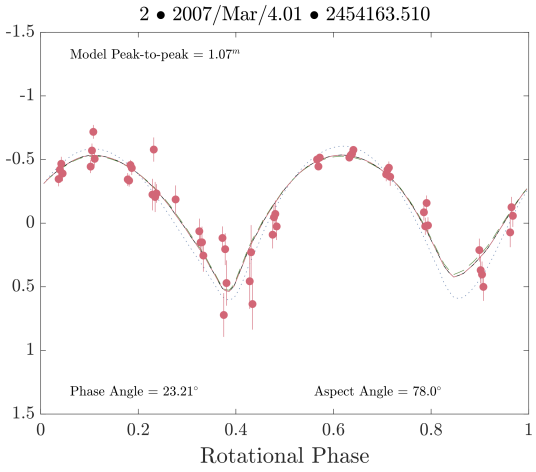

(c) Non-convex model (with shadowing)

Figure 3.9: A comparison of an observed and synthetic lightcurve for the asteroid (85990) 1999 JV6 (Rożek et al., 2019a), using (a) a convex hull model, (b) a non-convex radar model with no self-shadowing calculations, and (c) the same non-convex model with self-shadowing calculations applied. The real observations are plotted with red points. Within each panel, four synthetic lightcurves were plotted using different scattering laws, which are shown as solid black, dashed green, dotted blue, and solid red lines. These correspond to Hapke, Lommel-Seeliger, Lambertian and combined Lambertian & Lommel-Seeliger scattering laws respectively. The convex hull model has a slightly different pole, period, and T_0 than the non-convex model, meaning that the asteroid is simulated at a different rotation phase and viewing geometry. Note that the non-convex model with shadowing is the best fit, and also has the least variation between scattering laws. As 1999 JV6 is a bilobate asteroid, shadowing is essential for reproducing the lightcurve amplitude as one lobe casts shadows upon the other. The convex model produces a reasonable fit, but shows the greatest sensitivity to scattering laws. This shows that convex hull models can accurately reproduce lightcurves, and that while non-convex models are superior, the effects of self-shadowing can be critical.

$$\vec{r}_{i,j} \cdot \vec{a}_i = s_{i,j}(\vec{a}_i \cdot \vec{a}_i) + t_{i,j}(\vec{b}_i \cdot \vec{a}_i) \tag{3.19}$$

$$\vec{r}_{i,j} \cdot \vec{b}_i = s_{i,j}(\vec{a}_i \cdot \vec{b}_i) + t_{i,j}(\vec{b}_i \cdot \vec{b}_i) \tag{3.20}$$

Then taking these simultaneous equations and solving for $s_{i,j}$ and $t_{i,j}$ gives:

$$s_{i,j} = \frac{(\vec{r}_{i,j} \cdot \vec{b}_j)(\vec{a}_j \cdot \vec{b}_j) - (\vec{r}_{i,j} \cdot \vec{a}_j)(\vec{b}_j \cdot \vec{b}_j)}{(\vec{a}_j \cdot \vec{b}_j)^2 - (\vec{a}_j \cdot \vec{a}_j)(\vec{b}_j \cdot \vec{b}_j)} \tag{3.21}$$

$$t_{i,j} = \frac{(\vec{r}_{i,j} \cdot \vec{a}_j)(\vec{a}_j \cdot \vec{b}_j) - (\vec{r}_{i,j} \cdot \vec{b}_j)(\vec{a}_j \cdot \vec{a}_j)}{(\vec{a}_j \cdot \vec{b}_j)^2 - (\vec{a}_j \cdot \vec{a}_j)(\vec{b}_j \cdot \vec{b}_j)} \tag{3.22}$$

Many terms included in these calculations do not depend on viewing geometry. To minimise computation time for the ray tracing algorithm, these values are recorded and read in as necessary. For each step of the asteroid's rotation, every facet that is shadowed has $\mu_\odot$ or $\mu_\oplus$ set to zero in Equation 3.16 and thus does not contribute to the total simulated brightness of the asteroid. The process for constructing a lightcurve is otherwise the same as it is for a non-convex model, only with shadowed facets effectively being subtracted from the cumulative flux. As this method does not account for partially shadowed facets, it is most effective with high numbers of facets to increase the 'resolution' of self-shadowing calculations, although it remains effective for relatively coarse shape models.

3.3.2 Measuring rotational acceleration via phase offset anaylsis

As previously discussed in Section 1.3.2.3, rotational acceleration can be measured by comparing synthetic lightcurves with real observations. If an asteroid is experiencing a constant rate of acceleration, then synthetic lightcurves produced by a constant-period model will fall out of phase with the real observations, with the offset increasing

quadratically over time.

To measure these phase offsets, each synthetic lightcurve is shifted in phase in steps up to ±180°, with the χ^2 fit of the synthetic lightcurve to the real data being recorded for each tested offset. The phase offset that produces the lowest χ^2 is taken as the phase offset measurement for that lightcurve. After the phase offset for all lightcurves, a curve is fitted to a plot of phase offset against time. This curve comprises two linear components and one quadratic component:

$$\Delta\phi(t) = \Delta\phi_0 + \Delta\omega(t - t_0) + \frac{1}{2}\nu(t - t_0)^2 \tag{3.23}$$

Where the $\Delta\phi(t)$ is the phase offset at time t, $\Delta\omega$ is the period uncertainty, and ν is the rotational acceleration (i.e. YORP strength). Without YORP acceleration, the $\frac{1}{2}\nu(t - t_0)^2$ term would be zero and there should be no change in phase offset against time. There is, however, always a small linear trend in the measured progression of phase offsets, which is caused by non-zero values for initial phase $\Delta\phi_0$ and period error $\Delta\omega$.

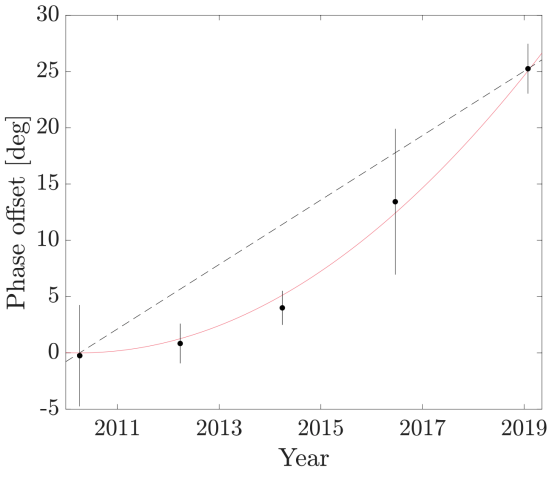

Figure 3.10: The results of a phase offset analysis of (68346) 2001 KZ66. The black points correspond to phase offset measurements, which are averaged by year. The solid red line corresponds to a YORP fit of $\nu = (8.43 \pm 0.69) \times 10^{-8}$ rad day^{-2}. The dashed black line, connecting the first and last measurement, highlights that the phase offsets deviate from a linear trend. This figure was reproduced from Zegmott et al. (2021).

.

After an initial fit, the $\frac{1}{2}\nu(t - t_0)^2$ term is subtracted. The asteroid's period is then adjusted and phase offsets are recalculated, iterating until the linear component, and thus $\Delta\omega$, is minimised. This small period correction ensures that period used to

propagate the model forward does not contribute to the phase offsets that are being measured. Similarly, $\Delta\phi$ is minimised by adjusting t_0 to ensure that the asteroid is correctly phased before it is propagated.

With $\Delta\phi_0$ and $\Delta\omega$ now negligible, the phase offsets can be recalculated to produce a better fit where $\Delta\phi(t) \simeq \frac{1}{2}\nu(t-t_0)^2$. Solving for ν provides a measurement for YORP. Where there is a high rate of YORP acceleration, or a long baseline, it is possible for an asteroid to be offset by one full rotation and come back into phase with its constant-period model. Similarly, lightcurves with double peaks can appear to have zero phase offset at 180°, or vice versa. If this is obviously occurring when there is otherwise a clear quadratic trend, individual measurements can be manually shifted by multiples of 180° or 360°. Care is taken to avoid forcing a fit when doing this, especially when there are relatively few measurements.

The uncertainty of the YORP measurement is estimated using the confidence intervals reported by the MATLAB curve fitting tools. The average of the distances from the fitted value to the upper and lower confidence interval bounds is taken as the uncertainty, and propagated into a corresponding rad day^{-2} uncertainty.

It can also be beneficial to average multiple phase offset measurements to reduce uncertainty. When doing this, bins typically range from a few days to an entire year. A minimum of three 'epochs' is required for a YORP fit, although it is beneficial to have more observations. It is especially useful to have multiple observations towards the end of the baseline, as this is where the quadratic is at its steepest where additional data can significantly constrain the YORP measurement.

This method has been used successfully to detect YORP, such as with the spin-up 2001 KZ66 (Zegmott et al., 2021), which was detected using a `SHAPE` model to perform a phase offset analysis. The subsequent chapters of this thesis present the results of phase offset analyses of several NEAs that were modelled as part of this work.

CHAPTER 4

OPTICAL AND RADAR OBSERVATIONS OF (23187) 2000 PN9

4.1 Introduction

The asteroid (23187) 2000 PN9 (herafter PN9) is an Apollo-class NEA that has been monitored throughout the YORP campaign. First discovered by the Lincoln Near-Earth Asteroid Research (LINEAR) tracking programme in August 2000 (Moravec et al., 2000), PN9 has an orbital period of 2.51 years, a semi-major axis of 1.85 AU, an eccentricity of 0.59 and an inclination of 51.3°. Designated as a PHA, PN9's minimum Earth orbit intersection distance (MOID) is 0.0149859 AU. Its closest post-discovery approach to Earth was in 2006, with a minimum separation of 7.9 lunar distances. The next closest approach is in 2134, when it will come within 8.8 lunar distances of Earth.

The most significant previous work on PN9 was performed by Belskaya et al. (2009), who used optical observations from 2001 and 2006 to determine a synodic rotation period of 2.5325±0.0004 h, a lightcurve amplitude of 0.13 mag, a polarimetrically-derived albedo of 0.24±0.06 and an absolute magnitude $H = 16.2$, resulting in a diameter of 1.6±0.3 km. A preliminary anaylsis by Busch et al. (2006) used radar observations from 2001 to determine that the asteroid is roughly spherical with an approximate diameter of 2 km. The authors of this work shared processed radar data and primitive shape models to support this work, although the work presented in this chapter was performed independently of any previous attempts to model the asteroid's shape and spin-state.

MIT-Hawaii Near-Earth Object Spectroscopic Survey (MITHNEOS) observations have lead to PN9 being classified as belonging to either the S/Sq, Sq or Sq/Q taxonomic types (Thomas et al., 2014; Binzel et al., 2019). This suggests that the asteroid should have a relatively high density and albedo, with the latter already being documented by Belskaya et al. (2009). In 2016, a synodic rotation period of 2.537±0.002 h was reported, using optical observations from Palmer Divide Station (Warner, 2016). This is consistent with previous observations, affirming that PN9 is a rapid rotator.

Asteroids close to the spin-breakup barrier are critical to understanding how YORP

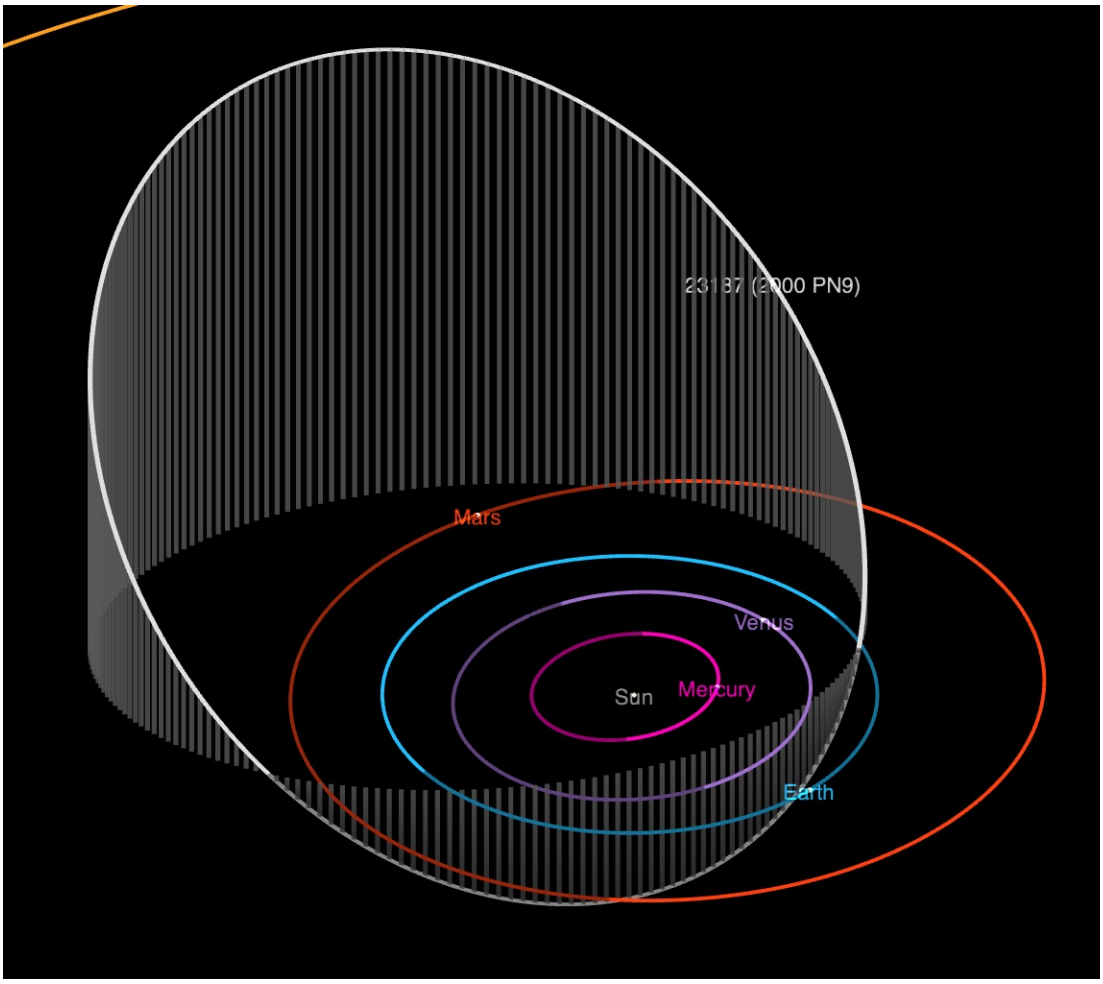

Figure 4.1: The orbit of (23187) 2000 PN9, which is shown with a white line. The orbits of the inner planets are also marked, with the positions of each object shown for 2024-01-01. This figure was produced using the JPL Orbit Viewer[a].

[a] `https://ssd.jpl.nasa.gov/tools/orbit_viewer.html`

influences asteroid evolution. Objects must either reach a state of rotational equilibrium or accelerate beyond the spin-breakup barrier and become disrupted. Probing asteroids like PN9, which are close to the breakup limit, makes it possible to link each asteroid's physical properties not only to its YORP state, but to its evolutionary track.

This chapter will outline the observations of PN9 that were utilised in this work, and present a detailed physical model and the results of a phase offset analysis. These results have been published in Dover et al. (2023), although further details and discussion are provided here.

4.2 Observations of 2000 PN9

PN9 was observed between 2001 and 2020 using a variety of optical and radar facilities, loosely clustered into five apparitions that are evenly spaced between 2001 and 2006. As shown in Figure 4.2, these observations cover a substantial range of viewing geometries, particularly during 2010. As previously discussed in Section 2.2.1, this is very important when developing a physical model, while the large baseline and repeated geometries are beneficial for detecting YORP.

The following sections provide details on the radar observations in 2001 and 2006, and the 14 years of lightcurve observations between 2006 and 2020. These data can be viewed in Figures A.2 through A.9.

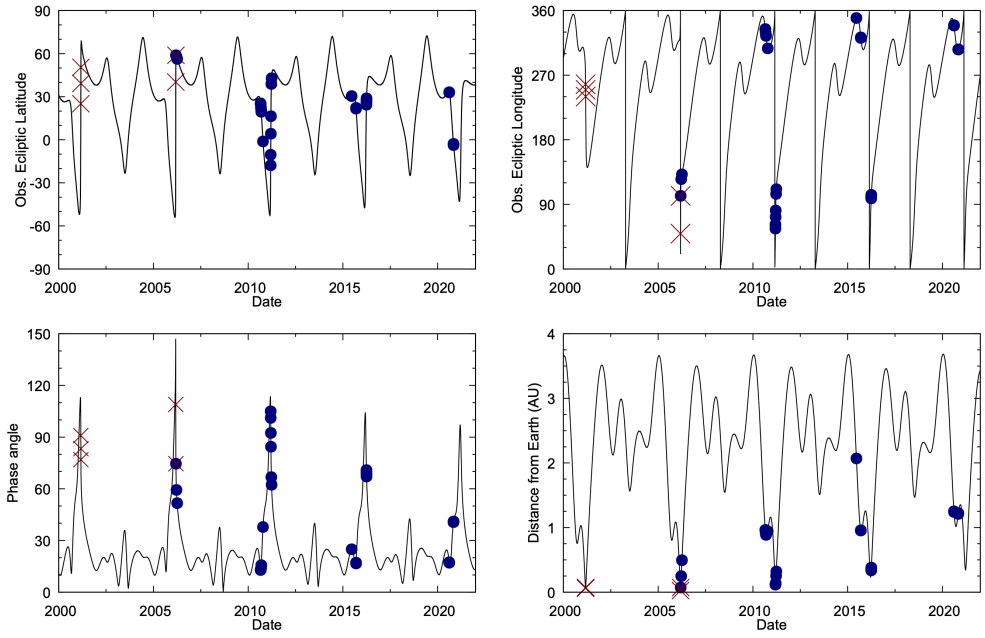

Figure 4.2: Observing geometries for (23187) 2000 PN9 from 2000 to the start of 2022. The top panels show the position of the asteroid in the ecliptic coordinate system (latitude and longitude) as observed from Earth. The bottom left panel shows the solar phase angle while the bottom right panel shows the geocentric distance to the asteroid. The marked points denote observations of the asteroid. Optical lightcurves are marked as blue circles and radar observations are represented by red crosses.

4.2.1 Optical lightcurves

This work utilises a total of 35 optical lightcurves from 10 different observatories, which are summarised in Table 4.1. The YORP programme accounts for 13 of these, with an additional 13 being previously published, and 9 provided via a collaboration with former members of the ISON collaboration (Molotov et al., 2019). Certain lightcurves were not included in the development of a shape model, or the spin-state analysis, due to their poor quality. Nevertheless, they are still useful when assessing the model's ability to reproduce lightcurves. The same subset of lightcurves were used for both the lightcurve analysis (Section 4.3.1) and combined lightcurve and radar analysis (Section 4.3.2).

As previously discussed, PN9 was observed over a large baseline with a favourable range of viewing geometries. Initial work on PN9 was conducted using data up to 2016, with the author expanding the dataset with two observing runs in 2020. Observing strategies vary between lightcurves, although they are generally consistent with the YORP campaign strategy described in Section 2.2.

Rotational lightcurves were extracted using relative photometry, comparing the asteroid's brightness to a selection of stable background stars. In some cases, sidereal tracking was used if a desirable SNR could be achieved on the asteroid without its FWHM profile exceeding atmospheric seeing. This ensured that a circular aperture with a radius of twice the FWHM profile could be used for photometry. Otherwise, the asteroid was differentially tracked and exposure times were set to avoid trailing of the background stars beyond atmospheric seeing. Consideration was also taken to ensure a sufficient temporal resolution was achieved, such that each exposure was not a significant fraction of the asteroid's rotation period.

For YORP campaign observations, which took place using the NTT, ESOD, TMO, Hale Telescope, and INT, lightcurves were extracted by the author using the steps described in Section 2.2.3. Lightcurves from other sources had already been extracted

using very similar techniques, although a small number were re-extracted by the author to verify the measurements.

YORP campaign observations initially used the R filter to maximise asteroid SNR. Because R filter imaging often needs to be de-fringed, additional processing steps and uncertainty are introduced. These often negate the advantages of the R filter, hence the YORP campaign largely changed to V filter observations from 2015. While the V and R filters constitute the majority of PN9 lightcurves, there are also B, I, and clear filter observations. The choice of broadband filter has a negligible impact on a relative lightcurve, hence it is permissible to combine BVRI and clear filter observations of PN9 when developing a shape model or performing a spin-state analysis.

Each of the facilities used to observe PN9 have been described in Section 2.2.1, with additional information provided below.

Chuhuiv Observatory (2006, 2010) – The 0.7 m telescope at Chuhuiv Observatory (Kharkiv, Ukraine) was used to observe PN9 in March 2006 and March 2011. The asteroid was imaged in 2006 with a 375×242 pixel CCD with a FOV of $10.5' \times 8.0'$ using the Johnson-Cousins BVRI filters. In 2011, observations were conducted in the Johnson-Cousins R filter using a 1056 x 1027 pixel CCD with an FOV of $16.9' \times 16.4'$. The lightcurves resulting from the 2006 apparition were previously published in Belskaya et al., 2009, and the 2010 lightcurves were extracted by the observers.

New Technology Telescope (2010, 2020) – ESO's 3.6 m NTT at La Silla Observatory (Chile) was used to observe PN9 in 2010 and 2020, using the configuration described in Section 2.2.1. For all NTT lightcurves, images were co-added to increase SNR on the asteroid. PN9 was observed using the Bessel R filter for two nights in August 2010 and one night in October 2010, and with the Bessel V filter for three nights in November 2020.

Danish Telescope (2010) – The 1.54 m Danish Telescope at La Silla Observatory (Chile) was used to observe PN9 for one night in September 2010 using the Bessel R filter, using the configuration described in Section 2.2.1. Images were co-added before lightcurve extraction.

Table Mountain Observatory (2010) – In September 2010, PN9 was observed in the R filter over three nights using JPL's 0.6 m telescope at Table Mountain Observatory (California, USA), which is again described by Section 2.2.1. The images were co-added for lightcurve extraction.

Abastumani Observatory (2011) – In March 2011, observations of PN9 were carried out with the 0.7 m Telescope at the Abastumani Astrophysical Observatory (Abastumani, Georgia). The asteroid was imaged without a filter using a 3072×2048 pixel CCD with an FOV of $44.4' \times 29.6'$. Lightcurves were extracted by the observers.

Hale Telescope (2015) – The 5.1 m Hale telescope at Palomar Observatory (California, USA), which is described in Section 2.2.1, was used to observe PN9 in June 2015. The central CCD chip was used with a Bessel R filter and images were co-added for lightcurve extraction.

Tien-Shan Observatory (2015) – In September 2015, there were observations of PN9 with the 1.0 m telescope at the Tien-Shan Astronomical Observatory (Almaty, Kazakhstan). The telescope has a 3072×3072 pixel CCD, which has an FOV of $18.9' \times 18.9'$. It was used with 2×2 binning using the Johnson R filter, and the lightcurves were extracted by the observers.

Shain Telescope (2015) – The asteroid was observed in September 2015 with the 2.6 m Shain Telescope at the Crimean Astrophysical Observatory (Nauchny, Ukraine). PN9 was imaged with a 2048×2048 pixel CCD, which has an FOV of $9.5' \times 9.5'$, using

2×2 binning without a filter, and the observers extracted the lightcurves.

Palmer Divide Station (2016) – This analysis includes six published lightcurves from the Palmer Divide Station (California, USA). PN9 was observed with three 0.35 m Meade LX200GPS telescopes equipped with commercial CCDs using the Johnson V filter. These lightcurves were obtained through the Asteroid Lightcurve Data Exchange Format (ALCDEF) database (Warner et al., 2011) and are discussed in Warner (2016). Note that observations taken with different telescopes during the same night are treated as separate lightcurves.

Isaac Newton Telescope (2020) – The author observed PN9 over two nights in August 2020 with the 2.5 m Isaac Newton Telescope (La Palma, Spain). Imaging was conducted in the Harris V filter with 1×1 binning using the central chip of the Wide Field Camera. The CCD was windowed to give a $10' \times 10'$ field with a resolution of 1820×1820. This was done to reduce CCD readout time and improve the temporal resolution of the lightcurves. Images were co-added for lightcurve extraction.

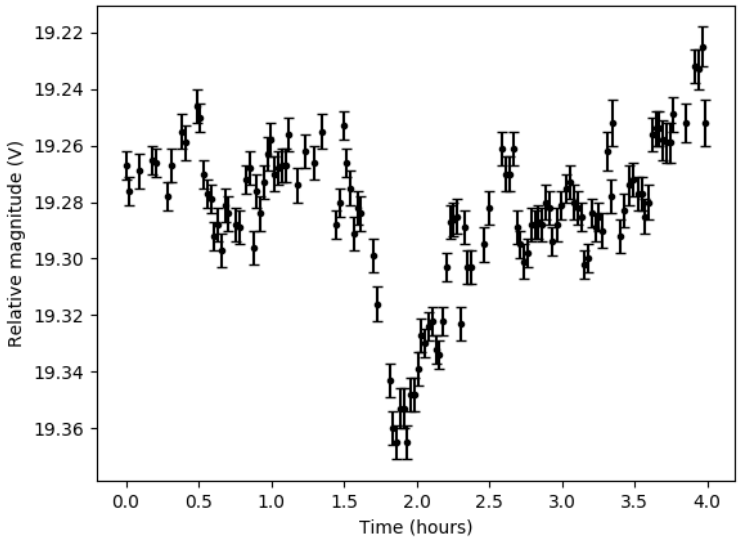

Figure 4.3: A lightcurve of 2000 PN9 taken with the INT on 2020-08-11, which corresponds to lightcurve 32 in Table 4.1.

ID	UT date [yyyy-mm-dd]	$R_\odot$ [AU]	$\Delta_\oplus$ [AU]	α [°]	λ_O [°]	β_O [°]	Total [hour]	Obs. facility	Filter	Included (model)	Included (ph. off)	Reference
1	2006-03-10	1.098	0.072	75.55	101.9	58.89	0.3	ChO	B			1
2		””	””	””	””	””	0.5	ChO	V			1
3		””	””	””	””	””	0.7	ChO	R			1
4		””	””	””	””	””	0.3	ChO	I			1
5	2006-03-20	1.099	0.249	59.37	125.2	57.85	4.2	ChO	R	•	•	1
6	2006-04-03	1.228	0.495	51.57	131.9	56.30	1.3	ChO	R			1
7	2010-08-28	1.927	0.965	12.96	334.2	25.3	2.4	NTT	R		•	
8	2010-08-29	1.920	0.956	12.87	333.5	25.0	3.3	NTT	R	•	•	
9	2010-09-03	1.876	0.915	13.36	329.1	22.5	1.3	ESOD	R			
10	2010-09-08	1.846	0.894	14.72	326.2	20.6	4.8	TMO	R			
11	2010-09-09	1.839	0.890	15.18	325.5	20.0	5.8	TMO	R			
12	2010-09-10	1.831	0.886	15.67	324.7	19.5	5.7	TMO	R			
13	2010-10-14	1.558	0.944	37.80	307.3	-1.2	3.9	NTT	R	•	•	
14	2011-03-10	0.956	0.118	105.00	56.3	-17.8	1.5	ChO	R		•	
15	2011-03-11	0.964	0.117	101.12	62.0	-10.4	0.7	ChO	R	•	•	
16	2011-03-13	0.981	0.122	92.43	72.5	4.2	1.8	ChO	R	•	•	
17	2011-03-15	0.998	0.139	84.44	81.5	16.4	3.8	AbAO	clear	•	•	
18	2011-03-23	1.069	0.254	66.78	104.5	38.9	2.5	ChO	R	•	•	
19		””	””	””	””	””	2.6	ChO	R	•	•	
20	2011-03-27	1.105	0.321	62.38	111.1	42.8	4.2	AbAO	R	•	•	
21	2015-06-18	2.398	2.070	24.92	349.6	30.4	3.5	PAL	R		•	
22	2015-09-10	1.886	0.958	16.68	322.6	22.2	1.4	TSAO	R			
23	2015-09-11	1.879	0.855	17.15	321.9	21.7	2.5	CrAO	clear	•	•	
24	2016-03-28	1.056	0.337	70.87	98.3	24.4	3.5	PDS	V	•	•	2
25		””	””	””	””	””	1.1	PDS	V		•	2

Table 4.1: All optical lightcurves of 2000 PN9 that were considered for this work (continues)

ID	UT date [yyyy-mm-dd]	$R_\odot$ [AU]	$\Delta_\oplus$ [AU]	α [°]	λ_O [°]	β_O [°]	Total [hour]	Obs. facility	Filter	Included (model)	Included (ph. off)	Reference
26	2016-03-29	1.065	0.351	69.54	100.1	26.0	2.4	PDS	V	•	•	2
27		””	””	””	””	””	1.0	PDS	V			2
28	2016-03-30	1.074	0.366	68.29	100.1	26.0	2.9	PDS	V	•	•	2
29	2016-03-31	1.083	0.381	67.12	103.3	28.9	3.3	PDS	V	•	•	2
30		””	””	””	””	””	1.4	PDS	V	•	•	2
31	2020-08-10	2.133	1.243	17.1	339.2	33.0	3.2	INT	V		•	
32	2020-08-11	2.127	1.231	16.9	338.7	32.9	4.1	INT	V	•	•	
33	2020-11-01	1.513	1.217	40.8	305.8	-3.3	2.6	NTT	V		•	
34	2020-11-02	1.504	1.223	41.0	305.9	-3.7	3.0	NTT	V	•	•	
35	2020-11-03	1.496	1.229	41.2	306.0	-4.1	2.9	NTT	V	•	•	

Notes. Each lightcurve has a chronologically assigned ID, then the UT date at the beginning of the night, the heliocentric ($R_\odot$) and geocentric ($\Delta_\oplus$) distances in AU, the solar phase angle (α), the observed ecliptic longitude (λ_O), the observed ecliptic latitude (β_O), the total time over which the target was observed, the observing facility and the photometric filter. Points in the ‘Included (model)’ column indicate which lightcurves were included in modelling, and points in the ‘Included (ph. off)’ column indicate lightcurves that were included in the phase offset analysis. References to published lightcurves are listed. Observing facility key: ChO – Chuhuiv Observatory 0.7 m Telescope (121 - Kharkiv, Ukraine); ESOD – European Southern Observatory Danish 1.54 m Telescope (809 - La Silla, Chile); NTT – European Southern Observatory 3.6 m New Technology Telescope (809 - La Silla, Chile); TMO – Table Mountain Observatory 0.6 m Telescope (673 - California, USA); AbAO – Abastumani Astrophysical Observatory 0.7 m Telescope (119 - Abastumani, Georgia); TSAO – Tien-Shan Astronomical Observatory 1.0 m Telescope (N42 - Almaty, Kazakhstan); CrAO – Crimean Astrophyscial Observatory 2.6 m Shain Telescope (095 - Nauchny, Ukraine); PAL – Palomar Observatory 5.1 m Hale Telescope (675 - California, USA); PDS – Palmer Divide Station 0.35 m (various) (U82 - California, USA); INT – Isaac Newton Group 2.54 m Isaac Newton Telescope (950 - La Palma, Spain)

References. (1) Belskaya et al., 2009; (2) Warner, 2016

Table 4.1: (continued)

Obs.	UT Date [yyyy-mm-dd]	RTT [s]	Baud [μs]	Res. [m]	Start-Stop [hh:mm:ss-hh:mm:ss]	Runs	Radar model	Note
Arecibo	2001-03-03	62	cw		09:40:32-09:56:40	8		
			cw		09:59:25-10:00:23	1		
			4	600	10:02:38-10:16:19	3		Ranging
			4.5	675	10:17:46-10:23:28	3		Ranging
			0.5	75	10:27:14-10:36:39	5		Ranging
Goldstone	2001-03-03	62	1.0	150	13:14:07-15:02:52	49	•	
Arecibo	2001-03-04	67	cw		09:04:03-09:16:47	6	•	
			0.2	30	09:18:59-09:24:35	3	•	
			0.1	15	09:27:01-09:38:27	3		
		68	0.1	15	10:09:44-10:31:28	10	•	
Arecibo	2001-03-05	76	cw		09:05:55-09:12:43	3	•	
		77	0.2	30	09:15:42-10:52:44	38	•	
Goldstone	2006-03-07	36	0.125	19	19:24:26-19:31:09	6	•	
			0.125	19	19:31:49-20:30:26	48	•	
Goldstone	2006-03-10	86	cw		12:02:53-14:42:14	58		Low SNR

Notes. "Obs." is the facility with which the observations were made. "UT Date" is the start date of the observations in universal time. "RTT" is the signal's round trip time to the object and back. "Baud" is the baud length and "Res" is the delay resolution; continuous wave observations are marked as "cw" and do not have spatial resolution. "Start-Stop" is the UT timespan in which the observations were made. "Runs" is the number of transmit-receive cycles that were completed.

Table 4.2: Radar observations of 2000 PN9

4.2.2 Radar data

As discussed in Section 3.2.2, radar observations are crucial for the reconstruction of an asteroid's non-convex shape. Unlike optical observations, planetary radar is limited to very close approaches. In the 21st century, there are only three approaches where PN9 comes within 50 lunar distances of Earth; these were in 2001, 2006 and 2011. These approaches took place at 7.8, 23.7 and 45.1 lunar distances respectively. As shown in the lower right panel of Figure 4.2, the asteroid was observed with planetary radar during the 2001 and 2006 approaches.

Radar imaging taken by Arecibo and Goldstone during these approaches are likely to be the highest quality radar data of PN9 collected this century. These data were reduced by Michael Busch and provided by Marina Brozović (priv. communication). Details of these observations are given below, and a list of observations is provided in Table 4.2.

Arecibo Observatory (2001) – As described in Section 2.3.1, Arecibo Observatory was the world's foremost planetary radar facility. It was used to observe PN9 on 3, 4 and 5 March 2001. The delay-Doppler imaging on 3 March were for ranging and ephemeris correction, hence they were excluded from the analysis. On 4 March, imaging was mostly conducted with a baud length of 0.1 μs giving a ~ 15 m resolution, with some further imaging at 0.2 μs (~ 30 m). On 5 March, a baud length of 0.2 μs (~ 30 m) was used for imaging. It should be noted that observations from 3 March were not obtained until late in the modelling process for PN9. Due to limited computational resources and the presence of data from subsequent days, these data were not used in this work. All but ten minutes of the delay-Doppler imaging from 3 March were at an extremely low resolution, and would not have significantly contributed to the model, although the continuous wave spectra from this date should be included in any future work.

Goldstone Solar System Radar (2001, 2006) – Delay-Doppler imaging of PN9 was conducted by GSSR - also described in Section 2.3.1 - on 3 March 2001 and 7 March 2006. The 2001 imaging used a baud length of 1.0 μs ($\sim$ 150 m) while the 2006 imaging used a baud length of 0.125 μs ($\sim$ 19 m). In 2006, GSSR also obtained cw spectra of PN9. These were not included in the analysis, as there are already higher quality radar data for this epoch and viewing geometry. Astrometric measurements from both 2001 and 2006 were used for ephemeris correction.

4.3 Physical modelling

As discussed in Chapter 3, there are two main techniques that can be used to measure the shape and spin-state of an asteroid: convex inversion of lightcurves, and radar modelling with `SHAPE`. As modelling with radar data is an iterative and computationally intensive process, and fitting procedures are highly sensitive to input parameters, it was more efficient to first perform a lightcurve-only analysis of PN9. This can allow the use of predetermined constraints on rotation period, pole orientation and shape, which greatly improves efficiency when later modelling the object with a combination of lightcurve and radar data.

4.3.1 Modelling with lightcurves

Of the 35 lightcurves listed in Table 4.1, 17 were not included in the modelling process. These lightcurves were deemed unsuitable due to poor temporal resolution, gaps in rotational coverage or low SNR. The exclusion of these lightcurves does not significantly affect coverage of different viewing geometries, or create gaps between groups of observations.

A search for PN9's sidereal rotation period was conducted between 2.500 and 2.570 h, a range based on the previously reported synodic periods (Galeev et al., 2007; Belskaya et al., 2009; Warner, 2016), using the convex inversion routines described in Section

3.1.2. For each iteration over the period scan range, a shape model was generated for six random and unique rotational poles. Each shape model was then optimised to best fit the lightcurve data across the period range. The results of this scan, shown in Figure 4.4, identify a best-fit rotation period of 2.532 ± 0.008 h.

A further period scan was conducted over a wider but more coarse range of periods, searching for solutions between 1 h and 10 h. This scan founds solutions close to integer multiples of the 2.532 h period, but these were later discounted due to their corresponding shape models being both physically extreme and inconsistent with radar imaging data. These alternative period solutions were further discounted with a radar period scan, described in Section 4.3.2.

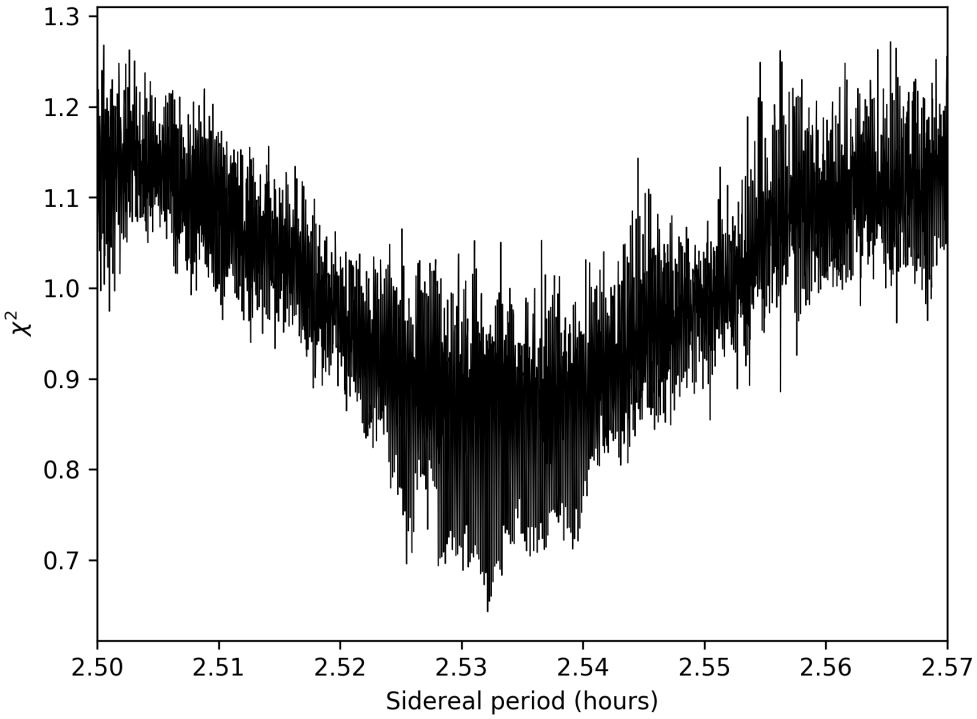

Figure 4.4: The results of a period search for asteroid (23187) 2000 PN9. For each period in the range shown, lightcurve data were used to optimise a model for six different rotational poles in the celestial sphere. The lowest χ^2 across the six models was recorded for the period being used. The best-fit sidereal rotation period for 2000 PN9 from this scan is 2.532 ± 0.008 h.

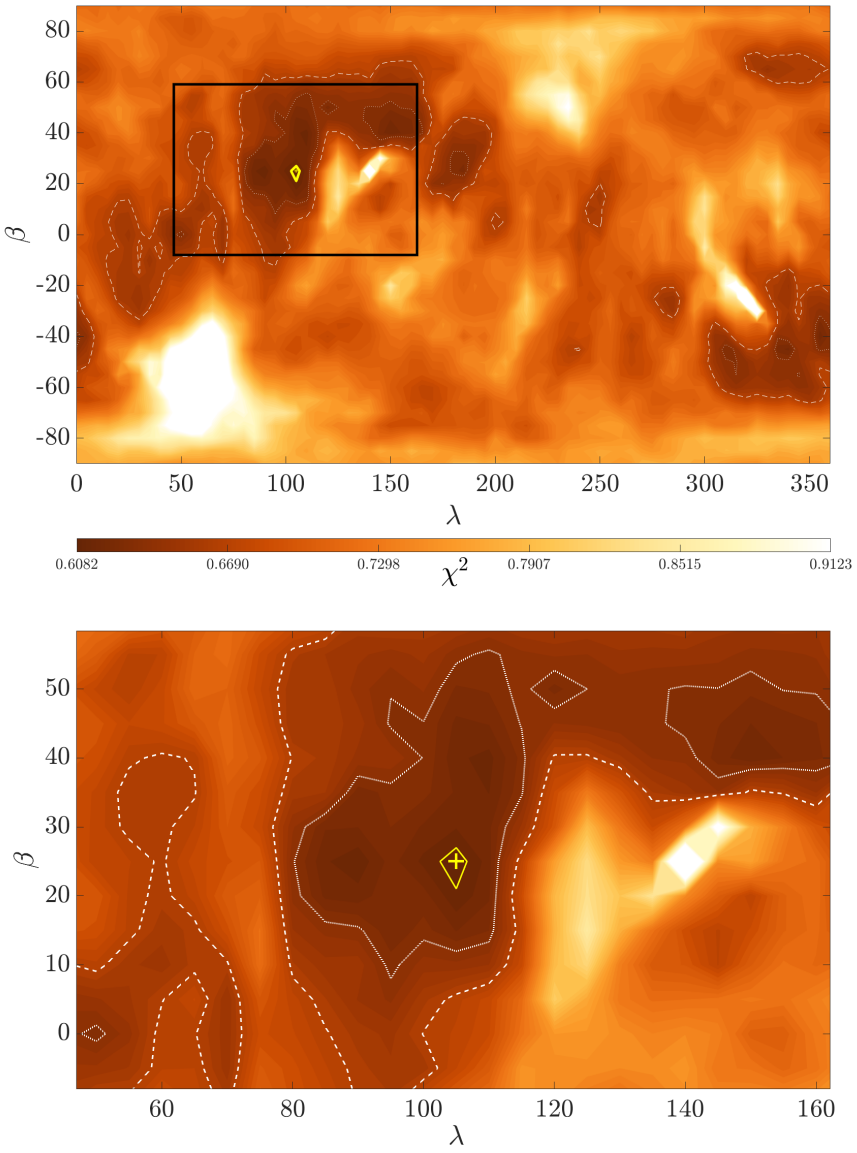

Figure 4.5: The results of a search for the rotational pole of (23187) 2000 PN9 using convex inversion of lightcurve data. For each pole solution in ecliptic coordinates λ and β, the χ^2 fit of the solution is plotted for a colour range where the global minimum χ^2 is black and solutions 50% greater than the minimum are white. The best solution is marked with a yellow '+'. The yellow line and the white dotted and dashed lines enclose regions where χ^2 is within 1%, 5% and 10% of the best solution respectively. The top panel shows the full celestial sphere, with the region enclosed by the black rectangle shown in the bottom panel.

Using an input period of 2.532 h from the period scan, a search for the asteroid's rotational pole was conducted using the method described in Sections 3.1.3 & 3.1.4. For each pole on a $5° \times 5°$ grid covering the celestial sphere, the model's period and

convex shape were optimised, assuming principal axis rotation. The scan was then repeated with the addition of YORP acceleration, for a range of YORP factors from -10^{-8} rad/day^2 to 10^{-8} rad/day^2 in steps of 2×10^{-9} rad/day^2. The goodness-of-fit for the global best solution within each YORP place does not converge towards any YORP value; this indicates that no YORP solution is found. Because of this, subsequent lightcurve-only analysis of PN9 only considered a constant-period model.

Figure 4.5 shows the results of the zero-YORP plane, where the pole does not converge to a single region in the celestial sphere. The best model's rotational pole lies at ecliptic longitude $\lambda = 105°$ and ecliptic latitude $\beta = +25°$ with a rotation period of 2.532 h. Models within 5% of the best solution have poles corresponding to opposite regions of the celestial sphere, and are consistent in shape and period. This result shows that the orientation of the rotational axis is constrained, although the data are insufficient for distinguishing between prograde and retrograde rotation. This is a common issue when modelling with low-amplitude lightcurves produced by highly symmetrical objects.

The convex hull model of the global best solution, shown in Figure 4.6, indicates that the asteroid is an oblate spheroid with signs of an equatorial ridge. There is a flattened section on the equator which could be interpreted as a crater, but could also be caused by a prominence or large boulder. The polar regions are also flattened, although this could be an artefact caused by uncertainty in the Z-axis. As shown in Figure A.2, the model is able to reproduce the shape of most lightcurves, although in some cases there is a small phase offset and a mis-match in amplitude. Since there is no coherent progression in phase offset, the phase offsets are the result of uncertainties which can be reduced with radar modelling. Convex hull models struggle to reproduce low-amplitude lightcurves due to the heightened dependence on surface features, which are not modelled, while general uncertainties in shape and pole can suppress or amplify brightness variation cased by the asteroid's overall shape. While this convex hull model is inadequate for a phase offset analysis, it has usefully constrained the shape, period

and spin-axis of PN9. As the initial radar modelling of PN9 did not include lightcurve data, early models produced by SHAPE can be considered to be independent of the convex hull model. This allowed for a useful test of this analysis, where the models produced by lightcurve and radar datasets were compared to ensure consistency before proceeding to develop a combined radar and lightcurve model using SHAPE.

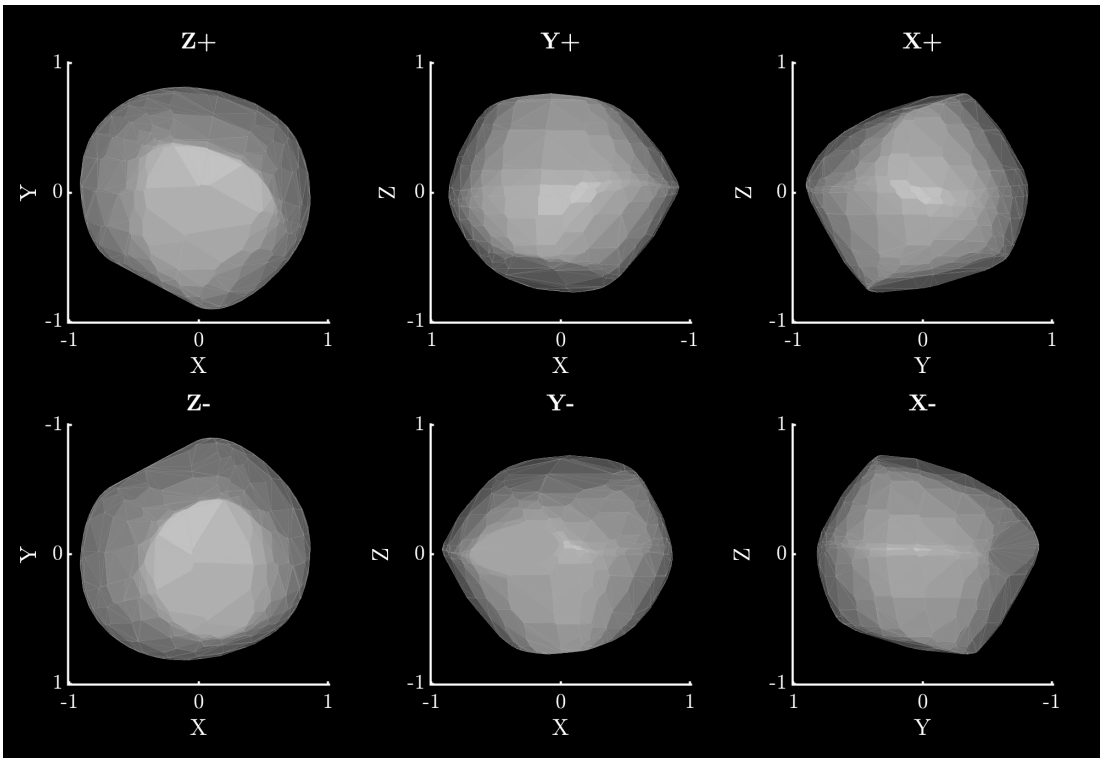

Figure 4.6: The best-fit convex hull model of (23187) 2000 PN9 with the rotational pole $\lambda = 105°$ $\beta = +25°$. This model assumes principal-axis rotation and a constant period of 2.532 h. The top row shows the model from the positive end of the Z, Y and X axes in the body-centric co-ordinate system. The bottom row shows the model from the negative end of the Z, Y and X axes. The Z-axis is aligned with the rotational pole, which is the shortest axis of inertia. The X-axis is arbitrarily set such that it is viewed from the positive end for the plane-of-sky at T_0. Axis lengths are in arbitrary units, as lightcurve inversion does not produce scaled models.

4.3.2 Modelling with radar

The SHAPE software package, which is described in Section 3.2.2, was used to develop a physical model of PN9 using radar data. The development of a radar model benefits from well-constrained input parameters, which in this case were taken from the convex

inversion analysis described in Section 4.3.1.

An input model was constructed for `SHAPE` comprising a triaxial ellipsoid with principal axis rotation. Both the convex hull model and inspection of delay-Doppler images indicate that PN9 has a spheroid shape, so a sphere with a 1.9 km diameter was used as the input model. This diameter was chosen as it was close to the 2 km estimate from an earlier unpublished analysis of the radar data (Busch et al., 2006), but also in agreement with a reported 1.6 ± 0.3 km diameter based on an estimated optical albedo of 0.24 ± 0.06 (Belskaya et al., 2009). The rotation period was set to 2.532 h, as previously determined with the lightcurve analysis.

A $10^\circ \times 10^\circ$ grid of poles was set up, covering the celestial sphere. For each fixed pole, the model's shape and period were optimised to fit the radar data marked in Table 4.2. The ellipsoid model for each pole was then converted to a vertex model with 1000 vertices and 1996 facets, to allow for the fitting of surface features through the adjustment of individual facets. The cw spectra were removed at this stage, as the model was sufficiently well-constrained and there was a risk of over-fitting to noise.

Early iterations of PN9's vertex model remained in good agreement with the convex hull model's shape, pole and period. As the radar model's initial parameters were derived from lightcurve data, a coarse radar period scan was conducted to confirm that the radar data independently favour a 2.5 h solution. This period scan utilised the same six-pole strategy used in convex inversion period scans. Computational limitations restricted this to a coarse resolution that can only show global minima, and not identify local minima required for a precise period measurement. The resolution was increased around multiples of 2.5 h, as these are the most likely alternate solutions. As shown in Figure 4.7, a coarse period scan with radar data indicates a clear global minimum close to 2.5 h.

As previously discussed, the radar model at this stage was consistent with independently-produced convex inversion model. This indicates that the two datasets produce results that are in agreement, and can be safely combined to produce a model that is fitted

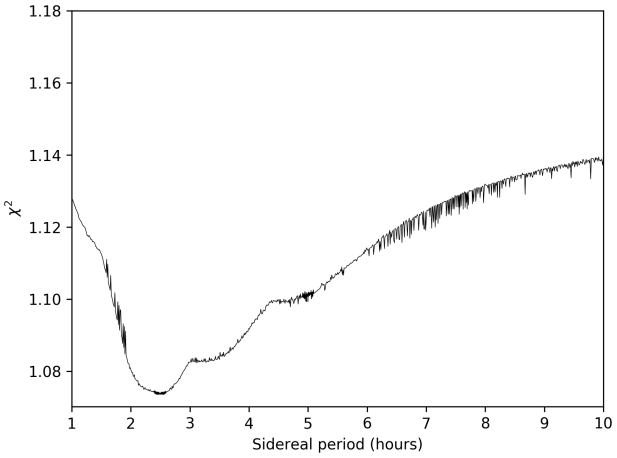

Figure 4.7: The results of a period search for asteroid (23187) 2000 PN9 with radar data. `SHAPE` was used to optimise an ellipsoid model for six different rotational poles in the celestial sphere to fit both continuous-wave and delay-Doppler data. The lowest χ^2 across the six models was recorded for the period being used, with a higher temporal resolution close to 2.5 h, 5 h and 7.5 h. This is a coarse scan intended to demonstrate a global minimum close to 2.5 h independently of lightcurve data.

to both optical and radar data. With this test being passed, lightcurve data were then progressively introduced in subsequent fitting runs to produce a combined radar and lightcurve model. The full subset of lightcurves, marked in Table 4.1, were not all included until the final iterations of modelling. Each additional lightcurve causes a significant increase in computation time whilst yielding diminishing returns, so is more efficient to gradually introduce the lightcurve dataset as the model improves.

During modelling, penalty functions (see Sect. 3.2.1.1) were applied to discourage certain features. The first penalty prevents excessive deviation of the centre of mass from the origin of the body-centric coordinate system. The second penalty prevents large divergence between the model's Z-axis and the axis of maximum inertia. A third penalty disallows non-principal axis rotation. A fourth penalty is used to suppress unphysical spikes that can occur when fitting a vertex model. Finally, a fifth penalty was applied to discourage deep concavities. The first three penalties were given a relatively high strength, and the latter two penalties were low in strength to ensure they only discouraged unphysical features without restricting the construction of craters, ridges and boulders.

The results of the SHAPE pole scan with both radar and lightcurve data are shown in Figure 4.8. The pole is again constrained to two opposite regions, with the best solution

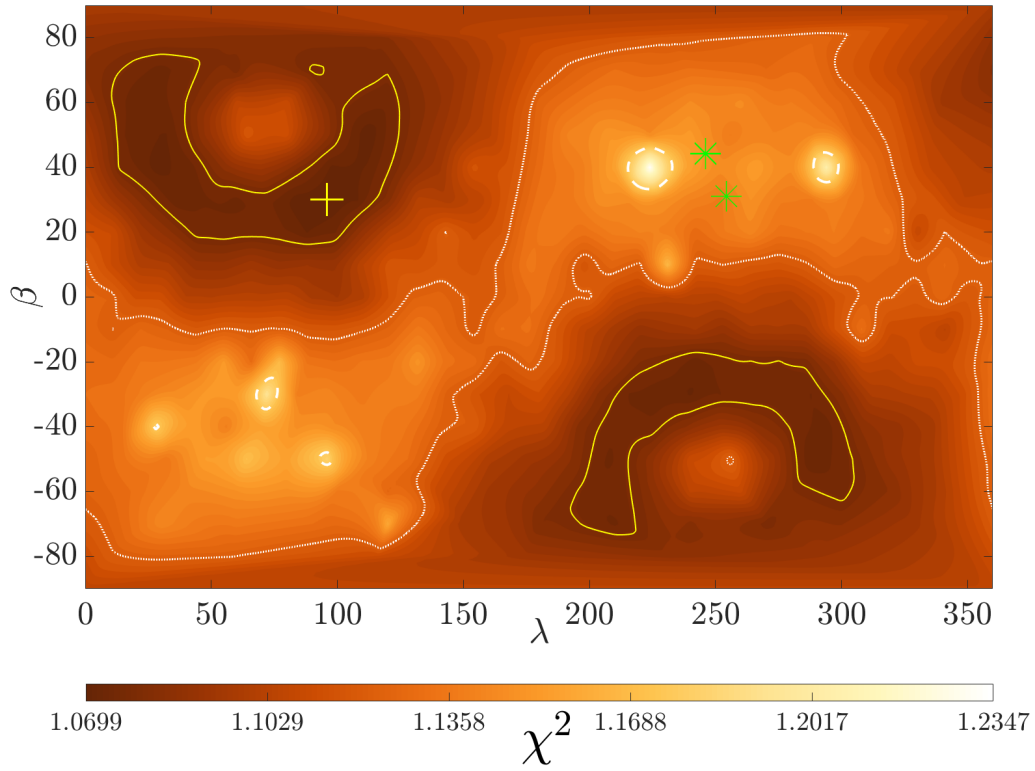

Figure 4.8: The results of a search for the rotational pole of (23187) 2000 PN9 using SHAPE with radar and lightcurve data. For each pole solution in ecliptic coordinates λ and β, the χ^2 fit of the solution is plotted for a colour range where the global minimum χ^2 is black and the maximum is white. The best solution is marked with a yellow '+'. The yellow lines enclose regions where χ^2 is within 1% of the best solution, and dotted and dashed white lines enclose regions where χ^2 is within 5% and 10% of the best solution respectively. Green stars indicate the ecliptic coordinates of the observer's line-of-sight for each date where delay-Doppler imaging was taken.

at ecliptic longitude $\lambda = 96°$ and ecliptic latitude $\beta = +30°$. Solutions within 1% of the global best fit in both the northern and southern hemispheres have consistent shapes and periods, again indicating an uncertainty as to whether PN9's rotation is prograde or retrograde. The best-fit model is able to produce synthetic lightcurves (Fig. 4.10) and delay-Doppler radar observations (Fig. 4.12) that are a good fit to observations. While a retrograde solution cannot be completely ruled out, the prograde solution is more clearly favoured in a lightcurve-only analysis (Fig. 4.5) and it produces better-fitting lightcurves (Fig. 4.9). As the two solutions have identical rotation periods and

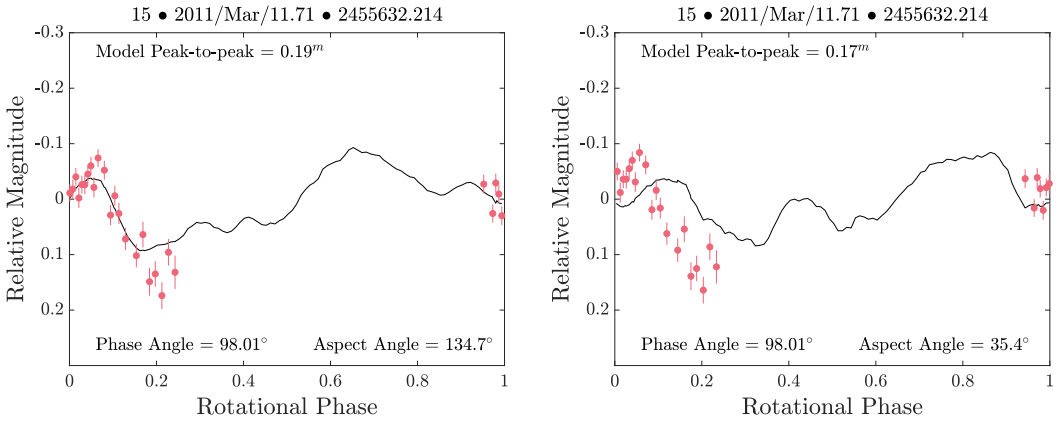

Figure 4.9: A comparison of lightcurve fits produced by the prograde (left panel) and retrograde (right panel) models of (23187) 2000 PN9 for lightcurve 15. The prograde model produces a better fit than the retrograde model, which has a smaller amplitude and a minor phase offset compared to the data.

very similar shapes, any qualitative analysis of the two solutions will yield the same conclusions. As such, subsequent sections of this work will only consider the prograde solution.

The best-fitting model was re-modelled with 2000 vertices to allow for closer fitting of surface features to the 15 m resolution radar imaging, although this yielded a negligible improvement in the χ^2 fit. Both the optical and radar observations cover the entire surface of the asteroid, leaving no 'unseen' surface area in either of the two wavelength regimes. The geometric parameters of this model are presented in Table 4.3 and the shape model is shown in Figure 4.11. The lightcurve fits, shown in Figure A.9, are an improvement upon those produced by the convex hull model (Fig. A.2). The majority of lightcurves are fitted well in terms of shape, phase and amplitude, with the few poor fits generally corresponding to low-quality lightcurves that were not used in the modelling process.

Parameter	Value
λ	$96 \pm 36°$
β	$+30 \pm 17°$
P	2.53216 ± 0.00015 h
Max. extent along (x, y, z) (±)	$1.82 \times 1.82 \times 1.77$ km ($0.08 \times 0.07 \times 0.11$ km)
Surface area	9.61 ± 0.80 km^2
Volume	2.62 ± 0.34 km^3
DEEVE dimensions (2a, 2b, 2c) (±)	$1.73 \times 1.73 \times 1.68$ km ($0.10 \times 0.09 \times 0.06$ km)
D_{eq}	1.71 ± 0.07 km

Notes. The maximum extents are measured along the three axes of a body-centric coordinate system. "DEEVE" stands for dynamically equivalent equal-volume ellipsoid. D_{eq} is the diameter of a sphere that has a equal volume to the model.

Table 4.3: Summary of parameters for the prograde radar and lightcurve model of (23187) 2000 PN9.

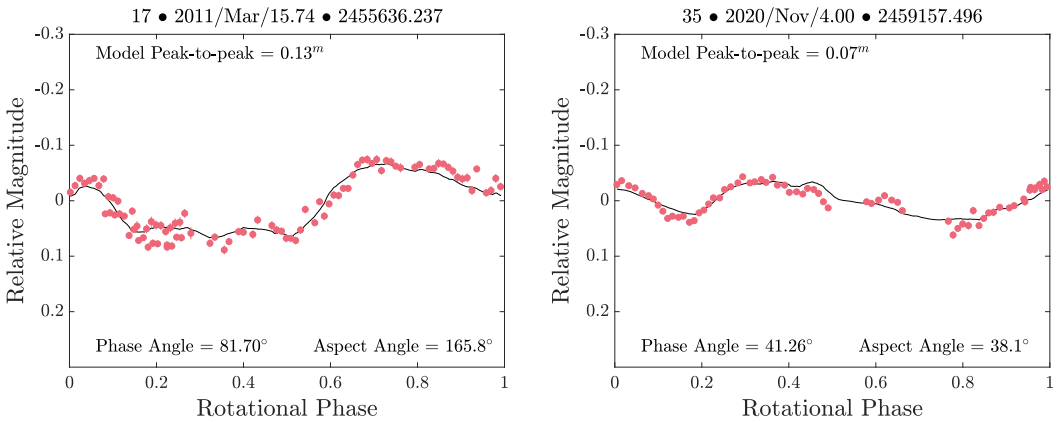

Figure 4.10: A comparison of observational data (red points) and the corresponding synthetic lightcurve (solid black line) for lightcurves 17 and 35 (Table 4.1). The synthetic lightcurves were generated using the combined radar and lightcurve model for (23187) 2000 PN9, with a combination of the Lambertian and Lommel-Seeliger scattering models. For plots of all 35 lightcurves, see Figure A.9.

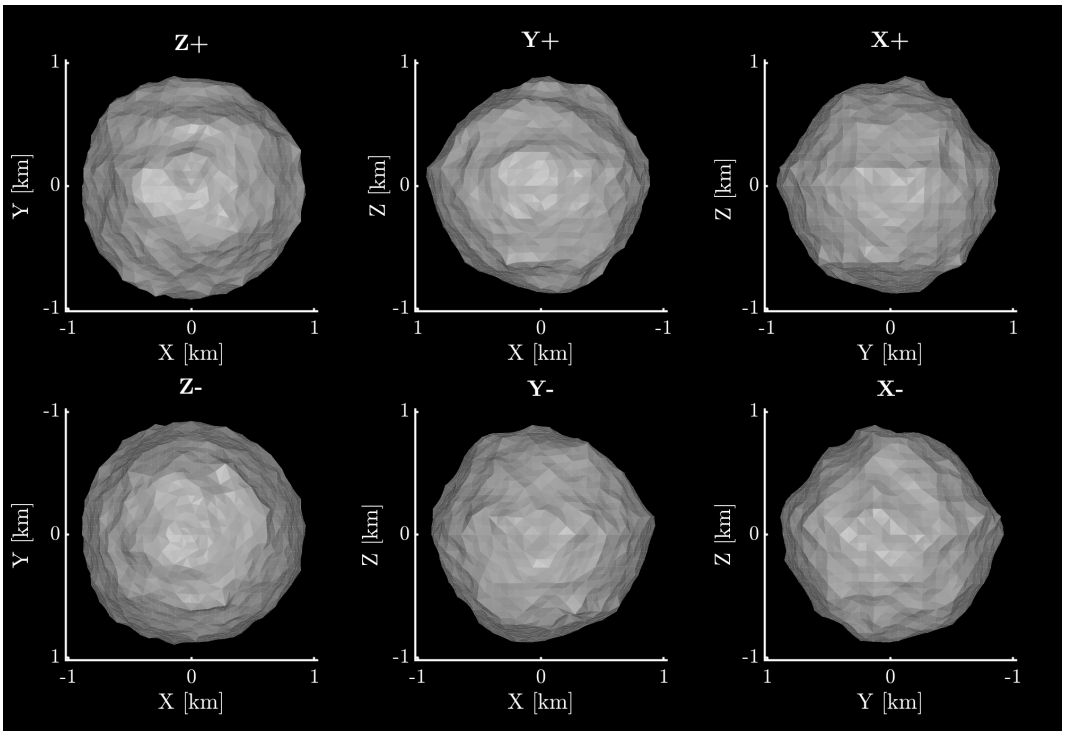

Figure 4.11: The best-fit shape model of (23187) 2000 PN9 constructed with radar and lightcurve data. This model has its rotational pole at ecliptic longitude $\lambda = 96°$ and ecliptic latitude $\beta = +30°$, and a sidereal rotation period of 2.53216 ± 0.00015 h. The top row shows the model from the positive end of the Z, Y and X axes in the body-centric co-ordinate system. The bottom row shows the model from the negative end of the Z, Y and X axes. The Z-axis is aligned with the rotational pole, which is the shortest axis of inertia. The X-axis is arbitrarily set such that it is viewed from the positive end for the plane-of-sky at T_0. Axis lengths are given in kilometres. It should be noted that the model for the antipode solution has a very similar shape, such that any discussion of this model's features will also apply to the antipode model.

4.3.2.1 Differences and limitations of the models

A comparison of the convex inversion and `SHAPE` pole scans (Figs. 4.5 and 4.8) shows that the latter method produces clearer convergence towards the global pole solution for PN9. For highly symmetrical asteroids such as PN9, optical lightcurves will be dominated by surface features and observations will be more affected by instrumental performance and atmospheric conditions. Combining lightcurves taken with different filters can amplify these issues, especially when considering scattering effects on the asteroid. In the case of PN9, lightcurves included in the analysis were taken in the

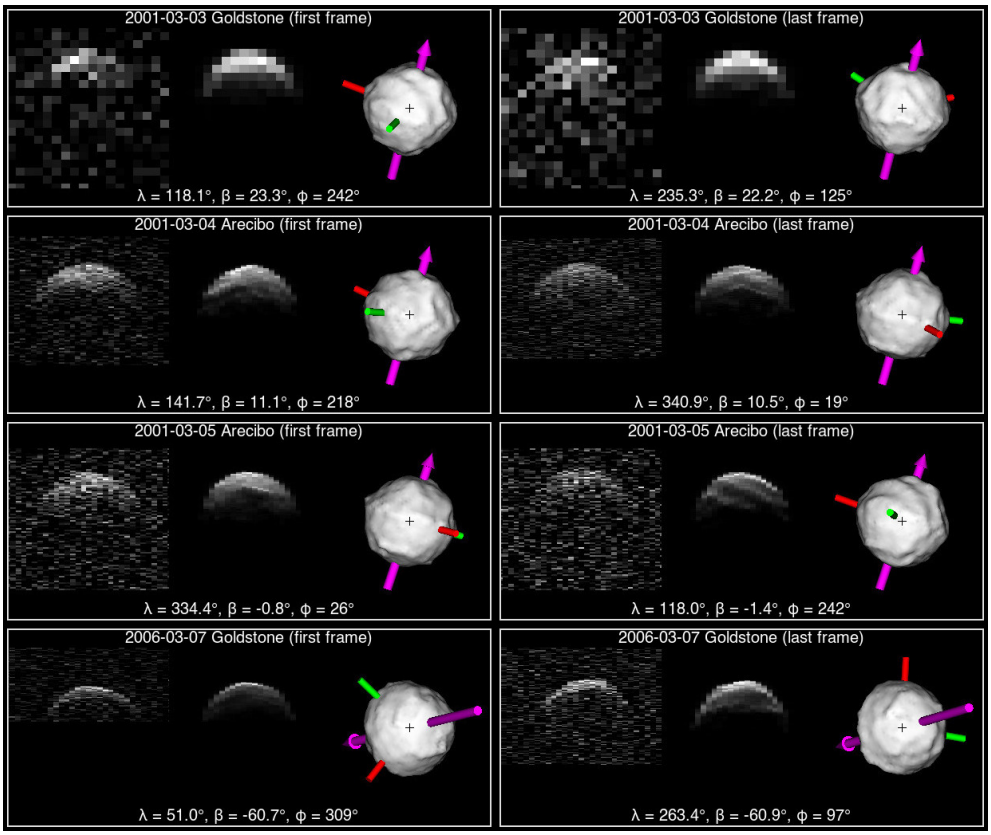

Figure 4.12: A comparison between delay-Doppler observations and the combined radar and lightcurve model for (23187) 2000 PN9, showing the first and last frame of each included dataset. Each three-panel image comprises the observational data (first panel), a synthetic echo (second panel) and a plane-of-sky projection of the model (third panel). On the first two panels, delay increases towards the bottom of the vertical axis and Doppler frequency increases along the horizontal axis. The plane-of-sky projections (third panel) are displayed with the celestial north at the top and east to the left, in an equatorial coordinate system. The rotation axis, which is closely aligned with the z-axis in the body-centric coordinate system, is marked with a purple arrow. The axes of minimum and intermediate inertia are indicated by red and green rods respectively. The body-fixed longitude λ and latitude β for the radar line-of-sight, and the rotational phase ϕ, are labelled for each image. These values were determined using the radar shape model's spin-state. The projected centre of mass is marked with a cross. The full sets of radar imaging data are shown in Figures A.3 through A.6.

V, R and clear filters. Separating these into different subsets to produce independent models is not a viable option, as each of the subsets alone does not provide an adequate number of rotations and viewing geometries to produce a good model.

For asteroids where global shape dominates both optical and radar features (e.g. Zegmott et al., 2021), combining the data will better constrain the model. For asteroids

like PN9, where surface properties are dominant, it can be difficult to reconcile the radar and optical data. Radar can penetrate several wavelengths into the surface of an asteroid, and is thus sensitive to features within the top layer of material. Optical observations, however, only represent the surface of the asteroid. If there are any surface features that do not correlate with sub-surface features, such as buried rocks, radar echoes will be produced from features that are not visible on the surface (Virkki and Muinonen, 2016), hence there can be a disparity between optical and radar observations. The heightened importance of scattering laws and albedo introduces further complexity, resulting in a model that is a compromise between fitting both the optical and radar data.

Searches using only the radar data were also conducted, although the pole was poorly constrained without the wide range of viewing geometries afforded by the lightcurves. The shape model also benefits from the inclusion of lightcurve data, as the wide range of viewing geometries results in shadowing effects that can be used to better constrain the surface.

Observations that only cover a range of low sub-observer latitudes (i.e. equatorial views of the asteroid) can cause inaccuracy in shape models. When modelling with `SHAPE`, this can cause models to assume a more spherical shape caused by uncertainty in the rotation axis. While the combined radar and lightcurve model for PN9 is highly spherical, the lightcurve and radar data span a sufficient range of viewing geometries to eliminate concerns as to whether PN9 could be more oblate than the model suggests. Goldstone radar imaging data from 2006 (Fig. A.5) are particularly useful in this regard, as they correspond to a sub-observer latitude of -61° over 148° of rotation.

4.4 Disk-integrated properties

Continuous wave (cw) spectra can be used to determine the asteroid's circular polarisation ratio (SC/OC), whereby the echo power is recorded in both the same circular

(SC) and opposite circular (OC) polarisations. Arecibo observations of PN9 from 4 and 5 March 2001 give SC/OC ratios of 0.234 ± 0.003 and 0.235 ± 0.006 respectively, which is consistent with the mean SC/OC ratio of 0.270 ± 0.079 for S and Q class NEAs (Benner et al., 2008). OC radar cross-sections were also measured on these dates, returning 0.20 ± 0.05 km^2 and 0.18 ± 0.05 km^2 on 4 and 5 March respectively. The radar albedo, which is determined by dividing the OC cross-section by the model's projected area, was determined to be an average of 0.08 ± 0.08 on both days. This is consistent with the mean radar albedo of 0.19 ± 0.06 for S and Q type NEAs reported in Virkki et al. (2022).

As explained in Section 2.3.2.1, the SC component depends upon surface roughness at scales comparable to the signal wavelength. For the Arecibo cw observations of PN9, this scale is 13 cm. As also explained in Section 2.3.2.1, asteroids with different surfaces and formation processes can have very similar SC/OC ratios. Didymos, which is a recently-visited S-complex asteroid with an SC/OC ratio of 0.20 ± 0.02 (Benner et al., 2008), is thought to be YORP evolved (Michel et al., 2022). Despite these similarities, a direct comparison is not advised. Didymos likely experienced spin-breakup to form Dimorphos, while it is not clear if PN9 has previously broken up and reformed. While radar polarimetry can be used to reliably infer the surface roughness of small bodies (e.g. Hickson et al., 2021), caution should be taken in assuming the surface roughness of PN9 from its SC/OC ratio.

Additional analysis of PN9 was conducted by Dr. Sam Jackson (then-PhD student, Open University), to determine its absolute magnitude and optical albedo. Using the HG photometric system (Bowell et al., 1989), values of $H = 15.947 \pm 0.036$ and $G = 0.108 \pm 0.016$ were measured. Using a radar-derived diameter of $D_{eq} = 1.71 \pm 0.07$ km, PN9's optical albedo was determined to be 0.25 ± 0.02, which is consistent with the value previously reported by Belskaya et al. (2009). Further details of this analysis are provided in Dover et al. (2023). While these parameters are derived from phase curves of PN9, they should not be used to infer physical properties due to shape-induced

brightness modulation (Jackson et al., 2022).

4.5 Geophysical properties

A geophysical analysis of PN9 was conducted by Dr. Ben Rozitis (Open University), using the combined radar and lightcurve model. This analysis found that PN9 is quantitatively similar to Tantalus (Rożek et al., 2022), which is also a rapidly rotating top-shaped rubble pile. The analysis finds that a minimum bulk density of ∼2070 kg m^{-3} is required to prevent mass shedding, and cohesive strength of ∼50 Pa is needed to revent rotational breakup. The results of this analysis, which are descibed in Dover et al. (2023), are consistent with recent resurfacing due to YORP spin-up. Furthermore, any continued spin-up could lead to mass shedding or rotational breakup to form a secondary object.

The data contain no evidence to suggest that PN9 already has a natural satellite. While the presence of a secondary can be difficult to detect with optical imaging, radar observations are particularly effective at identifying multiple systems (e.g. Brozović et al., 2011; Taylor et al., 2019a). A preliminary analysis finds there are no consistent peaks in the continuous wave spectra, nor any visible satellites in delay-Doppler images. As a secondary would most likely have formed from a previous breakup of the primary, its composition - and hence albedo - would be comparable to that of the primary. Assuming a similar albedo to the primary, any object with a mean diameter above 19 m would have been detected in the radar imaging, as it would occupy more than one delay bin in the highest-resolution imaging sequences with a similar peak SNR to the primary. The orbital motion of a secondary would make it separated from the primary in delay-Doppler space, and the coverage rules out the possibility of an object being hidden behind the primary in every image. An object smaller than 19 m would only affect the photometric brightness of the system by a maximum of $\sim 10^{-4}$ magnitudes during its orbit around the primary, so optical detection would not be possible. Moons

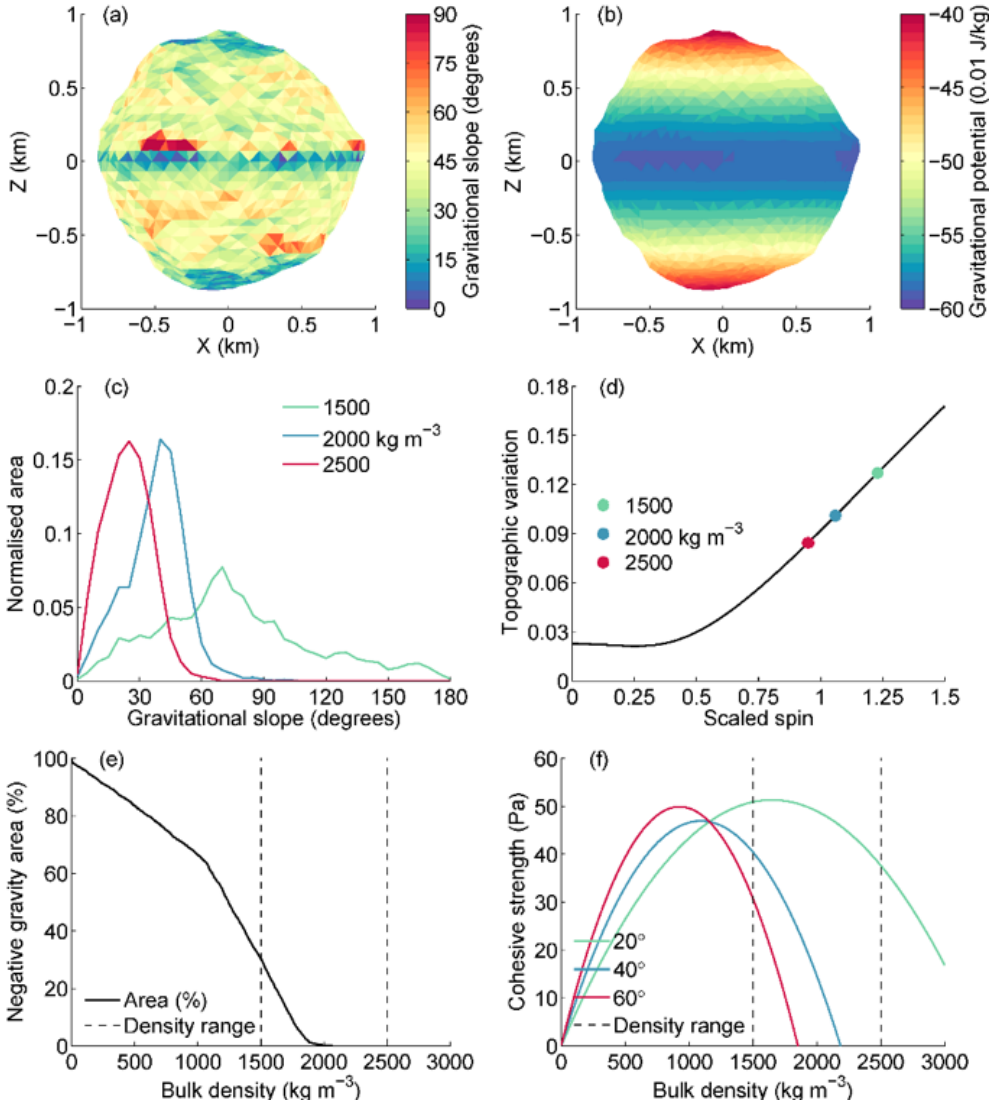

Figure 4.13: Geophysical analysis of asteroid (23187) 2000 PN9. (a) Gravitational slopes and (b) gravitational potential computed assuming a bulk density of 2000 kg m^{-3}. (c) Areal distribution from (a) for three different values of bulk density. (d) Topographic variation from (b) for three different values of bulk density. (e) Negative effective gravity area as a function of bulk density. (f) Cohesive strength as a function of bulk density and angle of friction. The vertical dashed lines in (e) and (f) show the bulk density range for a typical S-type rubble-pile asteroid. This figure was produced by Dr. Ben Rozitis (Open University).

of top-shaped asteroids typically have ∼1% of the mass of their primary (Hyodo and Sugiura, 2022). Assuming equal densities, in the case of PN9 this would correspond to a ∼370 m moon. A secondary of this size would be detectable in any of the radar imaging data.

The results of the geophysical analysis suggest two evolutionary paths that PN9 can follow. Recent reshaping may have reduced the magnitude of the YORP effect, halting spin acceleration and trapping PN9 in a state of equilibrium. Alternatively, if PN9 is still spinning up, it may soon begin to shed mass or break apart, after which it could form a small moon.

4.6 YORP analysis

A search for YORP was conducted using the phase offset analysis method described in Section 3.3.2. The combined optical and radar model presented in Section 4.3.2 was used to generate synthetic lightcurves using the techniques described in Section 3.3.1, assuming constant-period rotation. In this case, lightcurves were simulated using a combination of the Lambertian and Lommel-Seeliger models (Kaasalainen et al., 2001).These synthetic lightcurves were then compared to their corresponding observed lightcurves to search for offsets in rotational phase caused by YORP.

As PN9 is a highly symmetrical asteroid, brightness variations due to rotation are extremely small with lightcurve amplitudes often being as small as ∼0.05 magnitudes. Without observing clear turning points that can be reliably linked between lightcurves, it is difficult to detect a coherent progression in phase offsets caused by YORP. For example, in Figure A.12 there are clear turning points that repeat across multiple lightcurves, making it easy to see the progression in phase offset between lightcurves. Without these turning points to anchor the phase in observed lightcurves - as is the case with PN9 - the phase must instead be fitted to minor lightcurve features which can vary greatly with changes in viewing geometry.

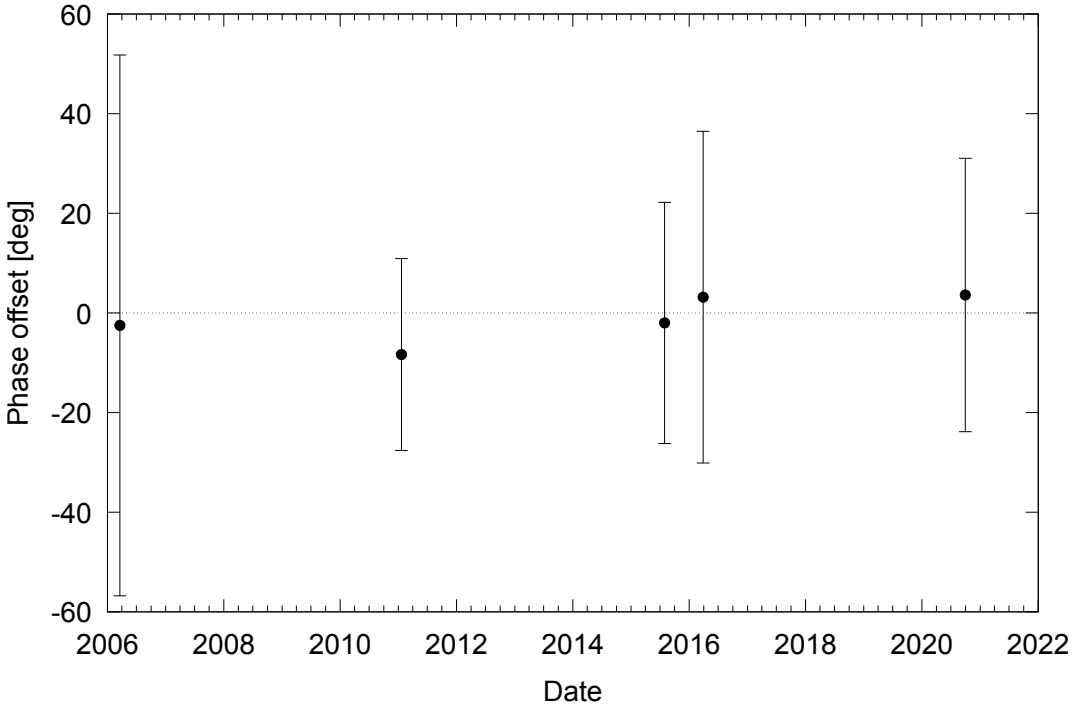

Figure 4.14: Phase offset measurements for the best-fit combined radar and lightcurve model of (23187) 2000 PN9 where T_0=2453815.29199 (March 2006). Phase offsets were measured against the 'ph. off' subset of lightcurves marked in Table 4.1. Phase offset measurements were averaged from groups of lightcurves, with groups being arranged such that there are a maximum of 180 days between consecutive lightcurves within a group. The straight dashed line represents a constant period model for reference.

PN9's lightcurves are extremely sensitive to surface detail and scattering parameters, so it is not always possible to identify turning points that repeat across both observed and synthetic lightcurves. There are, however, a small number of clear and repeated turning points within the optical dataset that can be used for a phase offset analysis.

Figure 4.14 shows the measured phase offsets for each epoch, where temporally clustered measurements are averaged. A total of 24 lightcurves were included in the YORP fitting process, which are indicated in 4.1. The excluded lightcurves produced unacceptably large phase uncertainties, generally due to the data being poor quality, or not offering sufficient rotational coverage to differentiate between peaks. The best-fit YORP strength for PN9 is $(0.2 \pm 1.6) \times 10^{-8}\,\mathrm{rad/day^2}$, which is comparable in magnitude to the smallest confirmed YORP detections (Table 1.1), and in line with

expectations for a ∼2 km asteroid. Although this measurement is poorly constrained, and it is not possible to rule out constant-period rotation, it does place an upper limit on YORP acceleration.

A case where YORP acceleration between each apparition induces close to 360° of additional rotation was also considered. This would produce an apparent phase offset of 0° at each apparition by bringing the asteroid's rotation back into phase with a constant-period model. For this to be the case, YORP acceleration would have to be close to an integer multiple of $4.8 \times 10^{-6}\,\mathrm{rad/day^2}$. This value is greater than the current strongest published YORP detection of $3.49 \times 10^{-6}\,\mathrm{rad/day^2}$ with (54509) YORP (Lowry et al., 2007; Taylor et al., 2007). Considering that the diameter PN9 is ∼15× greater than that of (54509) YORP, and that PN9 has high global symmetry, a YORP torque of this magnitude is considered to be unlikely. The analysis therefore finds no compelling evidence for ongoing rotational acceleration of PN9, within the limits of the data. This does not, however, discount the evidence of previous YORP spin-up discussed in Section 4.5.

4.7 Discussion

Both the convex inversion and `SHAPE` analyses show that PN9 is a YORPoid: it is a rapidly rotating rubble pile, it has a characteristic 'spinning top' shape and there are signs of resurfacing through YORP spin-up. Higher rates of YORP acceleration have been ruled out, but small torques could still be present and driving PN9 towards mass shedding or rotational breakup. Considering the mass and shape of PN9, it is more likely that PN9 is a case of YORP self-limitation. In either case, this characterisation of PN9 is a valuable addition to the small sample of known YORPoids.

4.7.1 YORPoids

YORPoids are believed to be ubiquitous within the inner Solar System, due to the rate they are being discovered through radar and spacecraft imaging. The number of well-modelled examples, however, is relatively low.

In addition to PN9, there are eleven top-shaped asteroids that have published models with full geometric parameters. These are summarised in Table 4.4. Some objects, such as (2867) Šteins (Keller et al., 2010) and (29075) 1950 DA (Busch et al., 2007; Zegmott, 2021) were excluded as their top-like shapes exhibit global asymmetries that differentiate them from more definitive examples such as Bennu (Lauretta et al., 2019a) or Moshup (Ostro et al., 2006). A larger number of YORPoid candidates have been identified, but they do not have publicly available models or geometric parameters. The author maintains an informal list of YORPoids which can be accessed online*.

In comparison to other YORPoids, several features of PN9 stand out. The majority of top-shaped asteroids listed in Table 4.4 are multiple systems. As discussed in Section 4.5, there is no evidence to suggest that PN9 has any satellites. To date, PN9 is the second largest top-shaped solitary asteroid with a fully developed shape model. In comparison to other top-shaped asteroids, PN9 has higher levels of global symmetry and a less pronounced equatorial ridge or bulge. This could be a result of PN9's greater mass, or the presence of internal cohesive forces.

*`https://www.lorddover.com/research/spintop`

Asteroid		Period [h]	Diameter [km]	Volume [km^3]	Rotational Pole (λ, β) [°]	Type	SC/OC	Multiplicity	Ref.
(2102)	Tantalus†	2.391	1.3	1.05	(180, +24)	Sr	0.19		1
(3200)	Phaethon‡	3.604	6.4	75	(316, -50)	B	0.19		2,3,4
(23187)	2000 PN9	2.532	1.82	2.627	(096, +30)	S/Sq/Q	0.23		this work, 5,6
(65803)	Didymos	2.260	0.84	0.249	(310, -84)	Sq	0.2	Binary	7,8,9
(66391)	Moshup§	2.765	1.53	1.195	(326, -65)	S	0.45	Binary	10,11
(101955)	Bennu	4.296	0.57	0.062	(086, -60)	B	0.18		12,13
(136617)	1994 CC	2.389	0.69	0.125	(336, +22)	Sq	0.40, 0.50	Triple	14
(153591)	2001 SN263	3.426	2.9	8.2	(309, -80)	B	0.17	Triple	15
(162173)	Ryugu	7.633	0.88	0.377	(179, -87)	Cg	N/A		16,17
(185851)	2000 DP107	2.775	0.99	0.337	(294, +78)	C	0.25	Binary	7,18,19,
(276049)	2002 CE26	3.293	3.65	21.7	(317, -20)	C	0.21	Binary	20
(341842)	2008 EV5	3.725	0.42	0.035	(189, -84)	C/X	0.38		21,22,23

Notes. "Period" is the sidereal rotation period of the asteroid. "Diameter" gives the maximum equatorial diameter. "Volume" is derived from the physical model of the asteroid. "Rotational Pole" denotes the spin-axis orientation of the asteroid in the ecliptic coordinate system. "Type" denotes the taxonomic classification(s) each asteroid has been given. "SC/OC", also known as the circular polarisation ratio, is the ratio between same circular and opposite circular polarised radar echo. "Multiplicity" denotes the number of known bodies in the asteroid system. Inclusion in this list is determined by the shape of the primary or 'Alpha' body, and physical parameters refer to the primary.
† Retrograde model; ‡ Values for the shape and spin-state are preliminary as of December 2022; § Also known as 1999 KW4.

References. (1) Rożek et al., 2022; (2) Marshall (priv. comm.); (3) Taylor et al., 2019b, (4) Green et al., 1985; (5) Thomas et al., 2014; (6) Binzel et al., 2019; (7) Benner et al., 2008; (8) Naidu et al., 2020; (9) Cheng et al., 2018, (10) Ostro et al., 2006; (11) Binzel et al., 2004; (12) Lauretta et al., 2019a; (13) Nolan et al., 2013; (14) Brozović et al., 2011; (15) Becker et al., 2015; (16) Watanabe et al., 2019; (17) Sugita et al., 2019; (18) Naidu et al., 2015; (19) Dandy et al., 2003; (20) Shepard et al., 2006; (21) Busch et al., 2011; (22) Somers et al., 2008; (23) Reddy et al., 2011

Table 4.4: Comparison of top-shaped NEAs with published physical models that are based on radar or spacecraft data.

Top-shaped asteroids are poor candidates for YORP detection. Their highly symmetrical shapes produce low-amplitude lightcurves that do not vary significantly between different viewing geometries. This makes it difficult to constrain the rotational pole and period, and increases the importance of accurate surface fitting and the performance of scattering models. While radar observations can somewhat mitigate the limitation, the only confirmed YORP detection on a top-shaped asteroid to date is derived from both radar and Hubble Space Telescope observations of (101955) Bennu (Nolan et al., 2019). Nevertheless, they may be crucial in distinguishing between components of NYORP, which is dominated by global shape, and TYORP, which is driven by irregularity across an asteroid's surface. Strong YORP detections on globally symmetric asteroids, which should have very small NYORP components, would imply a strong TYORP component. Separating the components of observational YORP detections can only be possible if both extremes are studied, as opposed to the current bias towards YORP analyses of highly asymmetric asteroids which have significant NYORP components.

As discussed in Section 1.3.2.1, the YORP effect is thought to be a key mechanism in the production of spinning-top rubble piles and multiple systems. Hirabayashi et al. (2020) conducted an analysis of the spin-driven evolution of (101955) Bennu and (162173) Ryugu, finding that reshaping at longer periods is driven by changes to surface structure, while reshaping at shorter periods is driven by the failure of internal structures.

Ryugu and Bennu, which are both C-complex asteroids, have measured bulk densities of 1190 kg m^{-3} (Scheeres et al., 2019; Watanabe et al., 2019). As an S-complex asteroid it is likely that PN9 has a higher density than this (Carry, 2012), which would suggest that a higher spin rate is required to induce rotational deformation. PN9's 2.53 h rotation period, which is close to the 2.2 h spin barrier for cohesionless asteroids (Pravec and Harris, 2000), favours the failure of internal structure being primarily responsible for any recent deformation PN9 has experienced.

YORP-driven deformation of near-Earth asteroids is likely to be self-limited by various mechanisms. As an asteroid approaches or crosses the spin-limit barrier, surface regolith may migrate from the poles towards the equator (Hirabayashi and Scheeres, 2019). In order to conserve angular momentum, the asteroid's period must increase, countering the YORP spin-up. Due to the YORP effect's strong dependence on shape, spin-driven reshaping into a more symmetrical top shape will decrease the strength of YORP torques. This self-governing must not occur in all cases, however, as it has been demonstrated that the YORP effect can form binaries through rotational breakup (Walsh et al., 2008).

Rotational breakup does not always produce a multiple system. Material can re-accrete towards the equator, producing an equatorial ridge (Hyodo and Sugiura, 2022), while the orbital evolution of satellites can lead to them migrating outward until they are lost. As PN9 is near-spherical and does not have a prominent equatorial ridge, there is no indication that it has previously experienced spin-breakup or lost a satellite.

It is also possible that PN9 is an example of an asteroid that is trapped in a state of rotational equilibrium, where normal and tangential YORP components enforce a constant rotation period over long time periods (Golubov and Scheeres, 2019). If a significant fraction of asteroids are found to have near-zero YORP acceleration, it would confirm the existence of 'sinks' that halt the YORP cycle. This would have a significant impact on theories of asteroid evolution. YORP equilibrium states are, however, expected to be seen in systems that are more physically complex than PN9 (Breiter and Murawiecka, 2015; Golubov et al., 2016).

4.7.1.1 Future work

In the next century, PN9 will not come within 100 lunar distances of Earth. This is beyond the range of current and near-future radar facilities, limiting any future observations to optical and infrared telescopes. The best opportunity to observe PN9 until at least 2030 will be from the northern hemisphere in mid-2025, when medium-sized

telescopes will be able to image the asteroid over several rotations. Larger northern telescopes should be able to image PN9 in early 2029, while facilities in the southern hemisphere are limited to the aforementioned mid-2025 apparition until after 2030. These observations could be used to better constrain PN9's pole and extend the baseline in the search for YORP, while any improvements to the physical model may improve upon the current phase offset measurements. It is unlikely that further ground-based observations will result in a YORP detection for PN9, however the current constraints could be significantly improved.

The non-detection of rotational acceleration of PN9, combined with its highly symmetrical shape and short rotation period, suggest that if it is indeed YORP-evolved then it is an example of self-limitation. In order to better understand the physical evolution of near-Earth asteroids, it is essential to understand the factors that determine if YORP spin-up of a rubble pile will self limit or continue past the spin-breakup barrier and form a binary. As YORPoids are unfavourable targets for YORP detection, analyses of objects that are in the late stages of YORP evolution are under-represented. Further study of these asteroids with future ground-based optical and radar facilities, as well as spacecraft observations, are essential to better understanding the influence of YORP on evolutionary pathways for small bodies.

CHAPTER 5

ROTATIONAL DECELERATION OF (29075) 1950 DA

5.1 Introduction

(29075) 1950 DA (herafter DA) is an Apollo-class asteroid that was discovered at Lick Observatory in February 1950 (Wirtanen and Vasilevskis, 1950), after which it was lost until its rediscovery in December 2000 at Lowell Observatory as 2000 YK66 (Ticha et al., 2001; Rogers et al., 2001). At the time of writing, DA has the second highest cumulative impact probability* out of all known PHAs and is thus one of the most well-known potential Earth impactors. DA has a 2.21 year period, a semi-major axis of 1.70 AU, an eccentricity of 0.51, an inclination of 12.2° and a MOID of 0.04 AU. Since its rediscovery in 2000, its closest approach was in 2001 at a distance of 20.3 lunar distances. Its next closest approach is in March 2032, when it will come within 29.5 lunar distances of Earth.

Shortly after its discovery, it was reported that there is a 0.04% chance of DA impacting Earth in 2880 (Giorgini et al., 2002). As discussed in Sections 1.3.1.1 & 1.3.2.1, non-gravitational forces can have a significant influence on impact probabilities. Various Yarkovksy drift rates have been measured for DA (Nugent, 2013; Farnocchia et al., 2013; Farnocchia and Chesley, 2014; Faggioli et al., 2016), which have reduced the 2880 impact probability to 0.003%†. These Yarkovsky measurements, which utilise radar observations, strongly favour a retrograde pole solution. Considering that the 2880 impact is highly dependent on Yarkovsky drift, which is itself dependent on YORP, it is especially important for DA to have its YORP acceleration measured.

As a prominent PHA, DA has been the subject of numerous studies. Rivkin et al. (2005) identified a lack of thermal emissions in the 2.5 μm region, which is attributed to a high (> 0.25) albedo or thermal beaming. A Tholen-system spectral type of E or M was suggested, although DA's spectrum closely resembled the X-type asteroid (3103) Eger. Later observations from NEOWISE, however, found DA's albedo to be 0.07±0.02 (Mainzer et al., 2011) with an estimated diameter of 2.0±0.2 km. These

*https://cneos.jpl.nasa.gov/sentry/

†https://cneos.jpl.nasa.gov/news/news208.html

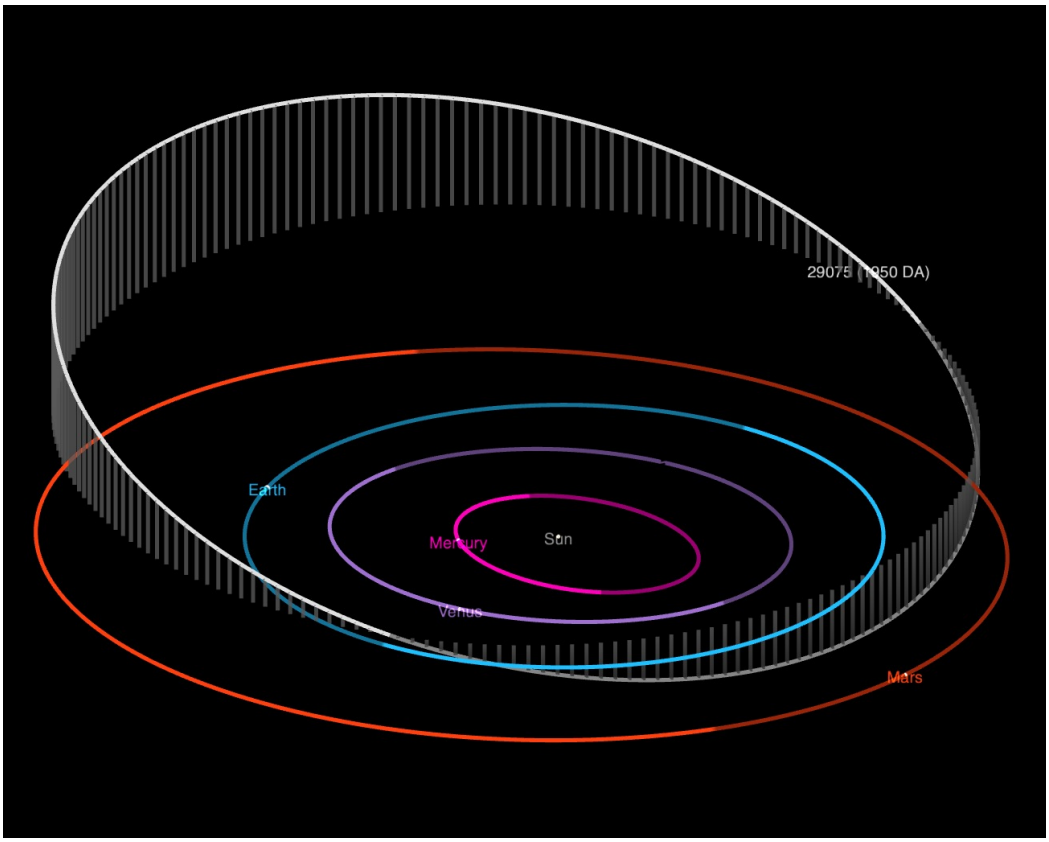

Figure 5.1: The orbit of (29075) 1950 DA, which is shown with a white line. The orbits of the inner planets are also marked, with the positions of each object shown for 2024-01-01. This figure was produced using the JPL Orbit Viewer[a].

[a] https://ssd.jpl.nasa.gov/tools/orbit_viewer.html

observations, along with a low SC/OC ratio, also ruled out an E-type classification.

Using the first optical lightcurves of DA, Pravec (2001) reported a period of 2.122 h, which is beyond the spin barrier for cohesionless rubble piles (Pravec and Harris, 2000), which was discussed in Section 1.2.2. Using a combination of lightcurve and radar observations, Busch et al. (2007) found two pole solutions - one prograde, and one retrograde - and published the corresponding shape models. The first model, with a pole at (88.6±5°, +77.5±5°) has a diameter of 1.16±0.12 km and a spheroid shape. The retrograde model has its pole at (187.4±5°, -89.5±5°), a diameter of 1.30±0.13 km with a slightly oblate shape. Both models have a period of 2.12160±0.00004 h.

Beyond the spin barrier, it is difficult to explain how DA could avoid catastrophic

disruption. If the asteroid was bound by gravity alone, it would need to be quasi-monolithic in order to reach the minimum density that is required to avoid spin-breakup. This would be not be consistent with measured bulk densities for other asteroids with comparable spectra and albedos, suggesting that other forces are at play.

Using the aforementioned retrograde model, Rozitis et al. (2014) investigated DA using the Advanced Thermophysical Model (Rozitis et al., 2013). A bulk density of 1.7±0.7 g cm^{-3} was determined, which is lower than the 3.5 g cm^{-3} that is necessary for gravity alone to prevent spin-breakup. Rozitis et al. (2014) concludes that cohesive forces, in form of small Van der Waals forces between constituent grains, are preventing the breakup of DA.

As part of the YORP campaign, a full analysis of DA was previously performed by then-PhD-student Dr. Tarik Zegmott and included in his thesis Zegmott (2021). The significance of Zegmott's results warranted a follow-up observing campaign and subsequent re-analysis, which form part of this work. This chapter will summarise the results from Zegmott's thesis (Zegmott, 2021), then present this author's continuation of the DA campaign. This work verifies and builds upon Zegmott's work, reinforcing a potentially major result that will continue to be investigated beyond this thesis before being written up for publication (Lowry et al. 2025).

5.1.1 Prior investigation

Between the YORP campaign and other observations, Zegmott assembled an optical dataset spanning from 2001 to 2019, which is detailed in Section 5.2.2. Radar observations from 2001 were also obtained, as described in Section 5.2.1.

Initially, a search for YORP was conducted using the existing models from Busch et al. (2007) with the newly expanded lightcurve dataset. Busch et al. (2007) noted that neither model was able to satisfactorily reproduce every lightcurve; this issue worsened when Zegmott used those models to construct synthetic lightcurves for post-2007 ob-

servations. Lightcurves generated with the Busch models showed a discrepancy in both phase and shape. The former could be caused by YORP, although this was not deemed to be the case due to the lack of any progressive offset. The shape of the synthetic lightcurves, more importantly, can only be wrong if the model does not accurately portray the shape and/or spin-state of the asteroid. This means that DA could have experienced a significant change in shape and spin-state between 2007 and 2019, which is plausible when considering the asteroid's rapid rotation. It is also possible that DA has unusually strong albedo features, which can make it difficult to reconcile optical and radar observations (Bartczak et al., 2024).

To resolve this, Zegmott first attempted to refine the existing radar models by re-fitting them to the new lightcurve data. At this point, the 2019 observations had not yet been conducted, so the 'new' lightcurve dataset only ran to 2014. Using `SHAPE` with the 2001 radar data and 2001-2014 lightcurves, Zegmott searched in regions around the two published pole solutions, using their corresponding shapes and periods as input values for `SHAPE`'s model parameters. This approach did not yield any noticeable changes to the models or lightcurve fits, so a decision was made to completely re-model DA 'from scratch'.

The development of a new model for DA is described in detail in Zegmott (2021). Initially, `convexinv` was used to conduct full pole and YORP scans by fitting to the 2001-2014 lightcurves. As the results did not converge towards any YORP plane, only constant-period models were considered. The best solution was a quasi-triangular shape model with its pole at λ=190 $\pm$ 5°, β=+34 $\pm$ 5°. Synthetic lightcurves generated using this convex model produce a better fit to the data than those generated using the previously published models, which are non-convex.

Similar to the development process for PN9 (Section 4.3), the results of convex inversion modelling were used to inform a `SHAPE` pole scan. Zegmott's analysis, however, went a step further. Utilising both the 2001-2014 optical data and the 2001 radar data, `SHAPE` was used to scan across YORP planes using the same logic as a `convexinv`

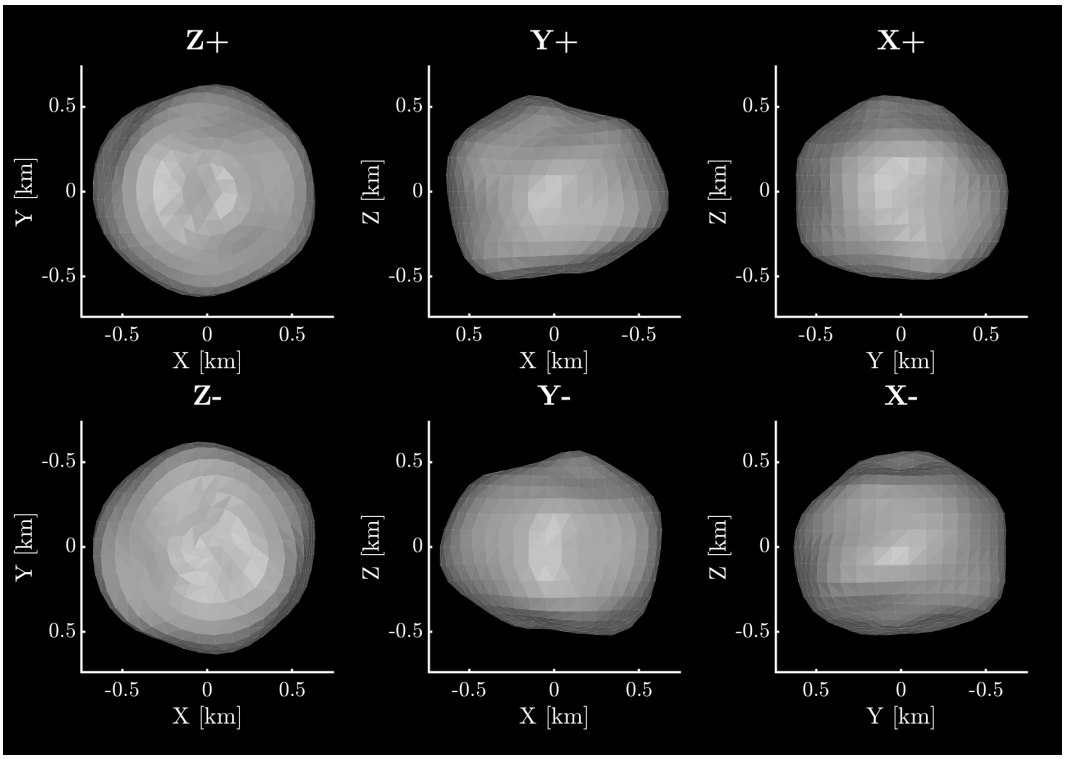

Figure 5.2: The best-fit shape model of (29075) 1950 DA, which was produced by Zegmott (2021) using a combination of radar and lightcurve data. This model has its rotational pole at ecliptic longitude $\lambda = 300°$ and ecliptic latitude $\beta = 0°$, and a sidereal rotation period of 2.121611 h. The top row shows the model from the positive end of the Z, Y and X axes in the body-centric co-ordinate system. The bottom row shows the model from the negative end of the Z, Y and X axes. The Z-axis is aligned with the rotational pole, which is the shortest axis of inertia. The X-axis is arbitrarily set such that it is viewed from the positive end for the plane-of-sky at T_0. Axis lengths are given in kilometres.

YORP scan. This `SHAPE` YORP scan did converge to a YORP plane, finding the best-fit model to be a highly oblate spheroid with its pole at λ=300 ± 30°, β=+0 ± 30° with a YORP acceleration of -2.1 ± 0.2×10^{-6} rad/day^2.

Using this model, a phase offset analysis was performed against the 2001-2019 lightcurves. The model was propagated forward at a constant period, ignoring the fitted YORP value. Fitting to the measured phase offsets, a rotational acceleration of -1.9 ± 0.4×10^{-5} rad/day^2 was measured. Note that this is an order magnitude greater than the value measured in the `SHAPE` YORP scan.

Facing a major disparity between the two primary methods to measure rotational

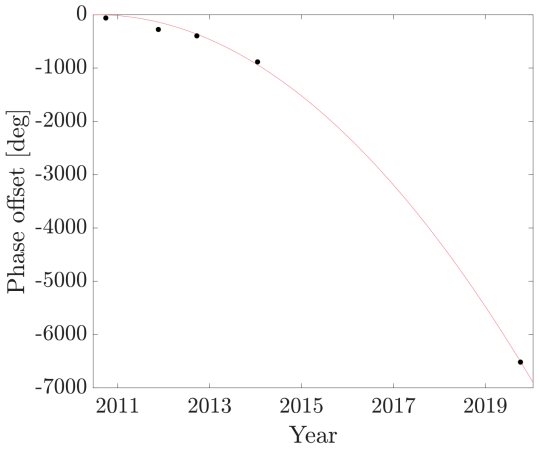

Figure 5.3: The (-2.0 ± 0.1)×10^{-5} rad/day^2 YORP fit resulting from Zegmott's analysis. The large phase offset values correspond to almost 20 full rotations that were 'lost' over ∼9 years due to DA's spin-down. This means that the phase offsets below -360° can be shifted by ±360°, but any reasonable fit will always result in a quadratic decrease in phase offset. This figure was reproduced from Zegmott (2021).

acceleration, but an indication that DA could be the first known case of YORP 'spin-down', Zegmott and YORP campaign collaborators - including this author - sought further observational data. Two observing runs were conducted in October 2019, on the INT and Nordic Optical Telescope (NOT). While Zegmott was still leading the analysis, the author of this work was the lead observer for the INT run.

With the lightcurve dataset now expanded to cover 2001-2019, Zegmott conducted a new `convexinv` YORP scan. This time, it did converge towards a YORP value of (-3.6 ± 0.8)×10^{-6} rad/day^2 with a pole of λ=35 ± 10°, β=-25 ± 10°.

Using the same radar model, the phase offset analysis was repeated with the addition of the 2019 lightcurves. This produced a new fit of (-2.0 ± 0.1)×10^{-5} rad/day^2. For clarity, Zegmott's various YORP measurements are summarised alongside new results in Table 5.2.

The addition of 2019 data thus compounded the problem: both `convexinv` and `SHAPE` YORP scans find a spin-down on the order of 10^{-6} rad/day^2, but phase offset analyses of the same models produce torques on the order of 10^{-5} rad/day^2.

For the higher rates of spin-down, phase offsets would exceed 360° between observations. This means that, for example, a relative phase offset of -400° could be interpreted as an offset of -40°, or vice versa. This means that different methods for measuring YORP cannot be expected to produce consistent results, as there is more than one

viable YORP solution for a given model. Noting this, Zegmott concluded that more observations should be taken over a short baseline (< 2 yr) to either verify or rule out the rapid spin-down scenario by constraining the gradient of phase offsets. The fact that all analyses consistently produced a negative acceleration is significant, as DA would be the first asteroid known to be experiencing YORP 'spin-down', with major implications for YORP theory.

5.2 Follow-up campaign

Following Zegmott's results, the author lead the preparations for a follow-up observing campaign to take place in 2021. The aim of this campaign was to determine which of Zegmott's two YORP solutions is valid, and if possible, produce a robust YORP spin-down measurement that is worthy of publication.

As previously discussed, baselines that are too long can be problematic as the asteroid can exceed one full additional rotation and briefly come back into phase with a constant-period model. While this can be resolved by manually shifting phase offset measurements by integer multiples of 2π, it becomes problematic when the entire curve is being fit to human-adjusted measurements. It is possible for there to be more than one combination of $2n\pi$ shifts that can be applied to produce a quadratic curve, resulting in multiple YORP solutions.

To avoid this issue, the follow-up campaign was designed so that observations in 2021 would only need to be combined with the October 2019 lightcurves to produce a well-constrained YORP fit. This keeps the maximum phase offset below 360° for the 10^{-5} rad/day^2 solution, while still providing enough of a baseline to constrain YORP in the case of the 10^{-6} rad/day^2 solution. An additional benefit of this strategy is that it means the new analysis will hinge upon new data, so it rules out the possibility of the result being a false positive caused by an undetected problem with the 2001-2014 lightcurve data.

To optimise observing time, the majority of observing proposals focused on the end of 2021, where the expected phase offset curve would be steepest and thus easier to constrain. To test this, projected phase offsets curves were plotted for a period spanning 2019-2021 to verify that new measurements could be used to differentiate between the two solutions. This is demonstrated in Figure 5.4, where projected phase offsets are shown for both YORP solutions, along with predicted phase offset measurements for each of the observing runs that ultimately took place. When planning the observing campaign, various combinations of proposed observing runs were used to test for different time allocation outcomes.

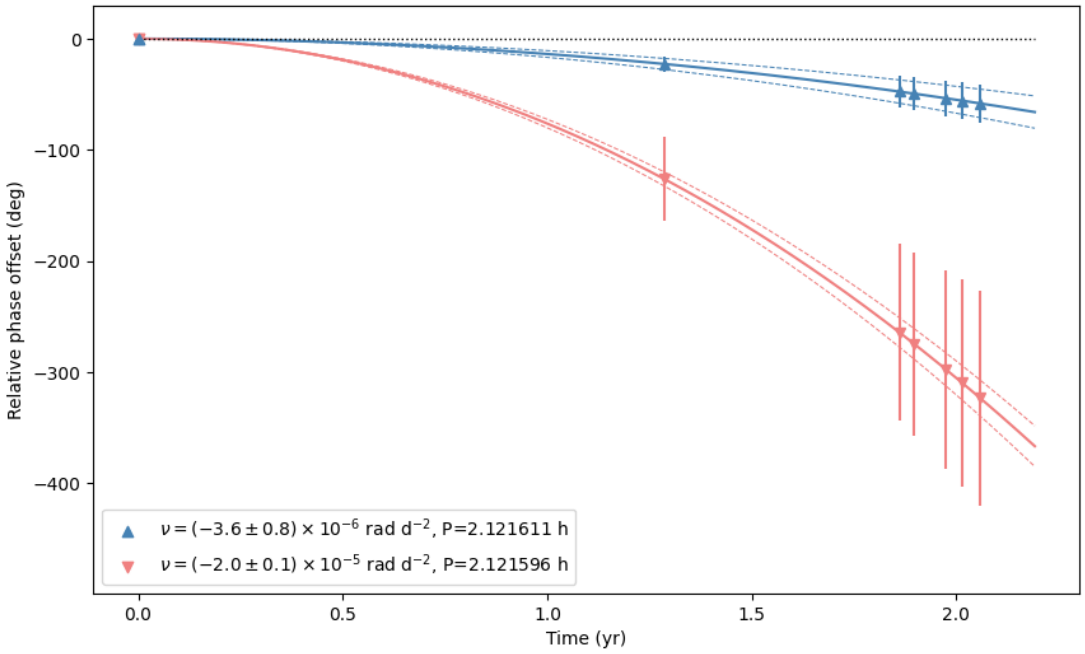

Figure 5.4: Projected phase offsets for 1950 DA, for both of the YORP solutions found by Zegmott (2021), from October 2019 to December 2021. The markers indicate the predicted phase offset measurements for both YORP solutions, with measurements corresponding to observing runs that took place for the follow-up campaign. For each YORP solution, uncertainty in projected phase offset is shown with a dashed line, and predicted phase offset measurements have been given a pessimistic uncertainty of 30%. Better measurements were expected, but 30% was chosen to demonstrate that even the 'worst case' measurements would be sufficient to differentiate between the two solutions. A dashed black line shows the case for constant-period rotation. This figure shows that the observing campaign should produce phase offset measurements that can be used to rule out one of the two YORP solutions, which are clearly differentiated in phase offset space.

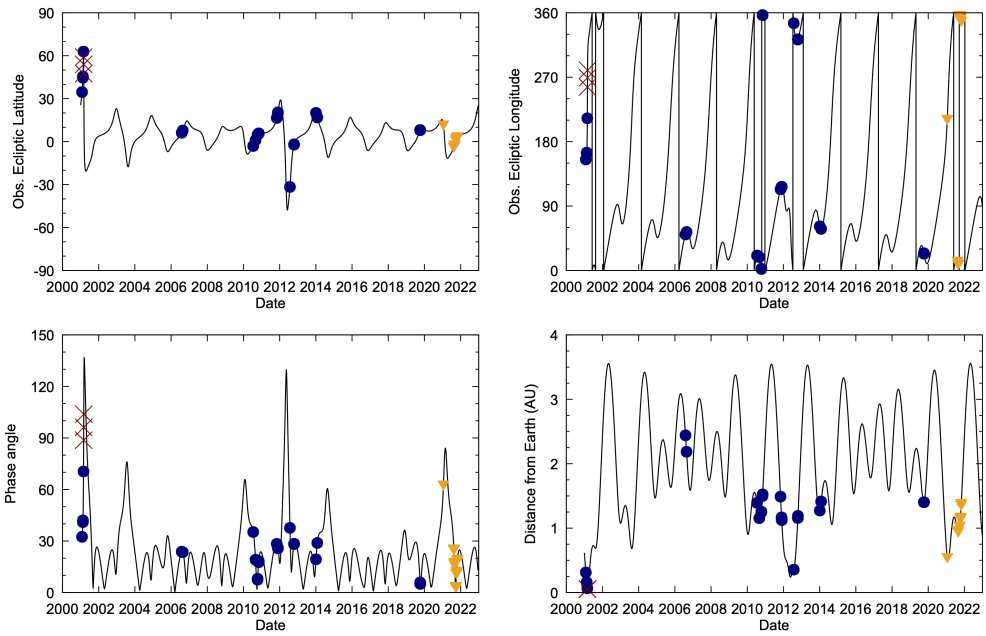

Figure 5.5: Observing geometries for (29075) 1950 DA from 2000 to the end of 2022. The top panels show the position of the asteroid in the ecliptic coordinate system (latitude and longitude) as observed from Earth. The bottom left panel shows the solar phase angle while the bottom right panel shows the geocentric distance to the asteroid. The marked points denote observations of the asteroid. Optical lightcurves taken during the original campaign (2000-2019) are marked as blue circles, and as orange triangles for the 2021 follow-up campaign. Radar observations are represented by red crosses.

The follow-up campaign, which took place in 2021, utilised a number of telescopes which are detailed below.

Isaac Newton Telescope – Three observing runs were planned for the INT. The first run took place in January 2021, however it was reduced to less than one full night due to a mix of poor weather and technical issues. A second observing run in August was successfully used to observe DA over three nights. A third observing run was scheduled for mid-October, however this was totally lost due to the Cumbre Vieja volcanic eruption. The telescope configuration and data reduction procedures are the same as described in Sections 2.2.1.1 & 4.2.1.

New Technology Telescope – There were two NTT runs for the follow-up campaign, in August and September 2021. Both of these runs were executed successfully, with the telescope configuration and reduction procedures being the same as described in Sections 2.2.1.1 & 4.2.1.

William Herschel Telescope – Eight hours of service-mode were awarded for the 4.2 m WHT (La Palma, Spain). These were scheduled for August, but ultimately no observations were executed due to a revised engineering schedule.

Very Large Telescope – Two runs were awarded on the 8.2 m VLT at Paranal Observatory (Chile). The first run, which took place in early October, was 2×0.75 nights. A second run at the end of October was for 2×0.50 nights. These observations utilised the *Antu* Unit Telescope (UT1) with the FORS2 instrument in imaging mode to conduct V filter observations. The telescope and instrument are described in further detail in Section 2.2.1.1.

The follow-up campaign produced a total of 55.6 hours of observations over 12 nights, averaging 1.6 rotations per lightcurve. Details of both the 2001-2019 and 2021 datasets are provided in Figure 5.5 and Table 5.1. Lightcurves from the 2021 observations were extracted by then-undergraduate student Ioannis Apergis (University of Kent), under the close supervision of Stephen Lowry. The author converted those lightcurves into the appropriate formats for analysis.

Two INT lightcurves were not included in the analysis, due to an issue with the CCD shutter which caused unknown exposure times across the field. One lightcurve each from the NTT and VLT were also not included, as poor weather lead to unacceptably low SNR on the target. The absence of these four lightcurves does not significantly affect the analysis, as other nights were successful during their respective runs.

ID	UT date [yyyy-mm-dd]	$R_\odot$ [AU]	$\Delta_\oplus$ [AU]	α [°]	λ_O [°]	β_O [°]	Total [hour]	Obs. facility	Filter	TJZ	LD	Reference
1	2001-01-29	1.235	0.313	32.46	155.1	34.6	1.6	Ond	R	•	•	1
2	2001-02-15	1.104	0.162	41.00	163.7	44.6	3.4	Ond	R	•	•	1
3	2001-02-16	1.097	0.154	42.03	164.7	45.5	8.1	Ond	R	•	•	1
4	2001-02-28	1.011	0.067	70.51	212.7	62.9	2.1	Ond	R	•	•	1
5	2006-08-03	2.481	2.441	23.78	50.3	6.2	4.2	PAL	R	•	•	2
6	2006-08-24	2.516	2.186	23.52	53.8	7.8	2.6	PAL	R	•	•	2
7	2010-07-16	1.759	1.392	35.26	20.9	-3.1	2.5	NTT	R	•	•	
8	2010-08-31	2.027	1.155	19.12	18.6	1.0	2.5	NTT	R	•	•	
9	2010-10-12	2.222	1.248	7.50	2.3	4.8	1.9	NTT	R	•	•	
10	2010-10-13	2.226	1.256	8.05	2.0	4.9	1.6	NTT	R	•	•	
11	2010-11-04	2.309	1.498	17.66	356.8	5.7	3.2	PAL	R	•	•	
12	2010-11-06	2.315	1.524	18.29	356.6	5.8	1.1	PAL	R	•	•	
13	2011-11-03	2.007	1.489	28.36	113.3	16.5	0.6	KPNO	R	•	•	3
14	2011-11-24	1.889	1.167	26.24	116.8	19.9	3.1	PAL	R	•	•	
15	2011-11-26	1.877	1.139	25.89	116.9	20.3	1.4	PAL	R	•	•	
16	2011-11-27	1.871	1.125	25.71	117.0	20.5	2.8	LT	V	•	•	
17	2012-07-27	1.274	0.356	37.65	345.4	-31.6	2.1	NTT	R	•	•	
18	2012-10-17	1.854	1.158	28.19	322.6	-2.1	2.5	NTT	V	•	•	
19	2012-10-19	1.866	1.19	28.42	323.0	-1.9	1.7	NTT	V	•	•	
20	2014-01-03	2.089	1.273	19.34	61.7	20.1	1.6	INT	r'	•	•	
21	2014-01-30	1.948	1.414	28.87	58.1	16.9	2.2	PAL	R	•	•	
22	2019-10-06	2.384	1.401	5.89	24.2	8.0	4.1	NOT	V	•	•	
23	2019-10-06	2.384	1.401	5.89	24.2	8.0	6.5	INT	V	•	•	
24	2019-10-07	2.387	1.402	5.45	23.8	8.1	7.2	NOT	V	•	•	
25	2019-10-07	2.387	1.402	5.45	23.8	8.1	6.6	INT	V	•	•	
26	2019-10-08	2.389	1.403	5.03	23.4	8.1	6.6	INT	V	•	•	
27	2021-01-19	1.103	0.547	62.96	212.0	11.9	3.2	INT	V		•	
28	2021-08-16	1.799	0.971	25.47	13.4	-3.6	2.1	NTT	V		•	

Table 5.1: All optical lightcurves of 1950 DA that were considered for this work (continues)

ID	UT date [yyyy-mm-dd]	$R_\odot$ [AU]	$\Delta_\oplus$ [AU]	α [°]	λ_O [°]	β_O [°]	Total [hour]	Obs. facility	Filter	TJZ	LD	Reference
29	2021-08-17	1.804	0.968	24.97	13.2	-3.5	1.5	NTT	V		•	
30	””	””	””	””	””	””	3.1	NTT	V		•	
31	2021-08-28	1.871	0.949	17.94	9.6	-2.2	3.4	INT	V			
32	2021-08-29	1.877	0.949	17.24	9.2	-2.1	5.6	INT	V			
33	2021-08-30	1.883	0.949	16.53	8.8	-2.0	3.8	INT	V		•	
34	””	””	””	””	””	””	1.6	INT	V		•	
35	2021-09-27	2.038	1.040	3.88	356.4	1.4	4.5	NTT	V		•	
36	2021-09-28	2.043	1.047	4.53	356.0	1.5	4.3	NTT	V			
37	2021-10-09	2.102	1.154	11.64	351.9	2.6	3.9	VLT	V		•	
38	2021-10-10	2.103	1.156	11.75	351.9	2.6	1.9	VLT	V		•	
39	2021-10-12	2.116	1.187	13.17	351.1	2.8	7.3	VLT	V		•	
40	2021-10-27	2.184	1.376	19.22	348.5	3.7	2.2	VLT	V		•	
41	””	””	””	””	””	””	2.6	VLT	V		•	
42	2021-10-29	2.192	1.404	19.83	348.4	3.7	4.6	VLT	V			

Notes. Each lightcurve has a chronologically assigned ID, then the UT date at the beginning of the night, the heliocentric ($R_\odot$) and geocentric ($\Delta_\oplus$) distances in AU, the solar phase angle (α), the observed ecliptic longitude (λ_O), the observed ecliptic latitude (β_O), the total time over which the target was observed, the observing facility and the photometric filter. Points in the ‘TJZ’ column indicate which lightcurves were included in Zegmott’s analysis, and points in the ‘LD’ column indicate lightcurves that were included in this analysis. References to published lightcurves are listed. Observing facility key: Ond – Ondřejov Observatory 2.0 m Telescope (557 - Czechia); PAL – Palomar Observatory 5.1 m Hale Telescope (675 - California, USA); NTT – European Southern Observatory 3.6 m New Technology Telescope (809 - La Silla, Chile); KPNO – Kitt Peak National Observatory 4.0 m Telescope (695 - California, USA); LT – 2.0 m Liverpool Telescope (950 - La Palma, Spain); INT – Isaac Newton Group 2.54 m Isaac Newton Telescope (950 - La Palma, Spain); NOT – 2.56 m Nordic Optical Telescope (950 - La Palma, Spain); VLT – 8.2 m Very Large Telescope *Antu* (309 - Cerro Paranal, Chile).
References. (1) Pravec (2001); (2) Busch et al. (2007); (3) Gwyn et al. (2012)

Table 5.1: (continued)

5.2.1 Phase offset analysis

As planned, a phase offset analysis was conducted using the new campaign lightcurves in combination with the October 2019 data. This analysis, which is shown in Figure 5.7, results in a YORP fit of (-2.1±0.3)×10^{-5} rad/day^2 (P=2.121578 h), which is in agreement with the (-2.0±0.1)×10^{-5} rad/day^2 result (P=2.121596) found by Zegmott. The larger uncertainty is to be expected, as the follow-up campaign data only have a baseline of two years.

This phase-offset indicates that a -10^{-6} rad/day^2 solution can be ruled out, and means that rotational deceleration has been measured using both the 2001-2014 and 2019-2021 datasets. This is an important verification of the result, and shows that the measured acceleration is indeed constant and not the result of impulsive spin changes that coincidentally form a quadratic curve in phase offset diagrams.

It should be noted that due to the handling of T_0 in the routines used to measure phase offsets, the measured phase offset is not zero for the start of the 2019 data. To address this, measurements in Figure 5.7 are shown relative to the first phase offset measurement, instead of as absolute measurements. This does not affect the YORP fit, but means that the plotted relative phase offsets don't correspond to the absolute measured phase offset for each lightcurve.

The single lightcurve in January 2021 is critical to this new torque measurement. As shown in Figure A.10, this particular lightcurve is not an especially good fit. For this reason, and in consideration of the implications of reporting such a rapid spin-down, the author is reluctant to call it a robust detection. Nevertheless, it is an important development that furthers a major result using a novel observing strategy to measure rotational acceleration over short time periods.

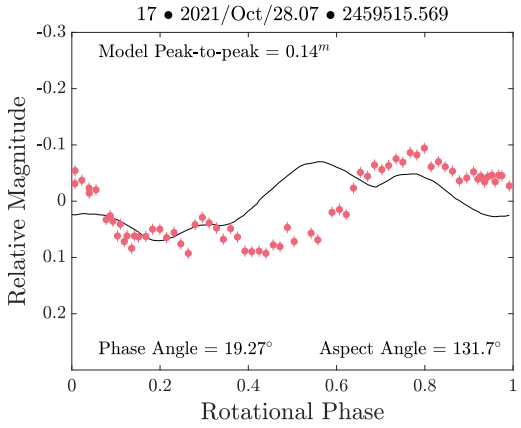

Figure 5.6: A comparison of observational data (red points) and the corresponding synthetic lightcurve (solid black line) for lightcurve 41 in Table 5.1. The synthetic lightcurve was generated using the radar model from Zegmott (2021), with a combination of the Lambertian and Lommel-Seeliger scattering models. The model was propagated forward with a constant period, meaning that the visible phase offset is due to 1950 DA's rotational acceleration. For plots of all 17 lightcurves from the follow-up campaign, see Figure A.10.

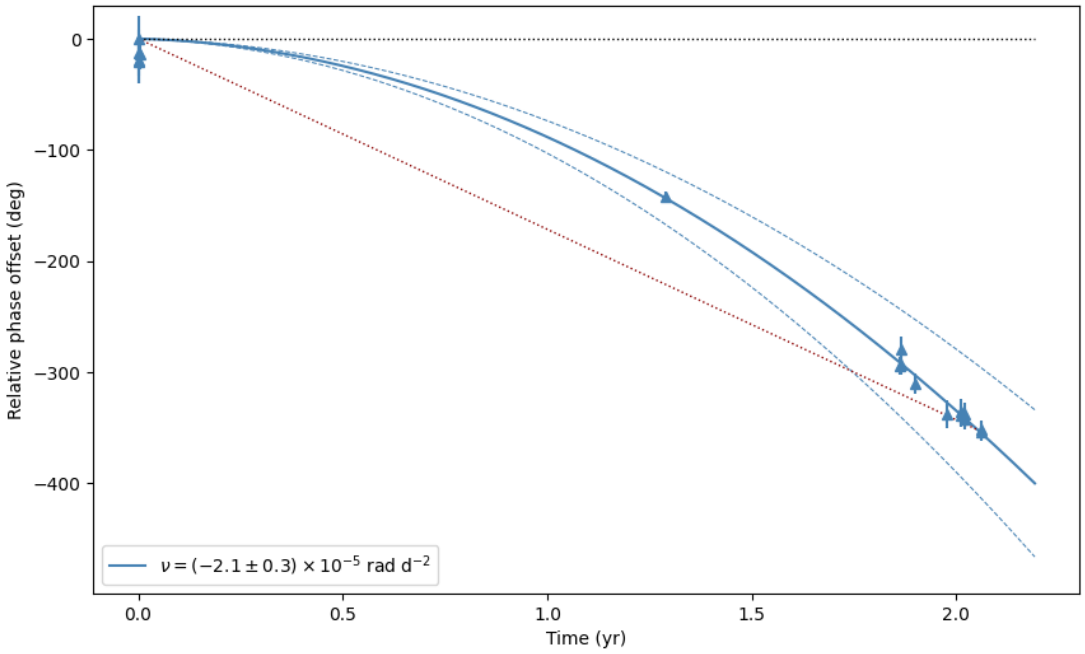

Figure 5.7: Phase offsets for (29075) 1950 DA, measured using the 2019-2021 lightcurves and the combined lightcurve and radar model from Zegmott (2021). These phase offset measurements correspond to lightcurves 22-30, 33-35, and 37-41 in Table 5.1. Blue triangular markers indicate phase offset measurements for individual lightcurves, with the fit and its uncertainty plotted with solid and dashed blue lines respectively. A dashed red line connects the first and last measurement to highlight the YORP fit's deviation from a linear trend. A dashed black line shows the case where there is zero rotational acceleration.

5.2.2 Convex inversion analysis

The phase offset analysis in Section 5.2.1 still relies upon a shape model that was developed using data taken between 2001-2014. Considering the significance of the result, the author opted to develop a new shape model using the full 2001-2021 dataset. Searching for rotational acceleration with an independently-developed model and an improved lightcurve dataset would produce results that either reinforce or contradict the results of Section 5.2.1.

Developing a new radar model is both time and resource intensive, and was ultimately not feasible within the scope of this work. Instead, a full convex inversion analysis was conducted where DA was treated as a 'new' asteroid to avoid biasing the result by taking parameters from previous models. Alongside this analysis, attempts were made to model DA using various subsets of the full 2001-2021 dataset, such as 2014-2021. None of these subsets were sufficient for an analysis, aside from the same 2001-2014 set that Zegmott used for his convex inversion analysis.

Using all the lightcurves indicated in Table 5.1, a wide period scan was conducted between 1 h and 11 h. Two potential solutions were found, near 2.12 h and 4.24 h. High resolution follow-up scans were conducted around these minima, ultimately resulting in a period of 2.1220 ± 0.0002 h. The combined results of these scans are shown in Figure 5.8.

Using this period, a full YORP scan was conducted using the methods previously described in Sections 3.1.3 & 3.1.4. This search covered a $5^\circ \times 5^\circ$ grid of poles and a YORP range of -3.0×10^{-5} rad/day^2 to 3.0×10^{-5} rad/day^2 in steps of 10^{-7} rad/day^2.

In this initial scan, which is shown in Figure 5.9, the goodness-of-fit of converged across YORP planes toward two solutions, with one near zero and the other close to -2×10^{-6} rad/day^2. Follow-up scans probed around these minima in higher resolution; the final 'YORPogram' is shown in Figure 5.10. The overall best model for DA has a YORP factor of $(-2.6 \pm 0.1) \times 10^{-6}$ rad/day^2, which is comparable to Zegmott's

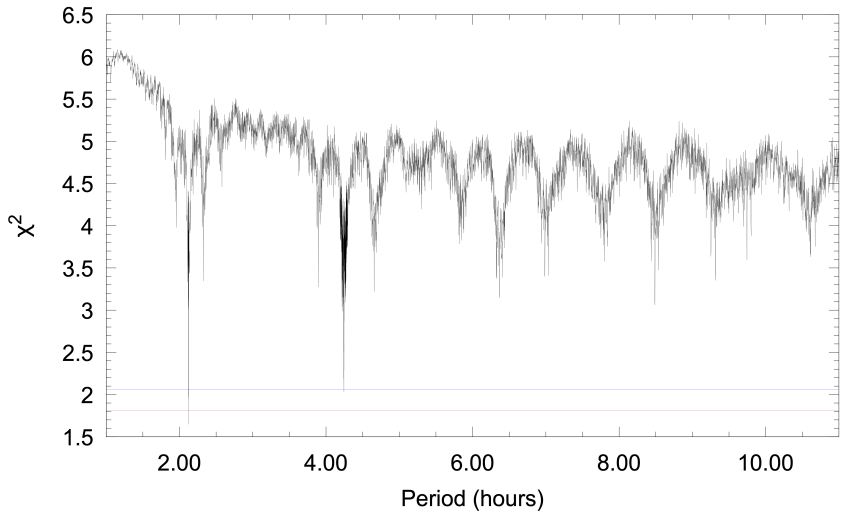

Figure 5.8: The results of a period search for asteroid (29075) 1950 DA. For each period in the range shown, lightcurve data were used to optimise a model for six different rotational poles in the celestial sphere. The lowest χ^2 across the six models was recorded for the period being used. The best-fit sidereal rotation period for 1950 DA from this scan is 2.1220 ± 0.0002 h. The red and blue lines correspond to increases of 10% and 25% over the minimum χ^2 respectively.

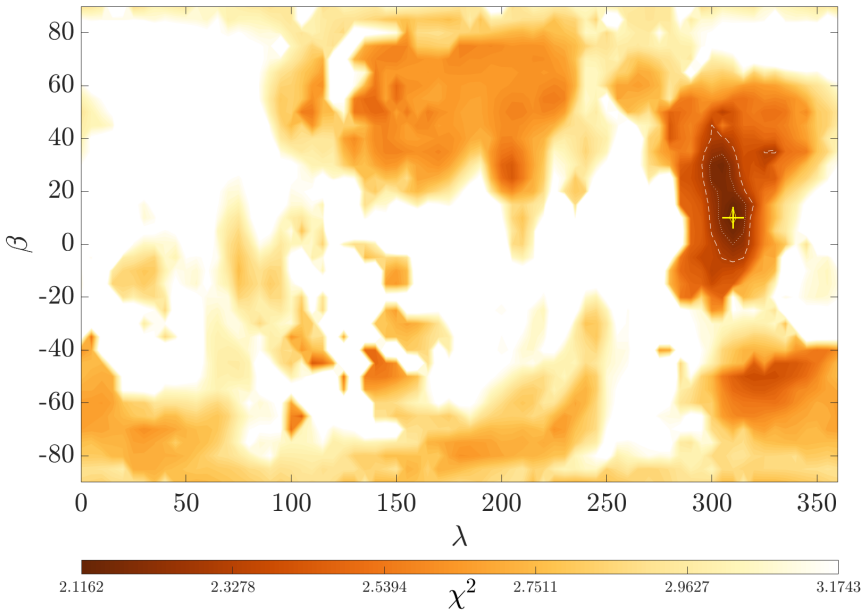

Figure 5.9: The results of a pole scan for (29075) 1950 DA using convex inversion of lightcurve data. For each pole solution in ecliptic coordinates λ and β, the χ^2 fit of the solution is plotted for a colour range where the global minimum χ^2 is black and solutions 50% greater than the minimum are white. The best solution, at (310±30°, 10±30°), is marked with a yellow '+'. The yellow line and the white dotted and dashed lines enclose regions where χ^2 is within 1%, 5% and 10% of the best solution respectively.

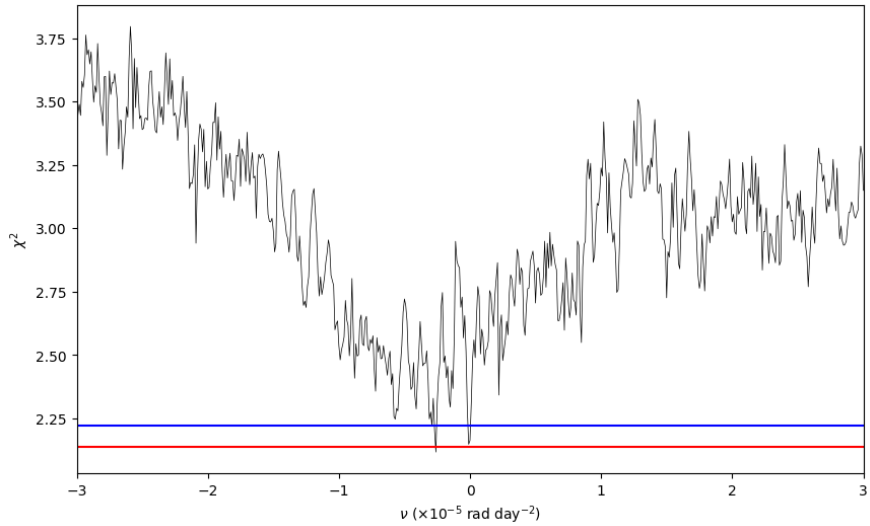

Figure 5.10: A YORPogram of 1950 DA. For each YORP step (or 'plane') a full `convexinv` pole scan was conducted using the corresponding YORP value as a fixed parameter. The χ^2 fit from each YORP plane's best-fitting model is shown. The best achievable fit converges across YORP planes towards two minima at -2.6×10^{-6} rad/day^2 and -0.1×10^{-6} rad/day^2. The red and blue lines correspond to 1% and 5% increases in χ^2 over the global minimum, respectively.

convex inversion YORP scan which found $(-3.6 \pm 0.8) \times 10^{-6}$ rad/day^2, but an order of magnitude smaller than results from various phase offset analyses. It was not possible to rule out the zero-YORP solution, although the spin-down model is the better fit.

The physical parameters of the spin-down model are consistent with other DA models; it is an oblate spheroid with a period of 2.1215 h and its pole at $\lambda = 310°$, $\beta = +10°$. This model is shown in Figure 5.11. The zero-YORP model has an almost identical shape and spin rate, but has a dissimilar pole solution at $\lambda = 195°$, $\beta = +70°$.

As previously discussed, the fact that `convexinv` produces a 10^{-6} rad/day^2 solution is likely to be a consequence of the asteroid's spin-down causing there to be several 'missed' rotations within the 20 yr baseline. Any initial period uncertainty will propagate through each additional 2π phase shift, meaning that uncertainties can increase with the YORP strength the model is being fitted to. This may create a bias where models fit to smaller YORP values will have inherently lower χ^2 value. This could only happen in cases where the real YORP strength and observational baseline are great

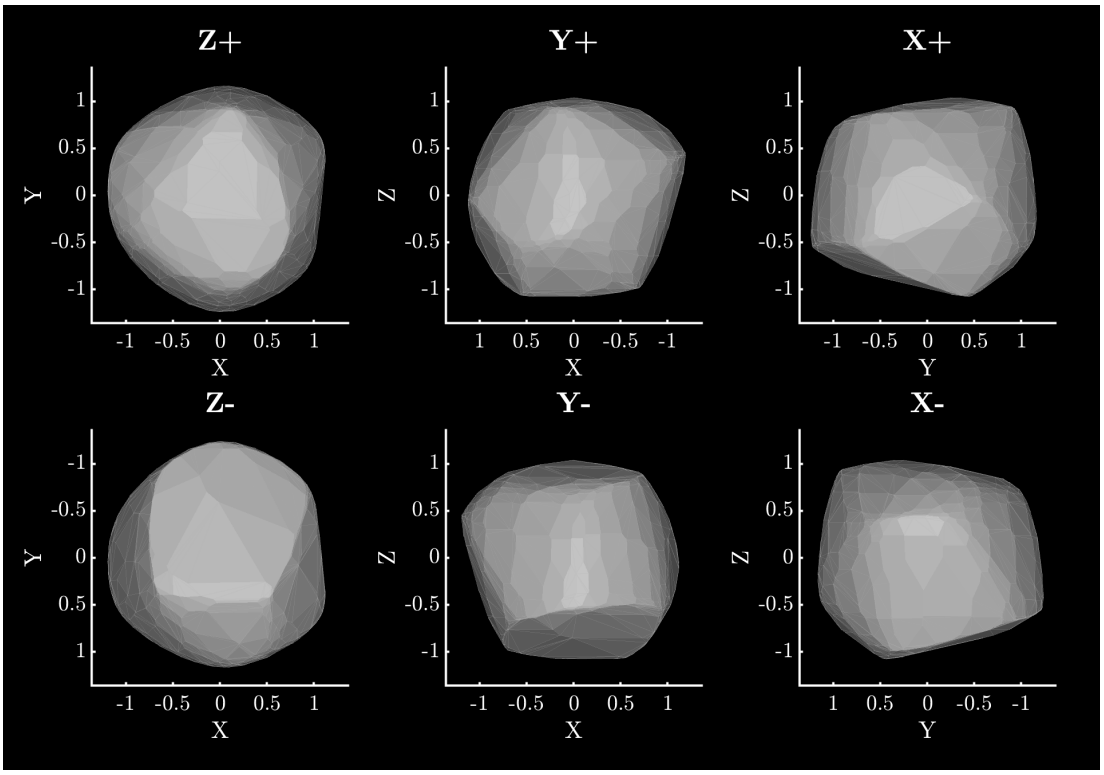

Figure 5.11: The best-fit convex hull model of (29075) 1950 DA with the rotational pole $\lambda = 310°$, $\beta = +10°$. This model assumes principal-axis rotation with an initial period of 2.1215 h and has a constant rotational acceleration of -2.6×10^{-6} rad/day^2. The top row shows the model from the positive end of the Z, Y and X axes in the body-centric co-ordinate system. The bottom row shows the model from the negative end of the Z, Y and X axes. The Z-axis is aligned with the rotational pole, which is the shortest axis of inertia. The X-axis is arbitrarily set such that it is viewed from the positive end for the plane-of-sky at T_0. Axis lengths are in arbitrary units, as lightcurve inversion does not produce scaled models.

enough that the asteroid has lost or gained several full rotations within the dataset. It is possible that DA is the first instance of this edge case limitation for convex inversion YORP scans.

Considering this, and recognising that a 10^{-6} rad/day^2 solution is wholly incompatible with the results from Section 5.2.1, the solution from this scan should not be taken as a reliable YORP measurement.

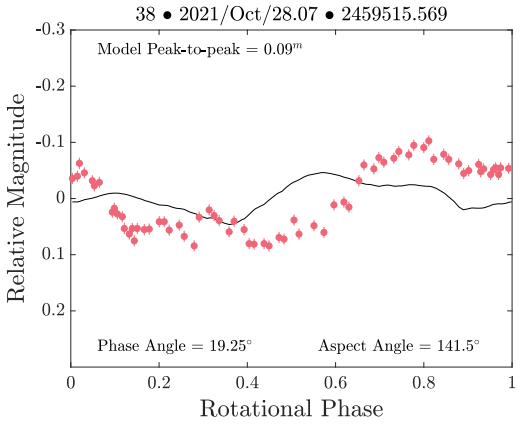

Figure 5.12: A comparison of observational data (red points) and the corresponding synthetic lightcurve (solid black line) for lightcurve 41 in Table 5.1. The synthetic lightcurve was generated using the new convex hull model for 1950 DA, with a combination of the Lambertian and Lommel-Seeliger scattering models. The model was propagated forward with a constant period, meaning that the visible phase offset is due to 1950 DA's rotational acceleration. For plots of all 38 lightcurves that were used to fit the model, see Figure A.11.

5.2.2.1 Phase offsets with the convex model

Using the newly developed convex model, a phase offset analysis was conducted using the 2019-2021 lightcurves. This is effectively a repeat of the analysis from Section 5.2.1, to investigate if the new model produces a result that is in agreement with the radar model.

In this case, phase offset measurements were grouped using a minimum separation of ten days, and then an average was calculated for each group. This was necessary due to the larger phase offset uncertainties when measuring against a convex shape.

As shown in Figure 5.13, this analysis produces a YORP fit of (-1.1±0.5)×10^{-5} rad/day^2. This is just beyond agreement with the results from Section 5.2.1, but again on the order of 10^{-5} rad/day^2. Similar to 2000 PN9 (see Section 4), DA produces low amplitude lightcurves that convex shape models struggle to reproduce, hence the larger uncertainty.

This result underscores the better-constrained (-2.1±0.3)×10^{-5} rad/day^2 measurement from the radar model, providing further evidence that DA is experiencing a rapid spin-down.

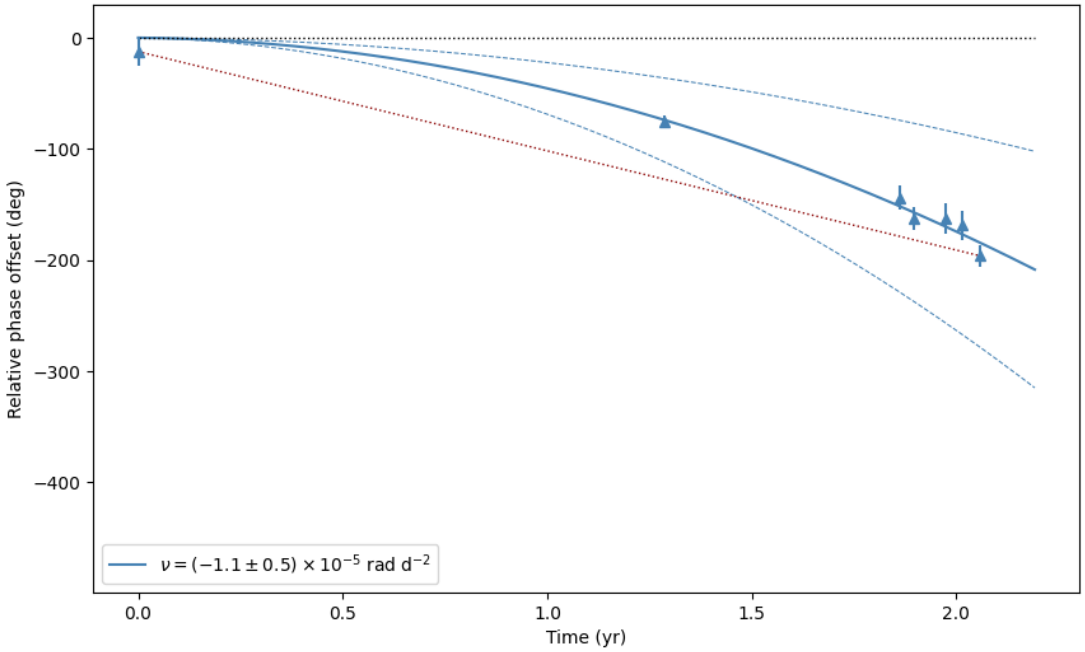

Figure 5.13: Phase offset measurements for the new convex hull model of (29075) 1950 DA. These phase offset measurements correspond to averaged phase offsets using lightcurves 22-26, 27, 28-30, 31, 32, 33-36, and 37-38 from Table 5.1. Blue triangular markers indicate these measurements, with the fit and its uncertainty plotted with solid and dashed lines respectively. A dashed red line connects the first and last measurement to highlight the YORP fit's deviation from a linear trend. A dashed black line shows the case where there is zero rotational acceleration.

5.3 Discussion

The strongest YORP detection to date is the asteroid (54509) YORP, which is spinning up at a rate of 0.349×10^{-5} rad/day^2 (Lowry et al., 2007; Taylor et al., 2007), which is only ∼16% of what has been measured for DA. This alone makes the DA detection unusual, but the issue is compounded when considering that (54509) YORP's diameter is only 0.1 km, while DA's mean axial diameter is 1.2 km (Zegmott, 2021).

For asteroids with diameters comparable to DA, YORP acceleration has not been seen beyond 0.006×10^{-5}rad/day^2. Even in the most extreme scenarios, it is difficult to envision YORP being able to secularly induce -2.1×10^{-5} rad/day^2 of rotational acceleration for an asteroid the size of DA. This leaves two possible explanations: the

result is a false positive, or a hitherto unknown physical phenomenon is able to rapidly spin down kilometre-scale asteroids at a constant rate that can be sustained for decades.

In the case of the latter, the phenomenon is likely to be something that 'switches off' over relatively short timescales. Otherwise, it would need to be an exceptionally rare occurrence to have avoided previous discovery through population statistics. Paradoxically, this means that the probability of observing such a rare case is vanishingly small, as only a few dozen asteroids have undergone a comprehensive YORP analysis. This does not entirely rule out the existence of a phenomenon that is sustained over large time scales, but it is an unlikely explanation.

For a short-term effect, one must consider the possibility of a rapid-cycling 'super YORP' effect. A significant modification of YORP theory would be required to provide an adequate explanation for this, and it would likely incorporate a coupling with other physical phenomena. While there are certainly thermal effects that aren't accounted for in contemporary YORP theory - such as thermal fracturing of surface boulders - it is difficult to envision a theoretical model that is able to reach the extremes of DA's spin-down over any timescale.

Step changes in period - which could be caused by landslides, tidal forces, impacts or outgassing - can be ruled out because the acceleration is consistent across both the 2010-2014 and 2019-2021 time periods. It is extremely unlikely - but not impossible - that successive step changes could coincidentally present as constant acceleration during both of these windows.

Another possible explanation is that because DA is supported beyond the spin-breakup by cohesive forces (Rozitis et al., 2014), it could be slowly reshaping if the cohesive forces are just below a stability threshold. To conserve angular momentum, DA's rotation would slow as it becomes more oblate about its spin-axis. This change might be expected to present itself through progressively worsening lightcurve fits, but this is not seen in Figures A.10 & A.11. In any case, this could be investigated through simulations as future work.

Model & analysis	Data range	λ [°]	β [°]	ν [$\times 10^{-5}$ rad/day^2]	Source
Conv. hull YORP scan	2001-2014 2001-2014	190 ± 5	35 ± 5	N/A	1
Radar model SHAPE YORP scan	2001-2014 2001-2014	300 ± 30	0 ± 30	-0.21 ± 0.02	1
Radar model phase offset	2001-2014 2010-2014	300 ± 30	0 ±30	-1.9 ± 0.4	1
Radar model phase offset (rev.)	2001-2014 2010-2019	300 ± 30	0 ± 30	-2.0 ± 0.1	1
Conv. hull (rev.) YORP scan	2001-2019 2001-2019	35 ± 10	-25 ± 10	-0.36 ± 0.08	1
Radar model phase offset (new)	2001-2014 2019-2021	300 ± 30	0 ± 30	-2.1 ± 0.3	This work
Conv. hull (new) YORP scan	2001-2021 2001-2021	310 ± 30	10 ± 30	-0.26 ± 0.01	This work
Conv. hull (new) phase offset	2001-2021 2019-2021	310 ± 30	10 ± 30	-1.1 ± 0.5	This work

Notes. For each result, the first column contains two rows describing the shape model and measurement technique that was used. The second column describes the range of input data that were used to develop the model, and the range used to make the measurement. Subsequent columns describe the model's pole (λ, β), the acceleration that was measured (ν), and the source for the result.
References. (1) Zegmott (2021)

Table 5.2: A summary of rotational acceleration measurements for 1950 DA.

5.3.1 Future work

The author cannot rule out the possibility that this YORP detection in genuine, but advises that efforts to understand DA should instead focus on searching for the cause of what is more likely to be a false positive. This approach will improve future YORP analyses, improve models describing DA, and still potentially reveal changes to DA's spin-state.

A full investigation is beyond the scope of this work, but some potential causes have been identified. Firstly, one must consider the possibility that the shape models are incorrect. Zegmott (2021) acknowledges that while the radar model produces good

lightcurve fits, it does not perfectly reproduce every delay-Doppler image, with sharper features missing from synthetic data.

The model produced by Busch et al. (2007) has a pole of λ=187°, β=-90°. This is in disagreement with the models presented within this and Zegmott's analyses, which all have their poles near the ecliptic. These models produce better lightcurve fits than the Busch model, and Zegmott notes that the Busch model does not produce good fits for post-2007 lightcurves. Using the Busch model, a Yarkovsky analysis by Farnocchia and Chesley (2014) concludes that there is a 99% probability of DA being a retrograde rotator. While this is within the uncertainties of the new models, an incorrect pole solution could contribute to a false positive for rapid YORP spin-down. This would require that the pole solutions produced by `convexinv` and `SHAPE` are incorrect, even with the former having produced consistent solutions with 2001-2014, 2001-2019 and 2001-2021 datasets.

The procedures used to model DA, and subsequent YORP analyses, assume that it does not have complex rotation. If it is in fact a non-principal axis rotator, or has pole precession, then it could explain the measured phase offsets. The radar model has a feature that could be speculatively interpreted as a second lobe, which can be seen in the Y+ and Y- views in Figure 5.2. This could be material that has been spun outwards, or a very close contact binary. These lobes could have different densities, shifting the centre of mass away from the centre of the body to produce unusual YORP torques, as was the case with (25143) Itokawa (Lowry et al., 2014), or complex rotation.

To resolve concerns about the pole and potentially complex rotation, the author recommends that a new model is developed using `SHAPE` to fit for complex rotation, and incorporate the new 2019 and 2021 lightcurves. Even if this does not reveal a cause for a false positive, it will still provide an improved model that could be used to better constrain rotational acceleration. This would be a productive approach, avoiding the risks associated with investing time and resources on more speculative avenues of investigation.

DA will make several close approaches over the next century, although it is unlikely that any of these will be close enough for radar observations with current or near-future facilities. The apparition in early 2032 is particularly favourable for ground-based facilities in both the northern and southern hemispheres, and is DA's closest approach until 2105. Further observations could be essential to explaining DA's apparent spin-down, although it may be difficult to justify substantial telescope time without first performing further modelling and analysis with the existing data.

Regardless of whether of not the measured spin-down of DA is genuine, it needs to be investigated further to provide an adequate explanation for the results presented by both Zegmott (2021) and in this work. The outcome of future work will be important to the field, and potentially alter the long-term impact probabilities for DA. At the time of writing, it is intended that the results of this analysis will be published (Lowry et al., 2025 in prep.) so the problem can be opened up to the wider NEA community.

CHAPTER 6

YORP ANALYSES OF 1999 AP10 AND 1994 LY

6.1 Introduction

This chapter focuses on two asteroids, which were modelled and analysed as part of this work. The first is (159402) 1999 AP10, which was a target of opportunity that emerged through other work being conducted by collaborators. The second is (85275) 1994 LY, which is a target from the YORP campaign. Both of these asteroids were observed extensively with the Open University's PIRATE telescope under the same agreement, and the analyses only consider lightcurve data, hence the results for both asteroids are presented together in this chapter.

6.2 1999 AP10

(159402) 1999 AP10 (herafter AP10) is an Armor-class NEA that was discovered by the Lincoln Near-Earth Asteroid Research (LINEAR) tracking programme in January 1999 (Tichy et al., 1999). It has an orbital period of 3.67 years, a semi-major axis of 2.37 AU, an eccentricity of 0.57 with an inclination of 7.6°. AP10 is not designated as potentially hazardous, with its closest post-discovery approach being at 29.5 lunar distances during October 2009. It will not come within 50 lunar distances of Earth again during this century, and the close approach in 2020 is the closest until after 2500.

AP10 has been observed with a variety of optical, radar and thermal facilities. Various lightcurve-derived measurements consistently indicate a synodic rotation period of 7.9 h (Franco et al., 2010; Hasegawa et al., 2018; Warner and Stephens, 2021b), although no sidereal measurements were published prior to this study.

Warm Spitzer observations have been used to measure a diameter of 1.20±0.29 km (Trilling et al., 2010; Mueller et al., 2011) and an albedo of 0.35±0.24 (Thomas et al., 2011). These observations indicate that AP10 is an Sq class asteroid (Thomas et al., 2014), although other spectroscopic observations have found AP10 to be more consistent with the S, Sw, or L classes (Hicks et al., 2009; Hicks and Lawrence, 2009).

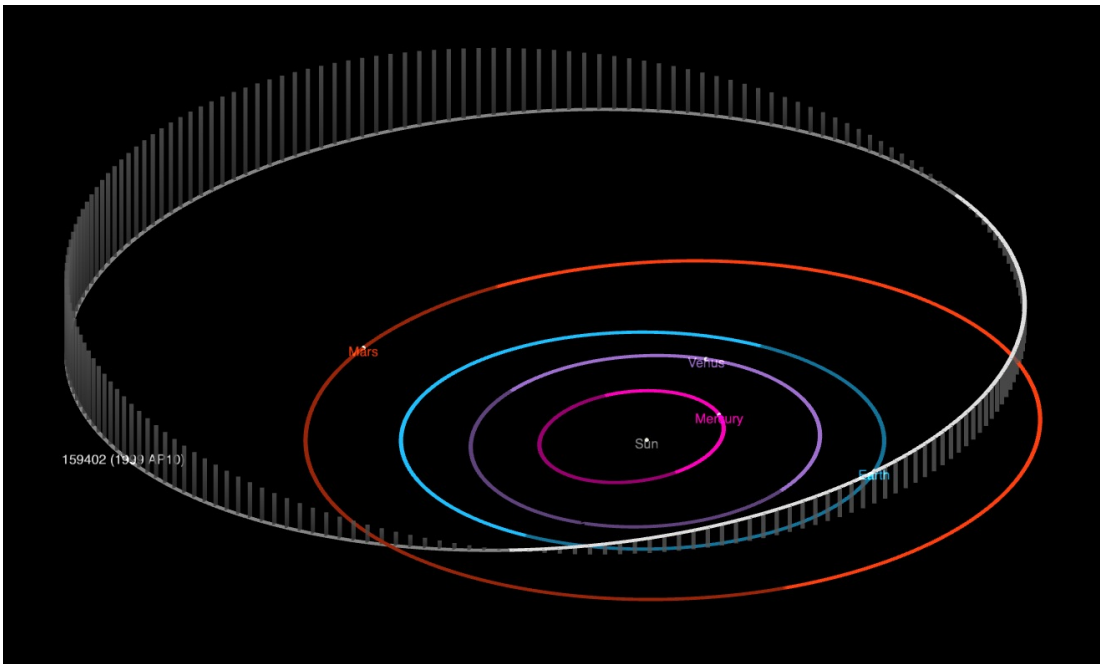

Figure 6.1: The orbit of (159402) 1999 AP10, which is shown with a white line. The orbits of the inner planets are also marked, with the positions of each object shown for 2024-01-01. This figure was produced using the JPL Orbit Viewer[a].

[a] https://ssd.jpl.nasa.gov/tools/orbit_viewer.html

Radar imaging data are available, although they were not included in modelling for reasons that are discussed in Section 6.2.2.1. Visual inspection of these data shows no sign of a secondary larger than 30 m, limiting the photometric contribution of an undetected secondary to below 0.004 magnitudes. Delay-Doppler images of AP10 show that it has a spheroid shape, producing echoes that are similar to known YORPoids. A circular polarisation ratio of 0.26 has been reported (Lunar & Planetary Institute, 2021), which is consistent with S or Q class bodies (Virkki et al., 2022). Goldstone observations in 2020 suggest a minimum diameter of 1.6 km (Benner, 2020), which is slightly larger than the previously measured Spitzer diameter.

The 2020 apparition of AP10 was extremely favourable for small telescopes, in terms of both brightness and rates of apparent motion. During this apparition an unusually wide range of viewing geometries could be achieved, as shown in Figure 6.3. This meant that small telescope data taken from 2020-2021 would be sufficient for devel-

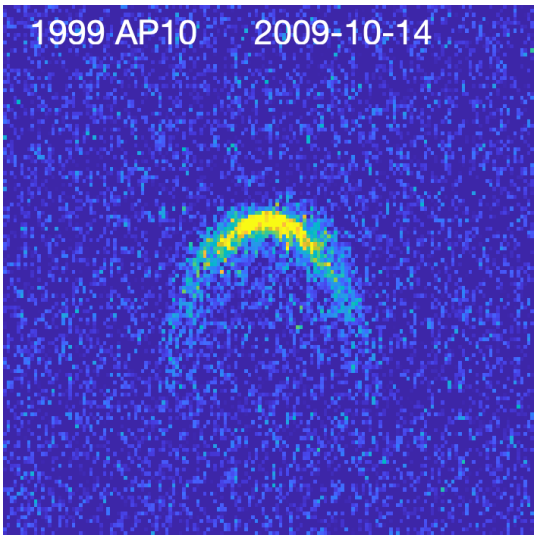

Figure 6.2: A delay-Doppler image of 1999 AP10 taken from Arecibo in October 2009, with a delay resolution of 30 m per pixel and a Doppler resolution of 0.2 Hz per pixel. Delay increases along the vertical axis, and Doppler frequency increases along the horizontal axis. Image provided by LPI[a].

[a] `https://www.lpi.usra.edu/resources/asteroids/asteroid/?asteroid_id=1999AP10`

oping a model with `convexinv`. Recognising this, and that data from 2009 are also available, it was decided that AP10 should be investigated for the YORP campaign. This coincided with a study led by Dr. Sam Jackson (then-PhD student, Open University) to investigate how aspect angles affect NEA phase curves. Jackson observed AP10 with PIRATE during the 2020 apparition and made the reduced lightcurves available for this work.

An early version of the AP10 shape model produced for this work was subsequently shared with Jackson, who used the model to confirm the predicted relationship between an asteroid's shape and its phase curve. Remarkably, this early version of the model was developed using data from a single apparition. The results of this study, including the early AP10 model produced by this author, were published by Jackson et al. (2022). This section presents the development of a more advanced physical model for AP10 that utilises a second apparition, and a subsequent YORP analysis.

6.2.1 Observations of 1999 AP10

The analysis of AP10 utilises 65 optical lightcurves, the vast majority of which were taken during the 2020 apparition. The only other lightcurves were taken during 2009, meaning that there are only two apparitions with which to measure phase offsets. In

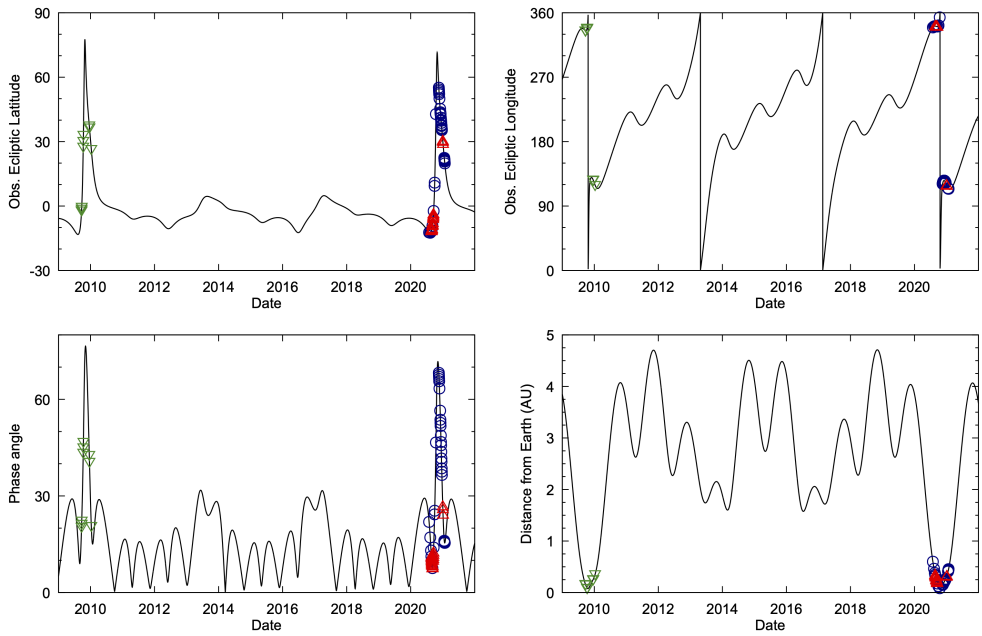

Figure 6.3: Observing geometries for (159402) 1999 AP10 from 2009 to the end of 2021. The top panels show the position of the asteroid in the ecliptic coordinate system (latitude and longitude) as observed from Earth. The bottom left panel shows the solar phase angle while the bottom right panel shows the geocentric distance to the asteroid. The marked points denote observations of the asteroid. Green inverted triangles, blue circles, and red triangles correspond to Lowell Observatory Near-Earth-Object Search(LONEOS) survey, PIRATE and Palmer Divide Station (PDS) lightcurves respectively.

most cases this would be insufficient for making a YORP detection, as it would mean that one is fitting a quadratic to what are effectively two measurements. In the case of AP10, the 2020 apparition provides over five months of coverage with observations generally separated by only a few days or weeks. This is comparable to the follow-up campaign for 1950 DA (Section 5.2), where a quadratic fit was constrained using densely packed observations over several months.

This observing strategy can only produce YORP detections in cases where there is very high acceleration, causing measurable progression in phase offset over the course of weeks or months.

The lightcurves, listed in Table 6.1, come from three sources which are summarised below.

LONEOS – As part of the LONEOS survey, nine lightcurves of AP10 were taken between September 2009 and January 2010 using a 0.6 m telescope at Lowell Observatory in Flagstaff, Arizona. A clear filter was used and photometric measurements were transformed to ATLAS r' (SR) magnitudes (Tonry et al., 2018). These data were obtained via the ALCDEF database (Warner et al., 2011).

PIRATE – From July 2020 to January 2021, 36 lightcurves of AP10 were taken by the PIRATE telescope at Teide Observatory in Tenerife. In its 'Mark III' configuration, PIRATE was a 0.4 m telescope equipped with a 4096 × 4096 pixel CCD with a square 43' field of view. The asteroid was imaged in V and R, then the V lightcurves were transformed to produce a single relative R-band lightcurve. This transformation, along with the image reduction and lightcurve extraction pipeline, is described by Jackson et al. (2021).

Palmer Divide Station – Between August 2020 to January 2021, PDS took 20 lightcurves of AP10, again using a clear filter transformed to ATLAS r' (SR) magnitudes. The telescope configuration was previously described in Section 4.2.1, and the data were again obtained via the ALCDEF database (Warner et al., 2011).

ID	UT date [yyyy-mm-dd]	$R_\odot$ [AU]	$\Delta_\oplus$ [AU]	α [°]	λ_O [°]	β_O [°]	Total [hour]	Obs. facility	Filter	Reference
1	2009-09-21	1.159	0.167	19.91	335.1	-2.5	2.6	LONEOS	clear	1
2	2009-09-22	1.153	0.162	20.84	335.1	-1.7	5.0	LONEOS	clear	1
3	2009-09-23	1.147	0.157	21.79	335.0	-0.9	5.2	LONEOS	clear	1
4	2009-10-10	1.064	0.091	42.56	337.5	26.3	3.0	LONEOS	clear	1
5	2009-10-11	1.060	0.088	44.18	338.0	28.9	2.5	LONEOS	clear	1
6	2009-10-12	1.056	0.086	45.86	338.6	31.6	3.1	LONEOS	clear	1
7	2009-12-18	1.036	0.077	56.90	345.2	50.5	7.1	LONEOS	clear	1
8	2009-12-20	1.031	0.076	60.65	349.3	57.1	7.6	LONEOS	clear	1
9	2010-01-10	1.303	0.351	20.98	119.4	26.7	8.5	LONEOS	clear	1
10	2020-07-29	1.550	0.605	22.09	339.4	-12.3	4.1	PIRATE	R	
11	2020-08-11	1.450	0.467	17.31	340.9	-12.5	4.2	PIRATE	R	
12	2020-08-20	1.382	0.384	13.30	341.3	-12.1	4.5	PIRATE	R	
13	2020-08-24	1.353	0.351	11.44	341.3	-11.7	4.9	PIRATE	R	
14	2020-08-24	1.353	0.351	11.44	341.3	-11.7	3.8	PDS	clear	2
15	2020-08-25	1.345	0.343	10.98	341.3	-11.6	3.6	PDS	clear	2
16	2020-08-26	1.338	0.335	10.54	341.3	-11.5	2.5	PDS	clear	2
17	2020-08-27	1.331	0.327	10.10	341.3	-11.3	4.9	PIRATE	R	
18	2020-08-27	1.331	0.327	10.10	341.3	-11.3	3.3	PDS	clear	2
19	2020-08-28	1.323	0.319	9.68	341.3	-11.2	3.3	PDS	clear	2
20	2020-08-29	1.316	0.312	9.29	341.3	-11.0	2.2	PDS	clear	2
21	2020-08-30	1.309	0.304	8.91	341.3	-10.8	4.1	PDS	clear	2
22	2020-08-31	1.302	0.297	8.57	341.2	-10.6	4.0	PDS	clear	2
23	2020-09-05	1.267	0.262	7.60	341.1	-9.4	5.2	PIRATE	R	
24	2020-09-05	1.267	0.262	7.60	341.1	-9.4	3.4	PDS	clear	2
25	2020-09-06	1.260	0.255	7.60	341.0	-9.1	4.3	PDS	clear	2
26	2020-09-07	1.253	0.248	7.67	341.0	-8.8	4.4	PDS	clear	2
27	2020-09-09	1.240	0.236	8.06	340.9	-8.0	4.7	PDS	clear	2
28	2020-09-13	1.214	0.211	9.67	340.8	-6.3	3.2	PDS	clear	2

Table 6.1: All optical lightcurves of 1999 AP10 that were considered for this work (continues)

ID	UT date [yyyy-mm-dd]	$R_\odot$ [AU]	$\Delta_\oplus$ [AU]	α [°]	λ_O [°]	β_O [°]	Total [hour]	Obs. facility	Filter	Reference
29	2020-09-14	1.207	0.205	10.21	340.8	-5.8	4.9	PDS	clear	2
30	2020-09-15	1.201	0.200	10.81	340.8	-5.2	4.8	PDS	clear	2
31	2020-09-16	1.195	0.194	11.45	340.7	-4.6	3.9	PDS	clear	2
32	2020-09-17	1.189	0.189	12.13	340.7	-4.0	5.3	PDS	clear	2
33	2020-09-19	1.177	0.178	13.61	340.7	-2.7	5.7	PIRATE	R	
34	2020-09-30	1.116	0.126	23.74	342.0	8.7	6.4	PIRATE	R	
35	2020-10-01	1.111	0.122	24.85	342.3	10.1	3.7	PIRATE	R	
36	2020-10-15	1.054	0.084	45.68	352.8	41.4	2.0	PIRATE	R	
37	2020-11-17	1.033	0.146	68.53	120.6	55.6	4.1	PIRATE	R	
38	2020-11-18	1.035	0.150	67.94	121.3	54.7	4.0	PIRATE	R	
39	2020-11-19	1.037	0.153	67.32	122.0	54.0	4.4	PIRATE	R	
40	2020-11-20	1.040	0.156	66.67	122.5	53.2	4.4	PIRATE	R	
41	2020-11-21	1.042	0.159	65.98	123.0	52.5	4.6	PIRATE	R	
42	2020-11-24	1.050	0.169	63.76	124.2	50.4	4.9	PIRATE	R	
43	2020-12-02	1.079	0.196	56.95	125.6	45.6	5.7	PIRATE	R	
44	2020-12-05	1.092	0.206	54.14	125.6	44.0	2.5	PIRATE	R	
45	2020-12-06	1.096	0.209	53.19	125.5	43.4	5.9	PIRATE	R	
46	2020-12-07	1.101	0.212	52.22	125.5	42.9	5.8	PIRATE	R	
47	2020-12-10	1.115	0.222	49.26	125.2	41.4	6.3	PIRATE	R	
48	2020-12-12	1.125	0.229	47.26	124.9	40.4	2.8	PIRATE	R	
49	2020-12-13	1.131	0.232	46.24	124.7	39.9	5.7	PIRATE	R	
50	2020-12-15	1.141	0.239	44.20	124.3	39.0	5.7	PIRATE	R	
51	2020-12-17	1.153	0.246	42.15	123.8	38.0	7.0	PIRATE	R	
52	2020-12-18	1.158	0.250	41.13	123.6	37.5	7.0	PIRATE	R	
53	2020-12-20	1.170	0.257	39.07	123.1	36.6	7.2	PIRATE	R	
54	2020-12-21	1.176	0.261	38.05	122.8	36.1	7.1	PIRATE	R	
55	2020-12-22	1.182	0.265	37.03	122.5	35.6	6.2	PIRATE	R	
56	2021-01-01	1.246	0.307	27.27	119.5	30.7	7.3	PDS	clear	2

Table 6.1: (continued)

ID	UT date [yyyy-mm-dd]	$R_\odot$ [AU]	$\Delta_\oplus$ [AU]	α [°]	λ_O [°]	β_O [°]	Total [hour]	Obs. facility	Filter	Reference
57	2021-01-02	1.253	0.312	26.37	119.2	30.2	7.8	PDS	clear	2
58	2021-01-04	1.266	0.322	24.63	118.6	29.2	2.9	PDS	clear	2
59	2021-01-17	1.359	0.398	16.55	115.3	23.1	9.5	PIRATE	R	
60	2021-01-18	1.367	0.405	16.23	115.1	22.7	9.6	PIRATE	R	
61	2021-01-19	1.374	0.413	15.97	114.9	22.2	9.1	PIRATE	R	
62	2021-01-20	1.381	0.420	15.76	114.7	21.8	9.5	PIRATE	R	
63	2021-01-21	1.389	0.427	15.60	114.5	21.3	9.2	PIRATE	R	
64	2021-01-22	1.396	0.435	15.49	114.4	20.9	9.3	PIRATE	R	
65	2021-01-24	1.411	0.451	15.41	114.1	20.1	9.1	PIRATE	R	

Notes. Each lightcurve has a chronologically assigned ID, then the UT date at the beginning of the night, the heliocentric ($R_\odot$) and geocentric ($\Delta_\oplus$) distances in AU, the solar phase angle (α), the observed ecliptic longitude (λ_O), the observed ecliptic latitude (β_O), the total time over which the target was observed, the observing facility and the photometric filter. References to published lightcurves are listed. Observing facility key: LONEOS – Lowell Observatory Near-Earth-Object Search 0.6 m Telescope (699 - Arizona, USA); PIRATE – 0.4 m Physics Innovations Robotic Astronomical Telescope Explorer Mark III (954 - Tenerife, Spain); PDS – Palmer Divide Station 0.35 m (various) (U82 - California, USA)
References. (1) Franco et al. (2010); (2) Warner and Stephens (2021a)

Table 6.1: (continued)

In total, this analysis utilises 341 hours of lightcurve data. Using the reported 7.9 h period for AP10, the mean rotational phase coverage for a single lightcurve is 66%. There are 16 lightcurves with greater than 85% coverage, including eight that cover more than one full rotation. No lightcurves were excluded from the analysis; this largely because the asteroid's apparent magnitude was between 12 and 17 for most observations, resulting in high SNR photometry.

6.2.2 Physical modelling

The 2009/2010 lightcurve data were not published to ALCDEF until after the author had already determined the period, pole and shape that were published in Jackson et al. (2022). After the 2009/2010 data were made available, the analysis of AP10 was repeated to incorporate the 'new' lightcurves. The initial period scan shown in this section corresponds to the original search using the 2020/2021 data, but all subsequent modelling and analysis of AP10 presented in this section is for the updated analysis using the full 2009-2021 lightcurve dataset. The period was re-fitted during the updated analysis, only using the earlier period as a starting value.

With AP10's synodic rotation period already being well established in the literature, a focused `convexinv` period scan was run between 7.9100 h and 7.9260 h, finding a best-fit sidereal rotation period of 7.9214±0.0008 h. The narrow range of this period scan lead to oversampling, which is evident in Figure 6.4. Other viable periods were found close to the best-fit value, but this is reflected in the uncertainty.

Taking this period, all 65 lightcurves were used to conduct a full YORP scan over a $5^\circ \times 5^\circ$ grid of poles, with YORP iterating from $-1.0 \times 10^{-6}\,\mathrm{rad/day^2}$ to $1.0 \times 10^{-6}\,\mathrm{rad/day^2}$ in steps of $10^{-8}\,\mathrm{rad/day^2}$. The overall best solution was found in the $\nu = 50 \times 10^{-8}\,\mathrm{rad/day^2}$ plane with a pole solution of $\lambda = 140^\circ$, $\beta = -20^\circ$. There is clear convergence across YORP planes towards this solution, but the 'YORP bowl' shown in Figure 6.5 is too wide to make this a strong indication of YORP spin-up. The shallow nature of the bowl means that the fit does not change significantly with the

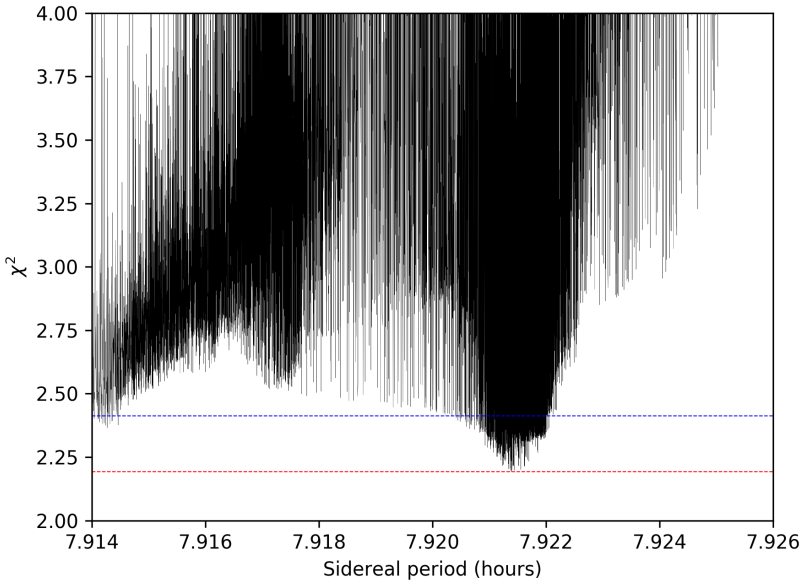

Figure 6.4: The results of a period search for asteroid (159402) 1999 AP10. For each period in the range shown, lightcurve data were used to optimise a model for six different rotational poles in the celestial sphere. The lowest χ^2 across the six models was recorded for the period being used. A horizontal red line shows the minimum χ^2, and a horizontal blue line shows a 10% increase of the minimum.

YORP strength, indicating that the limitations of the data, and flexibility of the model, are responsible for differences in the goodness-of-fit across the range. A robust YORP detection requires a narrow bowl with steep convergence towards the best solution. Furthermore, the scan would need to be expanded to extreme values of YORP to find the edges of the bowl. As seen in Chapter 5, YORP scans may become unreliable for very strong YORP due to a preference for phase offsets below 2π.

The physical models of AP10 are broadly consistent across YORP planes. They have a spheroid shape consistent with the previously discussed radar imaging data, and show a clear preference for retrograde rotation. Due to the uncertain nature of the `convexinv` YORP solution, the author considers the best-fitting constant period (ν=0) solution to be the most appropriate model to present in this work. This model, shown in Figures 6.6 & 6.7 has its pole at $\lambda = 10°$, $\beta = -40°$ with a period of 7.9209 $\pm$ 0.0005 h.

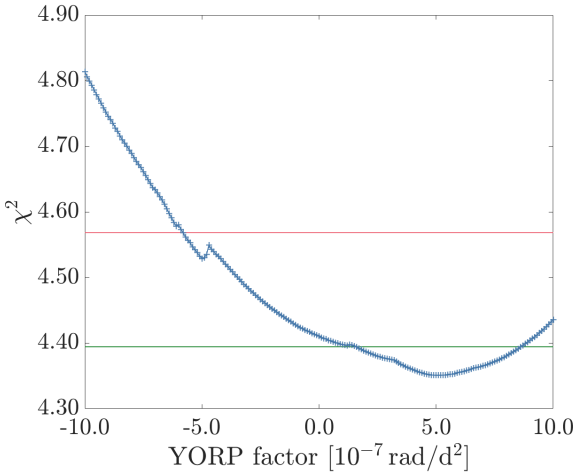

Figure 6.5: A YORPogram for (159402) 1999 AP10, showing a global minimum at 5.0×10^{-7} rad/day^2. The green and red lines correspond to solutions within 1% and 5% of the best solution, respectively. The shallow, continuous nature of the partial 'YORP bowl' means that the indicated YORP spin-up is not conclusive, and that adjusting scan range or resolution will not improve the measurement.

6.2.2.1 Phase offsets & discussion

Using the constant period model for a phase offset analysis produces a result of $(11.5\pm1.1)\times10^{-8}$ rad/day^2, which is close to the result from the `convexinv` YORP scan. The phase offsets are clear when inspecting the lightcurve fits, as is shown in Figure 6.17. A linear phase offset progression is, however, just as viable as a YORP fit. This is shown clearly in Figure 6.8; the lack of a third epoch means that the quadratic fit does not constitute a viable YORP detection. Because the phase offset analysis procedures explicitly fit for a quadratic solution, the uncertainties are grossly understated. This measurement was made using averaged phase offset measurements, but adjusting measurement groupings or using single measurements does not help. Considering that the rapid spin-down of 1950 DA was seen over the course of months, at the steepest part of the presumed quadratic curve, the lack of any measured progression in phase offset for 1999 AP10 means that rapid spin-up can be ruled out.

The phase offsets measured in 2020/2021 imply that AP10's period has shortened by ∼0.3 s since 2009. This is within the maximum error that could be caused by a propagated initial period uncertainty, although a period correction was applied during the analysis to remove linear progression in phase offsets (see Sec. 3.3.2). It is also possible that an impulsive period change has occurred, which considering AP10's slow

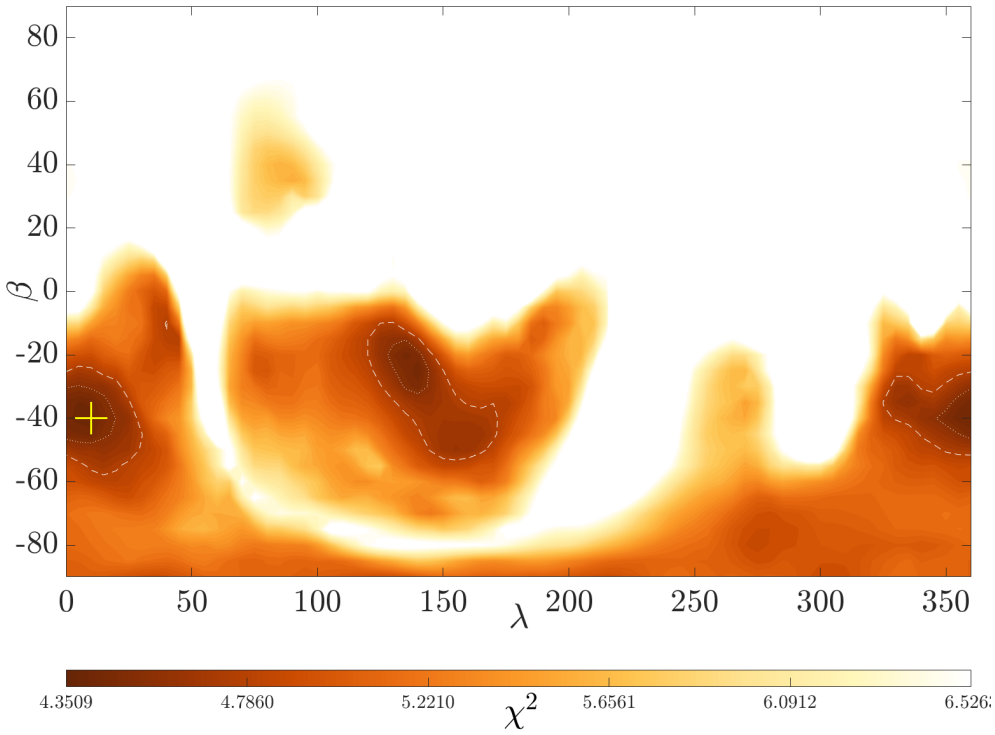

Figure 6.6: The results of a search for the rotational pole of (159402) 1999 AP10 using convex inversion of lightcurve data, assuming zero YORP. For each pole solution in ecliptic coordinates λ and β, the χ^2 fit of the solution is plotted for a colour range where the global minimum χ^2 is black and solutions 50% greater than the minimum are white. The best solution is marked with a yellow '+'. The white dotted and dashed lines enclose regions where χ^2 is within 5% and 10% of the best solution respectively. Note that while similar plots in this work include a solid yellow line to denote solutions within 1% of the best solution, in this case there were no other solutions within 1% of the best solution.

rotation, is most likely caused by minor impacts or gravitational encounters.

In summary, this analysis cannot decisively confirm whether AP10 has a constant rotation period or is experiencing a slow spin-up. This was to be expected, with the only real possibility of a YORP detection being if there was a very rapid spin-up (or spin-down) that could be constrained using the 2020/2021 data. Further refinement of the period, to reduce the propagating uncertainty, would confirm - or rule out - constant period rotation. Developing a radar model is unlikely to change this conclusion, as the convex hull model for AP10 produces excellent lightcurve fits and it would not address the fundamental issue of missing a 'middle' epoch to differentiate between

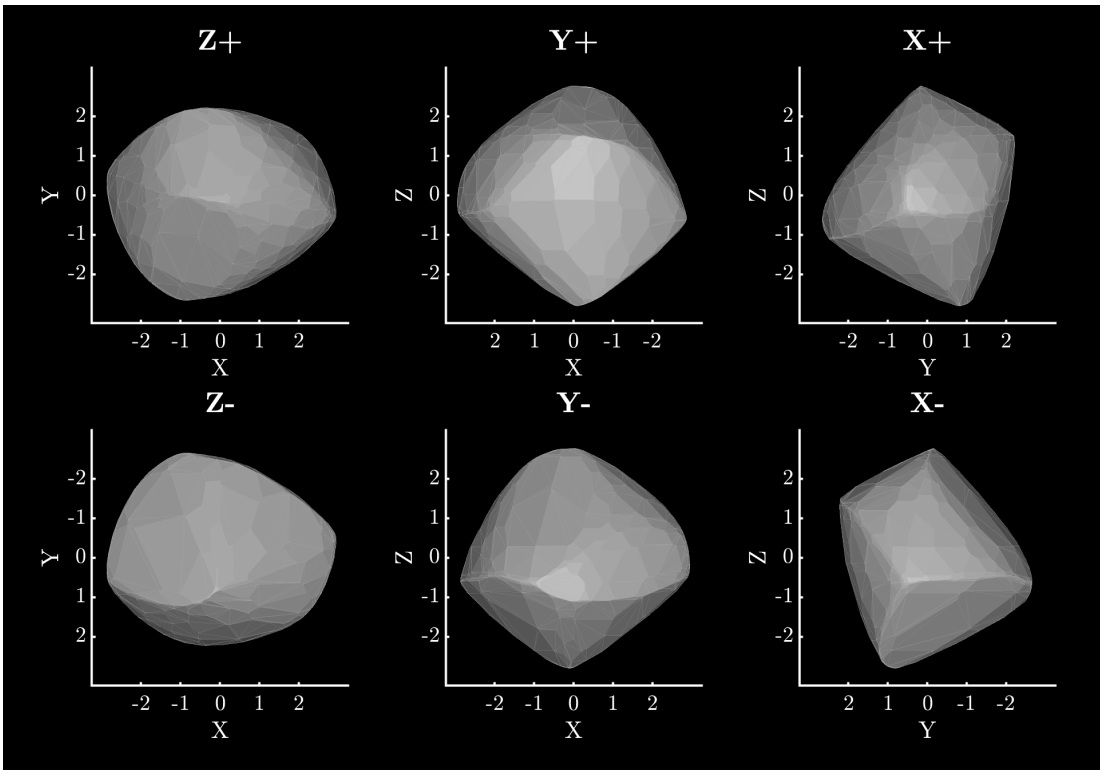

Figure 6.7: The best-fit convex hull model of (159402) 1999 AP10 with the rotational pole $\lambda = 10°$, $\beta = -40°$. This model assumes principal-axis rotation with a sidereal period of 7.9209 ± 0.0005 h with no rotational acceleration. The top row shows the model from the positive end of the Z, Y and X axes in the body-centric co-ordinate system. The bottom row shows the model from the negative end of the Z, Y and X axes. The Z-axis is aligned with the rotational pole, which is the shortest axis of inertia. The X-axis is arbitrarily set such that it is viewed from the positive end for the plane-of-sky at T_0. Axis lengths are in arbitrary units, as lightcurve inversion does not produce scaled models.

linear and quadratic progression in phase offset. The 2009 and 2020 apparitions were AP10's closest approaches in this century, leaving relatively sparse opportunities to observe AP10 in the coming decades. The close approach in December 2031 should be prioritised, as it will be the closest approach until 2156. The author advises against substantial future work prior to the acquisition of new lightcurves, especially considering that both software and hardware capabilities are likely to improve by 2031.

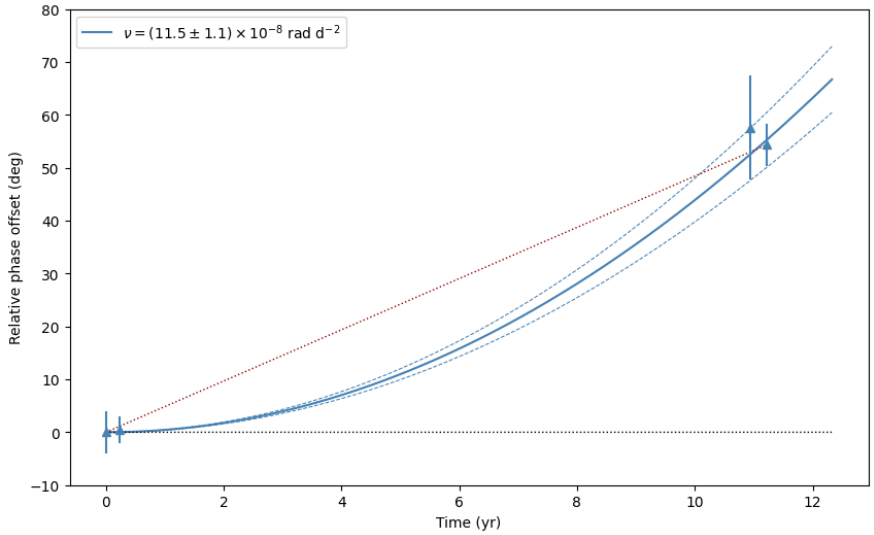

Figure 6.8: Relative phase offset measurements for (159402) 1999 AP10. These phase offset measurements correspond to averaged phase offsets, which were separated such that there are no more than 21 days between observations within each group. Blue triangular markers indicate these measurements, with the fit and its uncertainty plotted with solid and dashed lines respectively. A dashed red line connects the first and last measurement to highlight the YORP fit's deviation from a linear trend. A dashed black line shows the case where there is zero rotational acceleration.

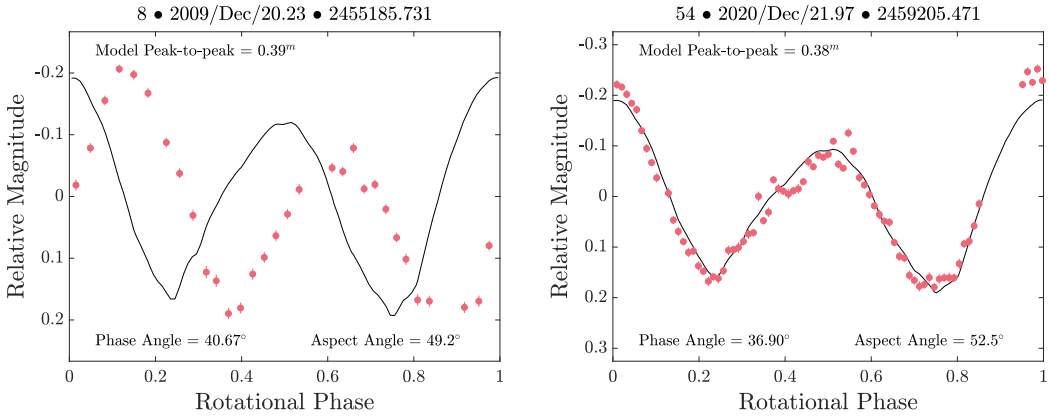

Figure 6.9: A comparison of observational data (red points) and the corresponding synthetic lightcurve (solid black line) for lightcurves 8 & 54 in Table 6.1. The synthetic lightcurve was generated using the convex hull model for 1999 AP10, using a combination of the Lambertian and Lommel-Seeliger scattering models. As the model's T_0 is in 2020 the phase offset is close to zero from lightcurves 10 onwards, with a visible offset in the earlier lightcurves. This offset could be caused by YORP spin-up, which was measured using the change in phase offset relative to the first lightcurves. For plots of all 65 lightcurves that were used to fit the model, see Figure A.12.

6.3 1994 LY

(85275) 1994 LY (herafter LY) is Amor-class NEA that was discovered at Palomar Observatory in June 1994. The asteroid has an orbital period of 2.60 years, a semi-major axis of 1.89 AU, an eccentricity of 0.44 and an inclination of 17.7°. Similar to AP10, it is not deemed to be potentially hazardous. Its closest approach is in 2171 at a separation of 38.8 lunar distances, with the second-closest post-discovery approach being the 2020 apparition.

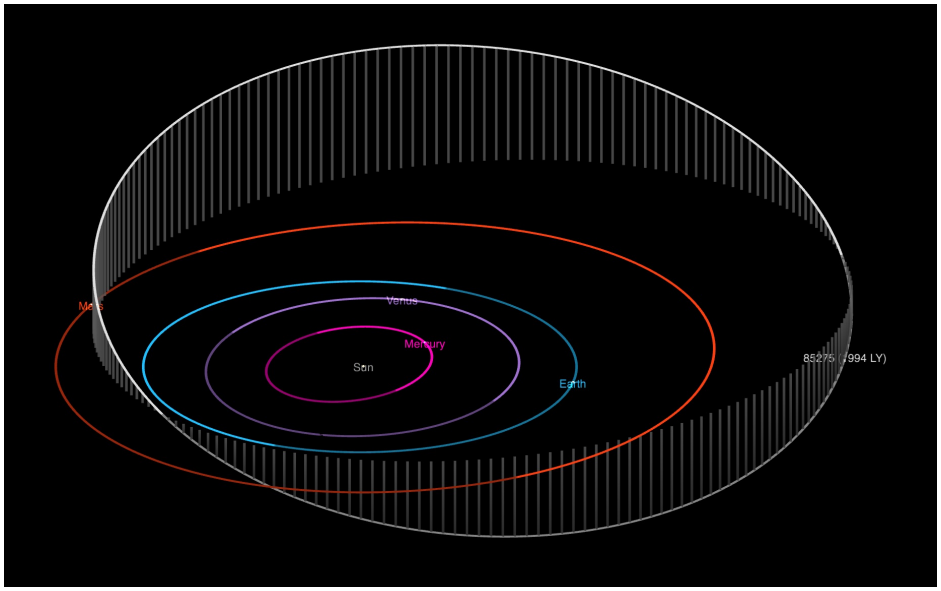

Figure 6.10: The orbit of (85275) 1994 LY, which is shown with a white line. The orbits of the inner planets are also marked, with the positions of each object shown for 2024-01-01. This figure was produced using the JPL Orbit Viewer[a].

[a] `https://ssd.jpl.nasa.gov/tools/orbit_viewer.html`

Prior to this work, LY had been observed with a number of optical and infrared facilities. Using optical lightcurves from small telescopes, Apostolovska et al. (2009) finds a synodic rotation period of 2.69±0.0003 h. Near-Earth Object Wide-field Infrared Survey Explorer (NEOWISE) observations of LY were used to determine a diameter of 2.50±0.99 km (Nugent et al., 2016), while MITHNEOS observations suggest a C- or X-type taxonomy (Binzel et al., 2019). Le Corre et al. (2018) notes that LY has an almost identical spectrum to (162173) Ryugu and (316720) 1998 BE7, suggesting

that the asteroids have similar regolith compositions. This suggests that Ryugu could be an ideal analogue for LY, as regolith samples have been returned to Earth for laboratory analysis, and there are a wealth of in-situ measurements of the asteroid from the Hayabusa2 spacecraft.

LY was observed by Arecibo during the course of this work, but no useful data were collected. In 2020, Howell (priv. comm.) used the NASA Infrared Telescope Facility (IRTF) to take near-infrared spectra of LY. A preliminary analysis suggests that LY is a D-type asteroid, which is unusual for an NEA (DeMeo et al., 2009). LY's thermal albedo was measured to be 0.14±0.03, with spectra being more consistent with the bottom of this range (∼0.11). This is also more consistent with typical D-type albedos.

This section presents the results of a `convexinv` analysis of LY, where YORP campaign data were used to develop a physical model and search for evidence of YORP acting on the asteroid.

6.3.1 Observations of 1994 LY

This analysis of LY includes 67 optical lightcurves. Similarly to AP10, the majority of lightcurves were taken in 2020. The full dataset spans 15 years, which can be loosely grouped into six epochs of observations. Both the number and temporal distribution of lightcurves make LY an attractive target for modelling and YORP analysis, especially when considering the densely-packed 2020 data which could constrain a potential phase offset gradient.

As previously discussed, IRTF and Arecibo observations took place in 2020 to coincide with this investigation. As the radar data were largely unsuccessful, they were not considered for this work. The infrared spectra were taken and analysed by Ellen Howell (Lunar & Planetary Institute), and it is intended that the results of this work will enable a more advanced analysis of the IRTF data. The largest source of lightcurves was ALCDEF, followed by the YORP campaign and PIRATE. A full summary of facilities

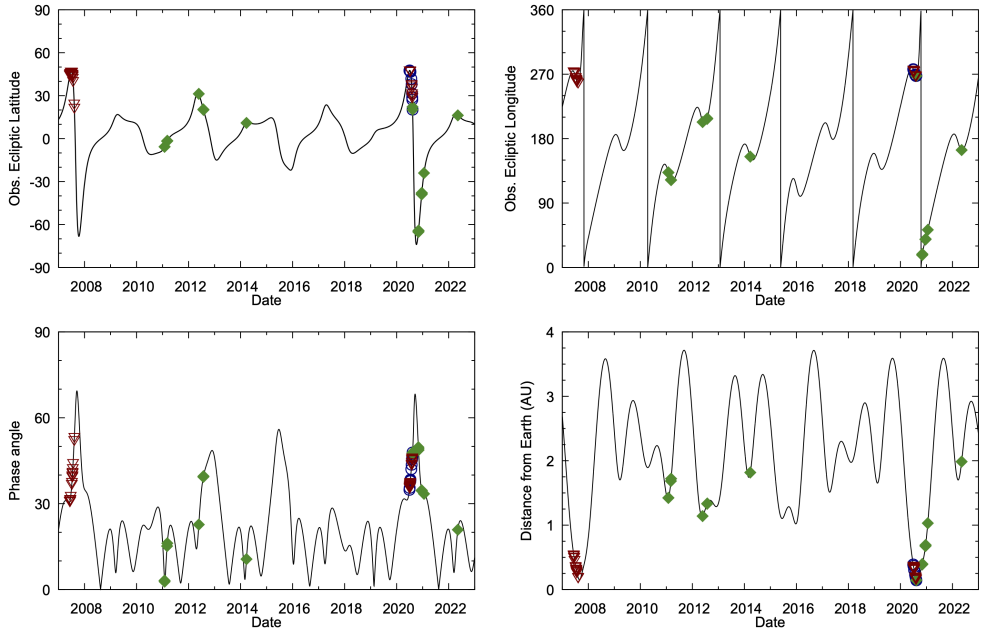

Figure 6.11: Observing geometries for (85275) 1994 LY from 2007 to the end of 2022. The top panels show the position of the asteroid in the ecliptic coordinate system (latitude and longitude) as observed from Earth. The bottom left panel shows the solar phase angle while the bottom right panel shows the geocentric distance to the asteroid. The marked points denote observations of the asteroid. Red inverted triangles, green diamonds, and blue circles correspond to ALCDEF, YORP campaign and PIRATE lightcurves respectively.

is given below.

0.7 m Telescope – From June to August 2007, a privately operated 0.66 m telescope in central Colorado was used to obtain 13 lightcurves of LY. These data were obtained from ALCDEF (Franco et al., 2010), although all but two of the lightcurves were rejected due to their poor quality. The asteroid was imaged using an Apogee AP8 CCD with a V filter.

Via Capote Telescope – The 0.7 m VCT in southern California obtained 7 lightcurves of LY in June/July 2007. These data were also obtained from ALCDEF (Franco et al., 2010), with two lightcurves being rejected. Imaging was conducted using the R filter.

New Technology Telescope – As part of the YORP campaign, LY was imaged using the NTT in 2011, 2012, 2014, and 2020, using the R and V filters. Further details on the NTT were previously given in Sections 2.2.1.1 & 4.2.1. Three lightcurves from 2011 were rejected.

Isaac Newton Telescope – The INT, which was previously described in Sections 2.2.1.1 & 4.2.1, was used to observe LY for the YORP campaign in 2012, 2020, 2021 and 2022 using the R, V and r filters.

Hale Telescope – The Hale telescope, previously discussed in Section 2.2.1, was used to image LY with the R filter in 2014.

PIRATE – In 2020, PIRATE collected 12 lightcurves of LY, with the same configuration and dual-filter processing that was used for AP10 in Section 6.2.1. One lightcurve was rejected.

Palmer Divide Station – In July/August 2020, PDS collected 15 lightcurves of LY, using the clear filter with measurements transformed to ATLAS r' (SR). These were obtained from ALCDEF (Warner and Stephens, 2021a), and four lightcurves were rejected. The PDS telescope configuration was previously described in Section 4.2.1.

The total number of lightcurves considered for this work add up to 231 hours of coverage, for an average of 129% phase coverage per lightcurve, with 46 lightcurves that cover more than one rotation. A relatively large portion of lightcurves were rejected; this is in part due to the fact that the asteroid is often only just bright enough for small telescopes, resulting in poor photometric results. The distribution of observations means that there is still good coverage from large telescopes between 2011 and 2022, with the ALCDEF and PIRATE data supplementing the YORP campaign data where possible.

ID	UT date [yyyy-mm-dd]	$R_\odot$ [AU]	$\Delta_\oplus$ [AU]	α [°]	λ_O [°]	β_O [°]	Total [hour]	Obs. facility	Filter	Included	Ref.
1	2007-06-08	1.444	0.546	30.81	273.9	44.5	1.2	CO	V		1
2	2007-06-09	1.438	0.538	30.91	273.7	44.7	4.0	CO	V		1
3	2007-06-10	1.432	0.530	31.03	273.6	45.0	5.5	CO	V		1
4	2007-06-11	1.426	0.523	31.15	273.4	45.2	3.5	CO	V		1
5	2007-06-14	1.408	0.501	31.57	272.8	45.8	2.5	CO	V		1
6	2007-06-15	1.402	0.494	31.73	272.6	46.0	2.8	CO	V		1
7	2007-06-21	1.366	0.452	32.86	271.0	46.8	2.6	VCS	R	•	1
8	2007-06-21	1.366	0.452	32.86	271.0	46.8	4.0	VCS	R	•	1
9	2007-07-06	1.279	0.358	37.13	265.6	46.6	2.3	CO	V	•	1
10	2007-07-08	1.268	0.347	37.85	264.9	46.3	2.3	VCS	R	•	1
11	2007-07-13	1.241	0.319	39.77	263.0	45.0	4.2	VCS	R	•	1
12	2007-07-13	1.241	0.319	39.77	263.0	45.0	5.0	CO	V		1
13	2007-07-14	1.236	0.314	40.17	262.6	44.6	4.0	VCS	R	•	1
14	2007-07-16	1.225	0.303	41.00	261.9	43.8	4.0	VCS	R		1
15	2007-07-17	1.220	0.298	41.42	261.6	43.4	4.0	VCS	R		1
16	2007-07-17	1.220	0.298	41.42	261.6	43.4	4.2	CO	V		1
17	2007-07-20	1.205	0.282	42.73	260.7	42.0	4.0	CO	V		1
18	2007-07-24	1.186	0.262	44.54	259.7	39.6	1.0	CO	V	•	1
19	2007-08-09	1.119	0.192	52.62	258.4	23.2	2.8	CO	V		1
20	2007-08-11	1.112	0.185	53.73	258.6	20.2	1.6	CO	V		1
21	2011-01-28	2.405	1.424	2.83	132.6	-5.6	1.2	NTT	R	•	
22	2011-01-29	2.408	1.427	2.50	132.2	-5.5	2.0	NTT	R		
23	2011-03-06	2.519	1.707	15.80	122.2	-1.6	3.0	NTT	R		
24	2011-03-08	2.524	1.732	16.43	121.9	-1.4	0.4	NTT	R		
25	2012-05-23	2.677	2.879	20.59	130.7	2.9	2.5	INT	R	•	
26	2012-05-25	2.679	2.908	20.36	131.2	3.0	2.0	INT	R	•	
27	2012-07-26	2.725	3.577	10.17	151.4	4.8	1.8	NTT	R	•	
28	2012-07-28	2.725	3.590	9.77	152.1	4.8	1.0	NTT	R	•	

Table 6.2: All optical lightcurves of 1994 LY that were considered for this work (continues)

ID	UT date [yyyy-mm-dd]	$R_\odot$ [AU]	$\Delta_\oplus$ [AU]	α [°]	λ_O [°]	β_O [°]	Total [hour]	Obs. facility	Filter	Inc.	Ref.
29	2014-03-24	2.724	1.822	10.95	154.6	11.0	3.0	PAL	R	•	
30	2020-06-28	1.307	0.384	35.02	276.8	47.5	5.0	PIRATE	V		
31	2020-07-01	1.290	0.364	35.71	276.0	47.6	1.0	PIRATE	V	•	
32	2020-07-01	1.290	0.364	35.71	276.0	47.6	7.0	PDS	clear	•	2
33	2020-07-02	1.284	0.358	35.95	275.8	47.6	7.0	PDS	clear	•	2
34	2020-07-03	1.279	0.351	36.19	275.5	47.6	6.0	PDS	clear	•	2
35	2020-07-04	1.273	0.345	36.45	275.2	47.5	3.0	PDS	clear	•	2
36	2020-07-05	1.268	0.338	36.70	274.9	47.5	7.0	PDS	clear	•	2
37	2020-07-06	1.262	0.332	36.97	274.6	47.4	4.0	PDS	clear		2
38	2020-07-07	1.257	0.326	37.24	274.3	47.3	5.2	PDS	clear		2
39	2020-07-08	1.251	0.319	37.51	274.0	47.2	7.0	PDS	clear		2
40	2020-07-09	1.246	0.313	37.79	273.7	47.0	7.0	PDS	clear		2
41	2020-07-10	1.241	0.307	38.07	273.4	46.9	2.5	PIRATE	V	•	
42	2020-07-11	1.235	0.301	38.36	273.1	46.7	1.8	PIRATE	V	•	
43	2020-07-12	1.230	9.015	38.65	272.8	46.4	4.0	PIRATE	V	•	
44	2020-07-24	1.171	0.226	42.31	269.3	41.2	3.0	PIRATE	V	•	
45	2020-07-29	1.149	0.199	43.85	268.3	37.2	3.5	PIRATE	V	•	
46	2020-07-29	1.149	0.199	43.85	268.3	37.2	5.1	PDS	clear	•	2
47	2020-07-30	1.145	0.194	44.16	268.2	36.3	5.1	PDS	clear	•	2
48	2020-08-01	1.137	0.184	44.77	267.9	34.1	5.0	PDS	clear	•	2
49	2020-08-04	1.126	0.170	45.72	267.7	30.4	3.0	PIRATE	V	•	
50	2020-08-04	1.126	0.170	45.71	267.7	30.4	4.3	PDS	clear	•	2
51	2020-08-05	1.122	0.165	46.04	267.6	29.0	4.2	PDS	clear	•	2
52	2020-08-06	1.118	0.161	46.37	267.6	27.5	2.0	PIRATE	V	•	
53	2020-08-06	1.118	0.161	46.36	267.6	27.5	4.0	PDS	clear	•	2
54	2020-08-07	1.115	0.156	46.71	267.6	25.9	2.0	PIRATE	V	•	
55	2020-08-07	1.115	0.156	46.71	267.6	25.9	2.1	PIRATE	V	•	
56	2020-08-10	1.105	0.144	47.80	267.7	20.6	5.0	INT	V	•	

Table 6.2: (continued)

ID	UT date [yyyy-mm-dd]	$R_\odot$ [AU]	$\Delta_\oplus$ [AU]	α [°]	λ_O [°]	β_O [°]	Total [hour]	Obs. facility	Filter	Inc.	Ref.
57	2020-08-11	1.102	0.140	48.20	267.8	18.5	5.0	INT	V	•	
58	2020-08-11	1.102	0.140	48.20	267.8	18.5	1.8	PIRATE	V	•	
59	2020-11-01	1.202	0.392	49.30	17.9	-64.8	3.0	NTT	V	•	
60	2020-11-01	1.202	0.392	49.30	17.9	-64.8	2.9	NTT	V	•	
61	2020-11-02	1.207	0.397	48.81	18.6	-64.3	5.0	NTT	V	•	
62	2020-11-03	1.212	0.402	48.32	19.3	-63.8	2.8	NTT	V	•	
63	2020-12-17	1.466	0.682	34.59	39.3	-38.5	3.0	NTT	V	•	
64	2020-12-18	1.472	0.691	34.49	39.7	-38.0	2.5	NTT	V	•	
65	2020-12-19	1.478	0.700	34.40	40.1	-37.4	3.0	NTT	V	•	
66	2021-01-18	1.662	1.028	33.44	52.5	-24.1	1.2	INT	V	•	
67	2022-03-09	2.683	1.720	6.55	178.1	15.6	2.5	INT	r	•	

Notes. Each lightcurve has a chronologically assigned ID, then the UT date at the beginning of the night, the heliocentric ($R_\odot$) and geocentric ($\Delta_\oplus$) distances in AU, the solar phase angle (α), the observed ecliptic longitude (λ_O), the observed ecliptic latitude (β_O), the total time over which the target was observed, the observing facility and the photometric filter. Lightcurves which were included in the analysis are indicated, and references to published lightcurves are listed. Observing facility key: CO – Private 0.7 m telescope (Colorado, USA); VCS – Via Capote Sky 0.7 m telescope (California, USA); PIRATE – 0.4 m Physics Innovations Robotic Astronomical Telescope Explorer Mark III (954 - Tenerife, Spain); PDS – Palmer Divide Station 0.35 m (various) (U82 - California, USA).
References. (1) Franco et al. (2010); (2) Warner and Stephens (2021a)

Table 6.2: (continued)

6.3.2 Physical modelling

Following the same strategy as other asteroids studied for this work, the first stage of LY's analysis was to use `convexinv` to determine its sidereal rotation period. The period search, along with subsequent analysis, utilised the 46 lightcurves marked in Table 6.2. A coarse period scan was conducted from 1 h to 11 h, which clearly favoured a 2.69 h period. This was then followed up by a high-resolution scan between 2.67 h and 2.72 h, which found LY's period to be 2.6970±0.0008 h. The combined results of these scans are shown in Figure 6.12.

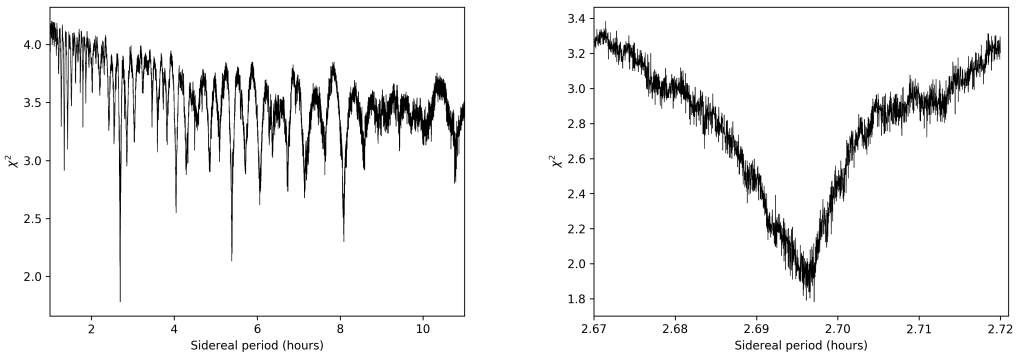

Figure 6.12: The results of a period search for asteroid (85275) 1994 LY. For each period in the range shown, lightcurve data were used to optimise a model for six different rotational poles in the celestial sphere. The lowest χ^2 across the six models was recorded for the period being used. A horizontal red line shows the minimum χ^2, and a horizontal blue line shows a 10% increase of the minimum. The panel on the left shows the combined results for the coarse and high-resolution scans, while the panel on the right shows the high-resolution scan only.

Using this input period, a full YORP scan was run over a $5° \times 5°$ grid of poles, iterating over YORP torques from -2×10^{-6} rad/day^2 to 2×10^{-6} rad/day^2 in steps of 0.01×10^{-6} rad/day^2. After this scan showed convergence for both the pole and YORP factor, follow-up scans were conducted with higher YORP resolution around the global minimum, with steps as small as 0.0005×10^{-6} rad/day^2. The full results of this are shown in Figure 6.13.

The overall best solution is at $\lambda = 80°$, $\beta = -40°$, with a YORP torque of $-11.0 \times$

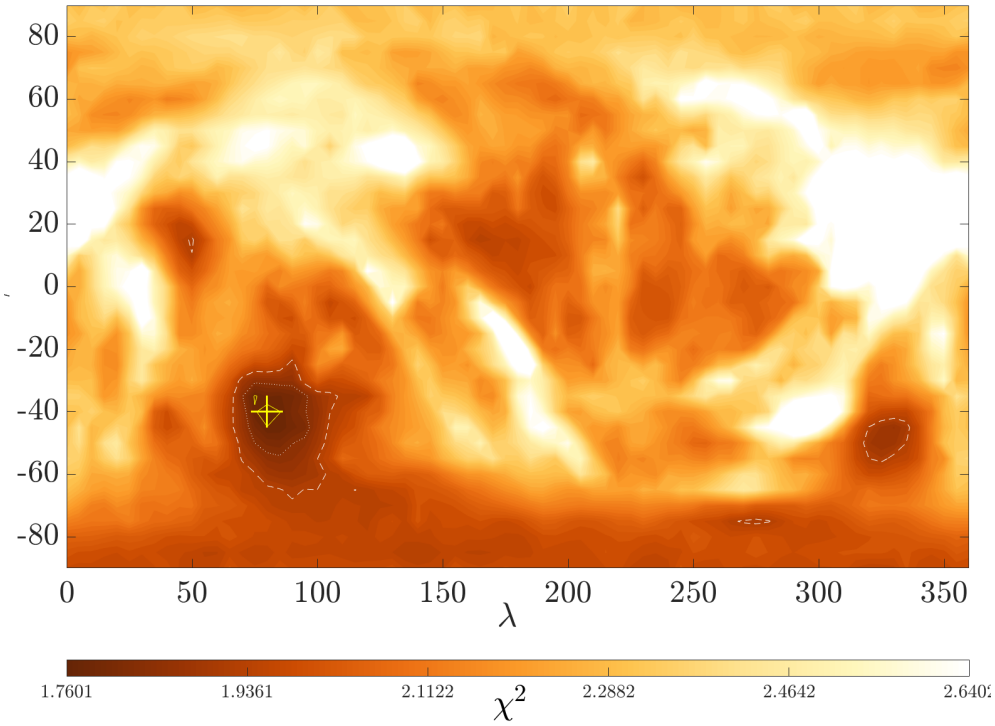

Figure 6.13: The results of a search for the rotational pole of (85275) 1994 LY using convex inversion of lightcurve data, in the -11.0×10^{-8} rad/day^2 plane. For each pole solution in ecliptic coordinates λ and β, the χ^2 fit of the solution is plotted for a colour range where the global minimum χ^2 is black and solutions 50% greater than the minimum are white. The best solution is marked with a yellow '+'. The solid yellow, white dotted and white dashed lines enclose regions where χ^2 is within 1%, 5%, and 10% of the best solution respectively.

10^{-8} rad/day^2. Poles are consistent across YORP planes, with the best zero-YORP solution also lying at $\lambda = 80°$, $\beta = -40°$. While there is a clear convergence towards the spin-down solution, the 'YORP bowl' in Figure 6.14 is broad enough that a zero-YORP solution cannot be ruled out.

While this evidence for the spin-down of LY may seem promising, an inspection of its convex hull model reveals an unrealistic aspect ratio. As shown in Figure 6.15, the asteroid is rotating about its longest axis. Stable rotation should be about the shortest axis, and unstable rotation would be apparent in the lightcurves. A rapid rotator would also be expected to be spherical, or extended along its X and Y axes. As the Z axis is the most difficult to constrain, there is little doubt that this is simply an inaccurate

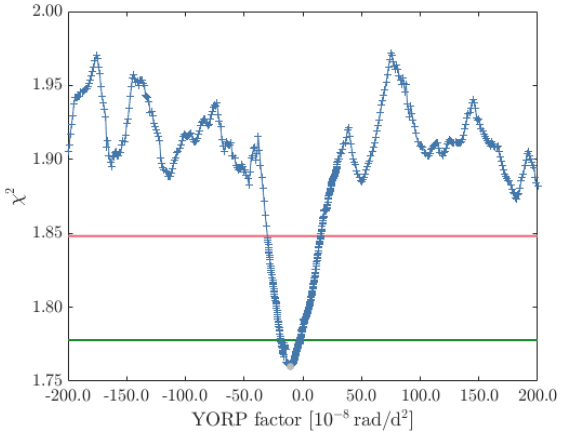

Figure 6.14: A YORPogram for (85275) 1994 LY, showing a clearly defined global minimum at -11.0×10^{-8} rad/day^2. The green and red lines correspond to solutions within 1% and 5% of the best solution, respectively.

model. This suggests that the preliminary YORP detection is a false positive, as the zero-YORP model (Figure 6.16) has a more plausible convex shape. Discounting the spin-down solution, the zero-YORP model is considered to be the best physical model for LY. Lightcurves generated using this model produce good fits to the data (Figure 6.17), with a few exceptions that can be attributed to low-quality data.

6.3.2.1 Phase offsets & discussion

A phase offset analysis using the zero-YORP model, shown in Figure 6.18, does not show any coherent change in phase offset. The second point, which corresponds to 2011/2012 data, may be an erroneous measurement as the double-peak shape of the lightcurve could cause a $\sim$90° shift in measured phase offset to appear to be a good fit due to the low quality of the data. The remaining points are consistent with constant-period rotation, indicating that LY's spin-state did not change significantly between 2007 and 2022. A YORP acceleration greater than $\sim 2 \times 10^{-8}$ rad/day^2 can be ruled out, but very small YORP torques remain a possibility.

After the completion of this analysis, Warner and Stephens (2021b) reported that 1994 LY is a binary system. The secondary's orbital period is unclear, with disparate solutions of 16.6 h and 48.5 h. The primary's rotation period is consistent with the period measured in this work. The secondary-to-primary diameter ratio is estimated

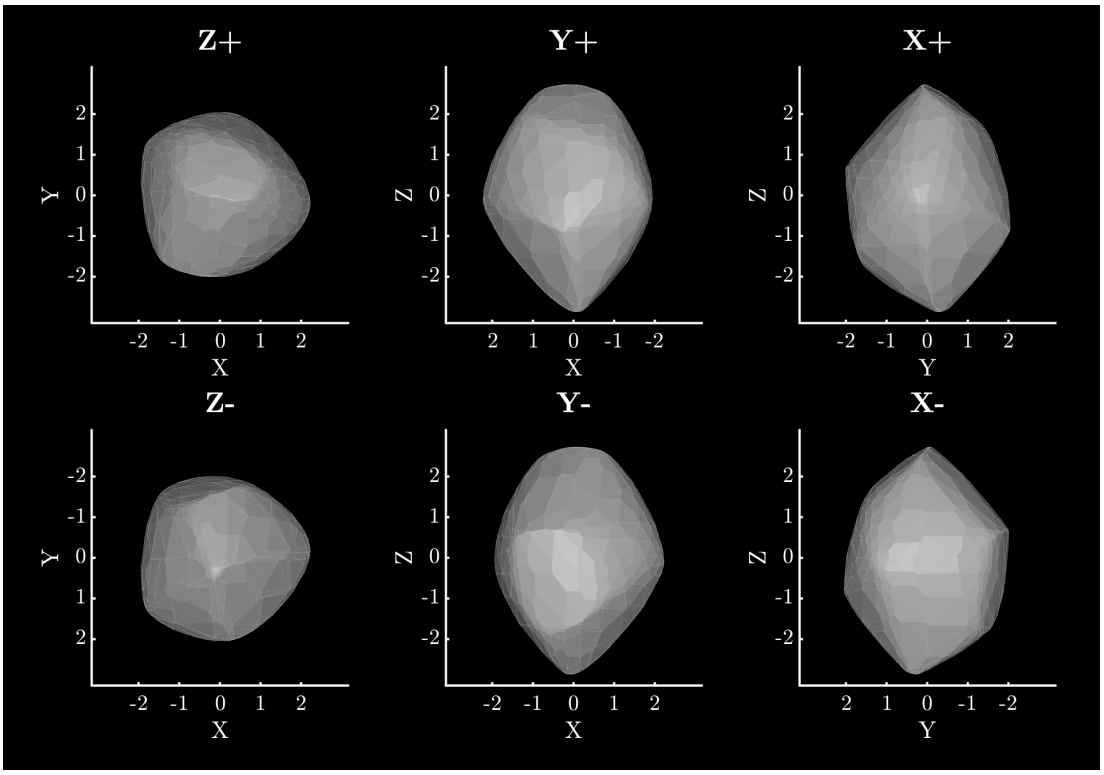

Figure 6.15: The best-fit convex hull model of (85275) 1994 LY, with a YORP acceleration of -11.0×10^{-8} rad/day^2. This model, which was developed assuming principal-axis rotation, has its rotational pole at $\lambda = 80°$, $\beta = -40°$, with sidereal period of 2.6970 ± 0.0001 h. The top row shows the model from the positive end of the Z, Y and X axes in the body-centric co-ordinate system. The bottom row shows the model from the negative end of the Z, Y and X axes. The Z-axis is aligned with the rotational pole, which is the shortest axis of inertia. The X-axis is arbitrarily set such that it is viewed from the positive end for the plane-of-sky at T_0. Axis lengths are in arbitrary units, as lightcurve inversion does not produce scaled models.

to be greater than 0.26, which corresponds to a photometric signal contribution of 0.07 magnitudes.

The presence of a secondary may have affected the physical model, and the subsequent YORP analysis. Due to the uncertain nature of LY's secondary, it is difficult to assess how this may have affected the results of this work. The measured convex shape and pole solution should be treated with caution in any further analysis. If radar imaging data were available, a more comprehensive model of the system could be developed, utilising the data collected for this work to search for BYORP in the system.

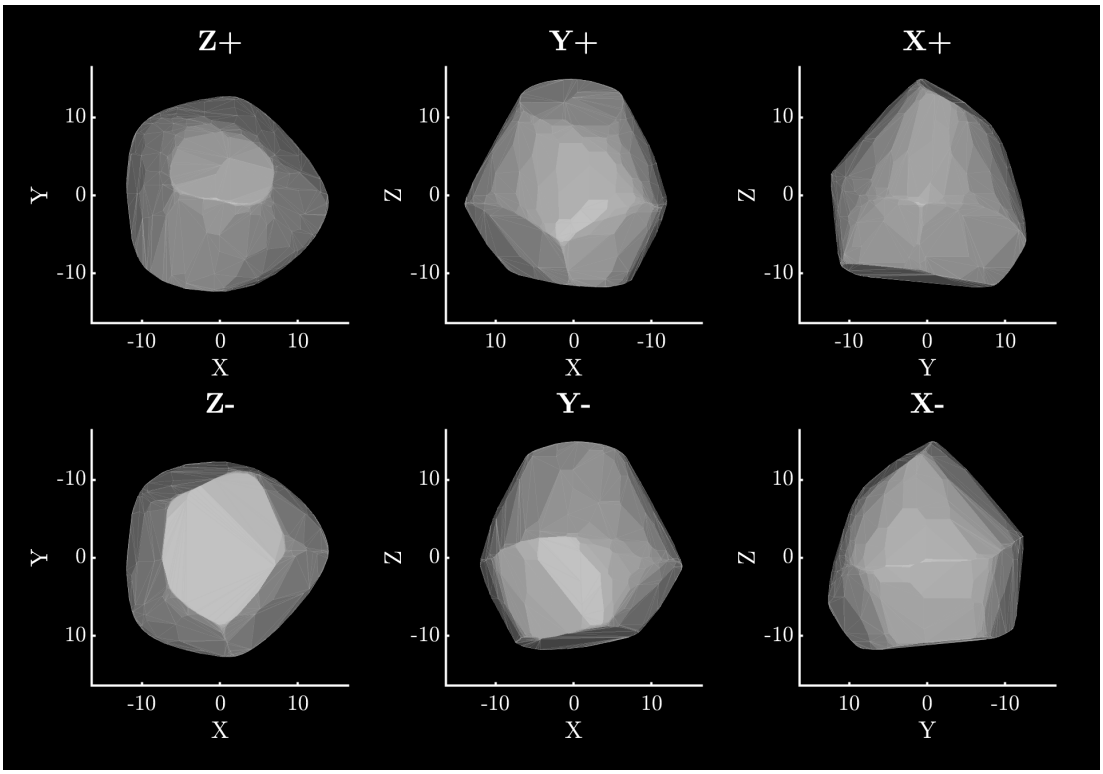

Figure 6.16: The same as Figure 6.15, but for the best fitting zero-YORP model. This model also has its pole at $\lambda = 80°$, $\beta = -40°$ with a sidereal rotation period of 2.6970 ± 0.0001 h.

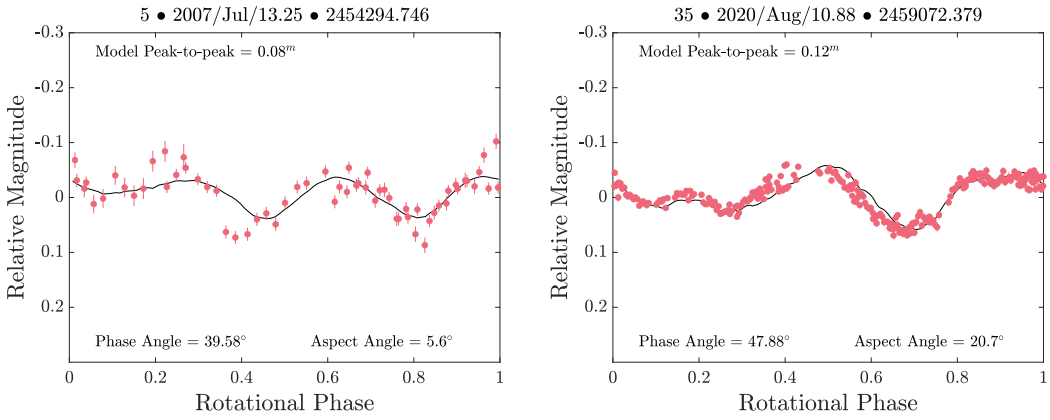

Figure 6.17: A comparison of observational data (red points) and the corresponding synthetic lightcurve (solid black line) for lightcurves 8 & 54 in Table 6.2. The synthetic lightcurve was generated using the convex hull model for 1994 LY, using a combination of the Lambertian and Lommel-Seeliger scattering models. For plots of all 46 lightcurves that were used to fit the model, see Figure A.13.

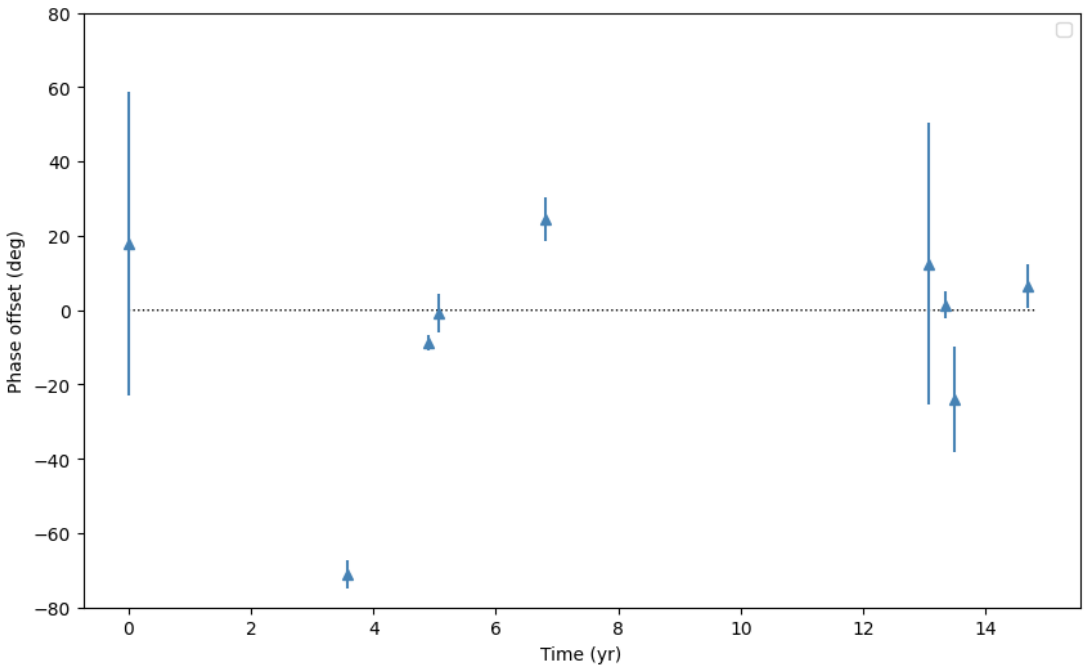

Figure 6.18: Phase offset measurements for (85275) 1994 LY. These phase offset measurements correspond to averaged phase offsets, which were separated such that there are no more than 30 days between observations within each group. Blue triangular markers indicate these measurements. A dashed black line shows constant-period rotation.

The next close approach for LY is in 2033, with a minimum separation of 48 lunar distances. This is an excellent opportunity to conduct further optical observations, but likely too distant for radar imaging. Considering the extensive lightcurve data that are available for LY, it remains a good candidate for future study of its secondary and the potential influence of YORP on the system.

CHAPTER 7

CONCLUSIONS & FUTURE WORK

7.1 Summary of findings

The primary motivation of this work was to detect and measure the YORP effect acting on small near-Earth asteroids, to expand the small sample of YORP detections that are informing theories of the Solar System's evolution. The methods used to search for YORP require that the asteroid's physical properties are characterised, and so this work has focused on measuring the shape, spin-state, size, surface composition and thermal properties of asteroids. This is a valuable exercise in its own right, as relatively few asteroids have been analysed with the detail presented in this work. Characterising asteroids helps build a picture of the overall population, produces analogues for other bodies, and more broadly informs understanding of the physical evolution of small bodies in the Solar System.

Four asteroids are highlighted in this work, although it should be noted that ancillary observations and analysis were also conducted as part of the wider YORP campaign and other related small bodies research programmes. The author conducted or otherwise supported observations of 18 YORP targets, and directly contributed to a published analysis of the YORP campaign target (2102) Tantalus (Rożek et al., 2022). Of the four asteroids presented here, two were subject to a particularly detailed analysis (Chapters 4 & 5), resulting in one publication (Dover et al., 2023) and one promising result that will be submitted for publication in the near future. The other two asteroids (Chapter 6) were analysed as far as is practicable with the available data, producing valuable results that have played a key role in one publication (Jackson et al., 2022) and will likely be used in future work (Lowry et al., 2025 in prep.). A total of five new publication-quality shape models were developed during this work, which are shown in Figure 7.3.

The comprehensive analysis of (23187) 2000 PN9 (Chapter 4; Dover et al. (2023)) used a combination of radar, optical and thermal observations to characterise the asteroid at a level of detail that has only been exceeded for a handful of asteroids that

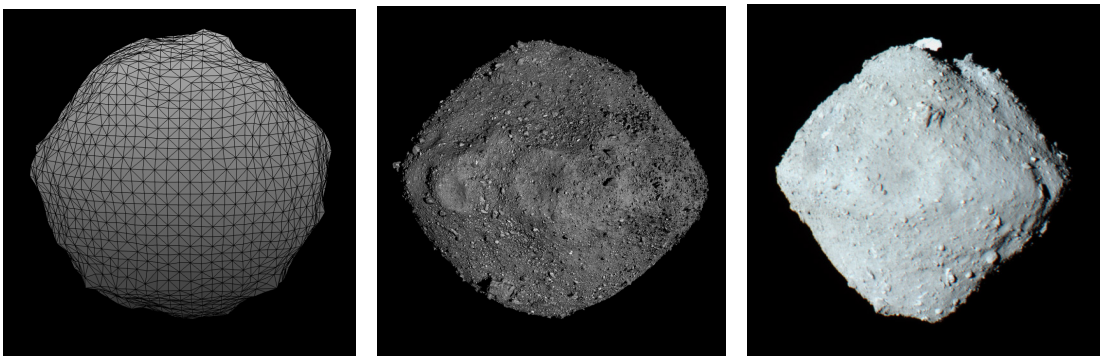

(a) (23187) 2000 PN9 (b) (101955) Bennu (c) (162173) Ryugu

Figure 7.1: A comparison showing the similarity between (23187) 2000 PN9 and other well-studied YORPoids. Images: ESA/NASA/Goddard/University of Arizona/JAXA

haven't been visited by spacecraft. Despite being a YORP non-detection, there is evidence that PN9 is a YORP-evolved object on the verge of spin-breakup but may be trapped in a state of YORP equilibrium or self-limitation. This has significant implications for YORP theory - including TYORP - as asteroids in this state are critical to explaining evolutionary pathways for small bodies in the Solar System. Furthermore, PN9 bears a striking resemblance to several asteroids that were visited by spacecraft during the course of this work: (101955) Bennu, (162173) Ryugu, (65803) Didymos, and (152830) Dinkinesh. Similarities and differences between PN9 and these asteroids, which are highlighted in Figure 7.1, could reveal important clues about the physical processes that shaped these bodies.

Fast-rotating top-shaped bodies are common among the sampled population, despite observational biases against them. Objects falling into this category are a known outcome of YORP evolution, which dominates the overall physical evolution of small asteroids, thus they are likely to be common in the overall population. While there is not yet a debiased sample of asteroid shapes, it follows that PN9 is likely to be representative of a significant fraction of the near-Earth asteroid population.

The second major component of this work, focusing on (29075) 1950 DA (Chapter 5), has produced promising results that enable substantial future work. The key results from this work are shown in Figure 7.2; following up on results from Zegmott

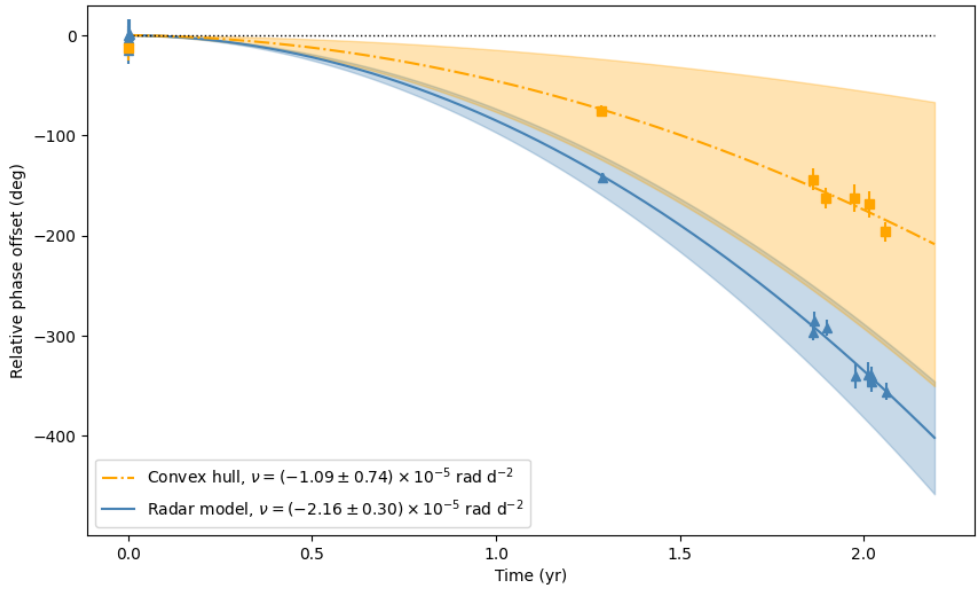

Figure 7.2: A comparison between the two phase offset derived YORP fits for 1950 DA. This figure combines the results presented in Figures 5.7 & 5.13, which are the key results from Chapter 5. The phase offset measurements are shown with orange square markers and blue triangular markers for the convex hull and radar models respectively, and YORP fits with dash-dot and solid lines respectively. Shaded regions correspond to uncertainty in the YORP fit; note the slight overlap between the two fits.

(2021), a subsequent and significant observing campaign verified that DA appears to be experiencing a rapid and constant rate of rotational deceleration, exceeding what is possible with known physical mechanisms. This presents a significant challenge, which will either reveal new physical processes or an unusual edge case for a false positive, which may still depend upon a hitherto unknown physical phenomenon. In either case, the outcome will be beneficial to the field of small bodies research. The study on DA has grown beyond the scope of this thesis, which has paved the way for several avenues of investigation in future work. A recent report from Sean Marshall (priv. comm.) indicates that another asteroid, (3200) Phaethon, is experiencing a rate of constant spin-up that is too strong to be caused by YORP, which could be related to what has been seen for 1950 DA.

At the time of writing, it is intended that the results for DA will be prepared for publication in the near future. These results will be published with a view that by

opening the problem to the community, new insights might offer an explanation for the rate of DA's apparent spin-down.

Finally, the analyses of (159402) 1999 AP10 and (85275) 1994 LY (Chapter 6) have also produced valuable results. As part of this work, a viable physical model was developed for AP10 using lightcurve data from a single apparition (Jackson et al., 2022). While the model was later refined with additional data, it is rare for a single apparition to be utilised so effectively. If a third epoch of lightcurve data can be captured in the future, ideally during the 2031 apparition, the results of this work are sufficient for simply extending the phase offset analysis with the existing model to measure YORP.

The modelling of LY has produced new results, although a more comprehensive analysis is held back by uncertainty as to the nature of its secondary. The data taken for this work will prove to be extremely valuable in future work to characterise the binary system, as the high-quality lightcurves could be used to constrain the primary and secondary periods. Using these periods, it may be possible to use the extensive long-baseline data for LY to search for BYORP, using a new model constructed with secondary-subtracted lightcurves.

While this work did not yield any robust YORP detections, its contributions to the field are nevertheless worthwhile, and future work stemming from this thesis will produce new results for the asteroids analysed here. It is difficult to determine a non-detection rate for YORP analyses, as many are presumed to remain unpublished, but it is likely to be high. The asteroids that are selected for these studies generally consist of 'low hanging fruit', but often prove to be more complicated than expected. It is important to report non-detections and investigate less obvious targets, lest a bias is formed in the sample of well-characterised NEAs. This can include large symmetric objects like PN9, which are critical to developing evolutionary YORP theory, or targets like 1999 AP10 which require intensive observing strategies with low chance of detection.

Nevertheless, the follow-up campaign for 1950 DA has proven that rotational accel-

eration can be measured over relatively short baselines. As that acceleration is unlikely to be secularly induced by YORP, this work (alongside Zegmott (2021)) is the most significant development to date in what could be the first detection of a new physical phenomenon that is more dominant than a secular YORP effect. While this author still considers a false positive to be more likely, the implications of a genuine detection are simply too great to ignore.

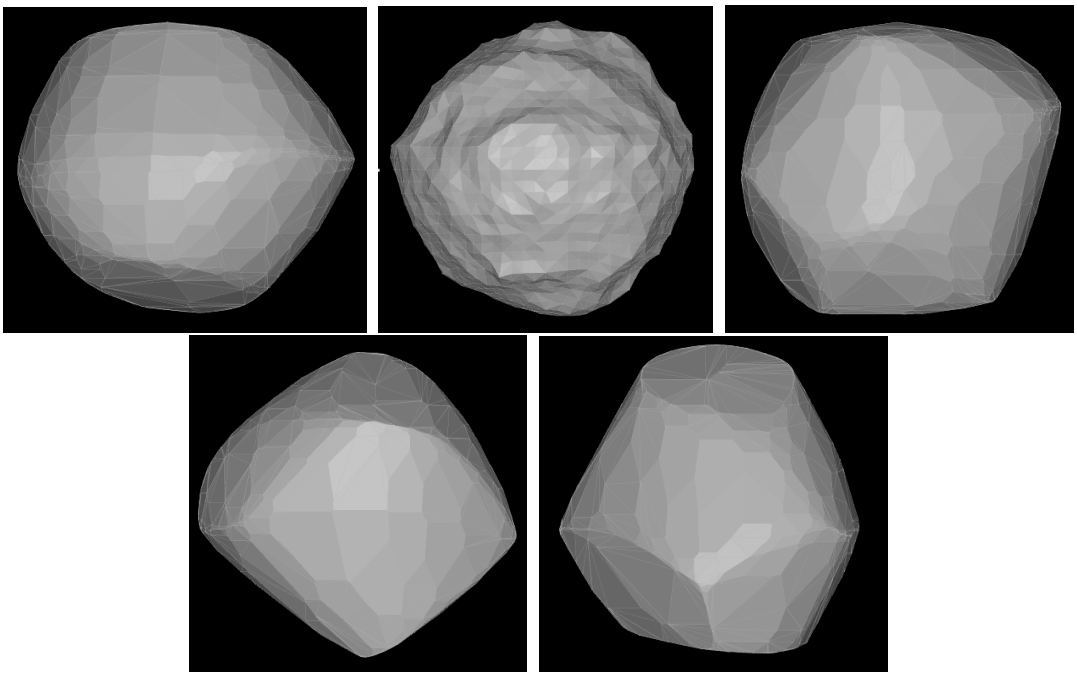

Figure 7.3: A montage of shape models developed as part of this work. Clockwise, they are: (23187) 2000 PN9 (convex); (23187) 2000 PN9 (radar); (29075) 1950 DA; (85275) 1994 LY; and (159402) 1999 AP10.

7.2 The future of asteroid characterisation & YORP research

During the course of this work, which began in 2019, there have been several major developments in the field. The most dramatic moments came from various missions to visit asteroids with spacecraft, with four missions sending back new data, two of which also returned samples to Earth.

7.2.1 Missions to small bodies

The first of these missions were the Hayabusa2 and OSIRIS-REx missions, which were already orbiting their targets when this work began. They continued to provide new insights that are relevant to this work, perhaps most notably with the observation of activity on Bennu caused by thermal fracturing of surface boulders (Lauretta et al., 2019b) and a preliminary detection of seasonal YORP variance on Bennu (M.C. Nolan, priv. comm.). Both of these missions returned samples to Earth during the course of this work, which have already produced exciting results, such as the discovery of amino acids in the Bennu sample (Glavin et al., 2025). Analysis of data from these missions, both from spacecraft data and laboratory analysis of the samples, will continue to provide new results over the coming years. New insights into the physical evolution of these asteroids, and the role of YORP, are extremely valuable to the field.

The third mission to take place during this work was the Double Asteroid Redirection Test (DART), which was a planetary defence mission to test the effectiveness of using impactors to modify an asteroid's orbit. Targeting Dimorphos, which is a companion of (65803) Didymos, the DART and LICIACube spacecraft broadcast imaging data of both bodies in the moments before and after impact respectively. These data caused immediate surprise when the shape of Didymos was clearly seen to be more elongated than radar models had predicted (Naidu et al., 2020; Daly et al., 2023). This has triggered discussion about the accuracy of radar models, which will ultimately lead to improvements in shape modelling techniques and an assessment of existing models.

Post-impact observations of the system have revealed that ejecta made a bigger contribution to the momentum transfer than the impact itself (Cheng et al., 2023). Dimorphos is thought to have experienced changes to both its shape and spin-state (Richardson et al., 2024; Pravec et al., 2024), the understanding of which will be critical to understanding how impacts affect the physical and spin-state evolution of small bodies. At the time of writing, the Hera mission (Michel et al., 2022) is en route to

Didymos, where it will provide a post-impact characterisation of the system. Observations of an expected impact crater will reveal information about the internal structure of Dimorphos, and the system may continue to change - through resurfacing and spin stabilisation - during the course of Hera's mission. Scheduled to arrive in December 2026, Hera may prove to be one of the most important missions of its generation.

The last of these four missions is Lucy, which conducted a flyby of (152830) Dinkinesh in November 2023. This is the first of eight systems that the spacecraft will visit over a thirteen-year mission. The Dinkinesh flyby provided another surprise to the community, with Lucy's imagery showing that the asteroid is in fact a binary system. The companion, since named Selam, is a contact binary. Using BYORP simulations to reproduce the current orbit, Merrill et al. (2024) shows that Selam is significantly younger than Dinkinesh. This is consistent with the claim that Dinkinesh, which is an archetypal spinning-top with a prominent equatorial ridge, gained its shape through YORP-induced mass shedding (Levison et al., 2024b), with the lost mass reforming into the present-day companion. The complexity of this YORP-evolved main belt asteroid pair was wholly unexpected, once again highlighting the shortcomings of purely ground-based observations and emphasising the importance of the YORP effect. With seven more flybys scheduled over the coming decade, there is potential for more surprising results from Lucy.

In addition to missions that reached asteroids during this work, several other visits to asteroid systems are already underway: the Psyche mission is en route to the large and metallic (16) Psyche; OSIRIS-APEX is en route to the infamous (99942) Apophis; and there is a possibility that the New Horizons spacecraft will conduct a flyby of a Kuiper Belt Object in the next few years.

The proliferation of inexpensive launch vehicles is providing new opportunities to explore the Solar System, and an accelerated pace of discovery can be expected. There are currently four missions planning to launch before 2030: Brokkr-2 is launching to an NEA this year; Tianwen-2 is planning to return a sample of (469219) Kamo'oalewa

to Earth by 2026; DESTINY+ will visit (3200) Phaethon, an asteroid which has been discussed in this thesis; Ramses will visit Apophis in 2029; and MBR Explorer plans to conduct flybys of six MBAs and land on a seventh. There is also the upcoming Comet Interceptor mission, which aims to visit a dynamically new comet, or possibly an interstellar object.

In the opinion of this author, near-future missions should focus on visiting larger numbers of asteroids, even if that means sacrificing the depth of investigation that each target is subjected to. To put it simply, knowing a lot about one asteroid isn't more useful than knowing a little about lots of asteroids. Missions such as OSIRIS-REx have undoubtedly had a huge impact in the field, but they are expensive, which in turn makes them risk-averse, subject to political pressures, and prone to delays. With so few asteroids having been visited by spacecraft, there would be an enormous benefit to having 'scout' missions provide a snapshot of hundreds of asteroids over the next 50 years. This is not to say that there should not be more 'flagship' missions to conduct in-depth studies of individual asteroids, but technological advances have widened the scope of what is now possible with smaller missions, so exploration strategies must adapt accordingly.

Unfortunately, recent developments in spaceflight have not all been positive for astronomy. As discussed in Section 2.2.3, the rise of megaconstellations is having a substantial impact on ground-based observatories. Despite substantial mitigation efforts from the community, the situation is likely to worsen over the coming decades, with the discovery, monitoring and characterisation of small bodies being increasingly hampered by commerical activity. Nevertheless, near-future observatories are going to be crucial to the future of small bodies research.

7.2.2 Future observatories

There are several upcoming observatories, or upgrades to existing observatories, that are particularly promising for the field. Perhaps the most eagerly awaited of these is

the Vera C. Rubin Observatory, which will soon begin the Legacy Survey of Space and Time (LSST). The LSST will dramatically increase the rate at which NEAs are discovered and characterised, with an anticipated order of magnitude increase in the number of objects with measured colours, rotation periods and convex shapes (Jones, 2015; Schwamb et al., 2018). These measurements will drive a significant increase in the number of Yarkovsky and YORP detections.

A new generation of extremely large telescopes is also on the horizon, with Extremely Large Telescope (ELT), Thirty Metre Telescope (TMT), and Giant Magellan Telescope (GMT) all expected to be operational within the next decade. With imaging resolutions as high as tens of milliarcseconds, these facilities will be able to resolve the shapes of asteroids and, in some cases, map their surfaces. Using high-resolution spectrographs, it will be possible to measure the distribution of surface materials across the surface of a small body. The measurement of chemical and topological variegation on an asteroid's surface will be invaluable to YORP theory, as current simulations of an asteroid's thermal response are, in most cases, limited to modelling with surface-averaged measurements.

The sensitivity of these new facilities will also allow them to take high-quality lightcurves of fainter objects, allowing for additional viewing angles and phase offset measurements outside of favourable apparitions. This will considerably reduce the minimum temporal baseline required for YORP detection on NEAs, especially for those that do not regularly make close approaches to Earth.

With the recent decommissioning of NEOWISE, there is a clear need for a new infrared space telescope dedicated to studying NEOs. Fortunately a successor, NEO Surveyor, is scheduled to launch in 2027. This telescope is a significant upgrade over NEOWISE, offering more detailed thermal characterisation of small bodies while being free of the operational limitations experienced by NEOWISE.

Other space telescopes, which were not specifically designed to observe small bodies, have also contributed to YORP research. Most significantly, the Hubble Space Tele-

scope played a critical role in the detection of YORP acceleration on Bennu (Nolan et al., 2019). It is hoped that the James Webb Space Telescope, and upcoming Nancy Grace Roman Space Telescope, will also be used to make direct detections of the YORP effect.

Space-borne transiting exoplanet surveys have also proven to be useful for characterising asteroids, with Transiting Exoplanet Survey Satellite (TESS) data having been used to construct asteroid lightcurves to measure rotational properties (Pál et al., 2018; Vavilov and Carry, 2025). Further exploitation of TESS data will produce new results in the coming years, while upcoming missions such as Planetary Transits and Oscillations of Stars (PLATO) and Atmospheric Remote-sensing Infrared Exoplanet Large-survey (ARIEL) will provide even more photometric data.

The future of planetary radar is less certain. The collapse of Arecibo in 2020 left a gaping hole in the community, leaving the ageing GSSR as the only operational planetary radar system. Since then, the community has been developing new capabilities for existing facilities, to form 'stop-gap' solutions to rebuild capacity until a true Arecibo successor can be built. These solutions all rely on using separate transmitters and receivers to conduct bi-static observations of NEAs.

The first of these is a pairing of Goldstone with various receivers in Europe (Pupillo et al., 2023), which serves as a technology demonstrator for a proposed development of more comprehensive European Space Agency (ESA) planetary radar capabilities.

In Australia, 12 m dishes were able to detect echoes from signals transmitted by the Canberra Deep Space Communication Complex (White et al., 2025). While it does not yet compare to observations made with Goldstone's transmitter, it is the only known system fully outside of the United States that is capable of using radar to detect asteroids.

The most promising development for has been the successful testing of a new 700 W transmitter on the Green Bank Telescope, which is a 100 m steerable dish that

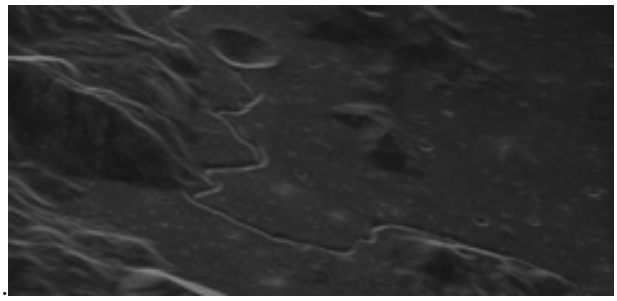

Figure 7.4: A radar image of the Moon taken with the Green Bank - VLBA bi-static system, showing the Apollo 15 landing site. This image, which was reproduced from Wilkinson et al. (2022), has a resolution of 5 m per pixel.

has previously been used for bi-static observations with Goldstone and Arecibo. This new transmitter has been used in conjunction with ten 25 m Very Long Baseline Array (VLBA) receivers to produce the highest-ever resolution images of the moon taken from Earth (shown in Figure **??**), and to detect the asteroid 2001 FO32 (Wilkinson et al., 2022). This pilot programme has shown the viability of installing a more powerful ($\sim$10 kW) transmitter (Taylor et al., 2023), which could be paired with receivers from the upcoming Next Generation Very Large Array (ngVLA) for bi-static observations (Taylor, 2023). Dubbed the Next Generation Planetary Radar System, this would be an upgrade over both previous and current capabilities, but it is still not a like-for-like replacement for Arecibo.

Roshi et al. (2023) proposes a Next Generation Arecibo Telescope (NGAT), which is a phased array of steerable 13 m dishes built on the site previously occupied by the 300 m Arecibo dish. There are several key advantages to this design, the first being that the Arecibo site already has existing infrastructure and both regulatory and popular approval for a large astronomical facility. This significantly reduces the time and resources that need to be committed before construction begins, and revives the educational and economic benefits of radar astronomy that were previously welcomed by the people of Puerto Rico. In an era when astronomers must consider the wishes of the local population - as so controversially highlighted by TMT - the value of local support cannot be overstated.

The second advantage of NGAT is that it mitigates the reliability issues that have plagued Arecibo and Goldstone. The bespoke nature of such powerful transmitters

means that part failures - particularly high-power klystrons - can cause months of downtime while replacements are procured, with no additional production capacity to generate spares. In a phased array, a component failure only means losing one dish, instead of the entire instrument. The lower power of each individual transmitter should dramatically reduce failure rates, and spares are more easily generated using 'off-the-shelf' components. Compared to an equivalent single dish, this design is cheaper to build, maintain and upgrade while having less downtime.

Thirdly, a fully steerable array would provide better sky coverage than the original fixed dish at Arecibo, and it would be able to slew faster than large steerable dishes like Green Bank. Finally - although further advantages remain undiscussed - the phased array would provide a greater resolution, frequency range and field of view over the original Arecibo telescope. These benefits would not exclusively benefit radar astronomers either, as these capabilities would make NGAT a prominent facility for radio astronomy and atmospheric research.

7.2.3 Modelling and theory

Running parallel to the need for new observational facilities, there is high demand for new computational tools and techniques that can process data more efficiently. There is currently a significant backlog of optical, thermal and radar observations that will continue to grow as new facilities become operational. The bottleneck in processing these data is caused by a finite capacity for human involvement, so automation is a high priority for the field.

For optical datasets, it is relatively straightforward to automate `convexinv` to develop basic models for large numbers of asteroids with minimal human involvement. While not as reliable as human-supervised modelling, the sheer volume of lightcurve data means that it is not feasible to manually model every asteroid. The most complex task is to extract or collate lightcurves from multiple sources, as they are spread across various databases (e.g. ALCDEF or the ESO archive), or in some cases not published

at all. This has been an ongoing frustration for the YORP campaign, as lightcurve data have to be pieced together from a mix of public and private sources, then converted into a standard format. There is also no general lightcurve extraction pipeline that can be used on any telescope, with some observatories such as PIRATE having excellent pipelines (Jackson et al., 2021) while others have nothing at all.

The most straightforward solution is to only consider data from a single telescope or survey, such as TESS or LSST, where full lightcurve datasets can be automatically extracted for thousands of objects and fed into `convexinv`. This strategy has already been used to develop shape models en-masse (Ďurech et al., 2018b; Hanus and Durech, 2024; Vavilov and Carry, 2025), and is likely to represent the future of optical asteroid characterisation. Nevertheless, the best option would be to develop an advanced general lightcurve extraction pipeline and a more comprehensive database of lightcurve data, although this of course runs the risk of just creating yet another database to further divide public data.

For radar data, there is still a human bottleneck but the situation is reversed. The data generally come from one or two facilities, and each object will only have a handful of observations. The issue is that `SHAPE` requires extensive human supervision and cannot feasibly be automated in its current form, while the software is not well optimised for modern hardware. There are only a few dozen researchers that have been trained to use `SHAPE`, and even fewer that can be considered to be `SHAPE` experts. Only a handful of robust radar shape models are produced every year, and it is unlikely that the pool of researchers be able to grow fast enough to keep up with the data produced by future facilities.

Engels et al. (2020) presents `CUDA-SHAPE`, which is an evolution of the original `SHAPE` that has been optimised for modern hardware. Using a GPU-accelerated fitting mode, it was able to model two asteroids 18.6x faster than the original `SHAPE` with no loss in accuracy. While this does not directly address the human bottleneck, shorter compute times allow researchers to more flexibly allocate their time. It is hoped that the

development of `CUDA-SHAPE` will continue in preparation for a public release.

Bartczak and Dudziński (2018) presents a new algorithm for modelling asteroids using lightcurve data. Aside from measuring spin-state, `Shaping Asteroid models using Genetic Evolution` (SAGE) is able to fit non-convex shapes from optical data alone. More recently, SAGE has incorporated features from `SHAPE` to produce models that combine optical and radar data (Bartczak et al., 2024). This method is able to fit models faster than `SHAPE`, and provides better uncertainty estimates for a model's geophysical properties. This promising development could have a major impact on the field.

Taking a more ambitious approach, Rożek et al. (2019c) presents a prototype and future pathway for the development of a machine learning model that could process radar data to produce spin and shape information with minimal human supervision. This would greatly increase the community's capacity for producing radar shape models, but it requires a significant initial investment. Recent breakthroughs in artificial intelligence research are reducing the cost of this investment, and the development of a neural network for shape modelling may have applications beyond NEA research. As such, the development of a machine learning based solution should be a top priority.

Finally, `All-Data Asteroid Modelling` (ADAM) (Viikinkoski et al., 2015a; Viikinkoski et al., 2015b) can develop non-convex shape models using a wide variety of data sources, including lightcurves, radar imaging, and resolved optical or thermal imaging (e.g. from SPHERE). This software is responsible for a substantial number of shape models (Hanuš et al., 2017; Vernazza et al., 2021), and is the most comprehensive current tool for developing asteroid shape models, but it has not displaced `convexinv` or `SHAPE` as they are generally seen as better options for less diverse datasets.

Looking towards the future of YORP theory, significant developments have been made in simulating the TYORP effect. As discussed in Chapter 4, simulations have shown that YORP cycles can be broken by the TYORP effect. For asteroids with highly irregular shapes, TYORP will sometimes cancel out NYORP and lock the body

into a state of rotational equilibrium (Golubov and Scheeres, 2019; Golubov et al., 2020). With up to 20% of asteroids estimated to be trapped in these 'sinks', TYORP is potentially responsible for a major evolutionary terminus.

Considering these developments in TYORP theory, there is an emerging need for more published YORP non-detections on well-characterised asteroids. If an irregularly-shaped asteroid was found to have constant-period rotation, despite the expectation of a strong NYORP component, then it would be a strong candidate TYORP sink object. These objects would be excellent benchmarks for testing YORP theory, as simulating TYORP and NYORP forces on the asteroid should yield equal and opposite torques.

For asteroids where YORP is detected, the NYORP and TYORP components cannot be isolated. There may be cases, however, where the two components can be heavily constrained via a YORP detection on a well-characterised YORPoid, as these objects are known to have a near-zero NYORP torque. Golubov and Lipatova (2022) shows that on Ryugu, TYORP could be up to ∼70x stronger than NYORP. A YORP detection on an asteroid like Ryugu would enabled well-constrained estimates of the strength of the TYORP effect.

Another development during this work is the proposal of a crater YORP effect (CYORP) (Zhou et al., 2022), which was previously discussed in Chapter 1. Subsequently, a theoretical boulder-induced YORP component has been presented (Baker and McMahon, 2024). Research is increasingly showing that YORP is highly dependent on small-scale surface effects, adding additional layers of complexity as various thermal phenomena work together or against each other to produce a net torque. There is much work to be done in understanding the various components of the YORP effect, with developments likely to come from a combination of theory and measurements of asteroid surfaces.

Aforementioned observational evidence of BYORP in the Dinkinesh and 2001 SL9 systems (Scheirich et al., 2021; Merrill et al., 2024), have also highlighted the importance of this effect. It is only a matter of time before a body of robust BYORP

detections is built up, which will provide new insights into the rate at which binary systems form and how long they survive.

Finally, there are continuing theoretical developments considering the role of extra-solar YORP in polluting planetless white dwarfs (Veras et al., 2021; Veras et al., 2022). As these models advance, cases may emerge where it can be stated with confidence that observed features of certain stellar systems are caused by the YORP-driven breakup of small bodies.

BIBLIOGRAPHY

Gordana Apostolovska, Violeta Ivanova, and Andon Kostov (Jan. 2009). "CCD Photometry of 967 Helionape, 3415 Danby, (85275) 1994 LY, 2007 DT103, and 2007 TU24". *Minor Planet Bulletin* 36.1, pp. 27–28.

I. Appenzeller, K. Fricke, W. Fürtig, W. Gässler, R. Häfner, R. Harke, H. -J. Hess, W. Hummel, P. Jürgens, R. -P. Kudritzki, K. -H. Mantel, W. Meisl, B. Muschielok, H. Nicklas, G. Rupprecht, W. Seifert, O. Stahl, T. Szeifert, and K. Tarantik (Dec. 1998). "Successful commissioning of FORS1 - the first optical instrument on the VLT." *The Messenger* 94, pp. 1–6.

Dahlia Baker and Jay McMahon (Aug. 2024). "Asteroid Obliquity Evolution due to Boulder-Induced YORP". *AAS/Division of Dynamical Astronomy Meeting*. Vol. 56. AAS/Division of Dynamical Astronomy Meeting, 500.02, p. 500.02.

P. Bartczak and G. Dudziński (Feb. 2018). "Shaping asteroid models using genetic evolution (SAGE)". *MNRAS* 473.4, pp. 5050–5065. DOI: 10.1093/mnras/stx2535.

Przemysław Bartczak, Agata Rożek, Richard Edmund Cannon, Mike Nolan, Adriano Campo Bagatin, Po-Yen Liu, and Paula Benavidez (Sept. 2024). "Synergy between SAGE and SHAPE algorithms for modelling the physical parameters of asteroids."

European Planetary Science Congress, EPSC2024-326, EPSC2024–326. DOI: 10.5194/epsc2024-326.

M. A. Barucci, A. Cellino, C. De Sanctis, M. Fulchignoni, K. Lumme, V. Zappala, and P. Magnusson (Dec. 1992). "Ground-based Gaspra modelling - Comparison with the first Galileo image". *A&A* 266.1, pp. 385–394.

M. A. Barucci, E. Dotto, and A. C. Levasseur-Regourd (Nov. 2011). "Space missions to small bodies: asteroids and cometary nuclei". *A&A Rev.* 19, 48, p. 48. DOI: 10.1007/s00159-011-0048-2.

Tracy M. Becker, Ellen S. Howell, Michael C. Nolan, Christopher Magri, Petr Pravec, Patrick A. Taylor, Julian Oey, David Higgins, Jozef Világi, Leonard Kornoš, Adrián Galád, Štefan Gajdoš, Ninel M. Gaftonyuk, Yurij N. Krugly, Igor E. Molotov, Michael D. Hicks, Albino Carbognani, Brian D. Warner, Frederic Vachier, Franck Marchis, and Joseph T. Pollock (Mar. 2015). "Physical modeling of triple near-Earth Asteroid (153591) 2001 SN_{263} from radar and optical light curve observations". *Icarus* 248, pp. 499–515. DOI: 10.1016/j.icarus.2014.10.048.

George Beekman (Aug. 2005). "The nearly forgotten scientist Ivan Osipovich Yarkovsky". *Journal of the British Astronomical Association* 115.4, p. 207.

Irina N. Belskaya, Sonia Fornasier, and Yurij N. Krugly (May 2009). "Polarimetry and BVRI photometry of the potentially hazardous near-Earth Asteroid (23187) 2000 PN9". en. *Icarus* 201.1, pp. 167–171. DOI: 10.1016/j.icarus.2008.12.026.

Lance Benner (2020). *Goldstone Radar Observations Planning: (159402) 1999 AP10*. https://echo.jpl.nasa.gov/asteroids/1999AP10/1999ap10.2020.planning.html.

Lance A. M. Benner, Steven J. Ostro, Christopher Magri, Michael C. Nolan, Ellen S. Howell, Jon D. Giorgini, Raymond F. Jurgens, Jean-Luc Margot, Patrick A. Taylor, Michael W. Busch, and Michael K. Shepard (Dec. 2008). "Near-Earth asteroid surface roughness depends on compositional class". *Icarus* 198.2, pp. 294–304. DOI: 10.1016/j.icarus.2008.06.010.

Richard Berry and James Burnell (2005). *The handbook of astronomical image processing*. Vol. 2.

R. P. Binzel, F. E. DeMeo, E. V. Turtelboom, S. J. Bus, A. Tokunaga, T. H. Burbine, C. Lantz, D. Polishook, B. Carry, A. Morbidelli, M. Birlan, P. Vernazza, B. J. Burt, N. Moskovitz, S. M. Slivan, C. A. Thomas, A. S. Rivkin, M. D. Hicks, T. Dunn, V. Reddy, J. A. Sanchez, M. Granvik, and T. Kohout (May 2019). "Compositional distributions and evolutionary processes for the near-Earth object population: Results from the MIT-Hawaii Near-Earth Object Spectroscopic Survey (MITHNEOS)". *Icarus* 324, pp. 41–76. DOI: 10.1016/j.icarus.2018.12.035.

Richard P. Binzel, Andrew S. Rivkin, J. Scott Stuart, Alan W. Harris, Schelte J. Bus, and Thomas H. Burbine (Aug. 2004). "Observed spectral properties of near-Earth objects: results for population distribution, source regions, and space weathering processes". *Icarus* 170.2, pp. 259–294. DOI: 10.1016/j.icarus.2004.04.004.

Jürgen Blum and Gerhard Wurm (Jan. 2000). "Experiments on Sticking, Restructuring, and Fragmentation of Preplanetary Dust Aggregates". *Icarus* 143.1, pp. 138–146. DOI: 10.1006/icar.1999.6234.

William F. Bottke, David Vokrouhlický, David P. Rubincam, and David Nesvorný (May 2006). "THE YARKOVSKY AND YORP EFFECTS: Implications for Asteroid Dynamics". en. *Annual Review of Earth and Planetary Sciences* 34.1, pp. 157–191. DOI: 10.1146/annurev.earth.34.031405.125154.

E. Bowell, B. Hapke, D. Domingue, K. Lumme, J. Peltoniemi, and A. W. Harris (1989). "Application of Photometric Models to Asteroids". *Asteroids II*. Ed. by R. P. Binzel, T. Gehrels, and M. S. Matthews. Tucson: The University of Arizona Press, pp. 524–556.

S. Breiter and M. Murawiecka (May 2015). "Tumbling asteroid rotation with the YORP torque and inelastic energy dissipation". *MNRAS* 449.3, pp. 2489–2497. DOI: 10.1093/mnras/stv433.

M. Brozović, B. J. Butler, J. Margot, S. P. Naidu, and T. J. W. Lazio (Dec. 2018). "Planetary Bistatic Radar". *Science with a Next Generation Very Large Array*. Ed. by Eric Murphy. Vol. 517. Astronomical Society of the Pacific Conference Series, p. 113. DOI: 10.48550/arXiv.1810.08712.

Marina Brozović, Lance A. M. Benner, Patrick A. Taylor, Michael C. Nolan, Ellen S. Howell, Christopher Magri, Daniel J. Scheeres, Jon D. Giorgini, Joseph T. Pollock, Petr Pravec, Adrián Galád, Julia Fang, Jean-Luc Margot, Michael W. Busch, Michael K. Shepard, Daniel E. Reichart, Kevin M. Ivarsen, Joshua B. Haislip, Aaron P. LaCluyze, Joseph Jao, Martin A. Slade, Kenneth J. Lawrence, and Michael D. Hicks (Nov. 2011). "Radar and optical observations and physical modeling of triple near-Earth Asteroid (136617) 1994 CC". *Icarus* 216.1, pp. 241–256. DOI: 10.1016/j.icarus.2011.09.002.

Schelte J. Bus and Richard P. Binzel (July 2002). "Phase II of the Small Main-Belt Asteroid Spectroscopic Survey. A Feature-Based Taxonomy". *Icarus* 158.1, pp. 146–177. DOI: 10.1006/icar.2002.6856.

M. W. Busch, S. J. Ostro, L. A. M. Benner, and J. D. Giorgini (May 2006). "Radar Images and Shape Models of Asteroids 10115 (1992 SK), 23187 (2000 PN9) and 29075 (1950 DA)". *Society for Astronomical Sciences Annual Symposium* 25, p. 169.

Michael W. Busch, Jon D. Giorgini, Steven J. Ostro, Lance A. M. Benner, Raymond F. Jurgens, Randy Rose, Michael D. Hicks, Petr Pravec, Peter Kusnirak, Michael J. Ireland, Daniel J. Scheeres, Stephen B. Broschart, Christopher Magri, Michael C. Nolan, Alice A. Hine, and Jean-Luc Margot (Oct. 2007). "Physical modeling of near-Earth Asteroid (29075) 1950 DA". *Icarus* 190.2, pp. 608–621. DOI: 10.1016/j.icarus.2007.03.032.

Michael W. Busch, Steven J. Ostro, Lance A. M. Benner, Marina Brozovic, Jon D. Giorgini, Joseph S. Jao, Daniel J. Scheeres, Christopher Magri, Michael C. Nolan, Ellen S. Howell, Patrick A. Taylor, Jean-Luc Margot, and Walter Brisken (Apr. 2011). "Radar Observations and the Shape of Near-Earth Asteroid 2008 EV5". *Icarus* 212.2. arXiv: 1101.3794, pp. 649–660. DOI: 10.1016/j.icarus.2011.01.013.

D. Čapek and D. Vokrouhlický (Dec. 2004). "The YORP effect with finite thermal conductivity". *Icarus* 172.2, pp. 526–536. DOI: 10.1016/j.icarus.2004.07.003.

V. Carruba, S. Aljbaae, and A. Lucchini (Sept. 2019). "Machine-learning identification of asteroid groups". *MNRAS* 488.1, pp. 1377–1386. DOI: 10.1093/mnras/stz1795.

B. Carry (Dec. 2012). "Density of asteroids". *Planet. Space Sci.* 73.1, pp. 98–118. DOI: 10.1016/j.pss.2012.03.009.

A. Cellino, V. Zappala, and P. Farinella (Apr. 1989). "Asteroid shapes and lightcurve morphology". *Icarus* 78.2, pp. 298–310. DOI: 10.1016/0019-1035(89)90178-4.

C. R. Chapman, D. Morrison, and B. Zellner (May 1975). "Surface Properties of Asteroids: A Synthesis of Polarimetry, Radiometry, and Spectrophotometry". *Icarus* 25.1, pp. 104–130. DOI: 10.1016/0019-1035(75)90191-8.

A. F. Cheng, P. Michel, M. Jutzi, A. S. Rivkin, A. Stickle, O. Barnouin, C. Ernst, J. Atchison, P. Pravec, D. C. Richardson, and AIDA Team (Feb. 2016). "Asteroid Impact & Deflection Assessment mission: Kinetic impactor". *Planet. Space Sci.* 121, pp. 27–35. DOI: 10.1016/j.pss.2015.12.004.

Andrew F. Cheng, Harrison F. Agrusa, Brent W. Barbee, Alex J. Meyer, Tony L. Farnham, Sabina D. Raducan, Derek C. Richardson, Elisabetta Dotto, Angelo Zinzi, Vincenzo Della Corte, Thomas S. Statler, Steven Chesley, Shantanu P. Naidu, Masatoshi Hirabayashi, Jian-Yang Li, Siegfried Eggl, Olivier S. Barnouin, Nancy L. Chabot, Sidney Chocron, Gareth S. Collins, R. Terik Daly, Thomas M. Davison, Mallory E. DeCoster, Carolyn M. Ernst, Fabio Ferrari, Dawn M. Graninger, Seth A. Jacobson, Martin Jutzi, Kathryn M. Kumamoto, Robert Luther, Joshua R. Lyzhoft, Patrick Michel, Naomi Murdoch, Ryota Nakano, Eric Palmer, Andrew S. Rivkin, Daniel J. Scheeres, Angela M. Stickle, Jessica M. Sunshine, Josep M. Trigo-Rodriguez, Jean-Baptiste Vincent, James D. Walker, Kai Wünnemann, Yun Zhang, Marilena Amoroso, Ivano Bertini, John R. Brucato, Andrea Capannolo, Gabriele Cremonese, Massimo Dall'Ora, Prasanna J. D. Deshapriya, Igor Gai, Pedro H. Hasselmann, Simone Ieva, Gabriele Impresario, Stavro L. Ivanovski, Michèle Lavagna, Alice Lucchetti, Elena M. Epifani, Dario Modenini, Maurizio Pajola, Pasquale Palumbo, Davide Perna, Simone Pirrotta, Giovanni Poggiali, Alessandro Rossi, Paolo Tortora, Marco Zannoni, and Giovanni Zanotti (Apr. 2023). "Momentum transfer from the DART mission kinetic impact on asteroid Dimorphos". *Nature* 616.7957, pp. 457–460. DOI: 10.1038/s41586-023-05878-z.

Andrew F. Cheng, Andrew S. Rivkin, Patrick Michel, Justin Atchison, Olivier Barnouin, Lance Benner, Nancy L. Chabot, Carolyn Ernst, Eugene G. Fahnestock, Michael Kueppers, Petr Pravec, Emma Rainey, Derek C. Richardson, Angela M. Stickle, and Cristina Thomas (Aug. 2018). "AIDA DART asteroid deflection test: Planetary defense and science objectives". *Planet. Space Sci.* 157, pp. 104–115. DOI: 10.1016/j.pss.2018.02.015.

Steven R. Chesley, Steven J. Ostro, David Vokrouhlický, David Čapek, Jon D. Giorgini, Michael C. Nolan, Jean-Luc Margot, Alice A. Hine, Lance A. M. Benner, and Alan B. Chamberlin (Dec. 2003). "Direct Detection of the Yarkovsky Effect by Radar Ranging to Asteroid 6489 Golevka". *Science* 302.5651, pp. 1739–1742. DOI: 10.1126/science.1091452.

Desireé Cotto-Figueroa, Thomas S. Statler, Derek C. Richardson, and Paolo Tanga (Apr. 2015). "Coupled Spin and Shape Evolution of Small Rubble-pile Asteroids: Self-limitation of the YORP Effect". *ApJ* 803.1, 25, p. 25. DOI: 10.1088/0004-637X/803/1/25.

Matija Ćuk and Joseph A. Burns (Aug. 2005). "Effects of thermal radiation on the dynamics of binary NEAs". *Icarus* 176.2, pp. 418–431. DOI: 10.1016/j.icarus.2005.02.001.

Matija Ćuk and David Nesvorný (June 2010). "Orbital evolution of small binary asteroids". *Icarus* 207.2, pp. 732–743. DOI: 10.1016/j.icarus.2009.12.005.

R. Terik Daly et al. (Apr. 2023). "Successful kinetic impact into an asteroid for planetary defence". *Nature* 616.7957, pp. 443–447. DOI: 10.1038/s41586-023-05810-5.

C. L. Dandy, A. Fitzsimmons, and S. J. Collander-Brown (June 2003). "Optical colors of 56 near-Earth objects: trends with size and orbit". *Icarus* 163.2, pp. 363–373. DOI: 10.1016/S0019-1035(03)00087-3.

Rogerio Deienno, Kevin J. Walsh, and Marco Delbo (Mar. 2021). "Efficiency characterization of the V-shape asteroid family detection method". *Icarus* 357, 114218, p. 114218. DOI: 10.1016/j.icarus.2020.114218.

D. N. Dellagiustina, J. P. Emery, D. R. Golish, B. Rozitis, C. A. Bennett, K. N. Burke, R. -L. Ballouz, K. J. Becker, P. R. Christensen, C. Y. Drouet D'Aubigny, V. E. Hamilton, D. C. Reuter, B. Rizk, A. A. Simon, E. Asphaug, J. L. Bandfield, O. S. Barnouin, M. A. Barucci, E. B. Bierhaus, R. P. Binzel, W. F. Bottke, N. E. Bowles, H. Campins, B. C. Clark, B. E. Clark, H. C. Connolly, M. G. Daly, J. De Leon, M. Delbo, J. D. P. Deshapriya, C. M. Elder, S. Fornasier, C. W. Hergenrother, E. S. Howell, E. R. Jawin, H. H. Kaplan, T. R. Kareta, L. Le Corre, J. -Y. Li, J. Licandro, L. F. Lim, P. Michel, J. Molaro, M. C. Nolan, M. Pajola, M. Popescu, J. L. Rizos Garcia, A. Ryan, S. R. Schwartz, N. Shultz, M. A. Siegler, P. H. Smith, E. Tatsumi, C. A. Thomas, K. J. Walsh, C. W. V. Wolner, X. -D. Zou, D. S. Lauretta, and Osiris-Rex Team (Mar. 2019). "Properties of rubble-pile asteroid (101955) Bennu from OSIRIS-REx imaging and thermal analysis". *Nature Astronomy* 3, pp. 341–351. DOI: 10.1038/s41550-019-0731-1.

Francesca E. DeMeo, Richard P. Binzel, Stephen M. Slivan, and Schelte J. Bus (July 2009). "An extension of the Bus asteroid taxonomy into the near-infrared". *Icarus* 202.1, pp. 160–180. DOI: 10.1016/j.icarus.2009.02.005.

A. Di Ruscio, A. Fienga, D. Durante, L. Iess, J. Laskar, and M. Gastineau (Aug. 2020). "Analysis of Cassini radio tracking data for the construction of INPOP19a: A new estimate of the Kuiper belt mass". *A&A* 640, A7, A7. DOI: 10.1051/0004-6361/202037920.

C. Dominik and A. G. G. M. Tielens (May 1997). "The Physics of Dust Coagulation and the Structure of Dust Aggregates in Space". *ApJ* 480.2, pp. 647–673. DOI: 10.1086/303996.

L. Dover, S. C. Lowry, A. Rożek, B. Rozitis, S. L. Jackson, T. Zegmott, Yu N. Krugly, I. N. Belskaya, A. Fitzsimmons, S. F. Green, C. Snodgrass, P. R. Weissman, M. Brozović, L. A. M. Benner, M. W. Busch, V. R. Ayvazian, V. Chiorny, R. Ya Inasaridze, M. Krugov, S. Mykhailova, I. Reva, and J. Hibbert (Sept. 2023). "Physical modelling of near-Earth asteroid (23187) 2000 PN9 with ground-based optical and radar observations". *MNRAS*. DOI: 10.1093/mnras/stad2528.

J. Durech, V. Sidorin, and M. Kaasalainen (Apr. 2010). "DAMIT: a database of asteroid models". *A&A* 513, A46, A46. DOI: 10.1051/0004-6361/200912693.

J Ďurech, D Vokrouhlický, A R Baransky, S Breiter, O A Burkhonov, W Cooney, V Fuller, N M Gaftonyuk, J Gross, R Ya Inasaridze, M Kaasalainen, Yu N Krugly, O I Kvaratshelia, E A Litvinenko, B Macomber, F Marchis, I E Molotov, J Oey, D Polishook, J Pollock, P Pravec, K Sárneczky, V G Shevchenko, I Slyusarev, R Stephens, Gy Szabó, D Terrell, F Vachier, Z Vanderplate, M Viikinkoski, and B D Warner (2012). "Analysis of the rotation period of asteroids (1865) Cerberus, (2100) Ra-Shalom, and (3103) Eger – search for the YORP effect". *A&A* 547, A10–9.

J Ďurech, D Vokrouhlický, M Kaasalainen, D Higgins, Yu N Krugly, N M Gaftonyuk, V G Shevchenko, V G Chiorny, H Hamanowa, H Hamanowa, V Reddy, and R R Dyvig (Sept. 2008a). "Detection of the YORP effect in asteroid (1620) Geographos". *A&A* 489.2, pp. L25–L28.

J Ďurech, D Vokrouhlický, P Pravec, J Hanuš, D Farnocchia, Yu N Krugly, R Y Inasaridze, V R Ayvazian, P Fatka, V G Chiorny, N Gaftonyuk, A Galád, R Groom, K Hornoch, H Kucakova, P Kušnirák, M Lehký, O I Kvaratskhelia, G Masi, I E Molotov, J Oey, J T Pollock, V G Shevchenko, J Vraštil, and B D Warner (Jan. 2018a). "YORP and Yarkovsky effects in asteroids (1685) Toro, (2100) Ra-Shalom, (3103) Eger, and (161989) Cacus". *A&A* 609, A86.

J. Ďurech and J. Hanuš (July 2023). "Reconstruction of asteroid spin states from Gaia DR3 photometry". *A&A* 675, A24, A24. DOI: 10.1051/0004-6361/202345889.

J. Ďurech, J. Hanuš, and V. Alí-Lagoa (Sept. 2018b). "Asteroid models reconstructed from the Lowell Photometric Database and WISE data". *A&A* 617, A57, A57. DOI: 10.1051/0004-6361/201833437.

J. Ďurech, V. Sidorin, and M. Kaasalainen (Apr. 2010). "DAMIT: a database of asteroid models". en. *Astronomy and Astrophysics* 513, A46. DOI: 10.1051/0004-6361/200912693.

J. Ďurech, D. Vokrouhlický, M. Kaasalainen, P. Weissman, S. C. Lowry, E. Beshore, D. Higgins, Y. N. Krugly, V. G. Shevchenko, N. M. Gaftonyuk, Y. -J. Choi, R. A.

Kowalski, S. Larson, B. D. Warner, A. L. Marshalkina, M. A. Ibrahimov, I. E. Molotov, T. Michałowski, and K. Kitazato (Sept. 2008b). "New photometric observations of asteroids (1862) Apollo and (25143) Itokawa - an analysis of YORP effect". *A&A* 488.1, pp. 345–350. DOI: 10.1051/0004-6361:200809663.

J. Ďurech, D. Vokrouhlický, P. Pravec, Yu. Krugly, D. Polishook, J. Hanuš, F. Marchis, A. Rożek, C. Snodgrass, L. Alegre, Z. Donchev, Sh. A. Ehgamberdiev, P. Fatka, N. M. Gaftonyuk, A. Galád, K. Hornoch, R. Ya. Inasaridze, E. Khalouei, H. Kučáková, P. Kušnirák, J. Oey, D. P. Pray, A. Sergeev, and I. Slyusarev (Dec. 2023). "Secular change in the spin states of asteroids due to radiation and gravitation torques. New detections and updates of the YORP effect". *arXiv e-prints*, arXiv:2312.05157, arXiv:2312.05157. DOI: 10.48550/arXiv.2312.05157.

J. Ďurech, D. Vokrouhlický, P. Pravec, Yu. N. Krugly, M. -J. Kim, D. Polishook, V. V. Ayvazian, T. Bonev, Y. -J. Choi, D. G. Datashvili, Z. Donchev, S. A. Ehgamberdiev, K. Hornoch, R. Ya. Inasaridze, G. V. Kapanadze, D. -H. Kim, H. Kučáková, A. V. Kusakin, P. Kušnirák, H. -J. Lee, I. E. Molotov, H. -K. Moon, S. S. Mykhailova, I. V. Nikolenko, A. Novichonok, J. Oey, Ch. T. Omarov, J. T. Pollock, I. V. Reva, V. V. Rumyantsev, and A. A. Zhornichenko (Jan. 2022a). "Rotation acceleration of asteroids (10115) 1992 SK, (1685) Toro, and (1620) Geographos due to the YORP effect". *A&A* 657, A5, A5. DOI: 10.1051/0004-6361/202141844.

Josef Ďurech, Mikko Kaasalainen, David Herald, David Dunham, Brad Timerson, Josef Hanuš, Eric Frappa, John Talbot, Tsutomu Hayamizu, Brian D. Warner, Frederick Pilcher, and Adrián Galád (Aug. 2011). "Combining asteroid models derived by lightcurve inversion with asteroidal occultation silhouettes". *Icarus* 214.2, pp. 652–670. DOI: 10.1016/j.icarus.2011.03.016.

Josef Ďurech, Michael Vávra, Radim Vančo, and Nicolas Erasmus (Feb. 2022b). "Rotation Periods of Asteroids Determined With Bootstrap Convex Inversion From ATLAS Photometry". *Frontiers in Astronomy and Space Sciences* 9, 809771, p. 809771. DOI: 10.3389/fspas.2022.809771.

M. Engels, S. Hudson, and C. Magri (July 2020). "Performance of CUDA-SHAPE on complex synthetic shapes and real data of asteroid (341843) 2008 EV5". *Astronomy and Computing* 32, 100401, p. 100401. DOI: 10.1016/j.ascom.2020.100401.

Jacob A. Englander, Matthew A. Vavrina, Lucy F. Lim, Lucy A. McFadden, Alyssa R. Rhoden, and Keith S. Noll (Jan. 2017). "Trajectory Optimization for Missions to Small Bodies with a Focus on Scientific Merit". *Computing in Science and Engineering* 19.4, pp. 18–28. DOI: 10.1109/MCSE.2017.3151246.

Laura Faggioli, Alessio Del Vigna, Andrea Milani, Federica Spoto, and Giovanni B. Valsecchi (Oct. 2016). "Detection of Yarkovsky effect and solar radiation pressure on Near-Earth Asteroids". *AAS/Division for Planetary Sciences Meeting Abstracts #48*. Vol. 48. AAS/Division for Planetary Sciences Meeting Abstracts, 311.07, p. 311.07.

Paolo Farinella and David Vokrouhlicky (Mar. 1999). "Semimajor Axis Mobility of Asteroidal Fragments". *Science* 283, p. 1507. DOI: 10.1126/science.283.5407.1507.

D. Farnocchia and S. R. Chesley (Feb. 2014). "Assessment of the 2880 impact threat from Asteroid (29075) 1950 DA". *Icarus* 229, pp. 321–327. DOI: 10.1016/j.icarus.2013.09.022.

D. Farnocchia, S. R. Chesley, D. Vokrouhlický, A. Milani, F. Spoto, and W. F. Bottke (May 2013). "Near Earth Asteroids with measurable Yarkovsky effect". *Icarus* 224.1, pp. 1–13. DOI: 10.1016/j.icarus.2013.02.004.

S. Ferrone, M. Delbo, C. Avdellidou, R. Melikyan, A. Morbidelli, K. Walsh, and R. Deienno (Aug. 2023). "Identification of a 4.3 billion year old asteroid family and planetesimal population in the Inner Main Belt". *A&A* 676, A5, A5. DOI: 10.1051/0004-6361/202245594.

Lorenzo Franco, Albino Carbognani, Patrick Wiggins, Bruce W. Koehn, and Richard Schmidt (July 2010). "Collaborative Lightcurve Photometry of Near-Earth Asteroid (159402) 1999 AP10". *Minor Planet Bulletin* 37.3, pp. 83–85.

A. Fujiwara, J. Kawaguchi, D. K. Yeomans, M. Abe, T. Mukai, T. Okada, J. Saito, H. Yano, M. Yoshikawa, D. J. Scheeres, O. Barnouin-Jha, A. F. Cheng, H. Demura, R. W. Gaskell, N. Hirata, H. Ikeda, T. Kominato, H. Miyamoto, A. M. Nakamura,

R. Nakamura, S. Sasaki, and K. Uesugi (June 2006). "The Rubble-Pile Asteroid Itokawa as Observed by Hayabusa". *Science* 312.5778, pp. 1330–1334. DOI: 10.1126/science.1125841.

A. Galeev, R. Gumerov, I. Bikmaev, G. Pinigin, I. Khamitov, and Z. Aslan (Jan. 2007). "Photometric Researches of Asteroids on 1.5-M Russian-Turkish Telescope". *Odessa Astronomical Publications* 20, p. 43.

J. D. Giorgini, S. J. Ostro, L. A. M. Benner, P. W. Chodas, S. R. Chesley, R. S. Hudson, M. C. Nolan, A. R. Klemola, E. M. Standish, R. F. Jurgens, R. Rose, A. B. Chamberlin, D. K. Yeomans, and J. -L. Margot (Sept. 2002). "Asteroid 1950 DA's Encounter with Earth in 2880: Physical Limits of Collision Probability Prediction". *AAS/Division of Dynamical Astronomy Meeting #33*. Vol. 33. AAS/Division of Dynamical Astronomy Meeting, 02.02, p. 02.02.

Daniel P. Glavin, Jason P. Dworkin, Conel M. O'D. Alexander, José C. Aponte, Allison A. Baczynski, Jessica J. Barnes, Hans A. Bechtel, Eve L. Berger, Aaron S. Burton, Paola Caselli, Angela H. Chung, Simon J. Clemett, George D. Cody, Gerardo Dominguez, Jamie E. Elsila, Kendra K. Farnsworth, Dionysis I. Foustoukos, Katherine H. Freeman, Yoshihiro Furukawa, Zack Gainsforth, Heather V. Graham, Tommaso Grassi, Barbara Michela Giuliano, Victoria E. Hamilton, Pierre Haenecour, Philipp R. Heck, Amy E. Hofmann, Christopher H. House, Yongsong Huang, Hannah H. Kaplan, Lindsay P. Keller, Bumsoo Kim, Toshiki Koga, Michael Liss, Hannah L. McLain, Matthew A. Marcus, Mila Matney, Timothy J. McCoy, Ophélie M. McIntosh, Angel Mojarro, Hiroshi Naraoka, Ann N. Nguyen, Michel Nuevo, Joseph A. III Nuth, Yasuhiro Oba, Eric T. Parker, Tanya S. Peretyazhko, Scott A. Sandford, Ewerton Santos, Philippe Schmitt-Kopplin, Frederic Seguin, Danielle N. Simkus, Anique Shahid, Yoshinori Takano, Kathie L. Thomas-Keprta, Havishk Tripathi, Gabriella Weiss, Yuke Zheng, Nicole G. Lunning, Kevin Righter, Harold C. Jr. Connolly, and Dante S. Lauretta (Jan. 2025). "Abundant ammonia and nitrogen-rich soluble organic matter in samples from asteroid (101955) Bennu". *Nature Astronomy*. DOI: 10.1038/s41550-024-02472-9.

O. Golubov, Y. Kravets, Yu. N. Krugly, and D. J. Scheeres (June 2016). "Physical models for the normal YORP and diurnal Yarkovsky effects". *MNRAS* 458.4, pp. 3977–3989. DOI: 10.1093/mnras/stw540.

O. Golubov and V. Lipatova (Oct. 2022). "Analytic theory for the tangential YORP produced by the asteroid regolith". *A&A* 666, A146, A146. DOI: 10.1051/0004-6361/202243320.

O. Golubov, D. J. Scheeres, and Yu. N. Krugly (Sept. 2014). "A THREE-DIMENSIONAL MODEL OF TANGENTIAL YORP". en. *The Astrophysical Journal* 794.1, p. 22. DOI: 10.1088/0004-637X/794/1/22.

Oleksiy Golubov and Yurij N. Krugly (June 2012). "TANGENTIAL COMPONENT OF THE YORP EFFECT". en. *AJ* 752.1, p. L11. DOI: 10.1088/2041-8205/752/1/L11.

Oleksiy Golubov and Daniel J. Scheeres (Mar. 2019). "Systematic Structure and Sinks in the YORP Effect". *AJ* 157.3, 105, p. 105. DOI: 10.3847/1538-3881/aafd2c.

Oleksiy Golubov, Daniel J. Scheeres, and Yurij N. Krugly (Mar. 2020). "YORP equilibria: ways out of YORP cycles". *IAU General Assembly*, pp. 15–15. DOI: 10.1017/S1743921319003259.

Oleksiy Golubov, Vladyslav Unukovych, and Daniel J. Scheeres (Apr. 2018). "A New Equilibrium State for Singly Synchronous Binary Asteroids". *ApJ* 857.1, L5, p. L5. DOI: 10.3847/2041-8213/aaba15.

R. Gomes, H. F. Levison, K. Tsiganis, and A. Morbidelli (May 2005). "Origin of the cataclysmic Late Heavy Bombardment period of the terrestrial planets". *Nature* 435.7041, pp. 466–469. DOI: 10.1038/nature03676.

Peter M. Gray (Aug. 2000). "Assembly and integration to first light of the four VLT telescopes". *Telescope Structures, Enclosures, Controls, Assembly/Integration/Validation, and Commissioning*. Ed. by Thomas A. Sebring and Torben Andersen. Vol. 4004. Society of Photo-Optical Instrumentation Engineers (SPIE) Conference Series, pp. 2–13. DOI: 10.1117/12.393913.

S. F. Green, A. J. Meadows, and J. K. Davies (June 1985). "Infrared observations of the extinct cometary candidate minor planet (3200) 1983TB". *MNRAS* 214, 29P–36P. DOI: 10.1093/mnras/214.1.29P.

Adam H. Greenberg, Jean-Luc Margot, Ashok K. Verma, Patrick A. Taylor, and Susan E. Hodge (Mar. 2020). "Yarkovsky Drift Detections for 247 Near-Earth Asteroids". *AJ* 159.3, 92, p. 92. DOI: 10.3847/1538-3881/ab62a3.

R. A. F. Grieve and E. M. Shoemaker (Jan. 1994). "The Record of Past Impacts on Earth". *Hazards Due to Comets and Asteroids*, p. 417.

C. Güttler, J. Blum, A. Zsom, C. W. Ormel, and C. P. Dullemond (Apr. 2010). "The outcome of protoplanetary dust growth: pebbles, boulders, or planetesimals?. I. Mapping the zoo of laboratory collision experiments". *A&A* 513, A56, A56. DOI: 10.1051/0004-6361/200912852.

Stephen D. J. Gwyn, Norman Hill, and J. J. Kavelaars (June 2012). "SSOS: A Moving-Object Image Search Tool for Asteroid Precovery". *PASP* 124.916, p. 579. DOI: 10.1086/666462.

Josef Hanus and Josef Durech (Oct. 2024). "Investigating Spin State Properties in Collisional Asteroid Families". *AAS/Division for Planetary Sciences Meeting Abstracts*. Vol. 56. AAS/Division for Planetary Sciences Meeting Abstracts, 105.04, p. 105.04.

J. Hanuš, M. Viikinkoski, F. Marchis, J. Ďurech, M. Kaasalainen, M. Delbo', D. Herald, E. Frappa, T. Hayamizu, S. Kerr, S. Preston, B. Timerson, D. Dunham, and J. Talbot (May 2017). "Volumes and bulk densities of forty asteroids from ADAM shape modeling". *A&A* 601, A114, A114. DOI: 10.1051/0004-6361/201629956.

A. W. Harris (Mar. 1996). "The Rotation Rates of Very Small Asteroids: Evidence for 'Rubble Pile' Structure". *Lunar and Planetary Science Conference*. Vol. 27. Lunar and Planetary Science Conference, p. 493.

A. W. Harris, M. Boslough, C. R. Chapman, L. Drube, P. Michel, and A. W. Harris (2015). "Asteroid Impacts and Modern Civilization: Can We Prevent a Catastrophe?" *Asteroids IV*, pp. 835–854. DOI: 10.2458/azu_uapress_9780816532131-ch042.

A. W. Harris, J. W. Young, E. Bowell, L. J. Martin, R. L. Millis, M. Poutanen, F. Scaltriti, V. Zappala, H. J. Schober, H. Debehogne, and K. W. Zeigler (Jan. 1989). "Photoelectric observations of asteroids 3, 24, 60, 261, and 863". *Icarus* 77.1, pp. 171–186. DOI: 10.1016/0019-1035(89)90015-8.

Sunao Hasegawa, Daisuke Kuroda, Kohei Kitazato, Toshihiro Kasuga, Tomohiko Sekiguchi, Naruhisa Takato, Kentaro Aoki, Akira Arai, Young-Jun Choi, Tetsuharu Fuse, Hidekazu Hanayama, Takashi Hattori, Hsiang-Yao Hsiao, Nobunari Kashikawa, Nobuyuki Kawai, Kyoko Kawakami, Daisuke Kinoshita, Steve Larson, Chi-Sheng Lin, Seidai Miyasaka, Naoya Miura, Shogo Nagayama, Yu Nagumo, Setsuko Nishihara, Yohei Ohba, Kouji Ohta, Youichi Ohyama, Shin-ichiro Okumura, Yuki Sarugaku, Yasuhiro Shimizu, Yuhei Takagi, Jun Takahashi, Hiroyuki Toda, Seitaro Urakawa, Fumihiko Usui, Makoto Watanabe, Paul Weissman, Kenshi Yanagisawa, Hongu Yang, Michitoshi Yoshida, Makoto Yoshikawa, Masateru Ishiguro, and Masanao Abe (Dec. 2018). "Physical properties of near-Earth asteroids with a low delta-v: Survey of target candidates for the Hayabusa2 mission". *PASJ* 70.6, 114, p. 114. DOI: 10.1093/pasj/psy119.

C. W. Hergenrother, C. K. Maleszewski, M. C. Nolan, J. -Y. Li, C. Y. Drouet D'Aubigny, F. C. Shelly, E. S. Howell, T. R. Kareta, M. R. M. Izawa, M. A. Barucci, E. B. Bierhaus, H. Campins, S. R. Chesley, B. E. Clark, E. J. Christensen, D. N. Dellagiustina, S. Fornasier, D. R. Golish, C. M. Hartzell, B. Rizk, D. J. Scheeres, P. H. Smith, X. -D. Zou, D. S. Lauretta, and OSIRIS-REx Team (Mar. 2019). "The operational environment and rotational acceleration of asteroid (101955) Bennu from OSIRIS-REx observations". *Nature Communications* 10, 1291, p. 1291. DOI: 10.1038/s41467-019-09213-x.

M. Hicks and K. Lawrence (Dec. 2009). "Planetary radar targets 1999 AP10, 2000 TO64, 2000 UJ1, and 2000 XK44: Four S-complex near-Earth asteroids." *The Astronomer's Telegram* 2323, p. 1.

Michael Hicks, Stephen Lowry, and Paul Weissman (Nov. 2009). "Long-slit CCD spectroscopy of planetary radar targets 1999 AP10 2000 TO64, and 2000 UJ1". *The Astronomer's Telegram* 2283, p. 1.

Dylan C. Hickson, Anne K. Virkki, Phil Perillat, Michael C. Nolan, and Sriram S. Bhiravarasu (Feb. 2021). "Polarimetric Decomposition of Near-Earth Asteroids Using Arecibo Radar Observations". *The Planetary Science Journal* 2.1, 30, p. 30. DOI: 10.3847/PSJ/abd846.

Masatoshi Hirabayashi, Ryota Nakano, Eri Tatsumi, Kevin J. Walsh, Olivier S. Barnouin, Patrick Michel, Christine M. Hartzell, Daniel T. Britt, Seiji Sugita, Sei-ichiro Watanabe, William F. Bottke, Daniel J. Scheeres, Ronald-Louis Ballouz, Yuichiro Cho, Tomokatsu Morota, Ellen S. Howell, and Dante S. Lauretta (Dec. 2020). "Spin-driven evolution of asteroids' top-shapes at fast and slow spins seen from (101955) Bennu and (162173) Ryugu". *Icarus* 352, 113946, p. 113946. DOI: 10.1016/j.icarus.2020.113946.

Masatoshi Hirabayashi and Daniel J. Scheeres (Jan. 2019). "Rotationally induced failure of irregularly shaped asteroids". *Icarus* 317, pp. 354–364. DOI: 10.1016/j.icarus.2018.08.003.

Keith A. Holsapple (Apr. 2007). "Spin limits of Solar System bodies: From the small fast-rotators to 2003 EL61". *Icarus* 187.2, pp. 500–509. DOI: 10.1016/j.icarus.2006.08.012.

— (Feb. 2010). "On YORP-induced spin deformations of asteroids". *Icarus* 205.2, pp. 430–442. DOI: 10.1016/j.icarus.2009.08.014.

R. S. Hudson, S. J. Ostro, and D. J. Scheeres (Feb. 2003). "High-resolution model of Asteroid 4179 Toutatis". *Icarus* 161.2, pp. 346–355. DOI: 10.1016/S0019-1035(02)00042-8.

Scott Hudson (Jan. 1994). "Three-dimensional reconstruction of asteroids from radar observations". *Remote Sensing Reviews* 8.1-3, pp. 195–203. DOI: https://doi.org/10.1080/02757259309532195.

Ryuki Hyodo and Keisuke Sugiura (Oct. 2022). "Formation of Moons and Equatorial Ridge around Top-shaped Asteroids after Surface Landslide". *ApJ* 937.2, L36, p. L36. DOI: 10.3847/2041-8213/ac922d.

Derek J. Ives, Simon Tulloch, and John Churchill (Mar. 1996). "INT prime focus mosaic camera". *Solid State Sensor Arrays and CCD Cameras*. Ed. by Constantine N. Anagnostopoulos, Morley M. Blouke, and Michael P. Lesser. Vol. 2654. Society of

Photo-Optical Instrumentation Engineers (SPIE) Conference Series, pp. 266–276. DOI: 10.1117/12.236118.

S. L. Jackson, B. Rozitis, L. R. Dover, S. F. Green, U. C. Kolb, A. E. Andrews, and S. C. Lowry (June 2022). "The effect of aspect changes on Near-Earth Asteroid phase curves". *MNRAS* 513.2, pp. 3076–3089. DOI: 10.1093/mnras/stac1053.

Samuel L. Jackson, Ulrich C. Kolb, and Simon F. Green (July 2021). "Asteroid Photometry with PIRATE: Optimizations and Techniques for Small Aperture Telescopes". *PASP* 133.1025, 075003, p. 075003. DOI: 10.1088/1538-3873/ac0f8c.

Seth A. Jacobson and Daniel J. Scheeres (July 2011a). "Dynamics of rotationally fissioned asteroids: Source of observed small asteroid systems". *Icarus* 214.1, pp. 161–178. DOI: 10.1016/j.icarus.2011.04.009.

— (July 2011b). "Long-term Stable Equilibria for Synchronous Binary Asteroids". *ApJ* 736.1, L19, p. L19. DOI: 10.1088/2041-8205/736/1/L19.

David Jewitt, Jessica Agarwal, Harold Weaver, Max Mutchler, and Stephen Larson (Jan. 2015). "Episodic Ejection from Active Asteroid 311P/PANSTARRS". *ApJ* 798.2, 109, p. 109. DOI: 10.1088/0004-637X/798/2/109.

A. Johansen, E. Jacquet, J. N. Cuzzi, A. Morbidelli, and M. Gounelle (2015). "New Paradigms for Asteroid Formation". *Asteroids IV*, pp. 471–492. DOI: 10.2458/azu_uapress_9780816532131-ch025.

A. Johansen, H. Klahr, and Th. Henning (May 2011). "High-resolution simulations of planetesimal formation in turbulent protoplanetary discs". *A&A* 529, A62, A62. DOI: 10.1051/0004-6361/201015979.

A. Johansen and A. Youdin (June 2007). "Protoplanetary Disk Turbulence Driven by the Streaming Instability: Nonlinear Saturation and Particle Concentration". *ApJ* 662.1, pp. 627–641. DOI: 10.1086/516730.

Lynne Jones (Aug. 2015). "Asteroid Detection with the Large Synoptic Survey Telescope (LSST)". *IAU General Assembly*. Vol. 29, 2256359, p. 2256359.

W. A. Joye and E. Mandel (Jan. 2003). "New Features of SAOImage DS9". *Astronomical Data Analysis Software and Systems XII*. Ed. by H. E. Payne, R. I. Jedrzejewski,

and R. N. Hook. Vol. 295. Astronomical Society of the Pacific Conference Series, p. 489.

M Kaasalainen and J Torppa (Sept. 2001). "Optimization Methods for Asteroid Lightcurve Inversion I. Shape Determination". *Icarus* 153.1, pp. 24–36.

M Kaasalainen, J Torppa, and K Muinonen (Sept. 2001). "Optimization Methods for Asteroid Lightcurve Inversion II. The Complete Inverse Problem". *Icarus* 153.1, pp. 37–51.

Mikko Kaasalainen, Josef Ďurech, Brian D. Warner, Yurij N. Krugly, and Ninel M. Gaftonyuk (Mar. 2007). "Acceleration of the rotation of asteroid 1862 Apollo by radiation torques". *Nature* 446.7134, pp. 420–422. DOI: 10.1038/nature05614.

O. Karatekin, S. Ulamec, N. Murdoch, P. Michel, M. Küppers, and I. Carnelli (Dec. 2018). "HERA planned mission and payload operations at close proximity of the moon of the binary asteroid Didymos after DART impact." *AGU Fall Meeting Abstracts*. Vol. 2018, P51A-14, P51A–14.

Hannu Karttunen, Pekka Kröger, Heikki Oja, Markku Poutanen, and Karl Johan Donner (2017). *Fundamental Astronomy*. DOI: 10.1007/978-3-662-53045-0.

H. U. Keller, C. Barbieri, D. Koschny, P. Lamy, H. Rickman, R. Rodrigo, H. Sierks, M. F. A'Hearn, F. Angrilli, M. A. Barucci, J. -L. Bertaux, G. Cremonese, V. Da Deppo, B. Davidsson, M. De Cecco, S. Debei, S. Fornasier, M. Fulle, O. Groussin, P. J. Gutierrez, S. F. Hviid, W. -H. Ip, L. Jorda, J. Knollenberg, J. R. Kramm, E. Kührt, M. Küppers, L. -M. Lara, M. Lazzarin, J. Lopez Moreno, F. Marzari, H. Michalik, G. Naletto, L. Sabau, N. Thomas, K. -P. Wenzel, I. Bertini, S. Besse, F. Ferri, M. Kaasalainen, S. Lowry, S. Marchi, S. Mottola, W. Sabolo, S. E. Schröder, S. Spjuth, and P. Vernazza (Jan. 2010). "E-Type Asteroid (2867) Steins as Imaged by OSIRIS on Board Rosetta". *Science* 327.5962, p. 190. DOI: 10.1126/science.1179559.

A. Kryszczyńska (Mar. 2013). "Do Slivan states exist in the Flora family? . II. Fingerprints of the Yarkovsky and YORP effects". *A&A* 551, A102, A102. DOI: 10.1051/0004-6361/201220490.

D. S. Lauretta, S. S. Balram-Knutson, E. Beshore, W. V. Boynton, C. Drouet d'Aubigny, D. N. DellaGiustina, H. L. Enos, D. R. Golish, C. W. Hergenrother, E. S. Howell, C. A. Bennett, E. T. Morton, M. C. Nolan, B. Rizk, H. L. Roper, A. E. Bartels, B. J. Bos, J. P. Dworkin, D. E. Highsmith, D. A. Lorenz, L. F. Lim, R. Mink, M. C. Moreau, J. A. Nuth, D. C. Reuter, A. A. Simon, E. B. Bierhaus, B. H. Bryan, R. Ballouz, O. S. Barnouin, R. P. Binzel, W. F. Bottke, V. E. Hamilton, K. J. Walsh, S. R. Chesley, P. R. Christensen, B. E. Clark, H. C. Connolly, M. K. Crombie, M. G. Daly, J. P. Emery, T. J. McCoy, J. W. McMahon, D. J. Scheeres, S. Messenger, K. Nakamura-Messenger, K. Righter, and S. A. Sandford (Oct. 2017). "OSIRIS-REx: Sample Return from Asteroid (101955) Bennu". *Space Sci. Rev.* 212.1-2, pp. 925–984. DOI: 10.1007/s11214-017-0405-1.

D. S. Lauretta, D. N. Dellagiustina, C. A. Bennett, D. R. Golish, K. J. Becker, S. S. Balram-Knutson, O. S. Barnouin, T. L. Becker, W. F. Bottke, W. V. Boynton, H. Campins, B. E. Clark, H. C. Connolly, C. Y. Drouet D'Aubigny, J. P. Dworkin, J. P. Emery, H. L. Enos, V. E. Hamilton, C. W. Hergenrother, E. S. Howell, M. R. M. Izawa, H. H. Kaplan, M. C. Nolan, B. Rizk, H. L. Roper, D. J. Scheeres, P. H. Smith, K. J. Walsh, C. W. V. Wolner, and Osiris-Rex Team (Mar. 2019a). "The unexpected surface of asteroid (101955) Bennu". *Nature* 568.7750, pp. 55–60. DOI: 10.1038/s41586-019-1033-6.

D. S. Lauretta, C. W. Hergenrother, S. R. Chesley, J. M. Leonard, J. Y. Pelgrift, C. D. Adam, M. Al Asad, P. G. Antreasian, R.-L. Ballouz, K. J. Becker, C. A. Bennett, B. J. Bos, W. F. Bottke, M. Brozović, H. Campins, H. C. Connolly, M. G. Daly, A. B. Davis, J. de León, D. N. DellaGiustina, C. Y. Drouet d'Aubigny, J. P. Dworkin, J. P. Emery, D. Farnocchia, D. P. Glavin, D. R. Golish, C. M. Hartzell, R. A. Jacobson, E. R. Jawin, P. Jenniskens, J. N. Kidd, E. J. Lessac-Chenen, J.-Y. Li, G. Libourel, J. Licandro, A. J. Liounis, C. K. Maleszewski, C. Manzoni, B. May, L. K. McCarthy, J. W. McMahon, P. Michel, J. L. Molaro, M. C. Moreau, D. S. Nelson, W. M. Owen, B. Rizk, H. L. Roper, B. Rozitis, E. M. Sahr, D. J. Scheeres, J. A. Seabrook, S. H. Selznick, Y. Takahashi, F. Thuillet, P. Tricarico, D.

Vokrouhlický, and C. W. V. Wolner (Dec. 2019b). "Episodes of particle ejection from the surface of the active asteroid (101955) Bennu". en. *Science* 366.6470, eaay3544. DOI: 10.1126/science.aay3544.

Lucille Le Corre, Juan A. Sanchez, Vishnu Reddy, Driss Takir, Edward A. Cloutis, Audrey Thirouin, Kris J. Becker, Jian-Yang Li, Seiji Sugita, and Eri Tatsumi (Mar. 2018). "Ground-based characterization of Hayabusa2 mission target asteroid 162173 Ryugu: constraining mineralogical composition in preparation for spacecraft operations". *MNRAS* 475.1, pp. 614–623. DOI: 10.1093/mnras/stx3236.

H. F. Levison, S. Marchi, K. S. Noll, J. R. Spencer, T. Statler, and Lucy Science Team (Mar. 2024a). "An Overview of NASA Lucy Misson's Encounter with the Main Belt Asteroid Dinkinesh". *LPI Contributions*. Vol. 3040. LPI Contributions, 1668, p. 1668.

Harold F. Levison, Martin J. Duncan, Ramon Brasser, and David E. Kaufmann (June 2010). "Capture of the Sun's Oort Cloud from Stars in Its Birth Cluster". *Science* 329.5988, pp. 187–190. DOI: 10.1126/science.1187535.

Harold F. Levison, Catherine B. Olkin, Keith S. Noll, Simone Marchi, III Bell James F., Edward Bierhaus, Richard Binzel, William Bottke, Dan Britt, Michael Brown, Marc Buie, Phil Christensen, Joshua Emery, Will Grundy, Victoria E. Hamilton, Carly Howett, Stefano Mottola, Martin Pätzold, Dennis Reuter, John Spencer, Thomas S. Statler, S. Alan Stern, Jessica Sunshine, Harold Weaver, and Ian Wong (Oct. 2021). "Lucy Mission to the Trojan Asteroids: Science Goals". *The Planetary Science Journal* 2.5, 171, p. 171. DOI: 10.3847/PSJ/abf840.

Harold F. Levison et al. (May 2024b). "A contact binary satellite of the asteroid (152830) Dinkinesh". *Nature* 629.8014, pp. 1015–1020. DOI: 10.1038/s41586-024-07378-0.

S. C. Lowry, A. Fitzsimmons, P. Pravec, D. Vokrouhlicky, H. Boehnhardt, P. A. Taylor, J.-L. Margot, A. Galad, M. Irwin, J. Irwin, and P. Kusnirak (Apr. 2007). "Direct Detection of the Asteroidal YORP Effect". en. *Science* 316.5822, pp. 272–274. DOI: 10.1126/science.1139040.

S. C. Lowry, P. R. Weissman, S. R. Duddy, B. Rozitis, A. Fitzsimmons, S. F. Green, M. D. Hicks, C. Snodgrass, S. D. Wolters, S. R. Chesley, J. Pittichová, and P. van Oers (Feb. 2014). "The internal structure of asteroid (25143) Itokawa as revealed by detection of YORP spin-up". en. *A&A* 562, A48. DOI: 10.1051/0004-6361/201322602.

Lunar & Planetary Institute (2021). *1999 AP10*. https://www.lpi.usra.edu/resources/asteroids/asteroid/?asteroid_id=1999AP10.

W. Lyra, A. Johansen, A. Zsom, H. Klahr, and N. Piskunov (Apr. 2009). "Planet formation bursts at the borders of the dead zone in 2D numerical simulations of circumstellar disks". *A&A* 497.3, pp. 869–888. DOI: 10.1051/0004-6361/200811265.

P. Magnusson (Mar. 1991). "Analysis of asteroid lightcurves. III. Albedo variegation." *A&A* 243.2, pp. 512–520.

P. Magnusson, M. A. Barucci, J. D. Drummond, K. Lumme, S. J. Ostro, J. Surdej, R. C. Taylor, and V. Zappalà (Jan. 1989). "Determination of pole orientations and shapes of asteroids." *Asteroids II*. Ed. by Richard P. Binzel, Tom Gehrels, and Mildred Shapley Matthews, pp. 66–97.

C. Magri, G. J. Consolmagno, S. J. Ostro, L. A. M. Benner, and B. R. Beeney (Dec. 2001). "Radar constraints on asteroid regolith compositions using 433 Eros as ground truth". *Meteoritics & Planetary Science* 36.12, pp. 1697–1709. DOI: 10.1111/j.1945-5100.2001.tb01857.x.

Christopher Magri, Ellen S. Howell, Michael C. Nolan, Patrick A. Taylor, Yanga R. Fernández, Michael Mueller, Ronald J. Vervack, Lance A. M. Benner, Jon D. Giorgini, Steven J. Ostro, Daniel J. Scheeres, Michael D. Hicks, Heath Rhoades, James M. Somers, Ninel M. Gaftonyuk, Vladimir V. Kouprianov, Yurij N. Krugly, Igor E. Molotov, Michael W. Busch, Jean-Luc Margot, Vladimir Benishek, Vojislava Protitch-Benishek, Adrian Galád, David Higgins, Peter Kušnirák, and Donald P. Pray (July 2011). "Radar and photometric observations and shape modeling of contact binary near-Earth Asteroid (8567) 1996 HW1". *Icarus* 214.1, pp. 210–227. DOI: 10.1016/j.icarus.2011.02.019.

Christopher Magri, Steven J. Ostro, Daniel J. Scheeres, Michael C. Nolan, Jon D. Giorgini, Lance A.M. Benner, and Jean-Luc Margot (Jan. 2007). "Radar observations and a physical model of Asteroid 1580 Betulia". en. *Icarus* 186.1, pp. 152–177. DOI: 10.1016/j.icarus.2006.08.004.

A. Mainzer, T. Grav, J. Bauer, J. Masiero, R. S. McMillan, R. M. Cutri, R. Walker, E. Wright, P. Eisenhardt, D. J. Tholen, T. Spahr, R. Jedicke, L. Denneau, E. DeBaun, D. Elsbury, T. Gautier, S. Gomillion, E. Hand, W. Mo, J. Watkins, A. Wilkins, G. L. Bryngelson, A. Del Pino Molina, S. Desai, M. Gómez Camus, S. L. Hidalgo, I. Konstantopoulos, J. A. Larsen, C. Maleszewski, M. A. Malkan, J. -C. Mauduit, B. L. Mullan, E. W. Olszewski, J. Pforr, A. Saro, J. V. Scotti, and L. H. Wasserman (Dec. 2011). "NEOWISE Observations of Near-Earth Objects: Preliminary Results". *ApJ* 743.2, 156, p. 156. DOI: 10.1088/0004-637X/743/2/156.

Jonathan C. McDowell (Apr. 2020). "The Low Earth Orbit Satellite Population and Impacts of the SpaceX Starlink Constellation". *ApJ* 892.2, L36, p. L36. DOI: 10.3847/2041-8213/ab8016.

Alfred S. McEwen, Jeffrey M. Moore, and Eugene M. Shoemaker (Jan. 1997). "The Phanerozoic impact cratering rate: Evidence from the farside of the Moon". *J. Geophys. Res.* 102.E4, pp. 9231–9242. DOI: 10.1029/97JE00114.

Jay McMahon and Daniel Scheeres (Oct. 2010). "Detailed prediction for the BYORP effect on binary near-Earth Asteroid (66391) 1999 KW4 and implications for the binary population". *Icarus* 209.2, pp. 494–509. DOI: 10.1016/j.icarus.2010.05.016.

C. C. Merrill, A. R. Kubas, A. J. Meyer, and S. D. Raducan (Apr. 2024). "Age of (152830) Dinkinesh I Selam constrained by secular tidal-BYORP theory". *A&A* 684, L20, p. L20. DOI: 10.1051/0004-6361/202449716.

P. Michel, R. -L. Ballouz, O. S. Barnouin, M. Jutzi, K. J. Walsh, B. H. May, C. Manzoni, D. C. Richardson, S. R. Schwartz, S. Sugita, S. Watanabe, H. Miyamoto, M. Hirabayashi, W. F. Bottke, H. C. Connolly, M. Yoshikawa, and D. S. Lauretta (May 2020). "Collisional formation of top-shaped asteroids and implications for the

origins of Ryugu and Bennu". *Nature Communications* 11, 2655, p. 2655. DOI: 10.1038/s41467-020-16433-z.

Patrick Michel, Michael Küppers, Adriano Campo Bagatin, Benoit Carry, Sébastien Charnoz, Julia de Leon, Alan Fitzsimmons, Paulo Gordo, Simon F. Green, Alain Hérique, Martin Juzi, Özgür Karatekin, Tomas Kohout, Monica Lazzarin, Naomi Murdoch, Tatsuaki Okada, Ernesto Palomba, Petr Pravec, Colin Snodgrass, Paolo Tortora, Kleomenis Tsiganis, Stephan Ulamec, Jean-Baptiste Vincent, Kai Wünnemann, Yun Zhang, Sabina D. Raducan, Elisabetta Dotto, Nancy Chabot, Andy F. Cheng, Andy Rivkin, Olivier Barnouin, Carolyn Ernst, Angela Stickle, Derek C. Richardson, Cristina Thomas, Masahiko Arakawa, Hirdy Miyamoto, Akiko Nakamura, Seiji Sugita, Makoto Yoshikawa, Paul Abell, Erik Asphaug, Ronald-Louis Ballouz, William F. Bottke, Dante S. Lauretta, Kevin J. Walsh, Paolo Martino, and Ian Carnelli (July 2022). "The ESA Hera Mission: Detailed Characterization of the DART Impact Outcome and of the Binary Asteroid (65803) Didymos". *Planetary Science Journal* 3.7, 160, p. 160. DOI: 10.3847/PSJ/ac6f52.

R. L. Millis, L. H. Wasserman, O. G. Franz, R. A. Nye, R. C. Oliver, T. J. Kreidl, S. E. Jones, W. Hubbard, L. Lebofsky, R. Goff, R. Marcialis, M. Sykes, J. Frecker, D. Hunten, B. Zellner, H. Reitsema, G. Schneider, E. Dunham, J. Klavetter, K. Meech, T. Oswalt, J. Rafert, E. Strother, J. Smith, H. Povenmire, B. Jones, D. Kornbluh, L. Reed, K. Izor, M. F. A'Hearn, R. Schnurr, W. Osborn, D. Parker, W. T. Douglas, J. D. Beish, A. R. Klemola, M. Rios, A. Sanchez, J. Piironen, M. Mooney, R. S. Ireland, and D. Leibow (Dec. 1987). "The size, shape, density, and Albedo of Ceres from its occultation of BD+8°471". *Icarus* 72.3, pp. 507–518. DOI: 10.1016/0019-1035(87)90048-0.

David L. Mitchell, Steven J. Ostro, R. Scott Hudson, Keith D. Rosema, Donald B. Campbell, Reinaldo Vélez, John F. Chandler, Irwin I. Shapiro, Jon D. Giorgini, and Donald K. Yeomans (Nov. 1996). "Radar Observations of Asteroids 1 Ceres, 2 Pallas, and 4 Vesta". *Icarus* 124.1, pp. 113–133. DOI: 10.1006/icar.1996.0193.

I. Molotov, V. Agapov, V. Kouprianov, V. Titenko, V. Rumyantsev, V. Biryukov, G. Borisov, Yu. Burtsev, Z. Khutorovsky, G. Kornienko, A. Erofeeva, E. Litvinenko, A. Aliev, R. Zalles, O. Grebetskaya, Yu. Likh, O. Rusakov, N. Minikulov, M. Guliamov, B. Abdulloev, N. Borisova, T. Irsmambetova, A. Vikhristenko, R. Inasaridze, E. Gubin, A. Erofeev, Yu. Ivaschenko, V. Yurkov, A. Matkin, A. Rybak, D. Karaush, A. Letsu, O. Tsibizov, B. Ermakov, and E. Siniakov (Mar. 2009). "ISON Worldwide Scientific Optical Network". *Fifth European Conference on Space Debris*. Ed. by H. Lacoste. Vol. 672. ESA Special Publication, 7, p. 7.

I. Molotov, M. Zakhvatkin, L. Elenin, L. Canals Ros, F. Graziani, P. Teofilatto, T. Schildknecht, S. Ehgamberdiev, A. Aliev, Y. Ivashchenko, R. Zalles, A. Streltsov, A. Krylov, A. Erofeeva, E. Chornaya, O. Rusakov, V. Stepanyants, V. Agletdinov, G. Borovin, and E. Pavlova (Apr. 2019). "ISON Network Tracking of Space Debris: Current Status and Achievements". *Revista Mexicana de Astronomia y Astrofisica Conference Series*. Vol. 51. Revista Mexicana de Astronomia y Astrofisica Conference Series, pp. 144–149.

Z. Moravec, P. Jelinek, L. Tesi, A. Boattini, M. Tombelli, G. Forti, S. Gajdos, J. Toth, M. Griesser, M. Dawson, G. J. Garradd, L. Sarounova, S. Kluegl, M. Busch, R. Stoss, M. Blythe, F. Shelly, M. Bezpalko, M. Elowitz, R. Huber, L. Manguso, J. Stuart, R. Sayer, J. B. Evans, H. Viggh, G. Hug, and C. W. Hergenrother (Aug. 2000). "2000 PN9". *Minor Planet Electronic Circulars* 2000-P48.

A. Morbidelli, H. F. Levison, K. Tsiganis, and R. Gomes (May 2005). "Chaotic capture of Jupiter's Trojan asteroids in the early Solar System". *Nature* 435.7041, pp. 462–465. DOI: 10.1038/nature03540.

A. Morbidelli, K. J. Walsh, D. P. O'Brien, D. A. Minton, and W. F. Bottke (2015). "The Dynamical Evolution of the Asteroid Belt". *Asteroids IV*, pp. 493–507. DOI: 10.2458/azu_uapress_9780816532131-ch026.

Michael Mueller, M. Delbo, J. L. Hora, D. E. Trilling, B. Bhattacharya, W. F. Bottke, S. Chesley, J. P. Emery, G. Fazio, A. W. Harris, A. Mainzer, M. Mommert, B. Penprase, H. A. Smith, T. B. Spahr, J. A. Stansberry, and C. A. Thomas (Apr. 2011).

"ExploreNEOs. III. Physical Characterization of 65 Potential Spacecraft Target Asteroids". *AJ* 141.4, 109, p. 109. DOI: 10.1088/0004-6256/141/4/109.

S. P. Naidu, L. A. M. Benner, M. Brozovic, M. C. Nolan, S. J. Ostro, J. L. Margot, J. D. Giorgini, T. Hirabayashi, D. J. Scheeres, P. Pravec, P. Scheirich, C. Magri, and J. S. Jao (Sept. 2020). "Radar observations and a physical model of binary near-Earth asteroid 65803 Didymos, target of the DART mission". *Icarus* 348, 113777, p. 113777. DOI: 10.1016/j.icarus.2020.113777.

S. P. Naidu, J. L. Margot, P. A. Taylor, M. C. Nolan, M. W. Busch, L. A. M. Benner, M. Brozovic, J. D. Giorgini, J. S. Jao, and C. Magri (Aug. 2015). "Radar Imaging and Characterization of the Binary Near-Earth Asteroid (185851) 2000 DP107". *AJ* 150.2, 54, p. 54. DOI: 10.1088/0004-6256/150/2/54.

David Nesvorný and William F. Bottke (Aug. 2004). "Detection of the Yarkovsky effect for main-belt asteroids". *Icarus* 170.2, pp. 324–342. DOI: 10.1016/j.icarus.2004.04.012.

David Nesvorný, Rogerio Deienno, William F. Bottke, Robert Jedicke, Shantanu Naidu, Steven R. Chesley, Paul W. Chodas, Mikael Granvik, David Vokrouhlický, Miroslav Brož, Alessandro Morbidelli, Eric Christensen, Frank C. Shelly, and Bryce T. Bolin (Aug. 2023). "NEOMOD: A New Orbital Distribution Model for Near-Earth Objects". *AJ* 166.2, 55, p. 55. DOI: 10.3847/1538-3881/ace040.

M C Nolan, E S Howell, D J Scheeres, J W McMahon, O Golubov, C W Hergenrother, J P Emery, K S Noll, S R Chesley, and D S Lauretta (Feb. 2019). "Detection of Rotational Acceleration of Bennu Using HST Light Curve Observations". *Geophysical Research Letters* 46.4, pp. 1956–1962.

Michael C. Nolan, Christopher Magri, Ellen S. Howell, Lance A. M. Benner, Jon D. Giorgini, Carl W. Hergenrother, R. Scott Hudson, Dante S. Lauretta, Jean-Luc Margot, Steven J. Ostro, and Daniel J. Scheeres (Sept. 2013). "Shape model and surface properties of the OSIRIS-REx target Asteroid (101955) Bennu from radar and lightcurve observations". *Icarus* 226.1, pp. 629–640. DOI: 10.1016/j.icarus.2013.05.028.

C. R. Nugent, A. Mainzer, J. Bauer, R. M. Cutri, E. A. Kramer, T. Grav, J. Masiero, S. Sonnett, and E. L. Wright (Sept. 2016). "NEOWISE Reactivation Mission Year Two: Asteroid Diameters and Albedos". *AJ* 152.3, 63, p. 63. DOI: 10.3847/0004-6256/152/3/63.

Carolyn Rosemary Nugent (Jan. 2013). "Solar Radiation and Near-Earth Asteroids: Thermophysical Modeling and New Measurements of the Yarkovsky Effect". PhD thesis. University of California, Los Angeles.

David P. O'Brien, Alessandro Morbidelli, and William F. Bottke (Nov. 2007). "The primordial excitation and clearing of the asteroid belt—Revisited". *Icarus* 191.2, pp. 434–452. DOI: 10.1016/j.icarus.2007.05.005.

Yasuhiro Oba, Yoshinori Takano, Yoshihiro Furukawa, Toshiki Koga, Daniel P. Glavin, Jason P. Dworkin, and Hiroshi Naraoka (Apr. 2022). "Identifying the wide diversity of extraterrestrial purine and pyrimidine nucleobases in carbonaceous meteorites". *Nature Communications* 13, 2008, p. 2008. DOI: 10.1038/s41467-022-29612-x.

Catherine B. Olkin, Harold F. Levison, Michael Vincent, Keith S. Noll, John Andrews, Sheila Gray, Phil Good, Simone Marchi, Phil Christensen, Dennis Reuter, Harold Weaver, Martin Pätzold, III Bell James F., Victoria E. Hamilton, Neil Dello Russo, Amy Simon, Matt Beasley, Will Grundy, Carly Howett, John Spencer, Michael Ravine, and Michael Caplinger (Oct. 2021). "Lucy Mission to the Trojan Asteroids: Instrumentation and Encounter Concept of Operations". *The Planetary Science Journal* 2.5, 172, p. 172. DOI: 10.3847/PSJ/abf83f.

E. J. Öpik (Jan. 1951). "Collision probability with the planets and the distribution of planetary matter". *Proc. R. Irish Acad. Sect. A* 54, pp. 165–199.

S. J. Ostro, J. F. Chandler, A. A. Hine, K. D. Rosema, I. I. Shapiro, and D. K. Yeomans (June 1990a). "Radar Images of Asteroid 1989 PB". *Science* 248.4962, pp. 1523–1528. DOI: 10.1126/science.248.4962.1523.

S. J. Ostro, R. Connelly, and L. Belkora (Jan. 1988). "Asteroid shapes from radar echo spectra: A new theoretical approach". *Icarus* 73.1, pp. 15–24. DOI: 10.1016/0019-1035(88)90083-8.

S. J. Ostro, R. S. Hudson, L. A. M. Benner, J. D. Giorgini, C. Magri, J. L. Margot, and M. C. Nolan (2002). "Asteroid Radar Astronomy". *Asteroids III*. University of Arizona Press, pp. 151–168.

S. J. Ostro, K. D. Rosema, and R. F. Jurgens (Apr. 1990b). "The shape of Eros". *Icarus* 84.2, pp. 334–351. DOI: 10.1016/0019-1035(90)90042-8.

Steven J. Ostro (Aug. 1988). *Radar investigation of asteroids and planetary satellites*. In NASA, Washington, Reports of Planetary Astronomy, p 107-108 (SEE N89-16624 08-89).

— (Oct. 1993). "Planetary radar astronomy". *Reviews of Modern Physics* 65.4, pp. 1235–1279. DOI: 10.1103/RevModPhys.65.1235.

— (2007). "Planetary Radar". *Encyclopedia of the Solar System*. Ed. by L. -A. Adams McFadden, P. R. Weissman, and T. V. Johnson, pp. 735–764. DOI: 10.1016/B978-012088589-3/50044-X.

Steven J. Ostro, Lance A. M. Benner, Christopher Magri, Jon D. Giorgini, Randy Rose, Raymond F. Jurgens, Donald K. Yeomans, Alice A. Hine, Michael C. Nolan, Daniel J. Scheeres, Stephen B. Broschart, Mikko Kaasalainen, and Jean-Luc Margot (Nov. 2005). "Radar observations of Itokawa in 2004 and improved shape estimation". *Meteorics and Planetary Science* 40.11, pp. 1563–1574. DOI: 10.1111/j.1945-5100.2005.tb00131.x.

Steven J. Ostro, Lance A. M. Benner, Michael C. Nolan, Christopher Magri, Jon D. Giorgini, Daniel J. Scheeres, Stephen B. Broschart, Mikko Kaasalainen, David Vokrouhlický, Steven R. Chesley, Jean-Luc Margot, Raymond F. Jurgens, Randy Rose, Donald K. Yeomans, Shigeru Suzuku, and Eric M. de Jong (Mar. 2004). "Radar observations of asteroid 25143 Itokawa (1998 SF36)". *Meteoritics & Planetary Science* 39.3, pp. 407–424. DOI: 10.1111/j.1945-5100.2004.tb00102.x.

Steven. J. Ostro, J.-L. Margot, L. A. M. Benner, J. D. Giorgini, D. J. Scheeres, E. G. Fahnestock, S. B. Broschart, J. Bellerose, M. C. Nolan, C. Magri, P. Pravec, P. Scheirich, R. Rose, R. F. Jurgens, E. M. De Jong, and S. Suzuki (Nov. 2006). "Radar

Imaging of Binary Near-Earth Asteroid (66391) 1999 KW4". en. *Science* 314.5803, pp. 1276–1280. DOI: 10.1126/science.1133622.

András Pál, László Molnár, and Csaba Kiss (Nov. 2018). "TESS in the Solar System". *PASP* 130.993, p. 114503. DOI: 10.1088/1538-3873/aae2aa.

F. C. Penrose (Nov. 1882). "comets a, b, and c 1882, observations at the Royal Observatory, Greenwich". *MNRAS* 43, p. 25. DOI: 10.1093/mnras/43.1.25.

Jean-Marc Petit, Alessandro Morbidelli, and John Chambers (Oct. 2001). "The Primordial Excitation and Clearing of the Asteroid Belt". *Icarus* 153.2, pp. 338–347. DOI: 10.1006/icar.2001.6702.

G. H. Pettengill and R. F. Jurgens (1979). "Radar observations of asteroids." *Asteroids*. Ed. by Tom Gehrels and Mildred Shapley Matthews, pp. 206–211.

P. Pravec and A. W. Harris (Sept. 2007). "Binary asteroid population. 1. Angular momentum content". *Icarus* 190.1, pp. 250–259. DOI: 10.1016/j.icarus.2007.02.023.

P. Pravec, A. J. Meyer, P. Scheirich, D. J. Scheeres, C. J. Benson, and H. F. Agrusa (Aug. 2024). "Rotational lightcurves of Dimorphos and constraints on its post-DART impact spin state". *Icarus* 418, 116138, p. 116138. DOI: 10.1016/j.icarus.2024.116138.

Petr Pravec (2001). *Table of unpublished periods of NEAs*. https://www.asu.cas.cz/~ppravec/tabper.htm.

Petr Pravec and Alan W. Harris (Nov. 2000). "Fast and Slow Rotation of Asteroids". *Icarus* 148.1, pp. 12–20. DOI: 10.1006/icar.2000.6482.

William H. Press, Saul A. Teukolsky, William T. Vetterling, and Brian P. Flannery (1992). *Numerical recipes in FORTRAN. The art of scientific computing*.

Giuseppe Pupillo, Simona Righini, Roberto Orosei, Claudio Bortolotti, Giuseppe Maccaferri, Mauro Roma, Marco Mastrogiuseppe, Tonino Pisanu, Luca Schirru, Stefano Cicalò, Antonio Tripodo, Jorma Harju, Antti Penttilä, Anne K. Virkki, Uwe Bach, Alexander Kraus, Alessio Margheri, Riccardo Ghiani, Maria N. Iacolina, Giuseppe Valente, Detlef Koschny, Richard Moissl, and Gunther Sessler (Dec. 2023). "Toward a European Facility for Ground-Based Radar Observations of Near-Earth Objects". *Remote Sensing* 16.1, 38, p. 38. DOI: 10.3390/rs16010038.

Sean N. Raymond and Alessandro Morbidelli (July 2014). "The Grand Tack model: a critical review". *Complex Planetary Systems, Proceedings of the International Astronomical Union*. Vol. 310, pp. 194–203. DOI: 10.1017/S1743921314008254.

Sean N. Raymond, David P. O'Brien, Alessandro Morbidelli, and Nathan A. Kaib (Oct. 2009). "Building the terrestrial planets: Constrained accretion in the inner Solar System". *Icarus* 203.2, pp. 644–662. DOI: 10.1016/j.icarus.2009.05.016.

Vishnu Reddy, Jorge M. Carvano, Daniela Lazzaro, Tatiana A. Michtchenko, Michael J. Gaffey, Michael S. Kelley, Thais Mothé-Diniz, Alvaro Alvarez-Candal, Nicholas A. Moskovitz, Edward A. Cloutis, and Erin L. Ryan (Nov. 2011). "Mineralogical characterization of Baptistina Asteroid Family: Implications for K/T impactor source". *Icarus* 216.1, pp. 184–197. DOI: 10.1016/j.icarus.2011.08.027.

Derek C. Richardson, Harrison F. Agrusa, Brent Barbee, Rachel H. Cueva, Fabio Ferrari, Seth A. Jacobson, Rahil Makadia, Alex J. Meyer, Patrick Michel, Ryota Nakano, Yun Zhang, Paul Abell, Colby C. Merrill, Adriano Campo Bagatin, Olivier Barnouin, Nancy L. Chabot, Andrew F. Cheng, Steven R. Chesley, R. Terik Daly, Siegfried Eggl, Carolyn M. Ernst, Eugene G. Fahnestock, Tony L. Farnham, Oscar Fuentes-Muñoz, Edoardo Gramigna, Douglas P. Hamilton, Masatoshi Hirabayashi, Martin Jutzi, Josh Lyzhoft, Riccardo Lasagni Manghi, Jay McMahon, Fernando Moreno, Naomi Murdoch, Shantanu P. Naidu, Eric E. Palmer, Paolo Panicucci, Laurent Pou, Petr Pravec, Sabina D. Raducan, Andrew S. Rivkin, Alessandro Rossi, Paul Sánchez, Daniel J. Scheeres, Peter Scheirich, Stephen R. Schwartz, Damya Souami, Gonzalo Tancredi, Paolo Tanga, Paolo Tortora, Josep M. Trigo-Rodríguez, Kleomenis Tsiganis, John Wimarsson, and Marco Zannoni (Aug. 2024). "The Dynamical State of the Didymos System before and after the DART Impact". *The Planetary Science Journal* 5.8, 182, p. 182. DOI: 10.3847/PSJ/ad62f5.

A. S. Rivkin, R. P. Binzel, and S. J. Bus (May 2005). "Constraining near-Earth object albedos using near-infrared spectroscopy". *Icarus* 175.1, pp. 175–180. DOI: 10.1016/j.icarus.2004.11.005.

Javier Rodríguez Rodríguez, Enrique Díez Alonso, Santiago Iglesias Alvarez, Saul Perez Fernandez, Javier Licandro, Miguel R. Alarcon, Miquel Serra-Ricart, Noemi Pinilla-Alonso, Susana Fernandez Menendez, and Francisco Javier de Cos Juez (Jan. 2024). "Improved models for near-Earth asteroids (2100) Ra-Shalom, (3103) Eger, (12711) Tukmit & (161989) Cacus". *MNRAS* 527.3, pp. 6814–6834. DOI: 10.1093/mnras/stad3488.

Nereida Rodriguez-Alvarez, Joseph S. Jao, Clement G. Lee, Martin A. Slade, Joseph Lazio, Kamal Oudrhiri, Kenneth S. Andrews, Lawrence G. Snedeker, Ronglin R. Liou, and Kevin A. Stanchfield (Jan. 2022). "The Improved Capabilities of the Goldstone Solar System Radar Observatory". *IEEE Transactions on Geoscience and Remote Sensing* 60, 3084861, p. 3084861. DOI: 10.1109/TGRS.2021.3084861.

J. E. Rogers, C. M. Bardwell Epoch, and T. B. Spahr (Jan. 2001). "1950 DA =". *Minor Planet Electronic Circulars* 2001-A26.

Anish D. Roshi, Sean Marshall, Amit Vishwas, Mike Sulzer, P. K. Manoharan, Maxime Devogele, Flaviane Venditti, Allison Smith, Sravani Vaddi, Arun Venkataraman, Phil Perillat, and Julie Brisset (May 2023). "The Next Generation Arecibo Telescope: A preliminary study". *arXiv e-prints*, arXiv:2305.07780, arXiv:2305.07780. DOI: 10.48550/arXiv.2305.07780.

A. Rossi, F. Marzari, and D. J. Scheeres (July 2009). "Computing the effects of YORP on the spin rate distribution of the NEO population". *Icarus* 202.1, pp. 95–103. DOI: 10.1016/j.icarus.2009.02.030.

A. Rożek (2017). "Understanding the Influence of Non-gravitational Forces on the Physical Evolution of Near-Earth Asteroids and Comets". PhD thesis.

A. Rożek, S. C. Lowry, M. C. Nolan, P. A. Taylor, L. A. M. Benner, A. Fitzsimmons, T. J. Zegmott, P. R. Weissman, S. F. Green, B. Rozitis, C. Snodgrass, W. D. Smythe, M. D. Hicks, E. S. Howell, A. K. Virkki, B. Aponte-Hernandez, E. G. Rivera-Valentín, L. A. Rodriguez-Ford, L. F. Zambrano-Marin, M. Brozović, S. P. Naidu, J. D. Giorgini, L. G. Snedeker, J. S. Jao, and F. D. Ghigo (Nov. 2019a). "Shape model and spin-state analysis of PHA contact binary (85990) 1999 JV6 from

combined radar and optical observations". en. *A&A* 631, A149. DOI: 10.1051/0004-6361/201936302.

A. Rożek, S. C. Lowry, B. Rozitis, S. F. Green, C. Snodgrass, P. R. Weissman, A. Fitzsimmons, M. D. Hicks, K. J. Lawrence, S. R. Duddy, S. D. Wolters, G. Roberts-Borsani, R. Behrend, and F. Manzini (July 2019b). "Physical model of near-Earth asteroid (1917) Cuyo from ground-based optical and thermal-IR observations". en. *A&A* 627, A172. DOI: 10.1051/0004-6361/201834162.

Agata Rożek, Michael W. Busch, Sean E. Marshall, Grace C. Young, Adam D. Cobb, Chedy Raïssi, Yarin Gal, Lance A. M. Benner, Patrick A. Taylor, and Stephen C. Lowry (Sept. 2019c). "Machine learning tools to develop 3D shape models of near Earth asteroids from radar observations". *EPSC-DPS Joint Meeting 2019*. Vol. 2019, EPSC-DPS2019-2074, EPSC-DPS2019–2074.

Agata Rożek, Stephen C Lowry, Benjamin Rozitis, Lord R Dover, Patrick A Taylor, Anne Virkki, Simon F Green, Colin Snodgrass, Alan Fitzsimmons, Justyn Campbell-White, Sedighe Sajadian, Valerio Bozza, Martin J Burgdorf, Martin Dominik, R Figuera Jaimes, Tobias C Hinse, Markus Hundertmark, Uffe G Jørgensen, Penélope Longa-Peña, Markus Rabus, Sohrab Rahvar, Jesper Skottfelt, and John Southworth (July 2022). "Physical properties of near-Earth asteroid (2102) Tantalus from multi-wavelength observations". *MNRAS*. stac1835. DOI: 10.1093/mnras/stac1835.

B. Rozitis, S. R. Duddy, S. F. Green, and S. C. Lowry (July 2013). "A thermophysical analysis of the (1862) Apollo Yarkovsky and YORP effects". *A&A* 555, A20, A20. DOI: 10.1051/0004-6361/201321659.

B. Rozitis and S. F. Green (June 2012). "The influence of rough surface thermal-infrared beaming on the Yarkovsky and YORP effects". *MNRAS* 423.1, pp. 367–388. DOI: 10.1111/j.1365-2966.2012.20882.x.

— (July 2013). "The influence of global self-heating on the Yarkovsky and YORP effects". *MNRAS* 433.1, pp. 603–621. DOI: 10.1093/mnras/stt750.

Ben Rozitis, Eric Maclennan, and Joshua P. Emery (Aug. 2014). "Cohesive forces prevent the rotational breakup of rubble-pile asteroid (29075) 1950 DA". *Nature* 512.7513, pp. 174–176. DOI: 10.1038/nature13632.

David Parry Rubincam (Nov. 2000). "Radiative Spin-up and Spin-down of Small Asteroids". en. *Icarus* 148.1, pp. 2–11. DOI: 10.1006/icar.2000.6485.

H. N. Russell (July 1906). "On the light variations of asteroids and satellites". *ApJ* 24, pp. 1–18. DOI: 10.1086/141361.

Adam R. Sarafian, Sune G. Nielsen, Horst R. Marschall, Francis M. McCubbin, and Brian D. Monteleone (Oct. 2014). "Early accretion of water in the inner solar system from a carbonaceous chondrite-like source". *Science* 346.6209, pp. 623–626. DOI: 10.1126/science.1256717.

D. J. Scheeres and R. W. Gaskell (Nov. 2008). "Effect of density inhomogeneity on YORP: The case of Itokawa". *Icarus* 198.1, pp. 125–129. DOI: 10.1016/j.icarus.2008.07.010.

D. J. Scheeres, J. W. McMahon, A. S. French, D. N. Brack, S. R. Chesley, D. Farnocchia, Y. Takahashi, J. M. Leonard, J. Geeraert, B. Page, P. Antreasian, K. Getzandanner, D. Rowlands, E. M. Mazarico, J. Small, D. E. Highsmith, M. Moreau, J. P. Emery, B. Rozitis, M. Hirabayashi, P. Sánchez, S. van Wal, P. Tricarico, R. -L. Ballouz, C. L. Johnson, M. M. Al Asad, H. C. M. Susorney, O. S. Barnouin, M. G. Daly, J. A. Seabrook, R. W. Gaskell, E. E. Palmer, J. R. Weirich, K. J. Walsh, E. R. Jawin, E. B. Bierhaus, P. Michel, W. F. Bottke, M. C. Nolan, H. C. Connolly, D. S. Lauretta, and Osiris-Rex Team (Mar. 2019). "The dynamic geophysical environment of (101955) Bennu based on OSIRIS-REx measurements". *Nature Astronomy* 3, pp. 352–361. DOI: 10.1038/s41550-019-0721-3.

P. Scheirich, P. Pravec, S. A. Jacobson, J. Durech, P. Kusnirak, K. Hornoch, S. Mottola, M. Mommert, S. Hellmich, D. Pray, D. Polishook, Yu. N. Krugly, R. Ya. Inasaridze, O. I. Kvaratskhelia, V. Ayvazian, I. Slyusarev, J. Pittichova, E. Jehin, J. Manfroid, M. Gillon, A. Galad, J. Pollock, J. Licandro, V. Ali-Lagoa, J. Brinsfield, and I. E. Molotov (Jan. 2015). "The binary near-Earth Asteroid (175706) 1996 FG_3 - An

observational constraint on its orbital evolution". *Icarus* 245, pp. 56–63. DOI: 10.1016/j.icarus.2014.09.023.

P. Scheirich, P. Pravec, P. Kusnirak, K. Hornoch, J. McMahon, D. J. Scheeres, D. Capek, D. P. Pray, H. Kucakova, A. Galad, J. Vrastil, Yu N. Krugly, N. Moskovitz, L. D. Avner, B. Skiff, R. S. McMillan, J. A. Larsen, M. J. Brucker, A. F. Tubbiolo, W. R. Cooney, J. Gross, D. Terrell, O. Burkhonov, K. E. Ergashev, Sh. A. Ehgamberdiev, P. Fatka, R. Durkee, E. Lilly Schunova, R. Ya Inasaridze, V. R. Ayvazian, G. Kapanadze, N. M. Gaftonyuk, J. A. Sanchez, V. Reddy, L. McGraw, M. S. Kelley, and I. E. Molotov (May 2021). "A satellite orbit drift in binary near-Earth asteroids (66391) 1999 KW4 and (88710) 2001 SL9 - Indication of the BYORP effect". *Icarus* 360, 114321, p. 114321. DOI: 10.1016/j.icarus.2021.114321.

Peter Schulte, Laia Alegret, Ignacio Arenillas, José A. Arz, Penny J. Barton, Paul R. Bown, Timothy J. Bralower, Gail L. Christeson, Philippe Claeys, Charles S. Cockell, Gareth S. Collins, Alexander Deutsch, Tamara J. Goldin, Kazuhisa Goto, José M. Grajales-Nishimura, Richard A. F. Grieve, Sean P. S. Gulick, Kirk R. Johnson, Wolfgang Kiessling, Christian Koeberl, David A. Kring, Kenneth G. MacLeod, Takafumi Matsui, Jay Melosh, Alessandro Montanari, Joanna V. Morgan, Clive R. Neal, Douglas J. Nichols, Richard D. Norris, Elisabetta Pierazzo, Greg Ravizza, Mario Rebolledo-Vieyra, Wolf Uwe Reimold, Eric Robin, Tobias Salge, Robert P. Speijer, Arthur R. Sweet, Jaime Urrutia-Fucugauchi, Vivi Vajda, Michael T. Whalen, and Pi S. Willumsen (Mar. 2010). "The Chicxulub Asteroid Impact and Mass Extinction at the Cretaceous-Paleogene Boundary". *Science* 327.5970, p. 1214. DOI: 10.1126/science.1177265.

Megan E. Schwamb, R. Lynne Jones, Steven R. Chesley, Alan Fitzsimmons, Wesley C. Fraser, Matthew J. Holman, Henry Hsieh, Darin Ragozzine, Cristina A. Thomas, David E. Trilling, Michael E. Brown, Michele T. Bannister, Dennis Bodewits, Miguel de Val-Borro, David Gerdes, Mikael Granvik, Michael S. P. Kelley, Matthew M. Knight, Robert L. Seaman, Quan-Zhi Ye, and Leslie A. Young (Feb.

2018). "Large Synoptic Survey Telescope Solar System Science Roadmap". *arXiv e-prints*, arXiv:1802.01783, arXiv:1802.01783. DOI: 10.48550/arXiv.1802.01783.

D. W. G. Sears (Nov. 2015). "The Explored Asteroids: Science and Exploration in the Space Age". *Space Sci. Rev.* 194.1-4, pp. 139–235. DOI: 10.1007/s11214-015-0202-7.

P. Ševeček, O. Golubov, D. J. Scheeres, and Yu. N. Krugly (Aug. 2016). "Obliquity dependence of the tangential YORP". en. *A&A* 592, A115. DOI: 10.1051/0004-6361/201628746.

Michael K. Shepard, Jean-Luc Margot, Christopher Magri, Michael C. Nolan, Joshua Schlieder, Benjamin Estes, Schelte J. Bus, Eric L. Volquardsen, Andrew S. Rivkin, Lance A. M. Benner, Jon D. Giorgini, Steven J. Ostro, and Michael W. Busch (Sept. 2006). "Radar and infrared observations of binary near-Earth Asteroid 2002 CE26". *Icarus* 184.1, pp. 198–210. DOI: 10.1016/j.icarus.2006.04.019.

Stephen M. Slivan (Sept. 2002). "Spin vector alignment of Koronis family asteroids". en. *Nature* 419.6902, pp. 49–51. DOI: 10.1038/nature00993.

Stephen M. Slivan, Richard P. Binzel, Lucy D. Crespo da Silva, Mikko Kaasalainen, Mariah M. Lyndaker, and Marko Krčo (Apr. 2003). "Spin vectors in the Koronis family: comprehensive results from two independent analyses of 213 rotation lightcurves". *Icarus* 162.2, pp. 285–307. DOI: 10.1016/S0019-1035(03)00029-0.

Stephen M. Slivan, Francis P. Wilkin, Claire McLellan-Cassivi, and Michael J. Person (Nov. 2023). "Spin vectors in the Koronis family: V. Resolving the ambiguous rotation period of (3032) Evans". *Icarus* 405, 115701, p. 115701. DOI: 10.1016/j.icarus.2023.115701.

Stephen Michael Slivan (Jan. 1995). "Spin-Axis Alignment of Koronis Family Asteroids". PhD thesis. Massachusetts Institute of Technology.

C. Snodgrass and B. Carry (June 2013). "Automatic Removal of Fringes from EFOSC Images". *The Messenger* 152, pp. 14–16.

Colin Snodgrass, Ivo Saviane, Lorenzo Monaco, and Peter Sinclaire (June 2008). "EFOSC2 Episode IV: A New Hope". *The Messenger* 132, pp. 18–19.

Donald L. Snyder (May 1987a). *Delay-Doppler radar imaging*. Semiannual Progress Report No. 2, 1 Dec. 1986 - 30 May 1987 Washington Univ., Saint Louis, MO. Electronic Systems and Signals Research Lab.

— (Nov. 1987b). *Delay-doppler radar imaging*. Semiannual Progress Report, 1 Jun. - 30 Nov. 1987 Washington Univ., Saint Louis, MO. Electronic Systems and Signals Research Lab.

James M. Somers, M. D. Hicks, and K. J. Lawrence (Sept. 2008). "Optical Characterization of Planetary Radar Targets". *AAS/Division for Planetary Sciences Meeting Abstracts #40*. Vol. 40. AAS/Division for Planetary Sciences Meeting Abstracts, 28.21, p. 28.21.

Federica Spoto, Andrea Milani, and Zoran Knežević (Sept. 2015). "Asteroid family ages". *Icarus* 257, pp. 275–289. DOI: 10.1016/j.icarus.2015.04.041.

Thomas S. Statler (Aug. 2009). "Extreme Sensitivity of the YORP Effect to Small-Scale Topography". *Icarus* 202.2. arXiv: 0903.1119, pp. 502–513. DOI: 10.1016/j.icarus.2009.03.003.

— (Mar. 2015). "Obliquities of "top-shaped" asteroids may not imply reshaping by YORP spin-up". *Icarus* 248, pp. 313–317. DOI: 10.1016/j.icarus.2014.10.050.

Robert Stephens and Brian D. Warner (Oct. 2018). "The ALCDEF Database and the NASA SBN/PDS: The Perfect Merger". *AAS/Division for Planetary Sciences Meeting Abstracts #50*. Vol. 50. AAS/Division for Planetary Sciences Meeting Abstracts, 417.03, p. 417.03.

S. Sugita et al. (Apr. 2019). "The geomorphology, color, and thermal properties of Ryugu: Implications for parent-body processes". *Science* 364.6437, pp. 252–252. DOI: 10.1126/science.aaw0422.

Hannah C. M. Susorney, Catherine L. Johnson, Olivier S. Barnouin, Michael G. Daly, Jeffrey A. Seabrook, Edward B. Bierhaus, and Dante S. Lauretta (June 2019). "The global surface roughness of 25143 Itokawa". *Icarus* 325, pp. 141–152. DOI: 10.1016/j.icarus.2019.01.021.

M. Tarenghi and R. N. Wilson (Sept. 1989). "The ESO NTT (New Technology Telescope): The first active optics telescope." *Active telescope systems*. Ed. by Francois J. Roddier. Vol. 1114. Society of Photo-Optical Instrumentation Engineers (SPIE) Conference Series, pp. 302–313. DOI: 10.1117/12.960835.

P. A. Taylor, J.-L. Margot, D. Vokrouhlicky, D. J. Scheeres, P. Pravec, S. C. Lowry, A. Fitzsimmons, M. C. Nolan, S. J. Ostro, L. A. M. Benner, J. D. Giorgini, and C. Magri (Apr. 2007). "Spin Rate of Asteroid (54509) 2000 PH5 Increasing Due to the YORP Effect". en. *Science* 316.5822, pp. 274–277. DOI: 10.1126/science.1139038.

P. A. Taylor, E. G. Rivera-Valentin, A. K. Virkki, B. D. Warner, J. Oey, F. C. F. Venditti, S. E. Marshall, L. F. Zambrano-Marin, M. Brozovic, S. P. Naidu, L. A. M. Benner, J. S. Jao, A. Bonsall, F. D. Ghigo, A. Aznar, P. Pravec, J. L. Margot, B. Aponte-Hernandez, S. S. Bhiravarasu, C. Rodriguez Sanchez-Vahamonde, R. McGlasson, B. Presler-Marshall, and J. D. Giorgini (Mar. 2019a). "Radar and Optical Observations of Equal-Mass Binary Near-Earth Asteroids (190166) 2005 UP156 and 2017 YE5". *50th Annual Lunar and Planetary Science Conference*. Lunar and Planetary Science Conference, 2945, p. 2945.

Patrick Taylor (Jan. 2023). "Next Generation Planetary Radar with the Green Bank Telescope". *American Astronomical Society Meeting Abstracts*. Vol. 241. American Astronomical Society Meeting Abstracts, 139.04, p. 139.04.

Patrick Taylor, Steven Wilkinson, Flora Paganelli, Ray Samaniego, Bishara Shamee, Aaron Wallace, and Anthony Beasley (Jan. 2023). "The Next Generation Planetary Radar System on the Green Bank Telescope". *American Astronomical Society Meeting Abstracts*. Vol. 241. American Astronomical Society Meeting Abstracts, 104.11, p. 104.11.

Patrick A. Taylor, Edgard G. Rivera-Valentín, Lance A. M. Benner, Sean E. Marshall, Anne K. Virkki, Flaviane C. F. Venditti, Luisa F. Zambrano-Marin, Sriram S. Bhiravarasu, Betzaida Aponte-Hernandez, Carolina Rodriguez Sanchez-Vahamonde, and Jon D. Giorgini (Mar. 2019b). "Arecibo radar observations of near-Earth aster-

oid (3200) Phaethon during the 2017 apparition". *Planet. Space Sci.* 167, pp. 1–8. DOI: 10.1016/j.pss.2019.01.009.

David James Tholen (Sept. 1984). "Asteroid Taxonomy from Cluster Analysis of Photometry." PhD thesis. University of Arizona.

C. A. Thomas, D. E. Trilling, J. P. Emery, M. Mueller, J. L. Hora, L. A. M. Benner, B. Bhattacharya, W. F. Bottke, S. Chesley, M. Delbó, G. Fazio, A. W. Harris, A. Mainzer, M. Mommert, A. Morbidelli, B. Penprase, H. A. Smith, T. B. Spahr, and J. A. Stansberry (Sept. 2011). "ExploreNEOs. V. Average Albedo by Taxonomic Complex in the Near-Earth Asteroid Population". *AJ* 142.3, 85, p. 85. DOI: 10.1088/0004-6256/142/3/85.

Cristina A. Thomas, Joshua P. Emery, David E. Trilling, Marco Delbó, Joseph L. Hora, and Michael Mueller (Jan. 2014). "Physical characterization of Warm Spitzer-observed near-Earth objects". *Icarus* 228, pp. 217–246. DOI: 10.1016/j.icarus.2013.10.004.

Jun Tian, Hai-Bin Zhao, and Bin Li (Dec. 2022). "Shape Model and Rotation Acceleration of (1685) Toro and (85989) 1999 JD6 from Optical Observations". *Research in Astronomy and Astrophysics* 22.12, 125004, p. 125004. DOI: 10.1088/1674-4527/ac977d.

J. Ticha, M. Tichy, L. Kornos, P. Koleny, P. Kusnirak, J. E. Rogers, M. E. Van Ness, D. P. Pray, and T. B. Spahr (Jan. 2001). "2000 YK66". *Minor Planet Electronic Circulars* 2001-A22.

M. Tichy, M. Tombelli, A. Boattini, L. Tesi, D. Guidetti, G. Forti, E. Masotti, S. Bartolini, M. Griesser, E. Meyer, E. Obermair, P. Pravec, P. Sicoli, A. Testa, M. Blythe, F. Shelly, M. Bezpalko, J. Stuart, H. Viggh, R. Sayer, G. Hug, G. Bell, and G. V. Williams (Jan. 1999). "1999 AP10". *Minor Planet Electronic Circulars* 1999-B05.

Doug Tody (Jan. 1986). "The IRAF Data Reduction and Analysis System". *Instrumentation in astronomy VI*. Ed. by David L. Crawford. Vol. 627. Society of Photo-Optical Instrumentation Engineers (SPIE) Conference Series, p. 733. DOI: 10.1117/12.968154.

J. L. Tonry, L. Denneau, H. Flewelling, A. N. Heinze, C. A. Onken, S. J. Smartt, B. Stalder, H. J. Weiland, and C. Wolf (Nov. 2018). "The ATLAS All-Sky Stellar Reference Catalog". *ApJ* 867.2, 105, p. 105. DOI: 10.3847/1538-4357/aae386.

D. E. Trilling, M. Mueller, J. L. Hora, A. W. Harris, B. Bhattacharya, W. F. Bottke, S. Chesley, M. Delbo, J. P. Emery, G. Fazio, A. Mainzer, B. Penprase, H. A. Smith, T. B. Spahr, J. A. Stansberry, and C. A. Thomas (Sept. 2010). "ExploreNEOs. I. Description and First Results from the Warm Spitzer Near-Earth Object Survey". *AJ* 140.3, pp. 770–784. DOI: 10.1088/0004-6256/140/3/770.

K. Tsiganis, R. Gomes, A. Morbidelli, and H. F. Levison (May 2005). "Origin of the orbital architecture of the giant planets of the Solar System". *Nature* 435.7041, pp. 459–461. DOI: 10.1038/nature03539.

D. E. Vavilov and B. Carry (Jan. 2025). "Rotation periods of asteroids from light curves of TESS data". *A&A* 693, A66, A66. DOI: 10.1051/0004-6361/202348940.

Julia Venturini, Maria Paula Ronco, and Octavio Miguel Guilera (July 2020). "Setting the Stage: Planet Formation and Volatile Delivery". *Space Sci. Rev.* 216.5, 86, p. 86. DOI: 10.1007/s11214-020-00700-y.

D. Veras, Y. Birader, and U. Zaman (June 2021). "Rocky debris pollution of single white dwarfs in systems with no planets". *AAS/Division of Dynamical Astronomy Meeting*. Vol. 53. AAS/Division of Dynamical Astronomy Meeting, 107.05, p. 107.05.

Dimitri Veras, Yusuf Birader, and Uwais Zaman (Mar. 2022). "Orbit decay of 2-100 au planetary remnants around white dwarfs with no gravitational assistance from planets". *MNRAS* 510.3, pp. 3379–3388. DOI: 10.1093/mnras/stab3490.

Dimitri Veras, Seth A. Jacobson, and Boris T. Gänsicke (Dec. 2014). "Post-main-sequence debris from rotation-induced YORP break-up of small bodies". *MNRAS* 445.3, pp. 2794–2799. DOI: 10.1093/mnras/stu1926.

Dimitri Veras and Daniel J Scheeres (Feb. 2020). "Post-main-sequence debris from rotation-induced YORP break-up of small bodies – II. Multiple fissions, internal strengths, and binary production". en. *Monthly Notices of the Royal Astronomical Society* 492.2, pp. 2437–2445. DOI: 10.1093/mnras/stz3565.

P. Vernazza, M. Ferrais, L. Jorda, J. Hanuš, B. Carry, M. Marsset, M. Brož, R. Fetick, M. Viikinkoski, F. Marchis, F. Vachier, A. Drouard, T. Fusco, M. Birlan, E. Podlewska-Gaca, N. Rambaux, M. Neveu, P. Bartczak, G. Dudziński, E. Jehin, P. Beck, J. Berthier, J. Castillo-Rogez, F. Cipriani, F. Colas, C. Dumas, J. Ďurech, J. Grice, M. Kaasalainen, A. Kryszczynska, P. Lamy, H. Le Coroller, A. Marciniak, T. Michalowski, P. Michel, T. Santana-Ros, P. Tanga, A. Vigan, O. Witasse, B. Yang, P. Antonini, M. Audejean, P. Aurard, R. Behrend, Z. Benkhaldoun, J. M. Bosch, A. Chapman, L. Dalmon, S. Fauvaud, Hiroko Hamanowa, Hiromi Hamanowa, J. His, A. Jones, D. -H. Kim, M. -J. Kim, J. Krajewski, O. Labrevoir, A. Leroy, F. Livet, D. Molina, R. Montaigut, J. Oey, N. Payre, V. Reddy, P. Sabin, A. G. Sanchez, and L. Socha (Oct. 2021). "VLT/SPHERE imaging survey of the largest main-belt asteroids: Final results and synthesis". *A&A* 654, A56, A56. DOI: 10.1051/0004-6361/202141781.

Matti Viikinkoski, Mikko Kaasalainen, and Josef Durech (Apr. 2015a). "ADAM: a general method for using various data types in asteroid reconstruction". *A&A* 576, A8, A8. DOI: 10.1051/0004-6361/201425259.

— (Feb. 2015b). *ADAM: All-Data Asteroid Modeling*. Astrophysics Source Code Library, record ascl:1502.004.

A. Virkki and K. Muinonen (May 2016). "Radar scattering by planetary surfaces modeled with laboratory-characterized particles". *Icarus* 269, pp. 38–49. DOI: 10.1016/j.icarus.2016.01.011.

Anne K. Virkki, Sean E. Marshall, Flaviane C. F. Venditti, Luisa F. Zambrano-Marín, Dylan C. Hickson, Anna McGilvray, Patrick A. Taylor, Edgard G. Rivera-Valentín, Maxime Devogèle, Eframir Franco Díaz, Sriram S. Bhiravarasu, Betzaida Aponte Hernández, Carolina Rodriguez Sánchez-Vahamonde, Michael C. Nolan, Phil Perillat, Israel Cabrera, Elliot González, Daniel Padilla, Victor Negrón, Juan Marrero, Johbany Lebrón, Adrian Bagué, Francisco Jiménez, Andy López-Oquendo, Daniel Repp, Riley A. McGlasson, Brynn Presler-Marshall, Ellen S. Howell, Jean-Luc Margot, and Sanjana Prabhu Desai (Sept. 2022). "Arecibo Planetary Radar Observations

of Near-Earth Asteroids: 2017 December-2019 December". *The Planetary Science Journal* 3.9, 222, p. 222. DOI: 10.3847/PSJ/ac8b72.

D. Vokrouhlický, W. F. Bottke, S. R. Chesley, D. J. Scheeres, and T. S. Statler (2015a). "The Yarkovsky and YORP Effects". *Asteroids IV*, pp. 509–531. DOI: 10.2458/azu_uapress_9780816532131-ch027.

D. Vokrouhlický, W. F. Bottke, N. Orbeck, A. Celletti, and A. Burns (Dec. 2011). *Yarkovsky and YORP effects*. last modified on 2013-10-26. DOI: doi:10.4249/scholarpedia.10599. URL: http://www.scholarpedia.org/article/Yarkovsky_and_YORP_effects.

D. Vokrouhlický, M. Brož, W. F. Bottke, D. Nesvorný, and A. Morbidelli (May 2006a). "Yarkovsky/YORP chronology of asteroid families". *Icarus* 182.1, pp. 118–142. DOI: 10.1016/j.icarus.2005.12.010.

D. Vokrouhlický, M. Brož, A. Morbidelli, W. F. Bottke, D. Nesvorný, D. Lazzaro, and A. S. Rivkin (May 2006b). "Yarkovsky footprints in the Eos family". *Icarus* 182.1, pp. 92–117. DOI: 10.1016/j.icarus.2005.12.011.

D. Vokrouhlický and D. Čapek (Oct. 2002). "YORP-Induced Long-Term Evolution of the Spin State of Small Asteroids and Meteoroids: Rubincam's Approximation". en. *Icarus* 159.2, pp. 449–467. DOI: 10.1006/icar.2002.6918.

David Vokrouhlický, Davide Farnocchia, David Čapek, Steven R. Chesley, Petr Pravec, Petr Scheirich, and Thomas G. Müller (May 2015b). "The Yarkovsky effect for 99942 Apophis". *Icarus* 252, pp. 277–283. DOI: 10.1016/j.icarus.2015.01.011.

David Vokrouhlický, David Nesvorný, and William F. Bottke (Sept. 2003). "The vector alignments of asteroid spins by thermal torques". en. *Nature* 425.6954, pp. 147–151. DOI: 10.1038/nature01948.

K. J. Walsh and S. A. Jacobson (2015). "Formation and Evolution of Binary Asteroids". *Asteroids IV*, pp. 375–393. DOI: 10.2458/azu_uapress_9780816532131-ch020.

Kevin J. Walsh, Alessandro Morbidelli, Sean N. Raymond, David P. O'Brien, and Avi M. Mandell (July 2011). "A low mass for Mars from Jupiter's early gas-driven migration". *Nature* 475.7355, pp. 206–209. DOI: 10.1038/nature10201.

Kevin J. Walsh, Derek C. Richardson, and Patrick Michel (July 2008). "Rotational breakup as the origin of small binary asteroids". en. *Nature* 454.7201, pp. 188–191. DOI: 10.1038/nature07078.

Brian D. Warner (July 2016). "Near-Earth Asteorid Lightcurve Analysis at CS3-Palmer Divide Station: 2016 January-April". *Minor Planet Bulletin* 43.3, pp. 240–250.

Brian D. Warner, Alan W. Harris, and Petr Pravec (July 2009). "The asteroid lightcurve database". *Icarus* 202.1, pp. 134–146. DOI: 10.1016/j.icarus.2009.02.003.

Brian D. Warner and Robert D. Stephens (Apr. 2021a). "Near-Earth Asteroid Lightcurve Analysis at the Center for Solar System Studies: 2020 September to 2021 January". *Minor Planet Bulletin* 48.2, pp. 170–179.

— (Jan. 2021b). "On Confirmed and Suspected Binary Asteroids Observed at the Center for Solar System Studies". *Minor Planet Bulletin* 48.1, pp. 40–49.

Brian D. Warner, Robert D. Stephens, and Alan W. Harris (July 2011). "Save the Lightcurves". *Minor Planet Bulletin* 38.3, pp. 172–174.

S. Watanabe, M. Hirabayashi, N. Hirata, Na. Hirata, R. Noguchi, Y. Shimaki, H. Ikeda, E. Tatsumi, M. Yoshikawa, S. Kikuchi, H. Yabuta, T. Nakamura, S. Tachibana, Y. Ishihara, T. Morota, K. Kitazato, N. Sakatani, K. Matsumoto, K. Wada, H. Senshu, C. Honda, T. Michikami, H. Takeuchi, T. Kouyama, R. Honda, S. Kameda, T. Fuse, H. Miyamoto, G. Komatsu, S. Sugita, T. Okada, N. Namiki, M. Arakawa, M. Ishiguro, M. Abe, R. Gaskell, E. Palmer, O. S. Barnouin, P. Michel, A. S. French, J. W. McMahon, D. J. Scheeres, P. A. Abell, Y. Yamamoto, S. Tanaka, K. Shirai, M. Matsuoka, M. Yamada, Y. Yokota, H. Suzuki, K. Yoshioka, Y. Cho, S. Tanaka, N. Nishikawa, T. Sugiyama, H. Kikuchi, R. Hemmi, T. Yamaguchi, N. Ogawa, G. Ono, Y. Mimasu, K. Yoshikawa, T. Takahashi, Y. Takei, A. Fujii, C. Hirose, T. Iwata, M. Hayakawa, S. Hosoda, O. Mori, H. Sawada, T. Shimada, S. Soldini, H. Yano, R. Tsukizaki, M. Ozaki, Y. Iijima, K. Ogawa, M. Fujimoto, T. -M. Ho, A. Moussi, R. Jaumann, J. -P. Bibring, C. Krause, F. Terui, T. Saiki, S. Nakazawa, and Y. Tsuda (Apr. 2019). "Hayabusa2 arrives at the carbonaceous asteroid 162173

Ryugu—A spinning top-shaped rubble pile". *Science* 364.6437, pp. 268–272. DOI: 10.1126/science.aav8032.

Sei-ichiro Watanabe, Yuichi Tsuda, Makoto Yoshikawa, Satoshi Tanaka, Takanao Saiki, and Satoru Nakazawa (July 2017). "Hayabusa2 Mission Overview". *Space Sci. Rev.* 208.1-4, pp. 3–16. DOI: 10.1007/s11214-017-0377-1.

Oliver James White, Guifré Molera Calvés, Shinji Horiuchi, Jon Giorgini, Nick Stacy, Andrew Cole, Chris Phillips, Phil Edwards, Ed Kruzins, Jamie Stevens, Lance Benner, and Edwin Peters (Feb. 2025). "Development of Radar and Optical Tracking of Near-Earth Asteroids at the University of Tasmania". *arXiv e-prints*, arXiv:2502.02890, arXiv:2502.02890. DOI: 10.48550/arXiv.2502.02890.

Steven R. Wilkinson, Charlie Hansen, Barry Alexia, Bishara Shamee, Brian Lloyd, Anthony Beasley, Walter Brisken, Flora Paganelli, Galen Watts, Karen O'Neil, and Patrick Courtney (Jan. 2022). "A Planetary Radar System for Detection and High-Resolution Imaging of Nearby Celestial Bodies". *The Microwave Journal*.

F. Windmark, T. Birnstiel, C. Güttler, J. Blum, C. P. Dullemond, and Th. Henning (Apr. 2012). "Planetesimal formation by sweep-up: how the bouncing barrier can be beneficial to growth". *A&A* 540, A73, A73. DOI: 10.1051/0004-6361/201118475.

C. A. Wirtanen and S. Vasilevskis (Apr. 1950). "Observations of Minor Planets Made at Lick Observatory". *Minor Planet Circulars* 416, 1, p. 1.

Andrew N. Youdin and Jeremy Goodman (Feb. 2005). "Streaming Instabilities in Protoplanetary Disks". *ApJ* 620.1, pp. 459–469. DOI: 10.1086/426895.

T. J. Zegmott (2021). "Measuring the Thermal Response of Small Asteroids via the YORP Effect". PhD thesis. Univ. of Kent.

Tarik J. Zegmott, S. C. Lowry, A. Rożek, B. Rozitis, M. C. Nolan, E. S. Howell, S. F. Green, C. Snodgrass, A. Fitzsimmons, and P. R. Weissman (Nov. 2021). "Detection of the YORP effect on the contact binary (68346) 2001 KZ66 from combined radar and optical observations". *MNRAS* 507.4, pp. 4914–4932. DOI: 10.1093/mnras/stab2476.

Wen-Han Zhou, Yun Zhang, Xiao-Ran Yan, and Patrick Michel (Sept. 2022). "The crater-induced YORP effect". *European Planetary Science Congress*, EPSC2022-795, EPSC2022–795. DOI: 10.5194/epsc2022-795.

Xiaoduan Zou, Chunlai Li, Jianjun Liu, Wenrui Wang, Han Li, and Jinsong Ping (Feb. 2014). "The preliminary analysis of the 4179 Toutatis snapshots of the Chang'E-2 flyby". *Icarus* 229, pp. 348–354. DOI: 10.1016/j.icarus.2013.11.002.

ACRONYMS

ADAM All-Data Asteroid Modeling

ADU Analogue-to-Digital Unit

ALCDEF Asteroid Lightcurve Data Exchange Format

ALMA Atacama Large Millimeter Array

AO Adaptive Optics

ARIEL Atmospheric Remote-sensing Infrared Exoplanet Large-survey

AU Astronomical Unit

BYORP Binary YORP

CCD Charge-coupled Device

CMOS Complementary Metal-Oxide-Semiconductor

CRE Cosmic Ray Exposure

DAMIT Database of Asteroid Models from Inversion Techniques

DART Double Asteroid Redirection Test

DFOSC Danish Faint Object Spectrograph and Camera

DSS Deep Space Station

EFOSC2 ESO Faint Object Spectrograph and Camera - version 2

ELT Extremely Large Telescope

ESA European Space Agency

ESO European Southern Observatory

ESOD ESO Danish telescope

FALC Fourier Analysis of Lightcurves

FAST Five-hundred-metre Aperture Spherical Telescope

FITS Flexible Image Transport System

FORS2 FOcal Reducer and low dispersion Spectrograph 2

FOV Field of View

FWHM Full Width at Half Maximum

GMT Giant Magellan Telescope

GSSR Goldstone Solar System Radar System

INT Isaac Newton Telescope

IRTF InfraRed Telescope Facility

ISON International Scientific Optical Network

JAXA Japanese Aerospace Exploration Agency

JPL Jet Propulsion Lab

KBO Kuiper-belt Object

LCDB LightCurve DataBase

LINEAR Lincoln Near Earth Asteroid Research

LONEOS Lowell Observatory Near-Earth-Object Search

LP Large Programme

LPI Lunar and Planetary Institute

LSST Legacy Survey of Space and Time (interchangeable with Large Synoptic Survey Telescope)

LT Liverpool Telescope

MBA Main-belt Asteroid

MiNDSTEp Microlensing Network for the Detection of Small Terrestrial ExoPlanets

MITHNEOS MIT-Hawaii Near-Earth Object Spectroscopic Survey

MOID Minimum Orbit Intersection Distance

NASA National Aeronautics and Space Administration

NEA Near-Earth Asteroid

NEO Near-Earth Object

NEOROCKS Near Earth Object Rapid Observation, Characterisation and Key Simulations

NEOWISE Near-Earth Object Wide-field Infrared Survey Explorer

NGAT Next Generation Arecibo Telescope

ngVLA Next Generation Very Large Array

NIR Near Infrared

NOT Nordic Optical Telescope

NTT New Technology Telescope

NYORP Normal YORP

Pan-STARRS Panoramic Survey Telescope and Rapid Response System

PDS Palmer Divide Station

PHA Potentially Hazardous Asteroid

PIRATE Physics Innovations Robotic Telescope Explorer

PLATO PLAnetary Transits and Oscillations of stars

PSF Point Spread Function

SAGE Shaping Asteroid models using Genetic Evolution

SNR Signal-to-Noise Ratio

SPHERE Spectro-Polarimetric High-contrast Exoplanet REsearch

SSSB Solar System Small Body

TESS Transiting Exoplanet Survey Satellite

TMO Table Mountain Observatory

TMT Thirty Metre Telescope

TNO Trans-Neptunian Object

TYORP Tangential YORP

UT Unit Telescope

VIMOS VIsible MultiObject Spectrograph

VISIR VLT Imager and Spectrometer for mid-Infrared

VLBA Very Long Baseline Array

VLT Very Large Telescope

WFC Wide Field Camera

WHT William Herschel Telescope

YORP Yarkovsky-O'Keefe-Radzievskii-Paddack

APPENDIX A

SUPPLEMENTARY FIGURES AND TABLES

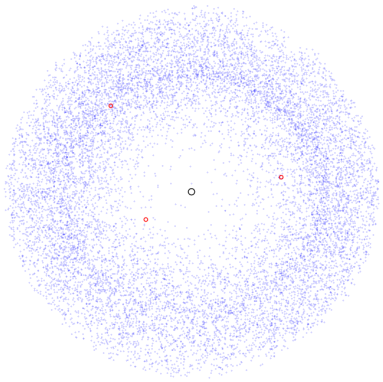

(a) Innermost Solar System (within 1.5 AU of the Sun)

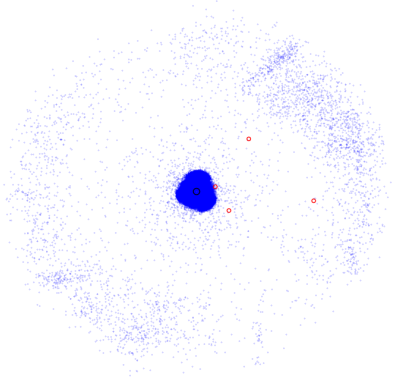

(b) Outer Solar System (within 50 AU of the Sun)

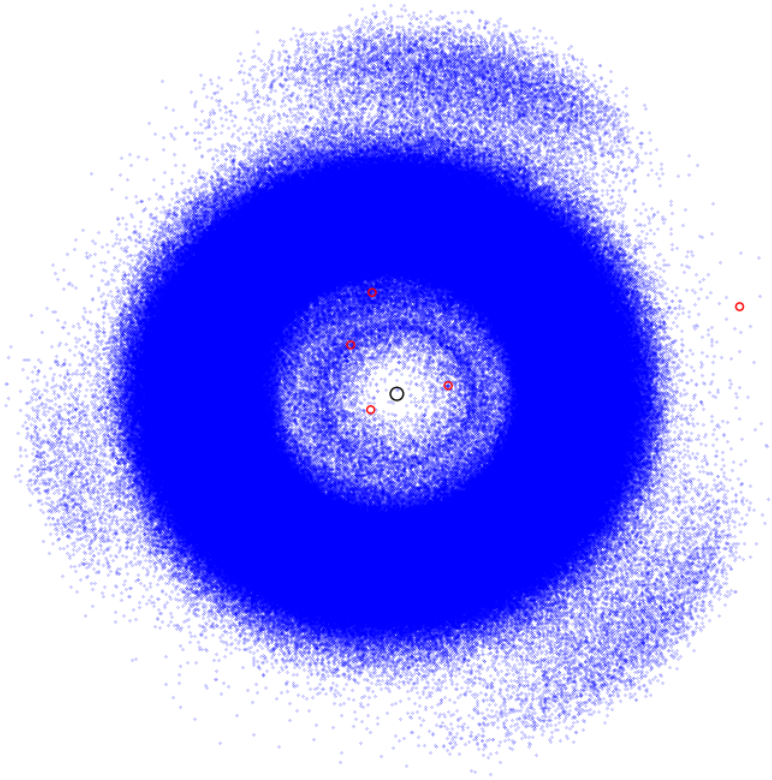

(c) Inner Solar System (within 5.5 AU of the Sun)

Figure A.1: The location of every known minor planet in the Solar System. In each panel, the Sun in marked in the centre with a black circle. Planets are marked with red circles, and asteroids with blue points. In this view, the planets and most minor planets are orbiting in the anti-clockwise direction. Note that in panel (c), the Jupiter Trojans can be seen 60° ahead and behind Jupiter. These images are reprinted from the Minor Planet Center[a].

[a] `https://www.minorplanetcenter.net/iau/lists/MPLists.html`

Asteroid		Hours	Notes/References
(1866)	Sisyphus	48	
(1917)	Cuyo	86	Published shape model (Rożek et al., 2019b) Possible spin-up; analysis ongoing
(2102)	Tantalus	29	Published shape model (Rożek et al., 2022)
(3554)	Amun	32	
(3838)	Epona	56	
(4957)	Brucemurray	65	
(5626)	1991 FE	24	
(6037)	1998 EG	21	
(6053)	1993 BW3	59	
(6456)	Golombek	109	
(6611)	1993 VW	31	
(7025)	1993 QA	42	
(7482)	1994 PC1	51	
(8567)	1996 HW1	71	Analysis ongoing; preliminary non-detection
(23187)	2000 PN9	34	Published shape model (Dover et al., 2023) YORP constrained
(26663)	2000 XK47	18	
(29075)	1950 DA	134	Spin-down seen (Zegmott, 2021) Analysis ongoing (this work)
(30825)	1990 TG1	39	
(31221)	1998 BP26	28	
(31345)	1998 PG	40	
(37655)	Illapa	27	
(65803)	Didymos	3	Target of DART mission; no longer eligible
(66251)	1999 GJ2	17	
(68346)	2001 KZ66	28	YORP detection (Zegmott et al., 2021)
(85275)	1994 LY	100	Analysis ongoing (this work)
(85938)	1999 DJ4	9	
(85990)	1999 JV6	39	Published shape model (Rożek et al., 2019a)
(89830)	2002 CE	46	
(101955)	1999 RQ36	13	
(11054)	1991 FA	15	
(136617)	1994 CC	15	
(136993)	1998 ST49	14	
(138175)	2000 EE104	13	
(141531)	2002 GB	27	
(142040)	2002 QE15	33	
(144898)	2004 VD17	2	
(322652)	1999 JO8	21	
(334673)	2003 AL18	10	
(374038)	2004 HW	9	
(523609)	2005 PJ2	5	

Notes. The hours column is approximate and may include non-science/non-imaging data for some objects.

Table A.1: A list of targets, in ascending order, for the YORP observing campaign described in Section 2.2.1. The 'hours' column lists how many hours of optical lightcurves have been obtained via the YORP campaign as of November 2023. Note that this does not include optical, infrared or radar data that may be available from other sources. An additional three asteroids from the ESO LP were dropped before any observations were taken.

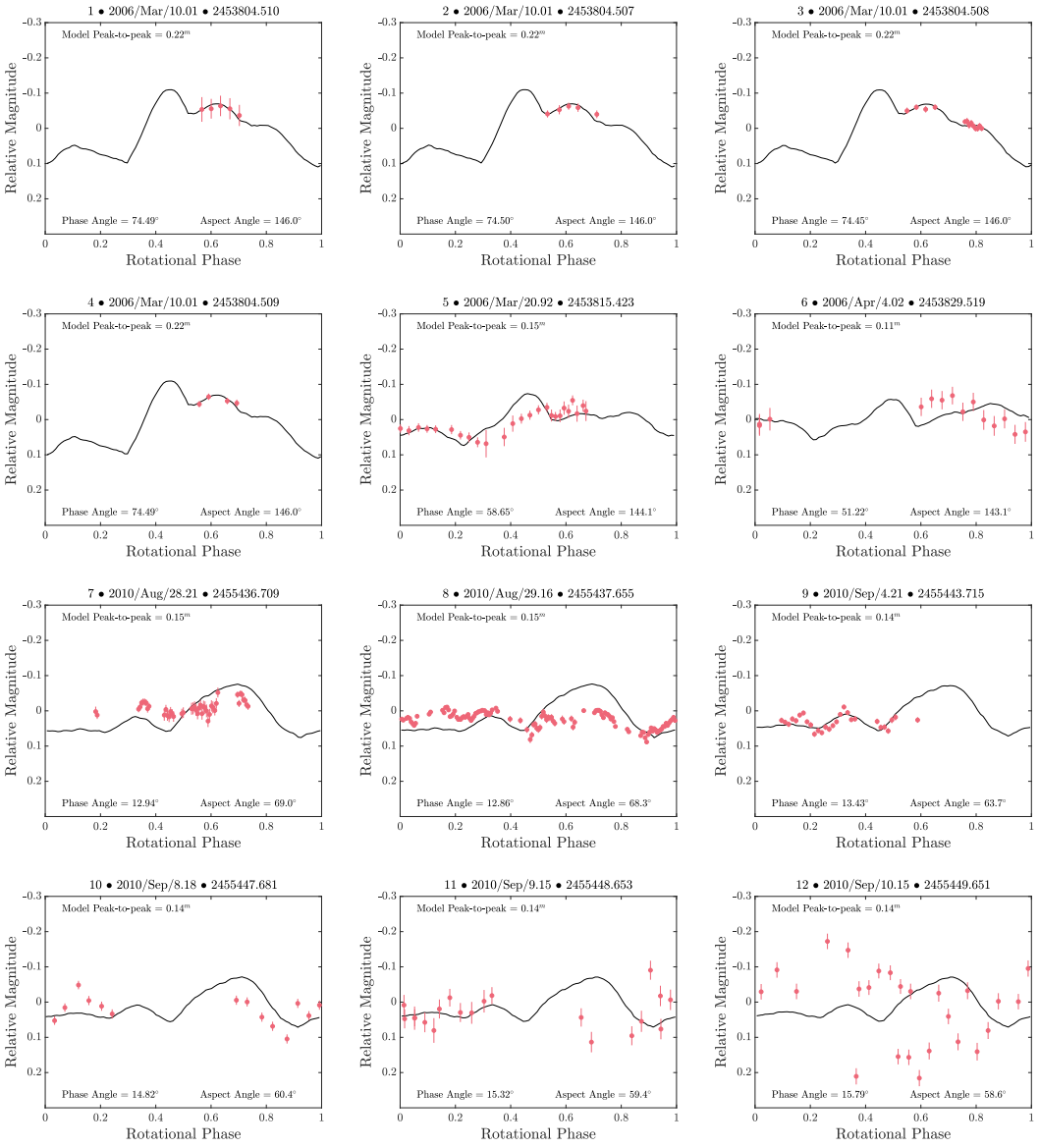

Figure A.2: A comparison of the observed and synthetic lightcurves of (23187) 2000 PN9 for each lightcurve listed in Table 4.1. The synthetic lightcurves were generated using the convex hull model presented in Section 4.3.1 using the methods described in Section 3.3.1 using the Lommel-Seelinger scattering model. Synthetic lightcurves are plotted as solid black lines, and observational data as red points. Lightcurve 12, which was not used in the analysis, has possible issues with the CCD that may be responsible for the poor fit.

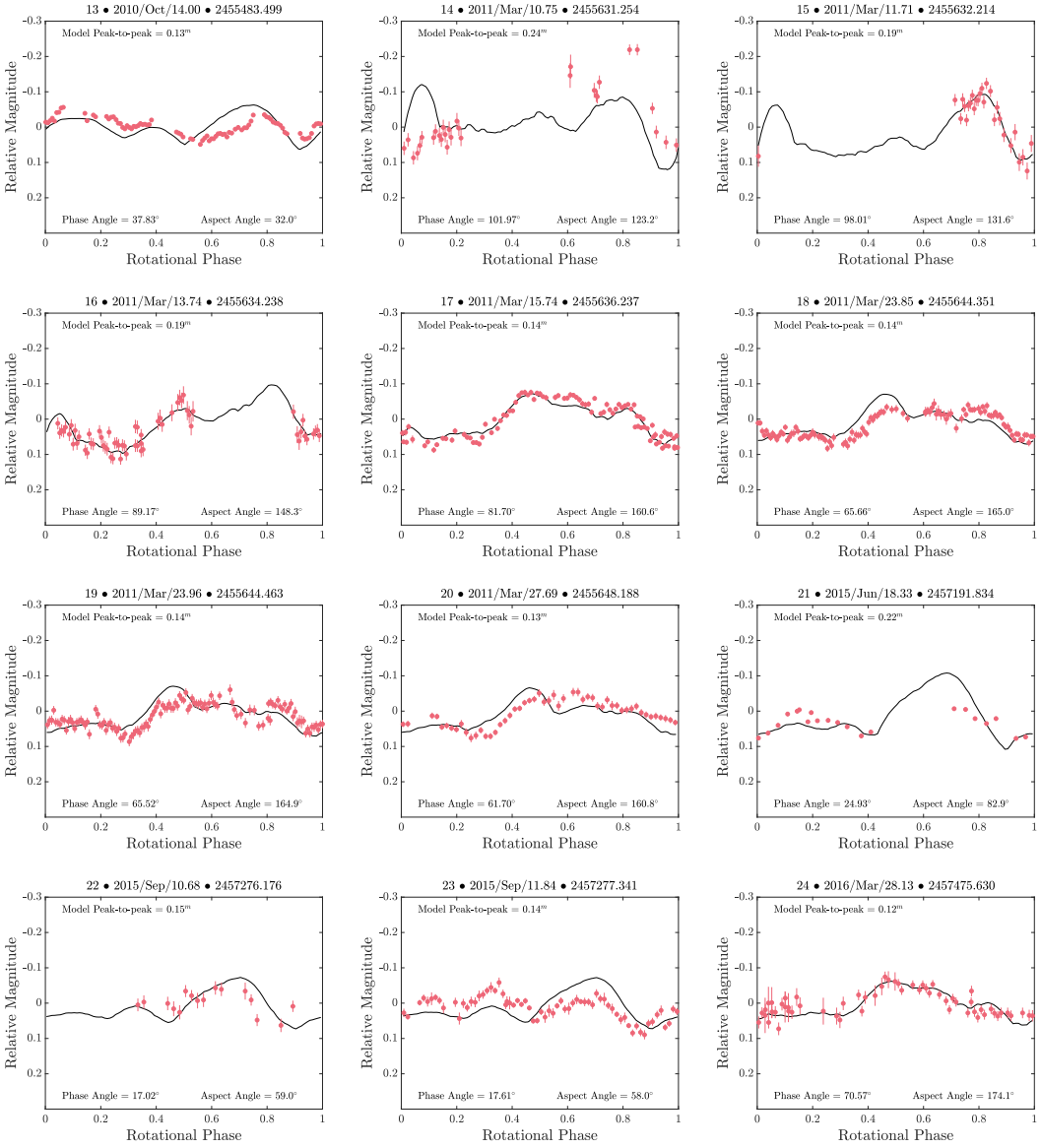

Figure A.2: (continued)

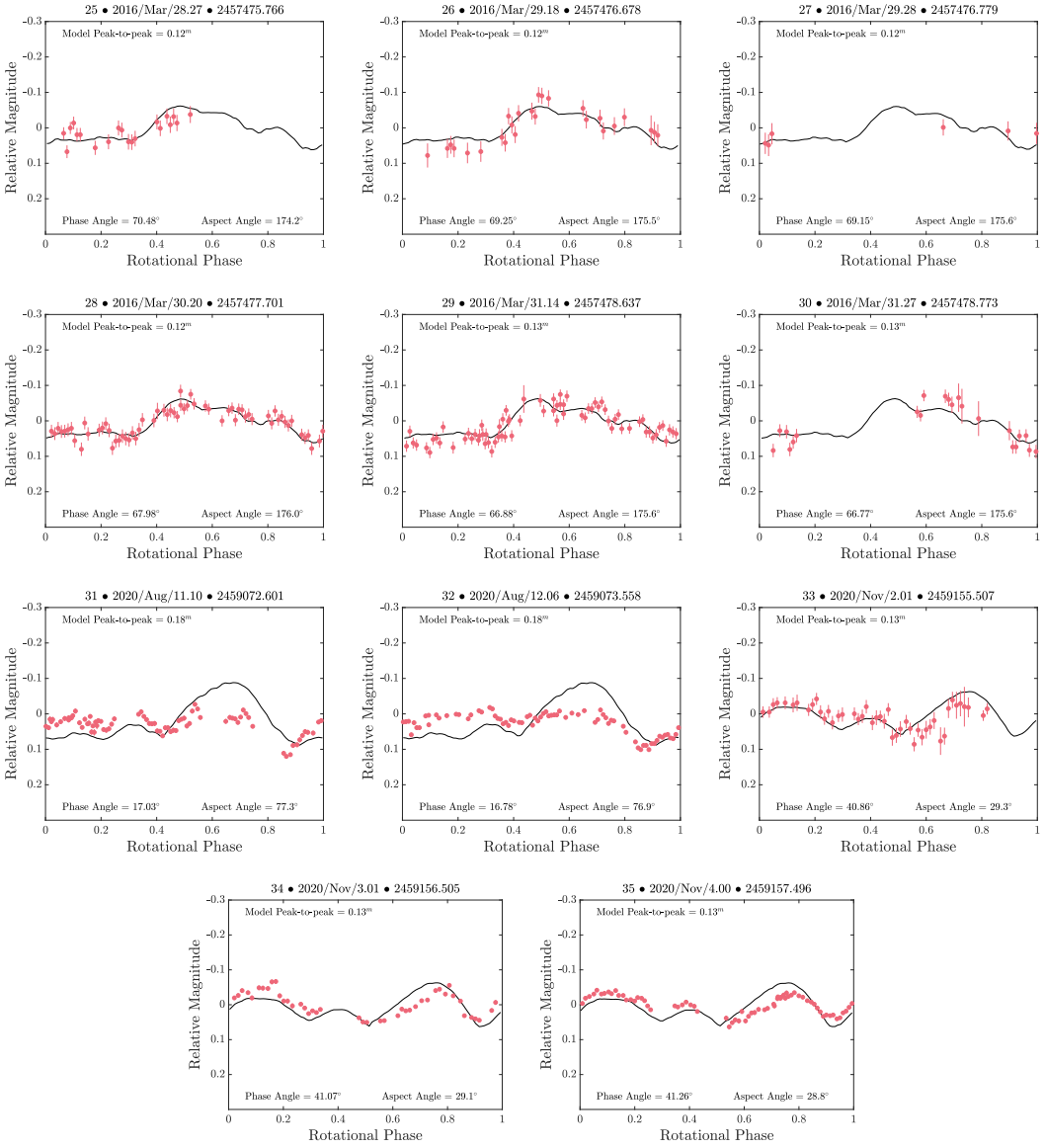

Figure A.2: (continued)

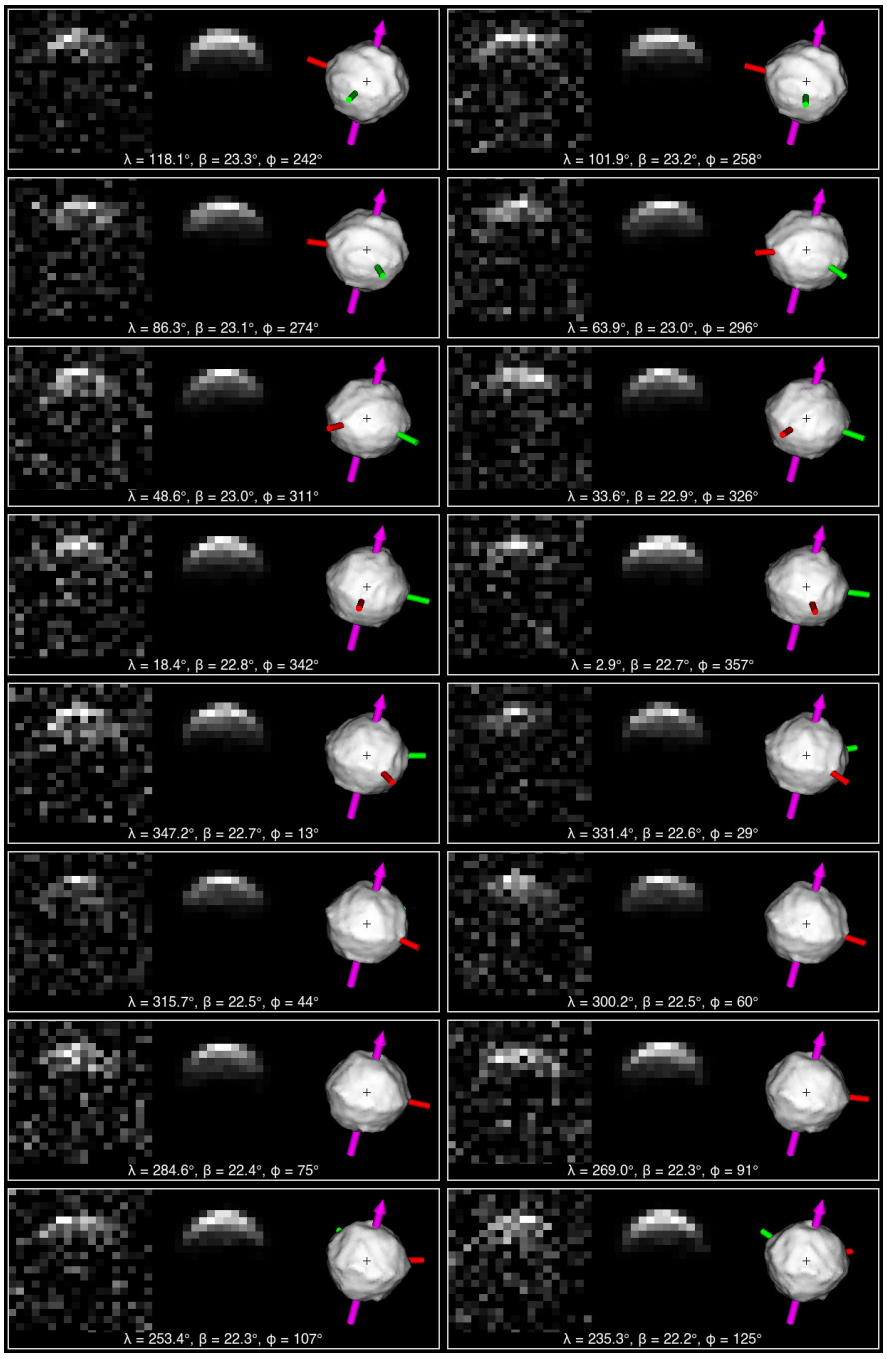

Figure A.3: A comparison of the combined radar and lightcurve model of asteroid (23187) 2000 PN9 to delay-Doppler radar data. Each three-panel image comprises the observational data (left panel), a synthetic echo (centre panel) and a plane-of-sky projection of the model (right panel). On the delay-Doppler images (left and centre panels), delay increases towards the bottom of the vertical axis and Doppler frequency increases along the horizontal axis. The plane-of-sky projections (right panel) are displayed with the celestial north at the top and east to the left, in an equatorial coordinate system. The rotational axis, which is closely aligned with the z-axis in the body-centric coordinate system, is marked with a purple arrow. The axes of minimum and intermediate inertia are indicated by red and green rods respectively. The body-fixed longitude λ and latitude β for the radar line-of-sight, and the rotational phase ϕ, are labelled for each image. These values were determined using the radar shape model's spin-state. The projected centre of mass is marked with a cross. The data in this figure correspond to radar observations with Goldstone on 2001-03-03, with a resolution of 1.0 μs $\times$ 6.15 Hz.

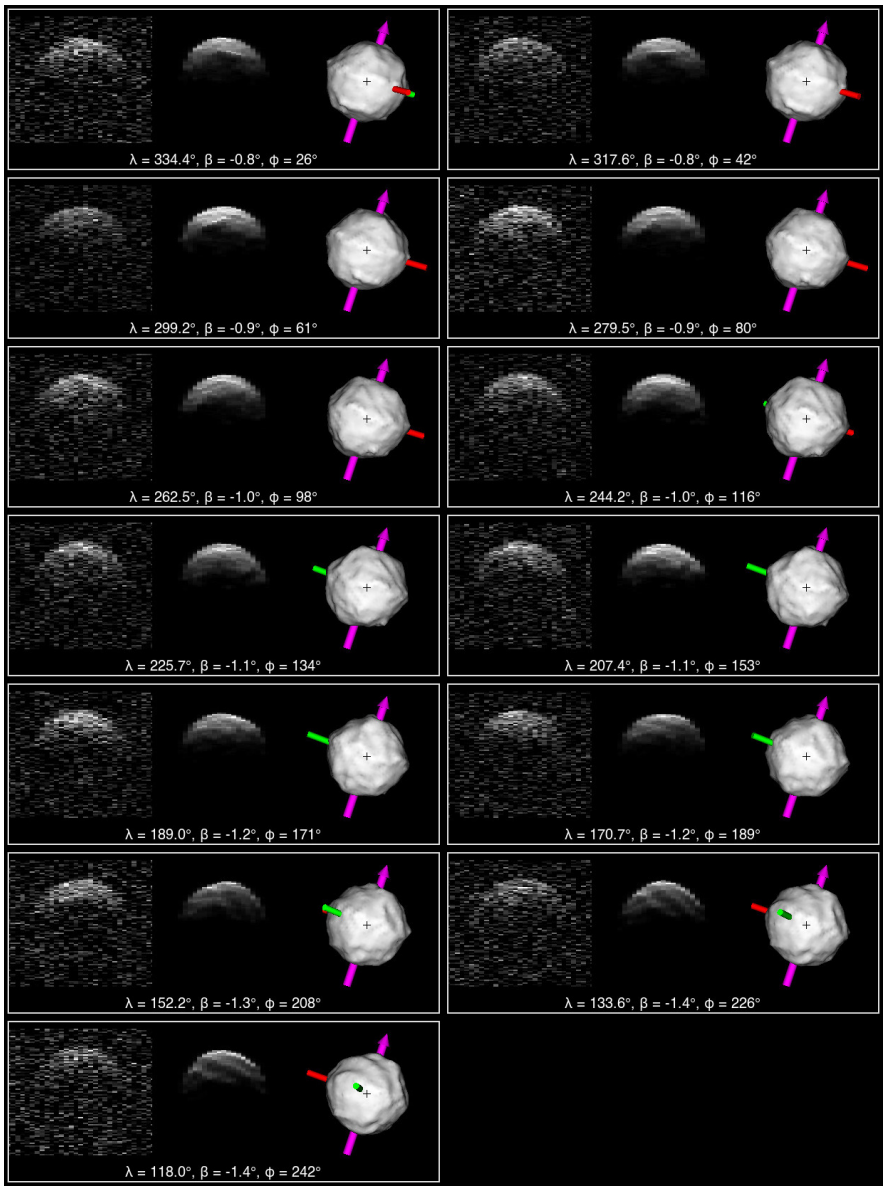

Figure A.4: This figure is the same as Figure A.3, but for observations with Arecibo on 2001-03-05 with a resolution of 0.2 μs $\times$ 1.00 Hz.

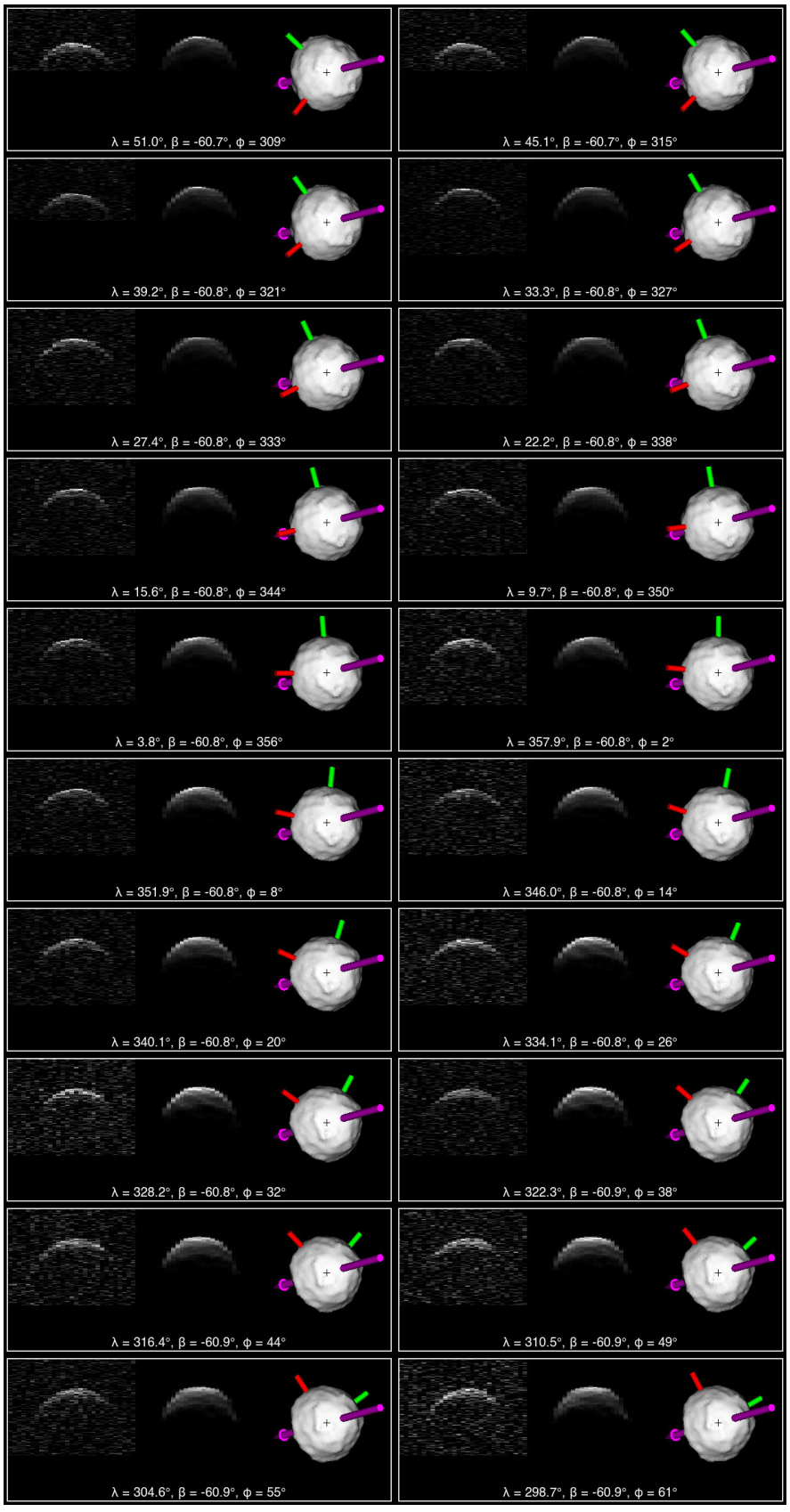

Figure A.5: This figure is the same as Figure A.3, but for observations with Goldstone on 2006-03-07 with a resolution of 0.125 μs $\times$ 2.00 Hz.

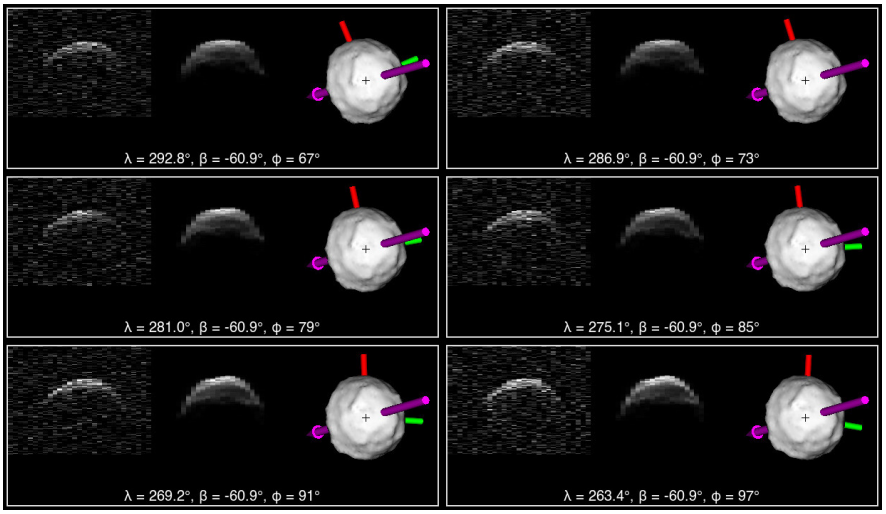

Figure A.5: (continued)

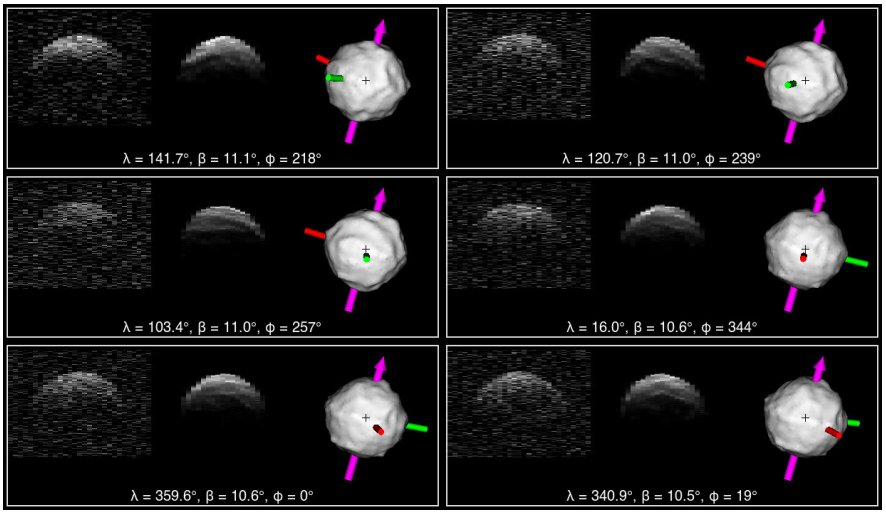

Figure A.6: This figure is the same as Figure A.3, but for observations with Arecibo on 2001-03-04. The first image has a resolution of 0.2 μs $\times$ 1.00 Hz, and the remaining five are at a resolution of 0.1 μs $\times$ 1.00 Hz.

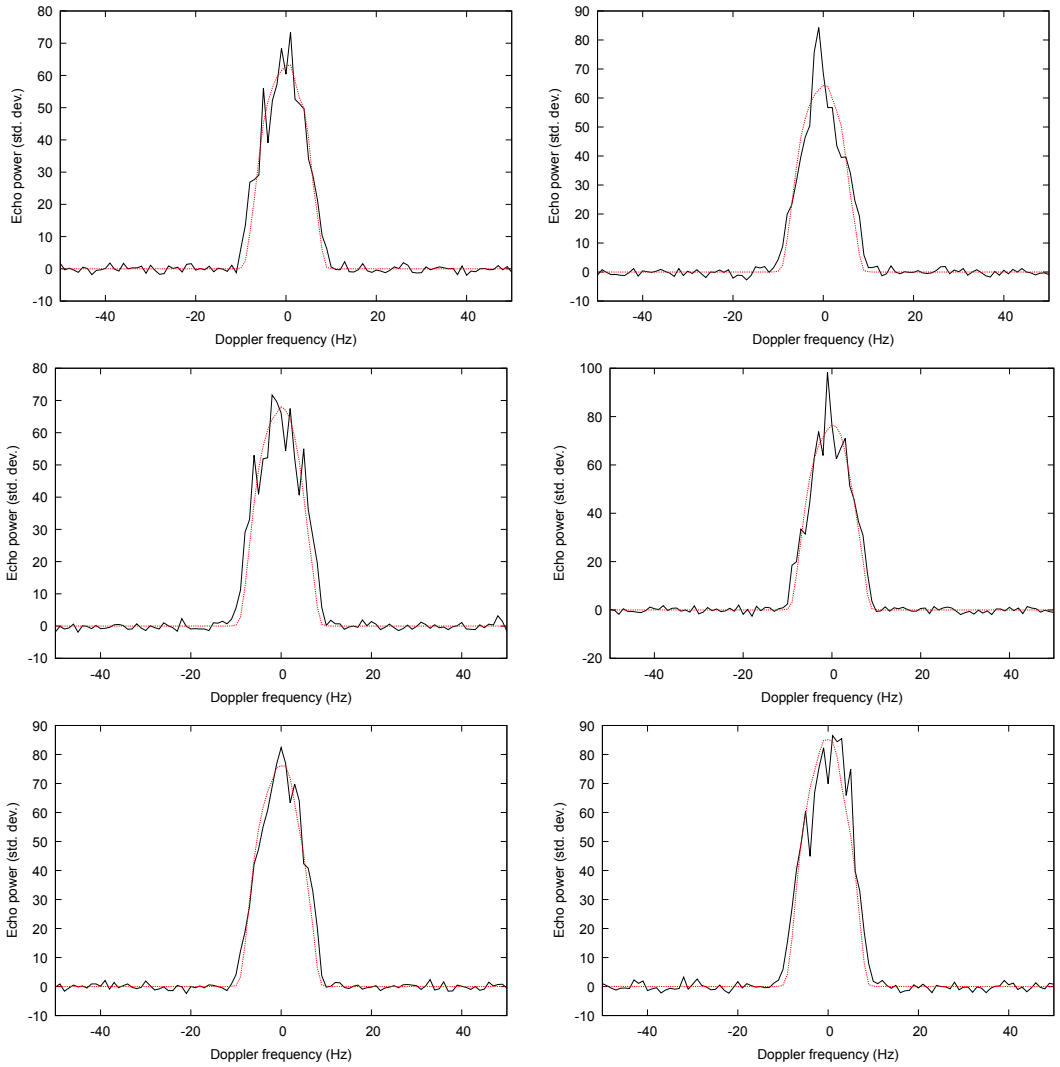

Figure A.7: A comparison of observed and simulated continuous-wave power spectra for observations with Arecibo on 2001-03-04. The best-fit radar model (Figure 4.11) was used to generate a synthetic echo for each corresponding observation. The solid black lines represent the observation (received OC spectra) while the dashed red lines represent the simulated echo. Echo power is measured in units of noise standard deviations and Doppler frequency offset, measured relative to the centre of mass, is measured in Hz. The frequency resolution is 1.0 Hz.

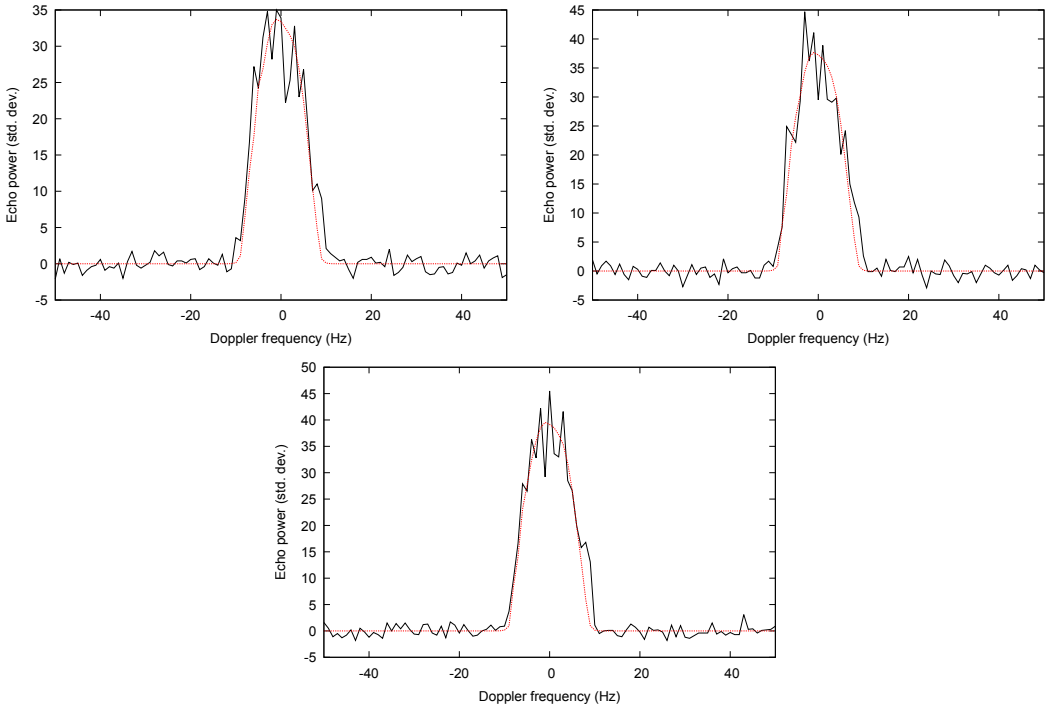

Figure A.8: The same as Figure A.7, but for observations with Arecibo on 2001-03-05. The frequency resolution is 1.0 Hz.

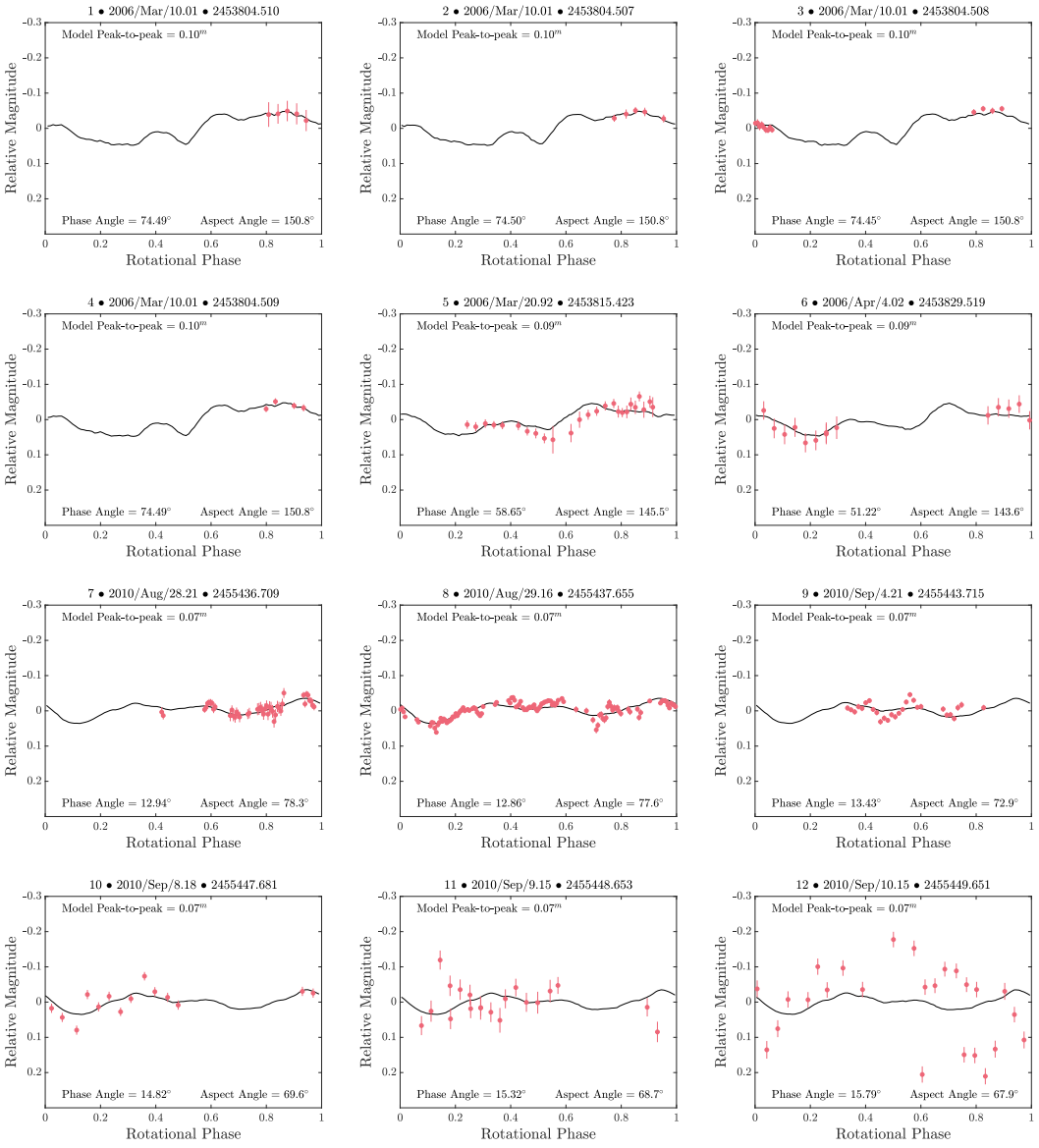

Figure A.9: A comparison of the observed and synthetic lightcurves of (23187) 2000 PN9 for each lightcurve listed in Table 4.1. The synthetic lightcurves were generated using the method described in Section 3.3.1, using the combined radar and lightcurve model presented in Section 4.3.2 with a combination of the Lambertian and Lommel-Seelinger scattering models. Synthetic lightcurves are plotted as solid black lines, and observational data as red points. Lightcurve 12, which was not used in the analysis, has possible issues with the CCD that may be responsible for the poor fit.

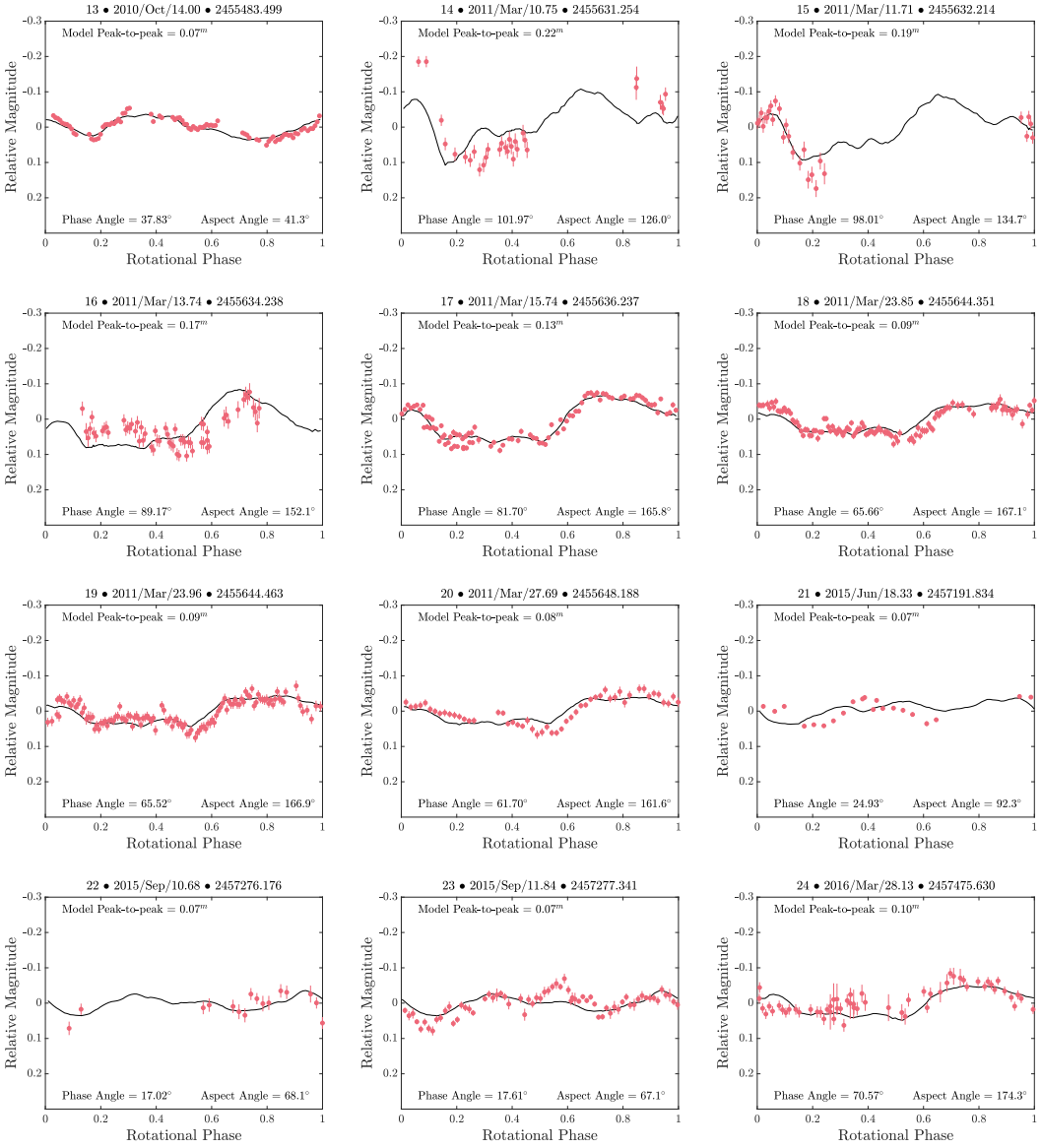

Figure A.9: (continued)

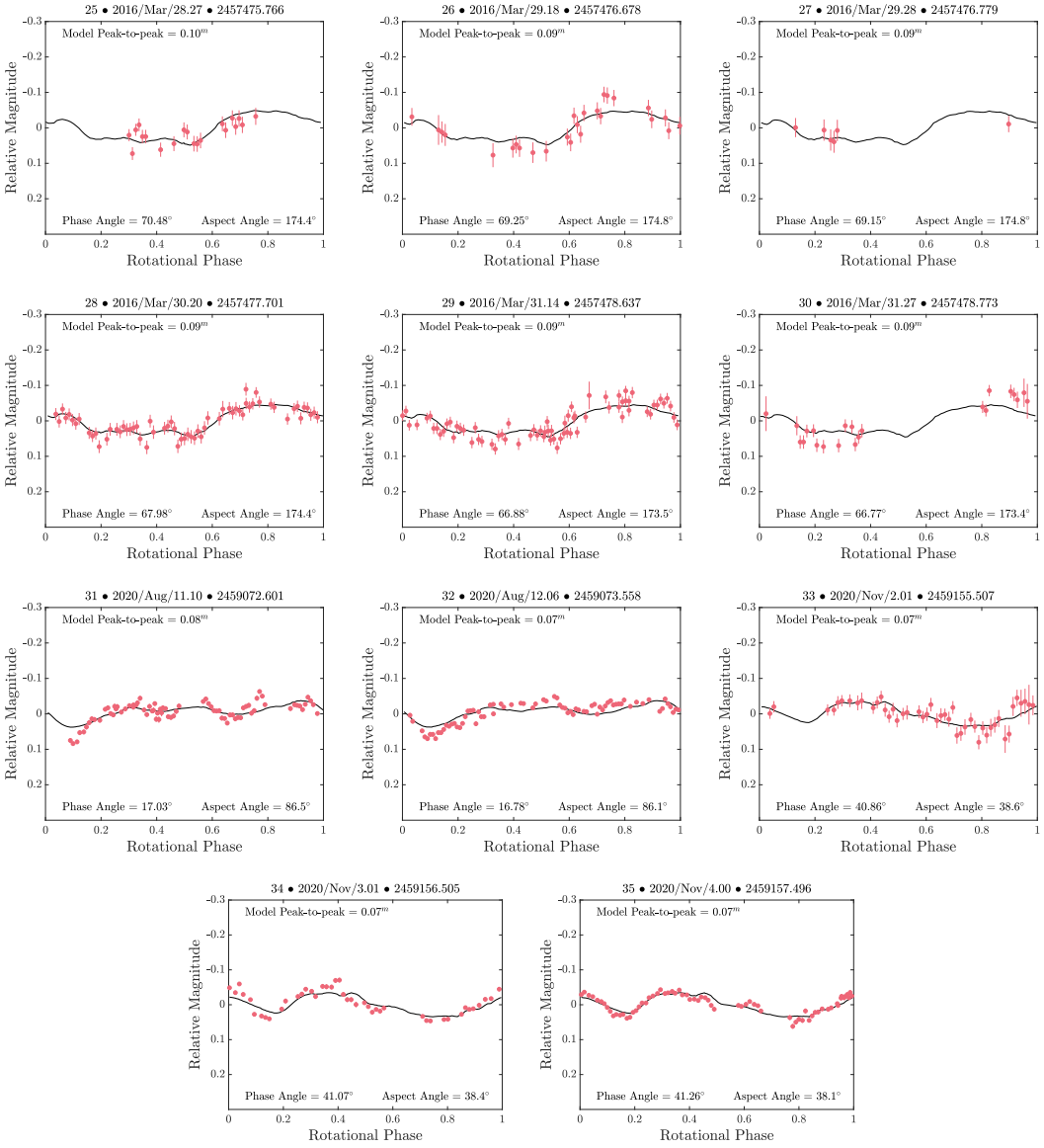

Figure A.9: (continued)

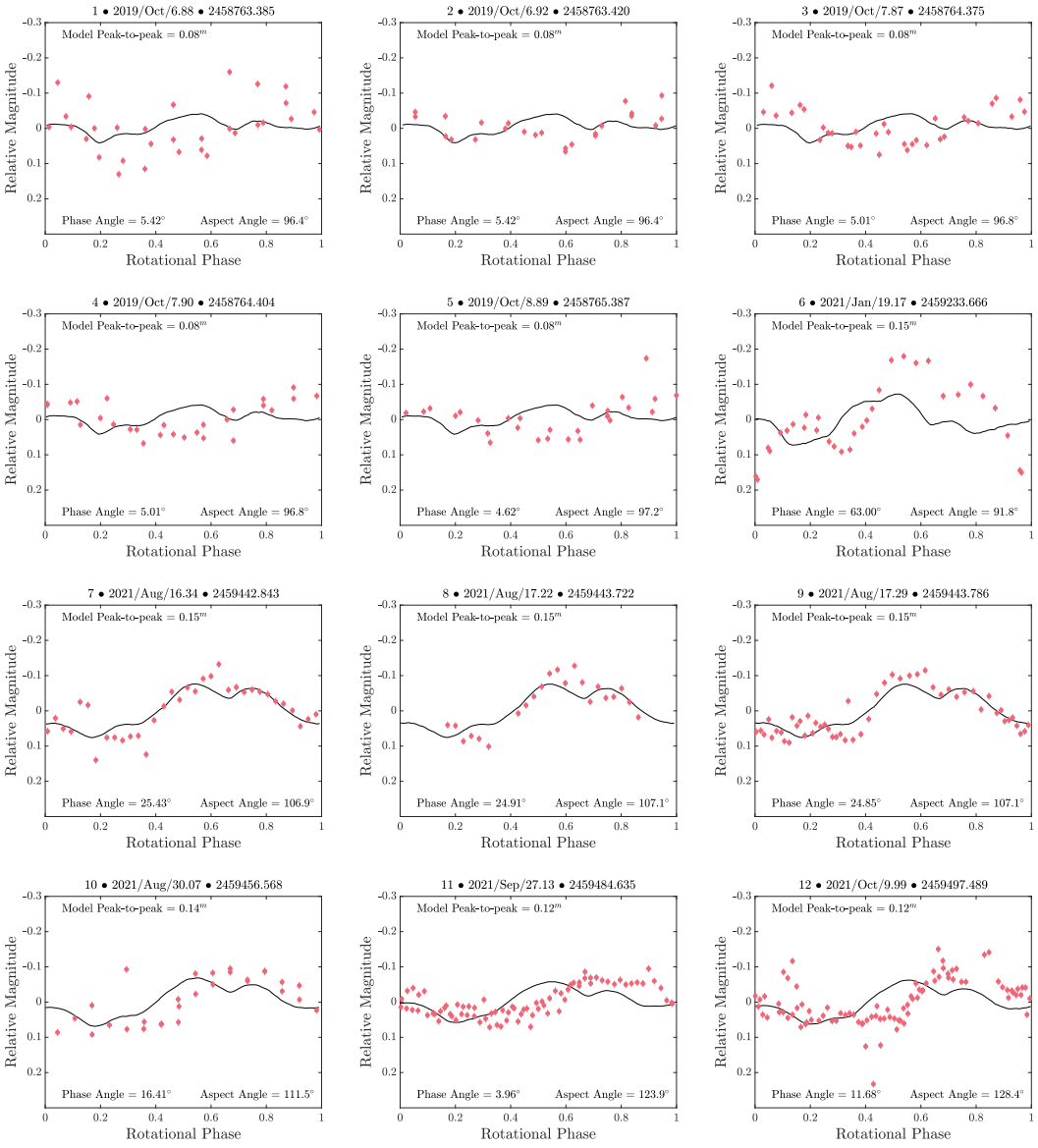

Figure A.10: A comparison of the observed and synthetic lightcurves of (29075) 1950 DA for the new follow-up campaign lightcurves listed in Table 5.1 (October 2019 onwards & marked 'LD'). The synthetic lightcurves were generated using the method described in Section 3.3.1, using the combined radar and lightcurve model produced by Zegmott (2021) with a combination of the Lambertian and Lommel-Seelinger scattering models. Synthetic lightcurves are plotted as solid black lines, and observational data as red points.

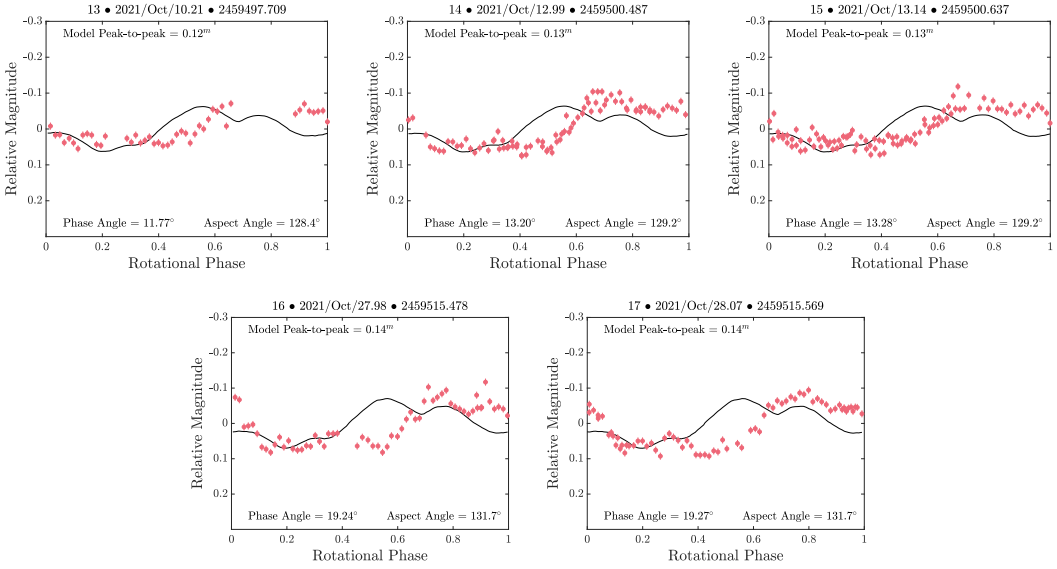

Figure A.10: (continued)

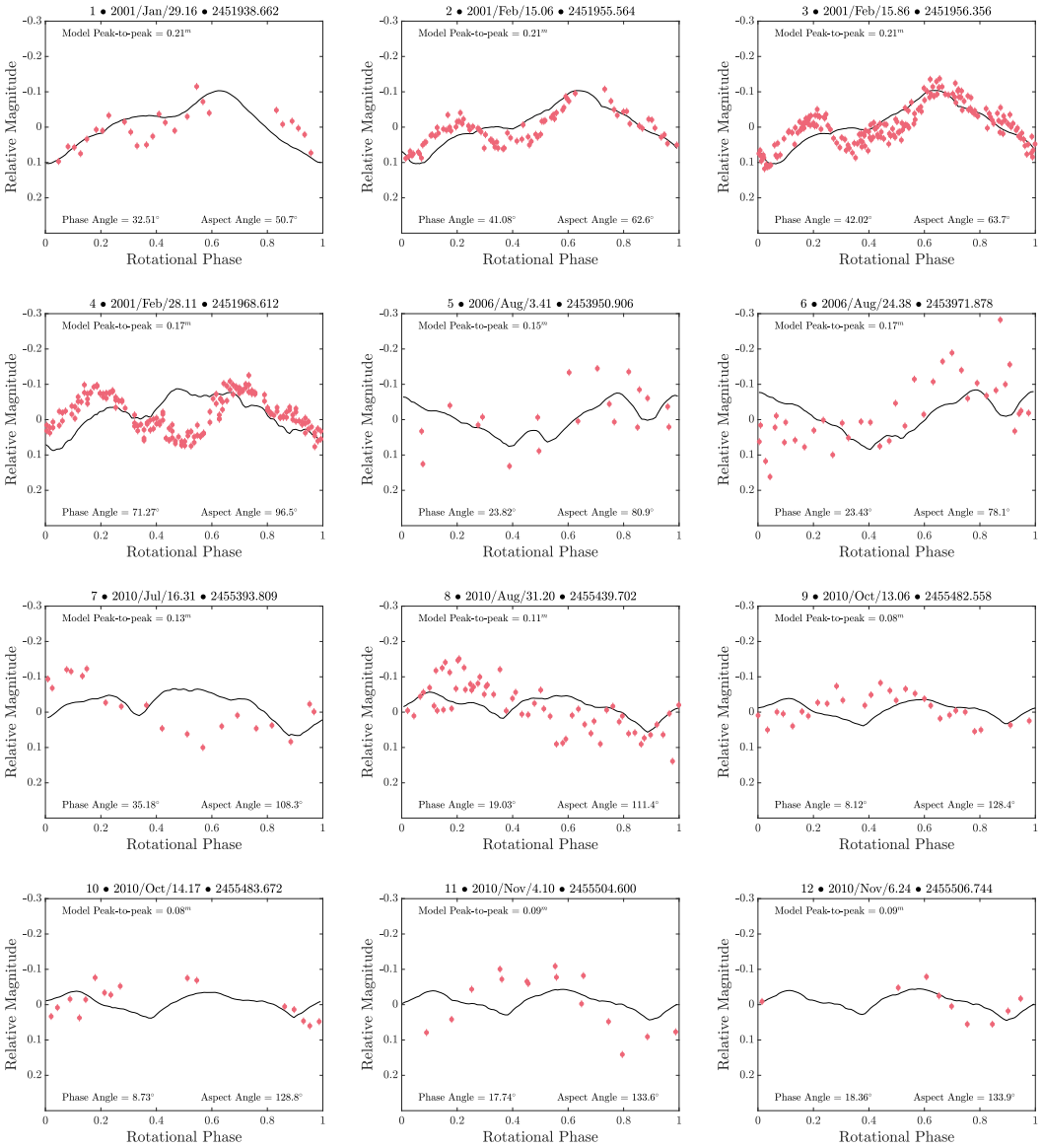

Figure A.11: A comparison of the observed and synthetic lightcurves of (29075) 1950 DA for every lightcurve that was used to develop the new convex hull model, marked as "LD" in Table 5.1. The synthetic lightcurves were generated using the convex hull model presented in Section 5.2.2 using the methods described in Section 3.3.1 using a combination of the Lambertian and Lommel-Seelinger scattering models. Synthetic lightcurves are plotted as solid black lines, and observational data as red points.

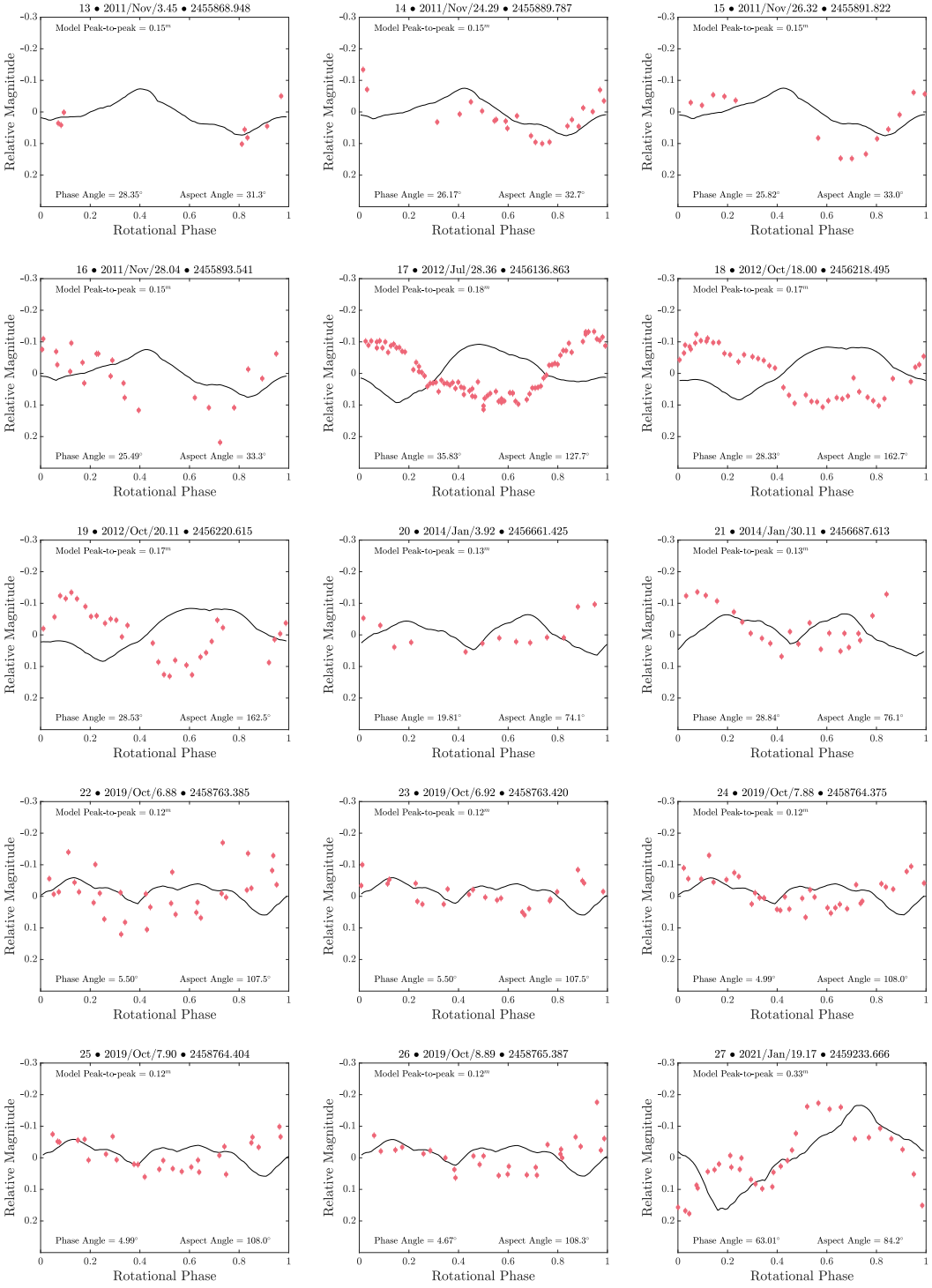

Figure A.11: (continued)

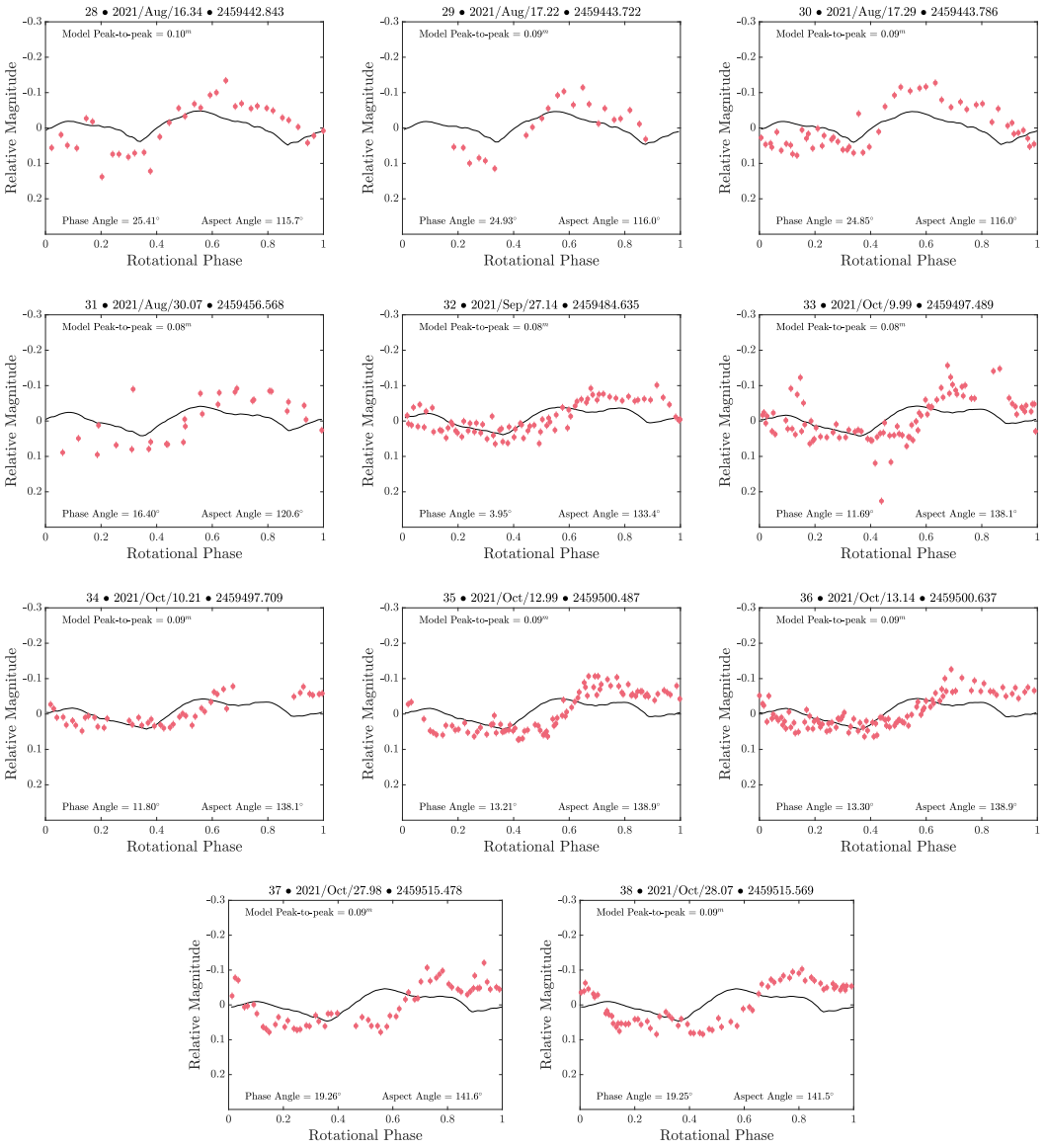

Figure A.11: (continued)

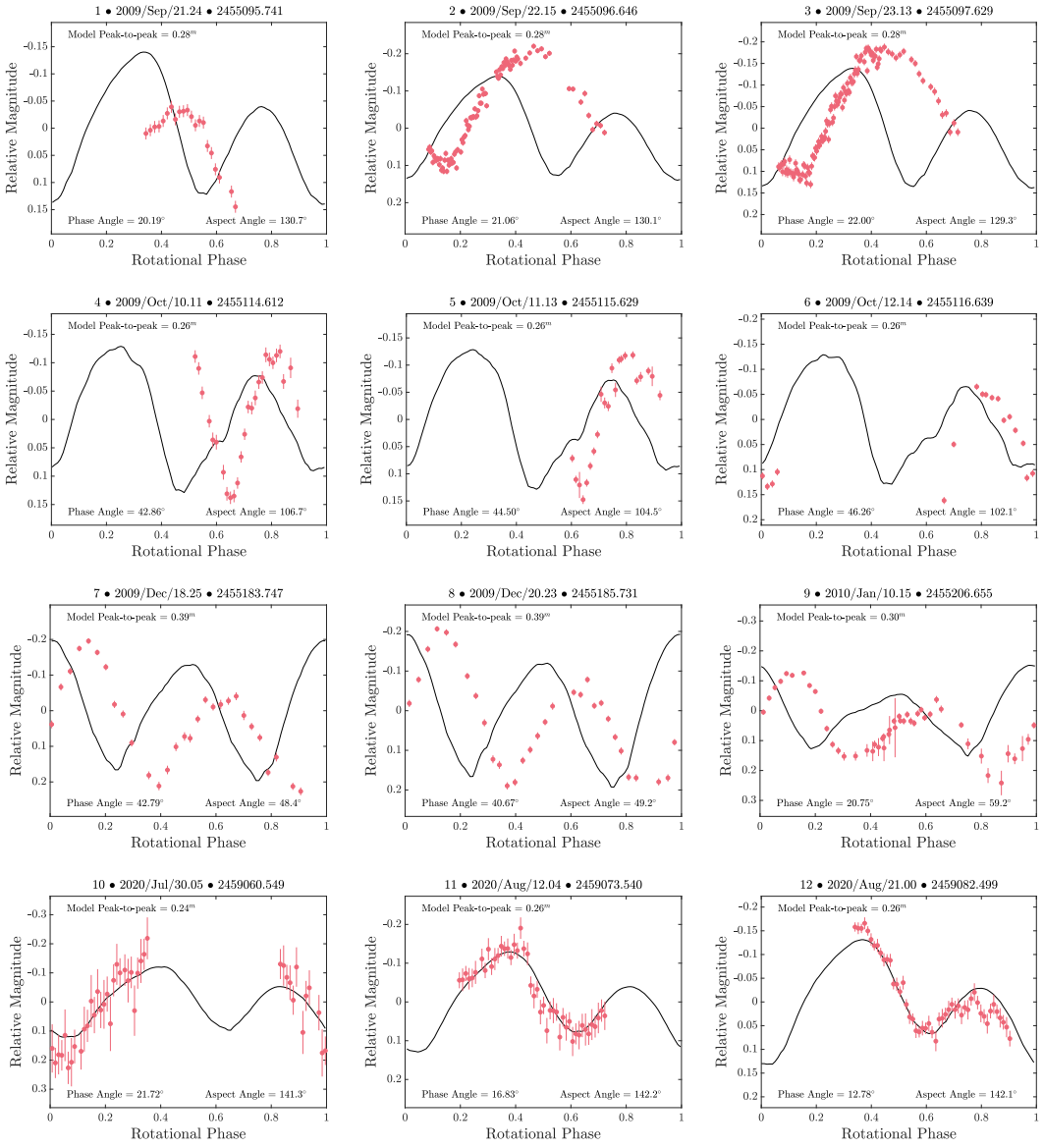

Figure A.12: A comparison of the observed and synthetic lightcurves of (159402) 1999 AP10 for every lightcurve in Table 6.1. The synthetic lightcurves were generated using the convex hull model presented in Section 6.2.2 using the methods described in Section 3.3.1 using a combination of the Lambertian and Lommel-Seelinger scattering models. Synthetic lightcurves are plotted as solid black lines, and observational data as red points. Note that the model's T_0 is in 2020, so the phase offset is close to zero from lightcurve 10 onwards, and negative for earlier lightcurves. This is adjusted to a relative phase offset from the first lightcurves for the phase offset analysis in Section 6.2.2.1.

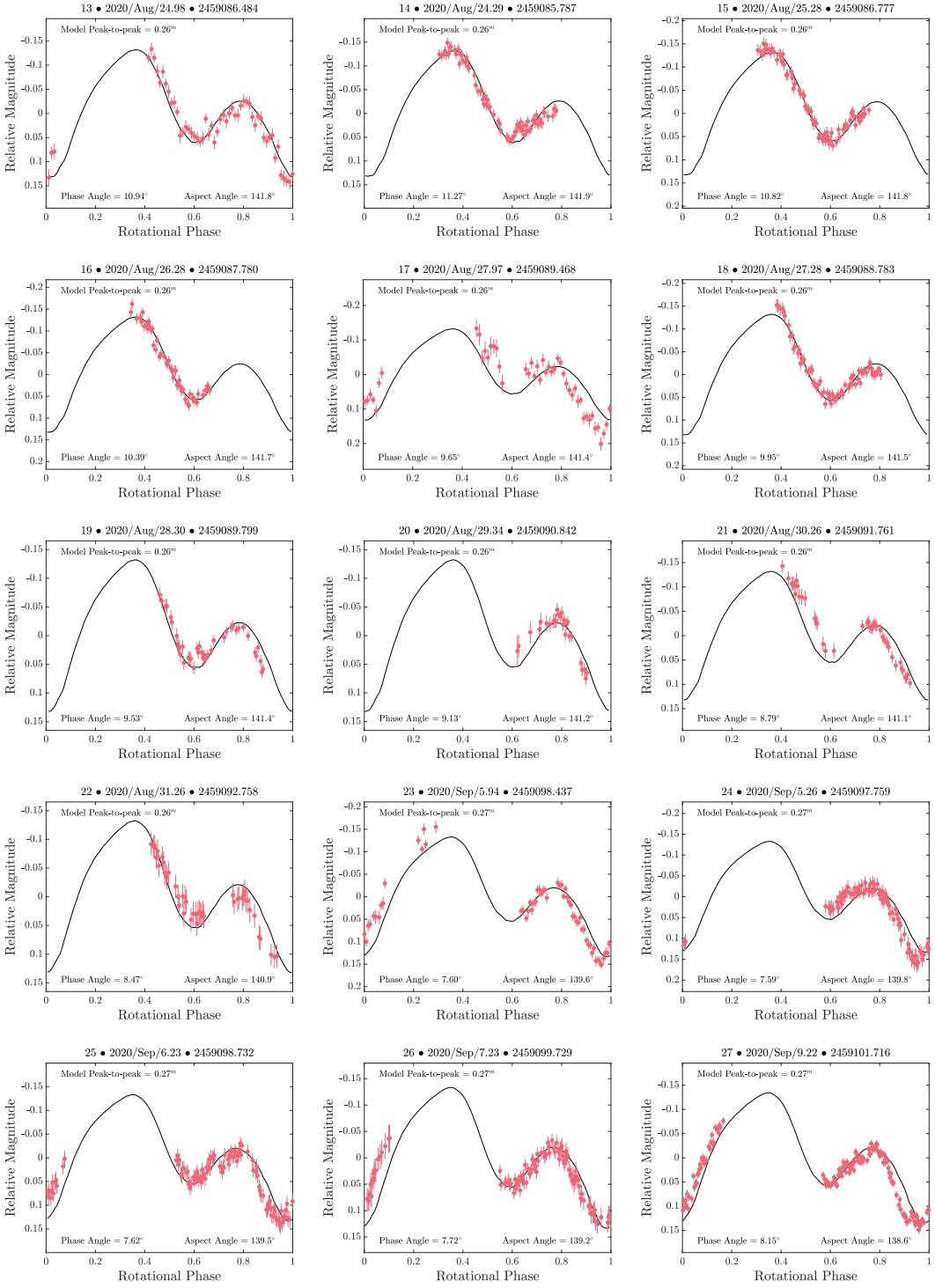

Figure A.12: (continued)

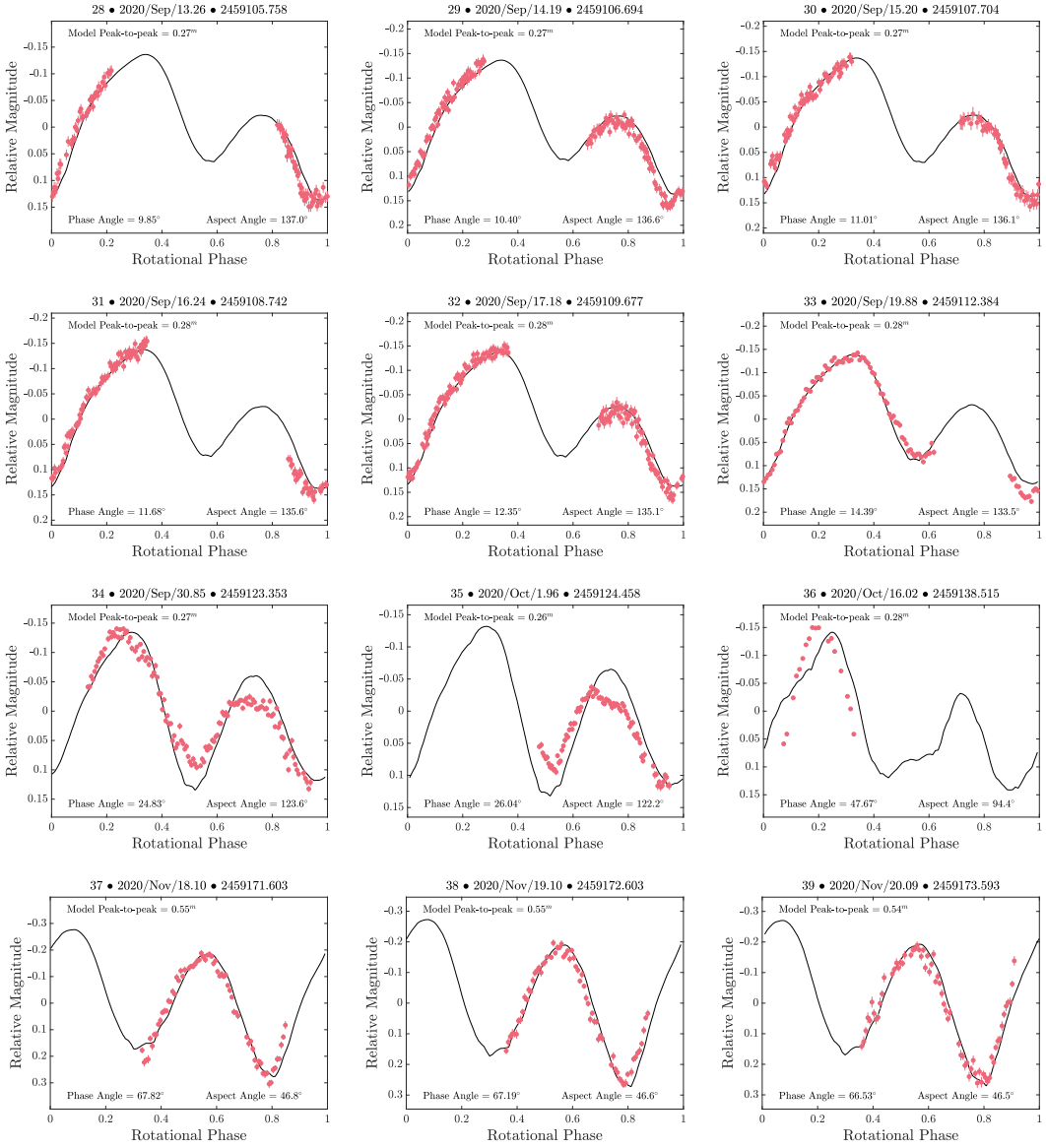

Figure A.12: (continued)

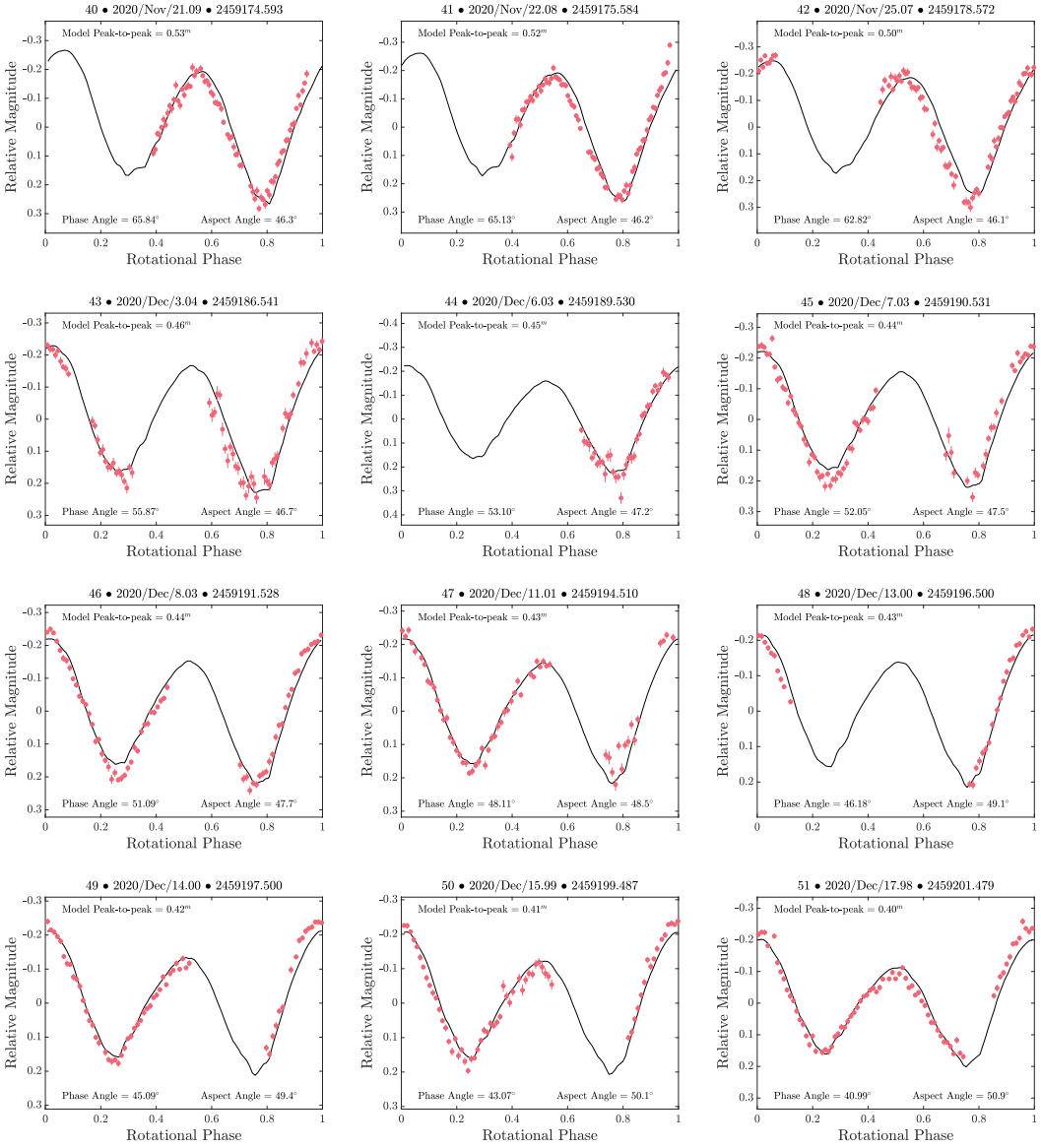

Figure A.12: (continued)

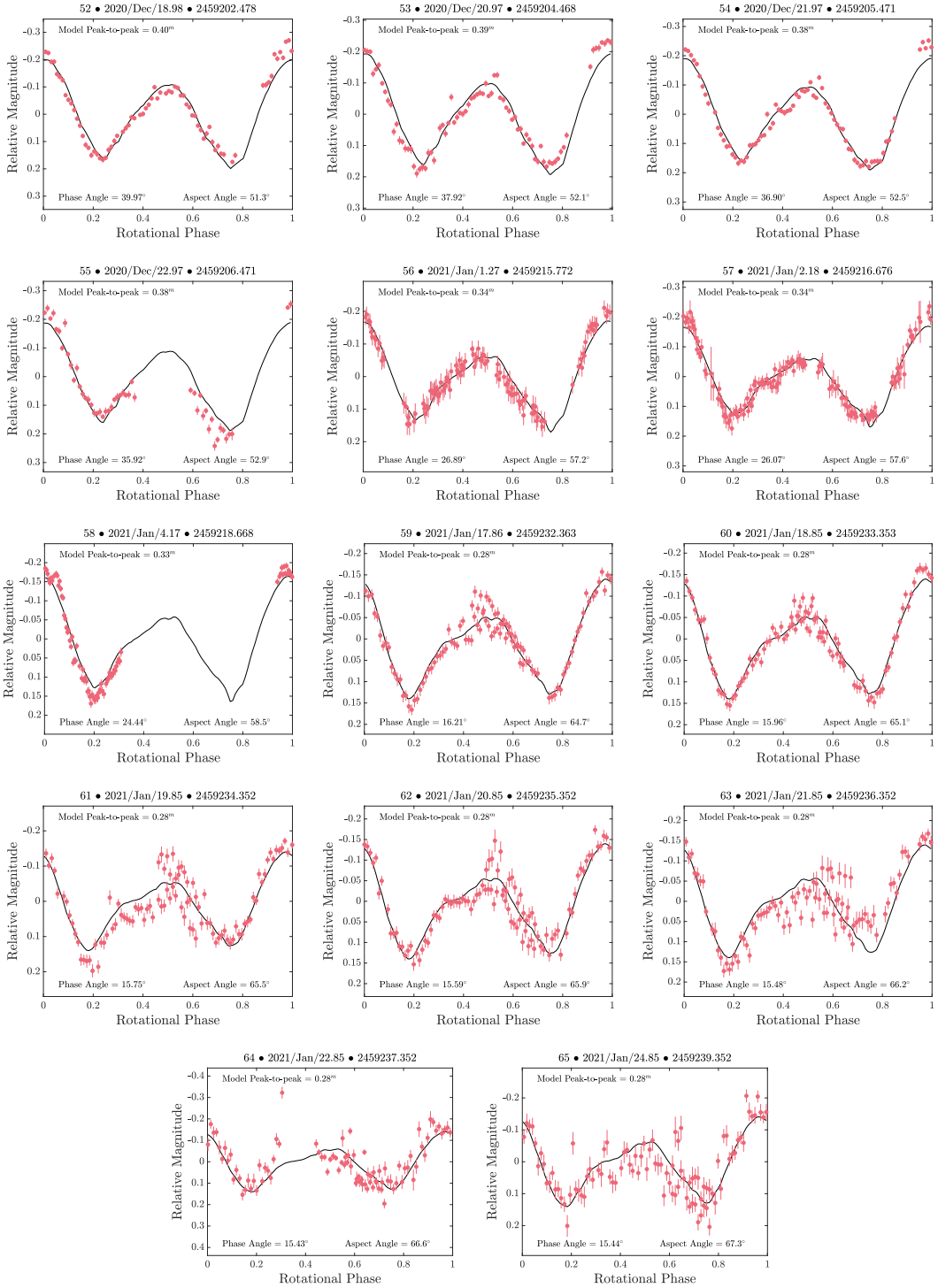

Figure A.12: (continued)

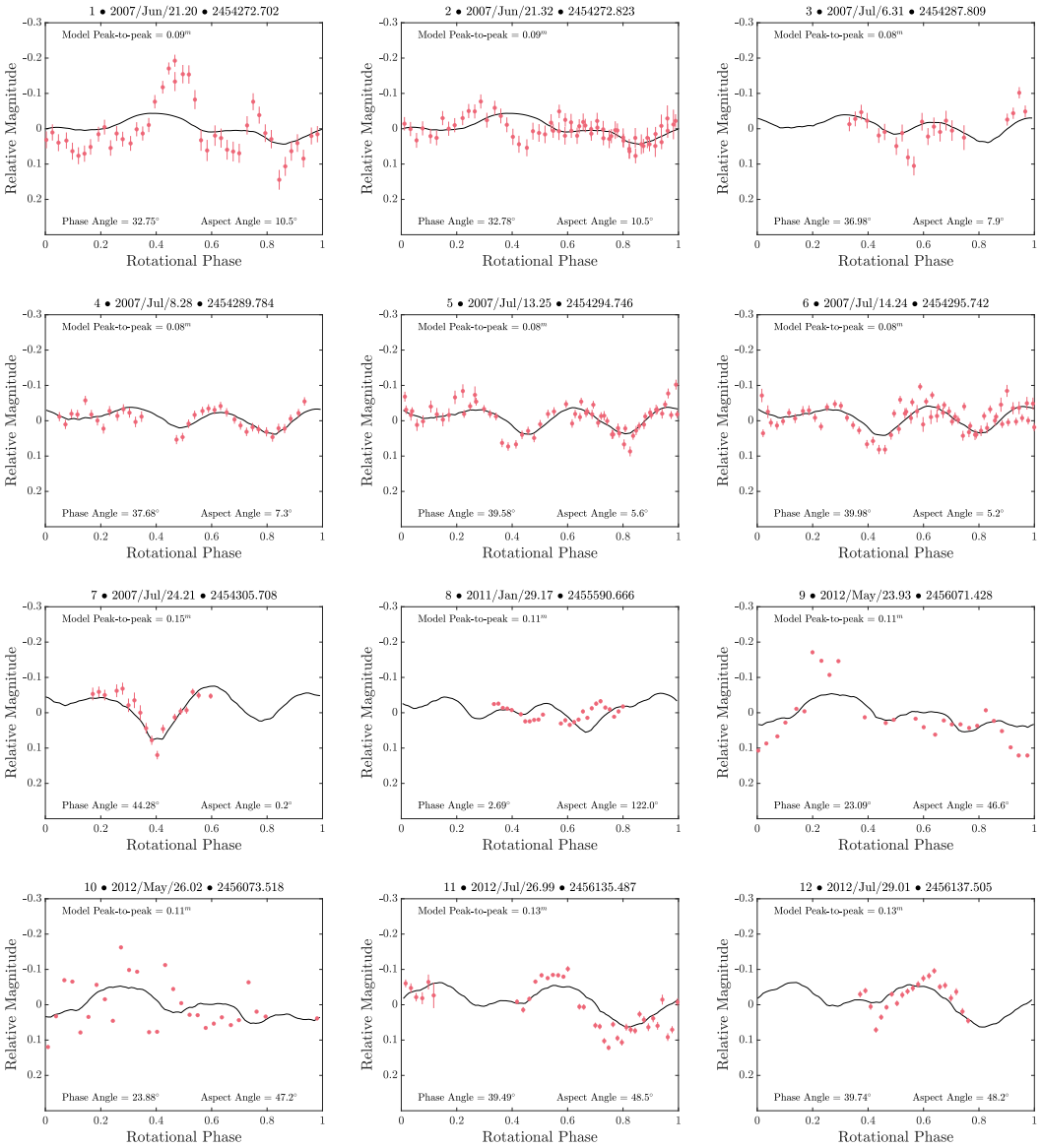

Figure A.13: A comparison of the observed and synthetic lightcurves of (85275) 1994 LY for every lightcurve that was used to develop the new convex hull model, marked as in Table 6.2. The synthetic lightcurves were generated using the convex hull model presented in Section 6.3 using the methods described in Section 3.3.1 using a combination of the Lambertian and Lommel-Seelinger scattering models. Synthetic lightcurves are plotted as solid black lines, and observational data as red points.

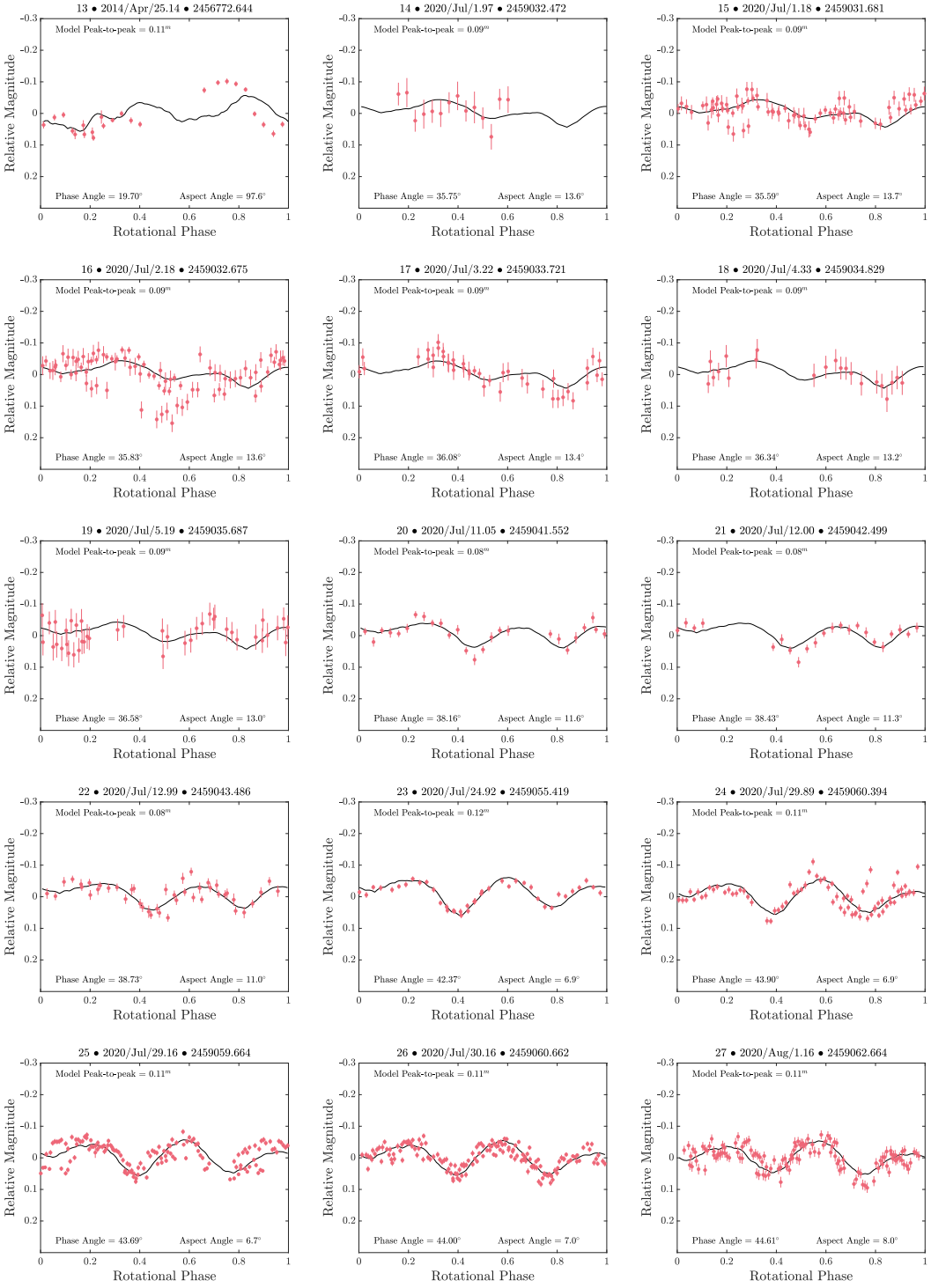

Figure A.13: (continued)

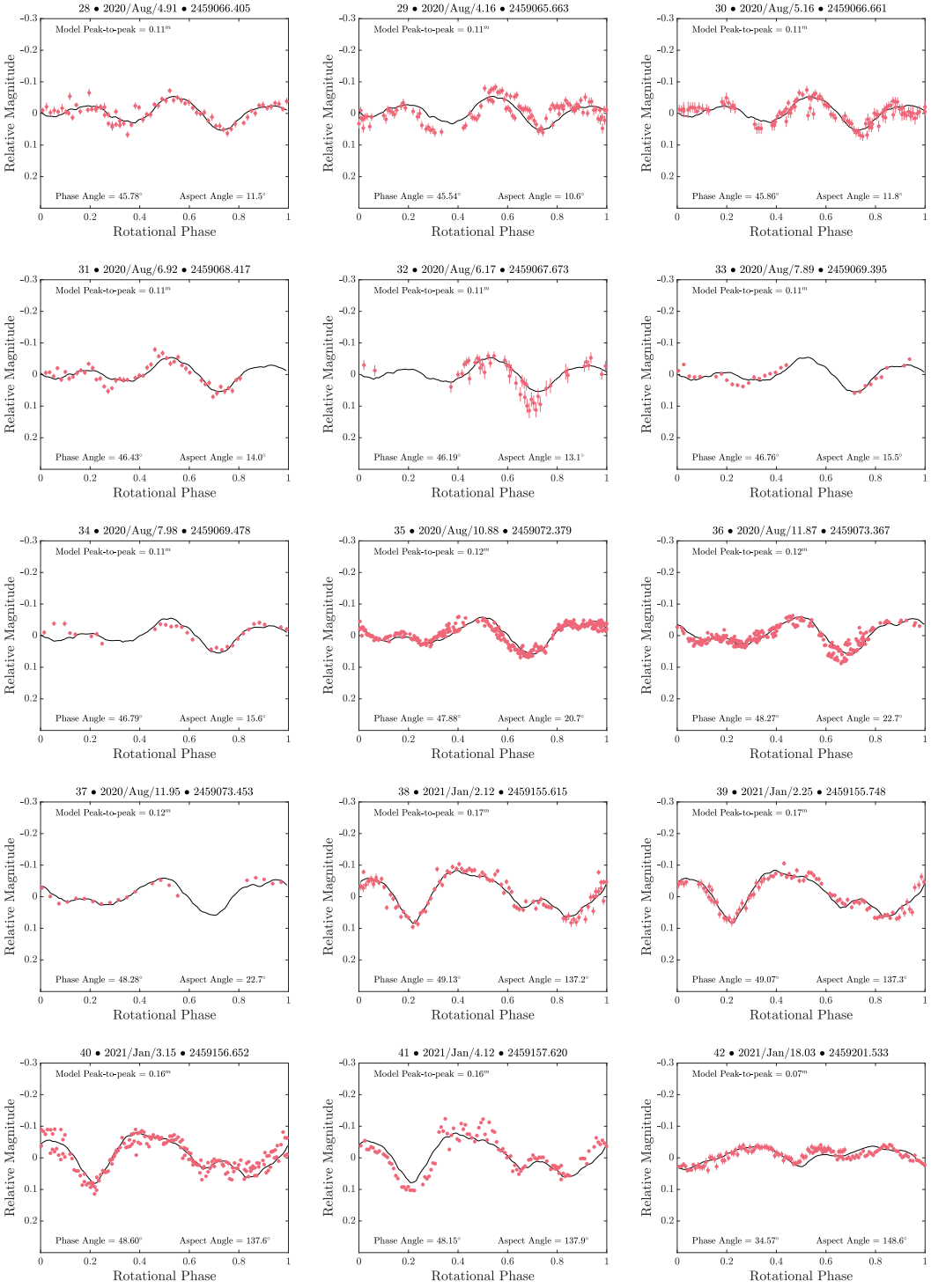

Figure A.13: (continued)

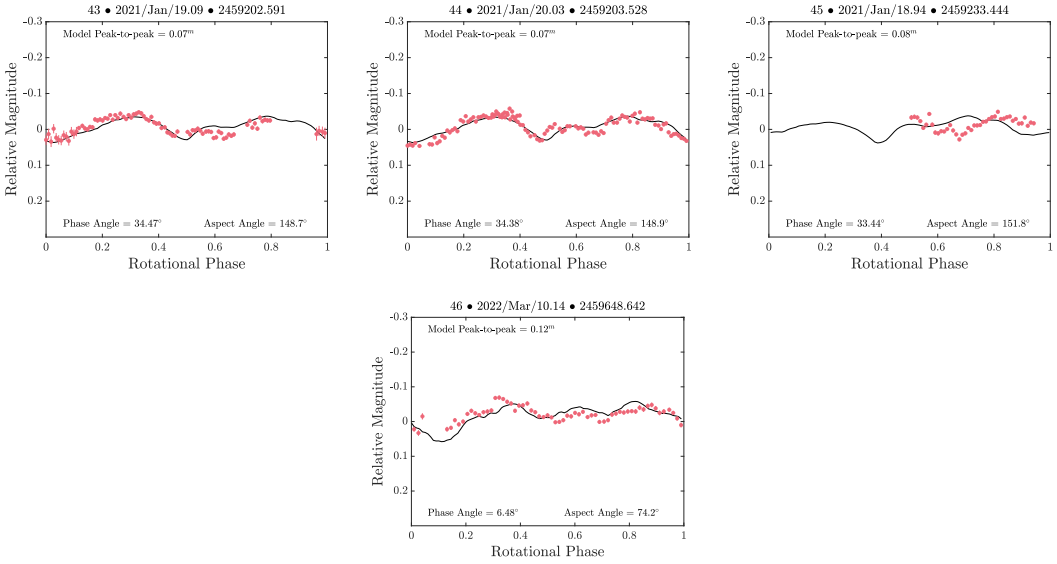

Figure A.13: (continued)

APPENDIX B

FILE FORMATS FOR MODELLING PROCEDURES

Lightcurve data for `convexinv` and `MATLAB`

By convention, lightcurves are typically stored as a three column array with an optional header to provide additional information. The three columns correspond to time, magnitude, and magnitude uncertainty, with a row for each photometric measurement. Time is typically given as the mid-exposure Julian date, although archival data sometimes uses Modified Julian Date or other more human-readable formats. For convenience, all timing data were converted to mid-exposure Julian date during this project. Magnitudes may be relative or calibrated, however the distinction is not necessary for the procedures used in this thesis. Files were stored in both space-delimited `.dat` format and comma-separated `.csv` files for interpretation by different procedures.

Files are named in an underscore-delimited format that includes the asteroid name, observatory IAU code and user comments that may describe the filter or a human-readable date. An example would be `23187_809_20201103V.dat`, which describes observations of the asteroid (23187) 2000 PN9 from La Silla Observatory (809) on 2020-01-03 using the V filter. An example of the contents of a 'standard' lightcurve file is shown in Figure B.1.

```
2458216.69378 21.484 0.107
2458216.69431 21.243 0.142
2458216.69483 21.319 0.108
2458216.69536 21.336 0.104
2458216.69589 21.195 0.093
2458216.69641 21.190 0.086
2458216.69694 21.197 0.120
2458216.69747 21.002 0.143
2458216.69800 21.099 0.248
2458216.69852 21.182 0.134
```

Figure B.1: An excerpt from a 'standard' lightcurve file, with a column for mid-JD, magnitude and magnitude uncertainty. Note that the Julian date is given to five decimal places, which corresponds to a precision of one second. Less precise timing data are not adequate for YORP fitting. Magnitudes and their uncertainties are given to three decimal places, which is sufficient for fitting procedures.

The `convexinv` and `MATLAB` procedures described in Sections 3.1 and 3.3 require

additional information. Instead of individual files, the full set of lightcurves is described in a single file that also contains information on viewing geometry. An example of one of these `convexinv`-format input files is shown in Figure B.2.

The first line contains a single column, with an integer describing the number of lightcurves described in the file. The lightcurve data follow this, with each lightcurve beginning with a line containing two columns. The first column lists how many measurements (rows) the lightcurve contains, and the second is a flag that indicates if the photometry is relative or calibrated. The data are then listed in eight columns. First is a mid-exposure Julian date which has been corrected to account for the asteroid-to-observer light travel time. This is followed by brightness, which is given in intensity units. The next three columns describe the vector from the asteroid to the Sun in ecliptic Cartesian coordinates, followed by another three columns describing the vector from the asteroid to the Earth in the same coordinate system. After the last row, the next lightcurve begins immediately with its two-column 'header' row.

The `convexinv`-formatted input files are generated automatically by a series of shell scripts that read in sets of standard lightcurve files, taking the asteroid name and IAU codes from filenames to query the JPL Horizons database and obtain the viewing geometry data for each row's corresponding Julian date. The magnitude-to-intensity conversion is also applied here. A secondary version of the output lightcurve dataset file is saved that includes a ninth row describing magnitude uncertainty, which can be read in by `MATLAB` for plotting purposes.

Files used with `SHAPE`

As described in Section 3.2, `SHAPE` requires an input model file, a parameter file and an observation file. Examples of these files, which have already been explained in the main body of this thesis, are given below.

```
1  65 %Number of lightcurves
2  3 0 %Lightcurve 1 (Number of rows followed by 0 for relative, or 1 for
       calibrated)
3  2455095.741151196 0.649232 -1.153395e+00 1.005508e-01 6.752020e-03
       -1.498206e-01 6.996782e-02 6.780504e-03
4  2455095.746394348 0.65283 -1.153372e+00 1.004511e-01 6.738790e-03
       -1.497964e-01 6.995891e-02 6.766851e-03
5  2455095.751637499 0.656448 -1.153350e+00 1.003513e-01 6.725560e-03
       -1.497722e-01 6.995001e-02 6.753192e-03
6  91 0 %Lightcurve 2 (Number of rows followed by 0 for relative, or 1 for
       calibrated)
7  2455096.645887076 0.5425 -1.149422e+00 8.333310e-02 4.468653e-03
       -1.457638e-01 6.824434e-02 4.502760e-03
8  2455096.647172113 0.545507 -1.149417e+00 8.330864e-02 4.465409e-03
       -1.457578e-01 6.824204e-02 4.499456e-03
9  2455096.648457151 0.539014 -1.149411e+00 8.328417e-02 4.462165e-03
       -1.457518e-01 6.823975e-02 4.496150e-03
10 ... %File continues
```

Figure B.2: The beginning of a lightcurve input file in the `convexinv` format, which is also used for `MATLAB` procedures. Line numbers are shown as a visual aid; line 1 declares that there are 65 lightcurves, and lines 2 and 6 declare the start of relative lightcurves that are 3 and 91 rows in length respectively. Note that the comments have only been added for this example, and should not be present in real input files as they will not be parsed correctly. This example shows the start of an input data file for (159402) 1999 AP10, with the first lightcurve truncated so that the start of the second lightcurve can be shown.

```
1  PARAMETERS {Declare that this is a parameter file}
2
3  action          write {Use the write action}
4  pos_pixels  201
5  pos_width       3.0
6  maskdir /data/lrd27/23187/masks/
7  nsinc2    1
8  sinc2width  6
9  dd_scaling  block
10 dd_maxsides bottom-right
11 scalefitobs separate
12 pos_scope local
13 plot_spinvec  yes
14 plot_subradar no
15 plot_com  no
16 plot_pa   yes yes yes
17 mark_unseen yes
18 list_unseen yes
19 listfit no
20
21 PENALTIES      0 {No penalties required for write action}
```

Figure B.3: This SHAPE parameter file declares the 'write' action (line 3), which writes the result of a fit. The subsequent lines (4-26) list parameters for the write action, followed by their values. Different actions use different parameters, and they do not all have to be specified. Note that the number of penalties is set to zero, as they are only relevant for the fitting action. See Section 3.2.1.1 for a full description SHAPE parameter files.

```
{SHAPE DESCRIPTION}
               1 {number of components}
{COMPONENT 0}
 c  0.000000e+00 {linear offset 0}
 c  0.000000e+00 {linear offset 1}
 c  0.000000e+00 {linear offset 2}
 c  0.000000e+00 {rotational offset 0}
 c  0.000000e+00 {rotational offset 1}
 c  0.000000e+00 {rotational offset 2}
         ellipse {component type}
 f      1.885000 {2a}
 f      1.011860 {a/b}
 f      1.035100 {b/c}
              20 {number of theta steps}

{PHOTOMETRIC FUNCTIONS}
               1 {number of radar scattering laws}
{RADAR SCATTERING LAW 0}
          cosine {type}
 c      1.000000 {R}
 f      0.848756 {C}
               1 {number of optical scattering laws}
{OPTICAL SCATTERING LAW 0}
     kaasalainen {type}
 c      0.100000 {R}
 c      0.682585 {wt}
 c      0.000000 {A0}
 c      5.314868 {D}
 c      0.000000 {k}


{SPIN STATE}
1999  2  3  0  0  0 {yyyy mo dd hh mm ss of t0}
 c   200.0000000000 {angle 0 (deg) lambda=110.000000}
 c    70.0000000000 {angle 1 (deg) beta=20.000000}
 f     0.0000000000 {angle 2 (deg)}
 c     0.0000000000 {spin 0 (deg/day)}
 c     0.0000000000 {spin 1 (deg/day)}
 f  3411.0128339357 {spin 2 (deg/day) P=2.532972}
 c   405.7512779148 {moment of inertia 0}
 c   470.4970660323 {moment of inertia 1}
 c   479.7490504153 {moment of inertia 2}
 c     0.0000000000 {spin 0 dot (deg/day/day)}
 c     0.0000000000 {spin 1 dot (deg/day/day)}
 c     0.0000000000 {spin 2 dot (deg/day/day)}
 c     0.0000000000 {Libration Amplitude (degrees)}
 c     0.0000000000 {Libration Frequency (degrees/day)}
 c     0.0000000000 {Libration Phase (degrees)}
                  0 {number of spin impulses}

{
volume  = 3.270774 km^3
com     = -0.000000 -0.000000 0.000087 km
inertia =  0.955874 -0.000000  0.000002
          -0.000000  0.967305 -0.000006
           0.000002 -0.000006  1.000000
}
```

Figure B.4: This SHAPE 'mod' file describes a slightly oblate single-component ellipsoid, the various radar and optical scattering parameters that should be applied to it, and the model's spin-state. The final section, describing the volume, centre of mass location, and moments of inertia, are updated automatically after a fitting run. Parameters set to 'c' are constant, and parameters set to 'f' are free and can be modified during fitting. See Section 3.2.1.2 for a full description of mod files.

```
{DATA FILE FOR SHAPE.C VERSION 2.10.5 BUILD Fri Mar 15 15:05:14 GMT 2019
    }

            3 {number of sets}

{SET 0}

-1 {is mpi node responsible for this set}

 c   0.000000e+00 c   0.000000e+00 c   0.000000e+00 {Euler angle offsets
    }
 c   0.000000e+00 c   0.000000e+00 c   0.000000e+00 {spin vector offsets
    }

delay-doppler {set type}

             0 {radar scattering law for this set}

             3 {number of ephemeris points}
{ yr mo dd hh mm ss     ra    dec    dist}
2001  3  4  9  0  0 251.76  21.89 0.067420
2001  3  4 10  0  0 251.56  22.42 0.067734
2001  3  4 11  0  0 251.36  22.94 0.068054

   2130.000000 {transmitter frequency (MHz)}

200 0.100000 1 1 short {delay: # bins, res (usec), spb, stride, code
    method}

100 1.000000 50.960000 41.000000 152 {dop: # bins, res (Hz), COM bin, DC
     bin, fftlen}

2001  3  4  9  0  0 {t0 of delcor poly}
             1 {order of polynomial}
 f  7.029865e+00 {coefficient 0}
 f  1.083724e+00 {coefficient 1}

 c  1.000000e+00 {Doppler scaling factor}

1    1.000 center {smearing: # views per frame, view interval (s), mode}

/data/lrd27/23187/arecibo2001 {data directory}

             5 {number of frames}
{                    name year mo dd hh mm ss          sdev
    calfact looks COM delay bin        weight mask}
2000pn9.mar04.p1us.nrm.01.rdf 2001  3  4  9 30 38 1.000000e+00 f
    2.672855e+02   100      50.540000 1.000000e+00    1
2000pn9.mar04.p1us.nrm.02.rdf 2001  3  4  9 37 56 1.000000e+00 f
    1.991512e+02   100      50.540000 1.000000e+00    1
2000pn9.mar04.p1us.nrm.03.rdf 2001  3  4 10 14 51 1.000000e+00 f
    3.423747e+02   100      50.540000 1.000000e+00    1
2000pn9.mar04.p1us.nrm.04.rdf 2001  3  4 10 21 44 1.000000e+00 f
    3.776012e+02   100      50.540000 1.000000e+00    1
2000pn9.mar04.p1us.nrm.05.rdf 2001  3  4 10 29 39 1.000000e+00 f
    3.311966e+02   100      50.540000 1.000000e+00    1
```

Figure B.5: This example `SHAPE` 'obs' file, which is continued in the following pages, describes one delay-Doppler set, one continuous wave set, and one lightcurve. Comments in this file describe each parameter, with further information available in Section 3.2.1.3. Note that unlike `convexinv` and `MATLAB`, `SHAPE` reads in 'standard' lightcurve files.

```
{SET 1}

-1 {is mpi node responsible for this set}

 c   0.000000e+00 c   0.000000e+00 c   0.000000e+00 {Euler angle offsets
    }
 c   0.000000e+00 c   0.000000e+00 c   0.000000e+00 {spin vector offsets
    }

       doppler {set type}

             0 {radar scattering law for this set}

             2 {number of ephemeris points}
{ yr mo dd hh mm ss     ra    dec    dist}
2001  3  4  9  0  0 251.76  21.89 0.067420
2001  3  4 10  0  0 251.56  22.42 0.067734

   2130.000000 {transmitter frequency (MHz)}

101 1.000000 51.000000 {dop: # bins, res (Hz), COM bin}

2001  3  4  9  0  0 {t0 of delcor poly}
             1 {order of polynomial}
 c  0.000000e+00 {coefficient 0}
 f  8.881034e+00 {coefficient 1}

 c  1.000000e+00 {Doppler scaling factor}

1    1.000 center {smearing: # views per frame, view interval (s), mode}

/data/lrd27/23187/areciboCW2001 {data directory}

             6 {number of frames}
{                    name year mo dd hh mm ss          sdev
    calfact looks       weight mask}
2000PN9.mar04.46.run1.1Hz.vig.dat 2001  3  4  9  4  1 1.000000e+00 f
    1.999452e+02   100 1.000000e+00    0
2000PN9.mar04.46.run2.1Hz.vig.dat 2001  3  4  9  6 21 1.000000e+00 f
    2.042625e+02   100 1.000000e+00    0
2000PN9.mar04.46.run3.1Hz.vig.dat 2001  3  4  9  8 41 1.000000e+00 f
    2.161914e+02   100 1.000000e+00    0
2000PN9.mar04.46.run4.1Hz.vig.dat 2001  3  4  9 11  1 1.000000e+00 f
    2.403412e+02   100 1.000000e+00    0
2000PN9.mar04.46.run5.1Hz.vig.dat 2001  3  4  9 13 21 1.000000e+00 f
    2.396185e+02   100 1.000000e+00    0
2000PN9.mar04.46.run6.1Hz.vig.dat 2001  3  4  9 15 41 1.000000e+00 f
    2.683838e+02   100 1.000000e+00    0
```

Figure B.5: (continued)

```
{SET 2}

-1 {is mpi node responsible for this set}

 c   0.000000e+00 c   0.000000e+00 c   0.000000e+00 {Euler angle offsets
    }
 c   0.000000e+00 c   0.000000e+00 c   0.000000e+00 {spin vector offsets
    }

    lightcurve {set type}

             0 {optical scattering law for this set}

             6 {number of asteroid ephemeris points} {03:51 to 07:01}
{ yr mo dd hh mm ss     ra    dec    dist}
2010 08 29 03 0 0 326.22722 12.98311 0.95529823910528
2010 08 29 04 0 0 326.20649 12.95903 0.95496496066709
2010 08 29 05 0 0 326.18575 12.93489 0.95463477517973
2010 08 29 06 0 0 326.16504 12.91068 0.95430759597086
2010 08 29 07 0 0 326.14441 12.88642 0.95398317102445
2010 08 29 08 0 0 326.12388 12.86210 0.95366110029784

             6 {number of solar ephemeris points}
{ yr mo dd hh mm ss     ra    dec    dist}
2010 08 29 03 0 0 157.34663   9.48033 1.00998560310193
2010 08 29 04 0 0 157.38511   9.46553 1.00997934755308
2010 08 29 05 0 0 157.42362   9.45075 1.00997062996284
2010 08 29 06 0 0 157.46211   9.43598 1.00995941007092
2010 08 29 07 0 0 157.50056   9.42123 1.00994581795448
2010 08 29 08 0 0 157.53892   9.40650 1.00993014517734

            -1 {number of calculated points}

1    1.000 center {smearing: # views per point, view interval (s), mode}


            153 {number of samples in lightcurve}
/data/lrd27/23187/LCfiles/23187_809_20100829R.dat f 1.00 1.000000e+00 {
   name, calfact, weight}
```

Figure B.5: (continued)